Lappeenranta
University of Technology

Ilya Petrov

COST REDUCTION OF PERMANENT MAGNET SYNCHRONOUS MACHINES

Thesis for the degree of Doctor of Science (Technology) to be presented with due permission of public examination and criticism in the Auditorium 1382 at Lappeenranta University of Technology, Lappeenranta, Finland on the 10th of June, 2015, at noon.

Acta Universitatis
Lappeenrantaensis 638

Supervisor Professor Juha Pyrhönen
Department of Electrical Engineering
LUT School of Energy Systems
Lappeenranta University of Technology
Finland

Dr. Pia Lindh
Department of Electrical Engineering
LUT School of Energy Systems
Lappeenranta University of Technology
Finland

Reviewers Professor Ion G. Boldea
Department of Electrical Engineering
University Politehnica of Timisoara
Romania

Dr. Luigi Alberti
Faculty of Science and Technology
Free University of Bozen-Bolzano
Italy

Opponent Professor Anouar Belahcen
Department of Electrical Engineering and Automation
Aalto University
Finland

Dr. Luigi Alberti
Faculty of Science and Technology
Free University of Bozen-Bolzano
Italy

ISBN 978-952-265-796-1
ISBN 978-952-265-797-8 (PDF)
ISSN-L 1456-4491
ISSN 1456-4491
Lappeenrannan teknillinen yliopisto
Yliopistopaino 2015

Abstract

Ilya Petrov

Cost Reduction of Permanent Magnet Synchronous Machines

Dissertation, Lappeenranta University of Technology
Lappeenranta 2015

Acta Universitatis Lappeenrantaensis 638
109 p.

ISBN 978-952-265-796-1
ISBN 978-952-265-797-8 (PDF)
ISSN-L 1456-4491
ISSN 1456-4491

Electrical machine drives are the most electrical energy-consuming systems worldwide. The largest proportion of drives is found in industrial applications. There are, however many other applications that are also based on the use of electrical machines, because they have a relatively high efficiency, a low noise level, and do not produce local pollution.

Electrical machines can be classified into several categories. One of the most commonly used electrical machine types (especially in the industry) is induction motors, also known as asynchronous machines. They have a mature production process and a robust rotor construction. However, in the world pursuing higher energy efficiency with reasonable investments not every application receives the advantage of using this type of motor drives. The main drawback of induction motors is the fact that they need slip-caused and thus loss-generating current in the rotor, and additional stator current for magnetic field production along with the torque-producing current. This can reduce the electric motor drive efficiency, especially in low-speed, low-power applications.

Often, when high torque density is required together with low losses, it is desirable to apply permanent magnet technology, because in this case there is no need to use current to produce the basic excitation of the machine. This promotes the effectiveness of copper use in the stator, and further, there is no rotor current in these machines. Again, if permanent magnets with a high remanent flux density are used, the air gap flux density can be higher than in conventional induction motors. These advantages have raised the popularity of PMSMs in some challenging applications, such as hybrid electric vehicles (HEV), wind turbines, and home appliances. Usually, a correctly designed PMSM has a higher efficiency and consequently lower losses than its induction machine counterparts. Therefore, the use of these electrical machines reduces the energy consumption of the whole system to some extent, which can provide good motivation to apply permanent magnet technology to electrical machines.

However, the cost of high performance rare earth permanent magnets in these machines may not be affordable in many industrial applications, because the tight competition between the manufacturers dictates the rules of low-cost and highly robust solutions, where asynchronous machines seem to be more feasible at the moment.

Two main electromagnetic components of an electrical machine are the stator and the rotor. In the case of a conventional radial flux PMSM, the stator contains magnetic circuit lamination and stator winding, and the rotor consists of rotor steel (laminated or solid) and permanent magnets. The lamination itself does not significantly influence the total cost of the machine, even though it can considerably increase the construction complexity, as it requires a special assembly arrangement. However, thin metal sheet processing methods are very effective and economically feasible. Therefore, the cost of the machine is mainly affected by the stator winding and the permanent magnets.

The work proposed in this doctoral dissertation comprises a description and analysis of two approaches of PMSM cost reduction: one on the rotor side and the other on the stator side. The first approach on the rotor side includes the use of low-cost and abundant ferrite magnets together with a tooth-coil winding topology and an outer rotor construction. The second approach on the stator side exploits the use of a modular stator structure instead of a monolithic one.

PMSMs with the proposed structures were thoroughly analysed by finite element method based tools (FEM). It was found out that by implementing the described principles, some favourable characteristics of the machine (mainly concerning the machine size) will inevitable be compromised. However, the main target of the proposed approaches is not to compete with conventional rare earth PMSMs, but to reduce the price at which they can be implemented in industrial applications, keeping their dimensions at the same level or lower than those of a typical electrical machine used in the industry at the moment.

The measurement results of the prototypes show that the main performance characteristics of these machines are at an acceptable level. It is shown that with certain specific actions it is possible to achieve a desirable efficiency level of the machine with the proposed cost reduction methods.

Keywords: permanent magnet synchronous machine, tooth-coil winding, fractional-slot non-overlapping winding, ferrite permanent magnet, modular stator structure.

Acknowledgements

The research described in this doctoral dissertation was carried out at the Department of Electrical Engineering at LUT School of Energy Systems at Lappeenranta University of Technology (LUT) between 2011 and 2015. The research was funded by LUT, EU regional funds, the City of Lappeenranta, the Academy of Finland, Konecranes and Industrial Technology Research Institute (ITRI).

First of all, I am very grateful to Professor Juha Pyrhönen for his guidance and patience during my studies. I was happy to have a supervisor who is not only a master in the field, but also a very responsible person with high management skills. Further, I am thankful to Dr. Julia Vauterin-Pyrhönen for giving me a chance to start studying in this great university. Many thanks go to my second supervisor Dr. Pia Lindh with her unquenchable source of optimism. Her belief in my research gave me additional motivation to concentrate my energy on it.

I am grateful to Dr. Markku Niemelä for his help at the beginning of my studies and providing high expertise during the assembly and measurements of the prototypes. His problem-solution-approach showed me how one should deal with a difficult problem. I would also like to thank Dr. Hanna Niemelä for the constructive and thorough correction of the English grammar of my publications within in a sometimes very limited time period.

I wish to thank Martti Lindh, Antti Suikki and Jouni Ryhänen who owing to their experience were able to solve many manufacturing issues during prototype assembly with high quality of the work.

I express my gratitude to Professor Ion Boldea and Dr. Luigi Alberti for the review of the dissertation and for their valuable comments. I would also like to thank Dr. Luigi Alberti and Professor Anouar Belahcen for finding time to be the opponents in the dissertation defense.

Many problems were solved with the help of my colleagues. I would like to thank my colleague and unofficial supervisor Pavel Ponomarev for his trust in my expertise and continuous generation of innovative ideas for further research. During intensive discussions with him, actual solutions have always been found. Further, I am grateful to Yulia Alexandrova and Maria Polikarpova for collaborative work together. During the research period you became not only colleagues but also close friends of mine.

I found many friends in LUT: Sultan Jumaev, Manuel Garcia Perez, Alexander Smirnov, Lyudmila Smirnova, Katteden Kamiev, Sergey Voronin, Polina Belova, Elvira Baygildina, Nikita Uzhegov, Maria Pronina, Kirill Murashko, Dmitry Kuleshov, Viktoria Kapusitna, Daria Nevstrueva, and Andrey Maglyas, to name but a few. They made my stay and work here filled with events and more fruitful.

Last but not least I am very grateful to the dearest women in my life − my mother Galina Petrova, my sister Ekaterina Petrova, my wife Daria Petrova and our daughter Ekaterina Petrova. Thank you for your support during these years. I am not afraid to face even the most difficult problem knowing that you are always ready to back me up if something goes wrong.

Ilya Petrov
June 2015
Lappeenranta, Finland

Contents

Abstract

Acknowledgements

Contents

List of publications **9**

Nomenclature **13**

1 Introduction **15**
1.1 Rare-earth PM free solutions 17
1.2 PMSMs with rotor embedded permanent magnets 25
1.3 Comparison of the outer rotor surface PMSM with the outer rotor embedded permanent magnet PMSM 29
1.4 Comparison of rotor surface PMSMs with different air gap flux densities 34
1.5 Outline of the work 39
1.6 Scientific contribution of the doctoral dissertation 41
1.7 Engineering contribution of the thesis 43

2 Outer rotor PMSM **45**
2.1 Tangential stress 50
2.2 Synchronous inductance 57
2.3 Torque ripple 68
2.4 AC losses 70
2.5 Measurement results 75

3 Segmented stator PMSM **83**
3.1 Influence of the stator segmentation arrangement on rotor-surface permanent magnet losses and rotor yoke losses 87
3.2 Influence of stator phase resistance on the machine performance 89
3.3 Challenges in segmented stator PMSMs 92
3.4 Suggestions for further research 95

4 Conclusion **97**

References **99**

List of publications

Publication I

Petrov, I., Pyrhönen, J., "Performance of Low-Cost Permanent Magnet Material in PM Synchronous Machines," *IEEE Transactions on Industrial Electronics* , vol.60, no.6, pp.2131−2138, June 2013

Publication II

Petrov, I., Polikarpova, M., and Pyrhönen, J., "Rotor surface ferrite magnet synchronous machine for generator use in a hybrid application — Electro-magnetic and thermal analysis," *in 39th Annual Conference of the IEEE Industrial Electronics Society, IECON 2013* , pp.3090−3095, 10−13 Nov. 2013

Publication III

Petrov, I., Ponomarev, P., Shirinskii, S., and Pyrhönen, J., "Inductance evaluation of fractional slot permanent magnet synchronous motors with non-overlapping winding by analytical approaches," *in 16th European Conference on Power Electronics and Applications (EPE'14-ECCE Europe), 2014* , pp.1−10, 26−28 Aug. 2014

Publication IV

Petrov, I., Ponomarev, P., and Pyrhönen, J., "Torque Ripple Reduction in 12-slot 10-pole Fractional Slot Permanent Magnet Synchronous Motors with Non-Overlapping Windings by Implementation of Unequal Stator Teeth Widths," *in XIX International Conference on Electrical Machines (ICEM), 2014*, pp.1−6, 2−5 Sept. 2014

Publication V

Petrov, I., Ponomarev, P., Alexandrova, Y., and Pyrhönen, J., "Unequal Teeth Widths for Torque Ripple Reduction in Permanent Magnet Synchronous Machines With Fractional-Slot Non-Overlapping Windings," *IEEE Transactions on Magnetics* , 2014

Publication VI

Ponomarev, P., Alexandrova, Y., Petrov, I., Lindh, P., Lomonova, E., and Pyrhönen, J., "Inductance Calculation of Tooth-Coil Permanent-Magnet Synchronous Machines," *IEEE Transactions on Industrial Electronics*, vol.61, no.11, pp.5966−5973, Nov. 2014

Publication VII

Ponomarev, P., Petrov, I., and Pyrhönen, J., "Influence of Travelling Current Linkage Harmonics on Inductance Variation, Torque Ripple and Sensorless Capability of Tooth-Coil Permanent-Magnet Synchronous Machines," *IEEE Transactions on Magnetics*, vol.50, no.1, pp.1−8, Jan. 2014

Publication VIII

Ponomarev, P., Petrov, I., and Pyrhönen, J., "Torque Ripple Reduction in Double-Layer 18/16 TC-PMSMs by Adjusting Teeth Widths to Minimize Local Saturation," *in XIX International Conference on Electrical Machines (ICEM), 2014*, vol., no., pp.1,6, 2-5 Sept. 2014

Author's contribution

Ilya Petrov is the principal author and investigator in papers I – V. In papers VI – VIII Dr. Pavel Ponomarev was the corresponding author and in paper VI Ilya Petrov calculated the synchronous inductance of the 12-slot 10-pole TCW PMSM and compared it with the measured values. In VII, Ilya Petrov took part in discussions together with the corresponding author about the reasons of the torque ripple in the TCW PMSM on the rotor side of the inner rotor permanent magnet arrangement. In VIII, an idea of torque ripple suppression used in the article was developed by Ilya Petrov.

Nomenclature

Abbreviations and symbols

J	current density	A/mm^2
A	linear current density	A/m
B	flux density	T
B_{PM}	permanent magnet flux density	T
B_δ	air gap flux density	T
b_d	tooth width	m
D_e	external diameter of the stator	m
D_δ	air gap diameter	m
D_s	stator diameter	m
H	magnetic field strength	A/m
h_d	tooth height	m
h_{ys}	height of stator yoke	m
h_{yr}	height of rotor yoke	m
h_{PM}	height of permanent magnet	m
I	current	A, RMS
i	current, instantaneous value $i(t)$	A
i_d	current along d-axis	A
i_q	current along q-axis	A
k_{Cu}	space factor for copper	-
k_w	winding factor	-
L_s	synchronous inductance	H
L_d	inductance along d-axis	H
L_q	inductance along q-axis	H
l_{PM}	permanent magnet length	m
l'	effective core length	m
l_{PM}	permanent magnet length	m
P	power, losses	W
p	number of pole pairs	-
R_δ	air gap radius	m
r_r	radius of rotor	m
S_{PM}	permanent magnet area	m^2
S_r	rotor area	m^2
S_u	slot area	m^2
S_c	cross-sectional area of conductor	m^2
T	torque	Nm
T_{rel}	reluctance torque	Nm
U	voltage	V, RMS
V	volume	m^3
Q_s	number of stator slots	
w_{PM}	permanent magnet width	m

z_{Q}	number of conductors in slot	
Ψ	magnetic flux linkage	Vs
Ψ_{PM}	permanent magnet flux linkage	Vs
φ	phase shift angle	rad, °
ζ	angle shift between air gap flux density and linear current density	rad, °
$\sigma_{F_{\mathrm{tan}}}$	tangential tension	Pa
δ	air gap	m
α_{PM}	relative permanent magnet width	

Subscripts

PMSM	Permanent magnet synchronous machine
PMASynRM	Permanent magnet assisted synchronous reluctance machine
PMSynRM	Permanent magnet synchronous reluctance machine
SRM	Synchronous reluctance machine
SMC	Soft magnetic composite
PM	Permanent magnet
TCW	Tooth-coil winding
MTPA	Maximum torque per amper
MTPV	Maximum torque per volt
HEV	Hybrid electric vehicle
FEM	Finite element method
DTC	Direct torque control
LCM	Least common multiple

1 Introduction

Electrical machines are a vital part of modern society. They are implemented in numerous applications and different systems worldwide. Moreover, according to a report by the U.S. Department of Energy in 1980, in the USA medium power motors from 0.75 kW to 90 kW consumed about 36 % of electricity generated in the USA, which is about 60 % of electricity supplied to the motors in total (Dorrell, 2014a). At present, 40 % of electricity produced worldwide is consumed by electrical machines in industrial applications (de Almeida et al., 2014). This together with the fact that energy consumption is constantly increasing — there has been a 50 % increase since 1980 to 2012 (Dorrell, 2014a) — demonstrates the importance of using high-efficiency electrical machines.

Induction motors are still considered the "workhorse" in industrial applications. This can be explained by their robust rotor construction and mature manufacturing technology. However, asynchronous machines suffer from additional losses in the rotor and stator windings. In order to reduce these losses additional actions should be taken. Many of these approaches (aiming at the loss reduction of the machine) increase the overall manufacturing cost. The approaches include a larger size of the machine, a copper cage winding in the rotor instead of aluminium one, the use of high-performance steel lamination with a high magnetic permeability and a low specific loss. Despite the fact that these actions lead to a higher price of the electrical machine (Parasiliti et al., 2004), they still cannot solve the inherent drawbacks of asynchronous machines, which are the requirement for an additional proportion of current in the stator (magnetizing current component) and a slip-based, loss-generating current flowing on the rotor side.

As it is mentioned above, if the efficiency of an induction machine is needed to be increased it usually leads to higher manufacturing cost compared to the original design, which is not very desirable for manufacturers. Therefore, special efficiency standards were developed. In each country there are specific efficiency standards for an electrical machine with a particular nominal power: for example, the USA and the EU have adopted the IEC standard (IE1−IE5). The minimum efficiency level of electrical machines is determined by this standard. It should be noted that there is a trend towards increasing the lower permitted efficiency limit for motors (Dorrell, 2014b).

As the use of high-efficiency electrical machines can pay back and cover their higher initial investment compared with their lower-efficiency counterparts over their life time, and the overall tendency is to limit the use of low-efficiency electrical machines, it is important to find solutions that provide lower losses, and consequently, a higher efficiency of the motor. However, from a motor manufacturer's point of view, low manufacturing cost a key issue, because they are among the key points that determine the manufacturer's competitiveness in the market. Therefore, the machine solution should also have competitive manufacturing costs compared with conventional induction motors.

In order to be able to analyse the losses in an asynchronous machine, it is necessary to have a clear picture of the origins of these losses. Figure 1.1 (a) shows the power loss distribution of a speed-controlled induction motor drive.

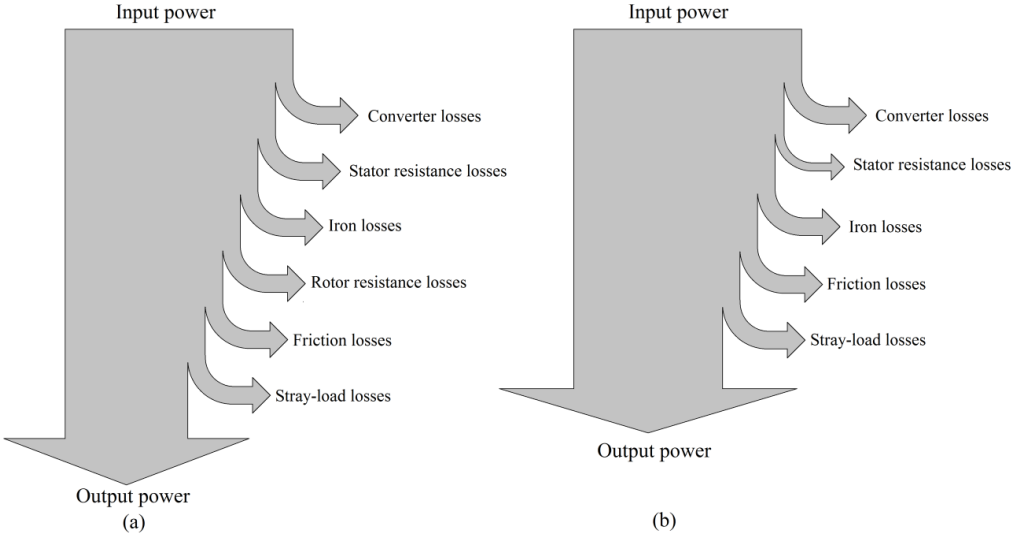

Figure 1.1: a) Loss distribution of an induction motor drive. b) Loss distribution of a permanent magnet synchronous motor drive. It should be noted that the reduced stator resistance losses shown in (b) are illustrated only to highlight that the stator resistance losses in PMSMs are typically lower compared with induction machines, but it does not mean that this loss component is smaller than other loss components in a PMSM.

Figure 1.1 (a) shows that all the losses in an induction motor drive can be divided into six different elements. Some of these loss components are inherent in all electrical motor drives with a controlled speed, these elements include for instance converter losses, iron losses, friction losses, stray-load losses, and stator resistive losses. Stator resistive losses are Joule losses in the stator winding, caused by the current running in it. This current can be divided into three components: magnetizing current, loss component, and torque production current. Additional stator losses produced by magnetizing currents (additional Joule losses) can be avoided if a PMSM is used instead of an induction motor, because PMSMs do not need to produce the magnetic flux in the machine by means of electricity. Even on the contrary, in high-performance PMSMs with advanced dynamic characteristics, also often referred to as servo motors (Puranen, 2006), the influence of armature current on the magnetic state of a machine has to be minimized, to increase the overload characteristics of this machine type.

Figure 1.1 (b) shows the loss distribution in a typical permanent magnet synchronous motor drive. We can see that there are no rotor resistive losses and the stator Joule losses are lower in PMSMs compared with induction machines. Therefore, if other losses (converter losses, iron losses and friction losses) are kept at the same level, it is

possible to significantly increase the efficiency of an electrical machine by exploiting permanent magnet technology (Petrov and Pyrhönen, 2013).

1.1 Rare-earth PM free solutions

One of the significant drawbacks of PMSMs in industrial applications is the fluctuating price of the rare-earth elements (i.e. neodymium, dysprosium), which are fundamental components of modern high performance permanent magnets (Morimoto et al., 2014a). It means that it is difficult to forecast the expenses of permanent magnet materials in the manufacturing process in the long term. The rapid increase in rare-earth magnet costs in 2011 boosted research on rare-earth-free electrical machine solutions even in some performance- or weight-critical applications, such as automotive electric propulsion systems (Boldea et al., 2014). Some of proposed approaches for rare-earth-free electrical machines found in the literature are: a synchronous reluctance ferrite permanent magnet assisted machine (Obata et al., 2014; Takeno et al., 2011), a switched reluctance motor (Kiyota et al., 2014), an axial flux ferrite permanent magnet synchronous machine (Chino et al., 2011), a ferrite spoke-type rotor PMSM (Kim et al., 2014), an outer rotor ferrite PMSM (Petrov et al., 2013), and even some interesting new ideas such as a wound-field synchronous motor, which is excited by space harmonics in the air gap (Aoyama and Noguchi, 2014). Most of the rare-earth-free solutions can be divided into two types: switched reluctance electrical machines and PMSMs applying ferrite permanent magnet technology.

Switched reluctance electrical machines have been intensively studied over the last few decades (Zhu and Liu, 2014; Vrenken et al., 2013; Silventoinen et al., 1999; Bianchi et al., 2002). However, the main problems related to these machines, for instance the specific requirements set by a unique converter structure and a high noise level, have not been solved yet.

The use of ferrite permanent magnets in electrical machines is another alternative to conventional PMSMs with rare-earth permanent magnets. The interest in this approach is increasing because of the abundant availability of these magnets and their low cost. However, ferrite magnets suffer from a low remanent flux density and a high demagnetization risk compared with rare-earth permanent magnets. Figure 1.2 shows, in the same scale, the volume of NdFeB, SmCo and Ferrite PM that have the same magnetic energy $V\times(BH)_{\max}$ (Petrov and Pyrhönen, 2013).

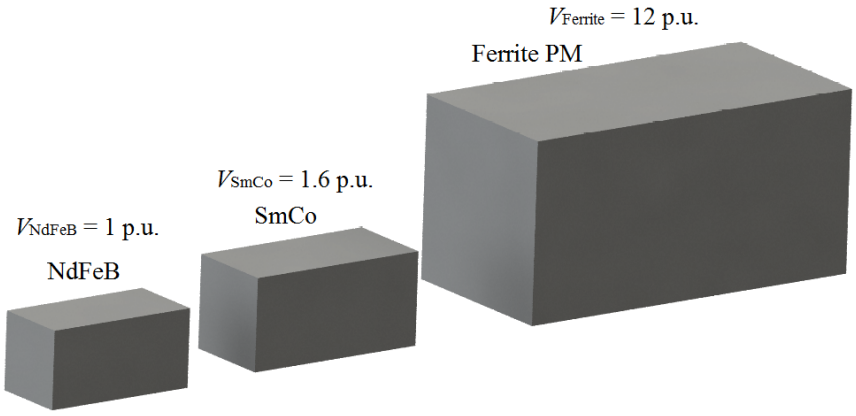

Figure 1.2 Volumes of rare-earth permanent magnets (NdFeB, SmCo) and Ferrite PM that have the same magnetic energy product.

Figure 1.2 shows that to reach the same excitation torque as in an electrical machine with rare-earth permanent magnets additional actions are required (magnetic flux concentration, larger air gap radius, the use of reluctance torque); otherwise, with the same machine structure, the maximum torque achievable can be much lower when ferrite magnets are used instead of rare-earth magnets.

Thus, it is challenging to design and construct a ferrite permanent magnet electrical machine with a power suitable for most industrial applications (0.75 − 90 kW). The weakness of ferrite magnets can be compensated by enhancing the magnetic flux concentration produced by these magnets; some examples are shown in Figure 1.3.

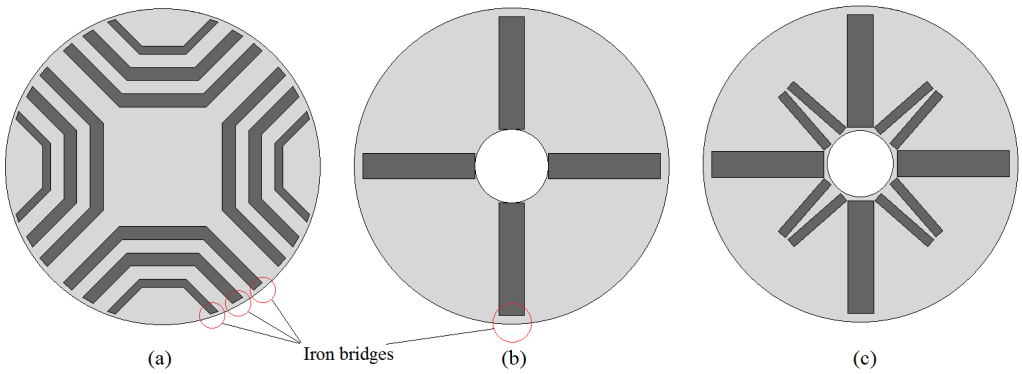

Figure 1.3: Approaches to magnetic flux concentration on the rotor side a) V-shape permanent magnet rotor. With this rotor structure it is possible to achieve inductance saliency (difference of the inductances along the d- and q-axes). b) Spoke type permanent magnet rotor. c) W-shape permanent magnet rotor; with this rotor structure, a significant flux concentration can be achieved (Chiba et al., 2013).

The use of magnetic flux concentration can be most efficient in spoke-type permanent magnet rotors with a high pole pair number, because in this case the amount of magnetic material in the rotor can be increased, whereas in rotor surface PMSMs the volume of the permanent magnet material at different pole pair numbers remains approximately at the same level, as it is shown in Figure 1.4 (c, d).

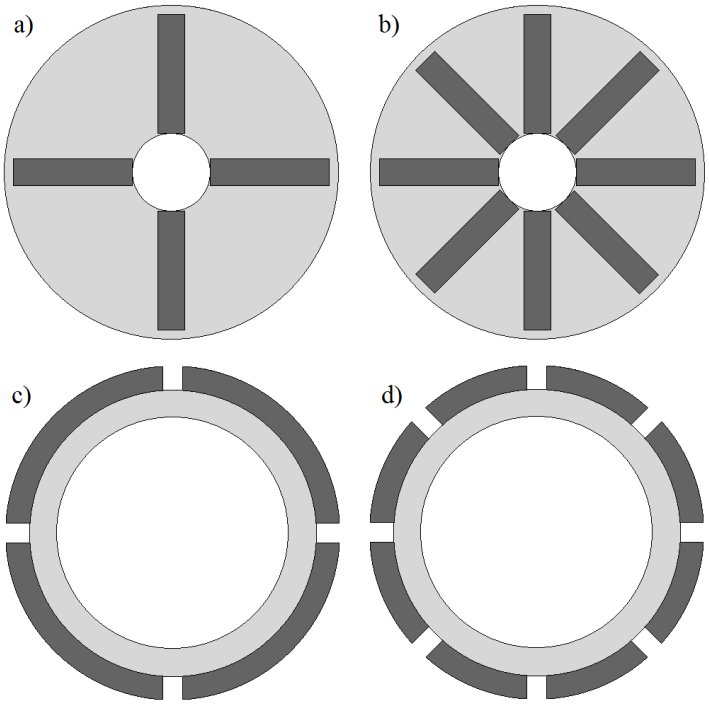

Figure 1.4: Rotor arrangements of PMSMs with different pole numbers, a) Spoke type permanent magnet rotor with four poles. b) Spoke type permanent magnet rotor with eight poles. c) Surface permanent magnet rotor with four poles, d) Surface permanent magnet rotor with eight poles.

Figure 1.4 shows that if a higher pole number is used in a spoke-type permanent magnet rotor, it is possible to increase the amount of permanent magnet material to concentrate the magnetic flux. However, in the case of rotor surface PMSMs with a higher pole number, the amount of permanent magnet material remains approximately the same. Therefore, no additional magnetic flux can be attained in rotor surface PMSMs with higher pole numbers.

It should be noted that in a spoke-type permanent magnet rotor there is a trade-off between the height of the magnet and its maximum possible width, because of the limited area in the inner rotor radius, as it can be seen in Figure 1.4 (b). This means that if the magnet has a higher height, the maximum magnet width is lower. The labelling of the permanent magnet dimensions is shown in Figure 1.5.

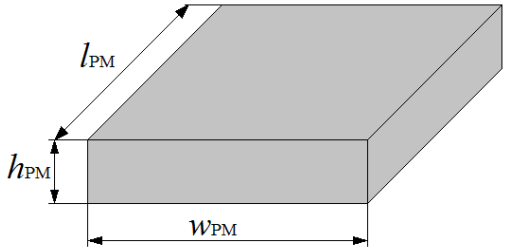

Figure 1.5: Labelling of the magnet dimensions. The length of the permanent magnet (l_{PM}) is given in the axial direction of the PMSM. The maximum width of the magnet (w_{PM}) is limited by the rotor dimensions, pole number, and permanent magnet height (h_{PM}) in spoke type rotor PMSMs.

The permanent magnet flux density is limited by its remanent flux density and magnetic circuit reluctance. However, by increasing the height of the permanent magnet it is possible to reduce the influence of an external magnetic circuit on the permanent magnet flux and keep the no-load permanent magnet flux density closer to its remanent flux density. The permanent magnet flux density in a magnetic circuit with silicon steel and an air gap can be estimated as

$$B_{\mathrm{PM}} = \frac{H_{\mathrm{C}} h_{\mathrm{PM}} \mu_{\mathrm{PM}} \mu_{\mathrm{Fe}} \mu_0}{\mu_{\mathrm{PM}} l_{\mathrm{Fe}} + \mu_{\mathrm{Fe}} h_{\mathrm{PM}} + \mu_{\mathrm{PM}} \mu_{\mathrm{Fe}} l_\delta} \tag{1.1}$$

Theoretically, in rotor surface PMSMs the larger permanent magnet height provides a higher flux density in the air gap, and consequently, a higher power with the same air gap radius. However, at some point (when the permanent magnet flux density is close to its remanence) it is not possible to increase the permanent magnet height any further, because no significant improvement in the air gap flux density can be achieved. In this case, the permanent magnet material is not used very efficiently, which impacts on the overall price of the machine. There may also be another problem related to approaching the remanent flux density at no-load. In such a case, it is possible that the armature reaction momentarily increases the flux density of the magnet material beyond B_{r}. Consequently, the magnetic material may be prone to hysteresis losses (Pyrhönen et al., 2015).

The magnetic flux of a PMSM depends on the permanent magnet flux density and its active surface ($S_{\mathrm{PM}} = l_{\mathrm{PM}} \times w_{\mathrm{PM}}$). In a rotor surface PMSM the active permanent magnet surface does not depend on the magnet height, and the maximum permanent magnet active surface can be obtained by

$$S_{\mathrm{PM.max}} = 2\pi R l_{\mathrm{PM}} \tag{1.2}$$

However, in the case of a spoke-type rotor, the permanent magnet height has an influence on the maximum active surface and can be estimated as

$$S_{\mathrm{PM.max}} = 4pw_{\mathrm{PM.max}}l_{\mathrm{PM}} \tag{1.3}$$

where the maximum magnet width can be written as

$$w_{\mathrm{PM.max}} = R - \frac{pR}{\pi}\cos^{-1}\left(1 - \frac{h_{\mathrm{PM}}^2}{2R^2}\right) \tag{1.4}$$

In Eqs. (1.3) and (1.4) we can see that in the spoke-type rotor PMSM (with constant air gap radius and machine length), the maximum magnet surface depends on both the magnet height and the number of poles. Therefore, a spoke-type permanent magnet rotor does not always have a larger maximum permanent magnet surface compared with a rotor surface PM as it is shown in Figure 1.6.

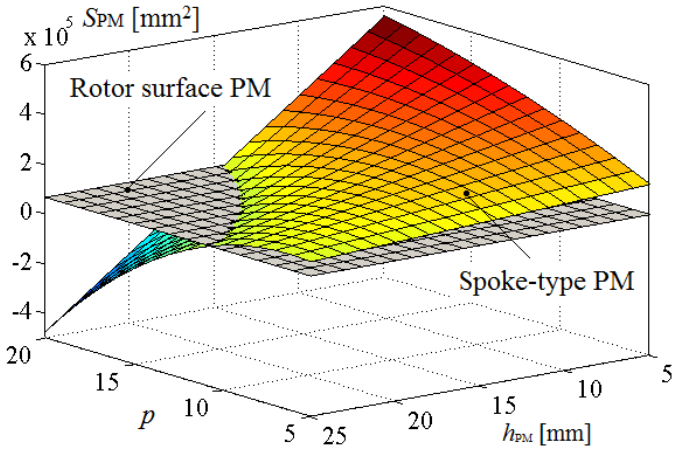

Figure 1.6: Maximum active permanent magnet surface in a spoke-type rotor and a rotor surface PM as a function of pole pair number and permanent magnet height. The rotor has the dimensions r = 100 mm and l_r = 100mm. If the permanent magnet surface area appears to be negative it means that this rotor construction is not realizable.

Figure 1.6 shows that at a moderate permanent magnet height and pole pair number it is possible to significantly increase the permanent magnet active surface, which has a direct influence on the permanent magnet flux, and consequently, on the flux density in the air gap.

It should be noted that in a spoke-type rotor, the flux path crosses only one permanent magnet, whereas in a rotor with surface PMs it crosses two permanent magnets, as it is shown in Figure 1.7. This means that if the height of one permanent magnet is the same in both rotor types, the effective total permanent height used in Eq. (1.1) to estimate the permanent magnet flux density in a spoke-type rotor should be only half of that of a rotor surface PM. Therefore, the permanent magnet flux density in a spoke-type rotor with the same permanent magnet height can be expected to be lower than that of a rotor surface PM.

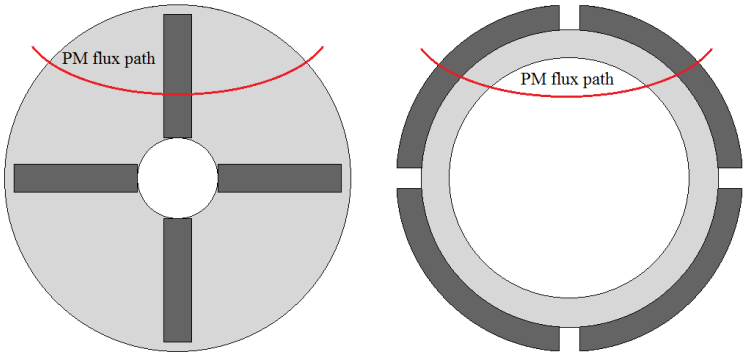

Figure 1.7: Flux paths in a) spoke type rotor and, b) rotor surface PM. In the spoke-type rotor the flux line crosses only one magnet, whereas in the rotor surface PM it crosses two magnets.

In order to validate the analytical results achieved above and to show the performance difference between the spoke-type rotor and the rotor surface-magnet PMSM, it was decided to verify the results by a FEM simulation. Figure 1.8 depicts two PMSMs, one with a rotor surface PM (a) and another one with a spoke-type rotor (b). They have the same external stator and rotor dimensions, the same permanent magnet height, and the same pole pair number, which are: r_δ = 126 mm, l =100 mm, h_{PM} = 13 mm, and p = 10. According to Eqs. (1.2)−(1.4), the maximum active permanent magnet surface in the machine of Figure 1.8 (a) is $S_{PM.max}$ = 0.079 m^2, and in the machine of Figure 1.8 (b) it is $S_{PM.max}$ = 0.337 m^2. This means that if the permanent magnet flux density were the same in both machines, the one with the spoke-rotor type would induce approximately 420 % back-EMF compared with the rotor surface PM. However, the permanent magnet flux density in these two machines is different because of the different effective permanent magnet heights, as it was described above.

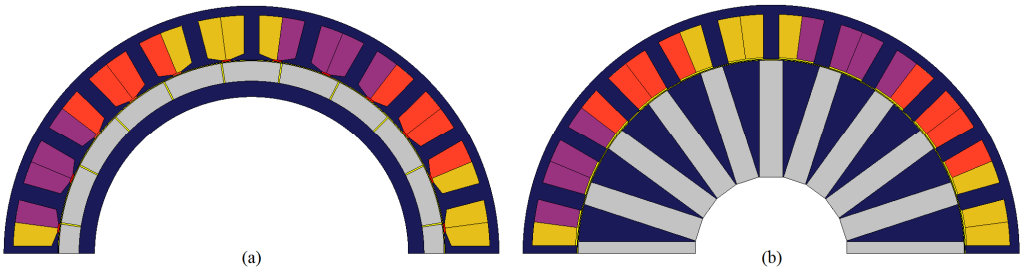

Figure 1.8: PMSMs model in the commercial FEM software. a) Rotor surface-magnet. b) Spoke-type rotor.

The flux density map of the machines under study at no-load is shown in Figure 1.9. The figure shows that the permanent flux density in the spoke-type rotor is lower than that of the rotor surface PM. This is due to the lower effective permanent magnet height in the spoke-type rotor and the slightly higher stator steel reluctance, which results from the higher flux density in it. Therefore, the increase in the back EMF is lower than only the ratio of the active permanent magnet surfaces in these two machines.

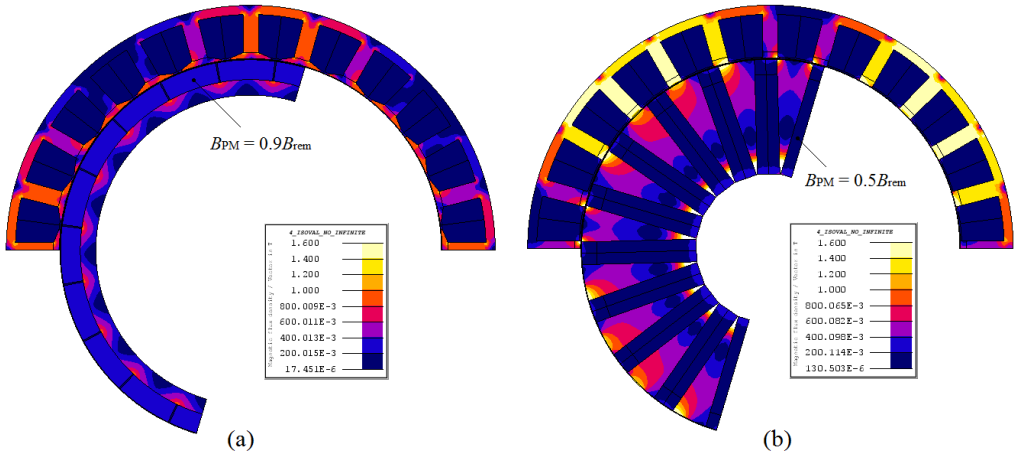

Figure 1.9: Flux maps of PMSMs at no-load. a) Rotor surface PM. b) Spoke-type rotor. The remanent flux density of the permanent magnets is B_{rem} = 0.34 T. The permanent magnet flux densities are different in these machines, because the effective permanent magnet height in the spoke-type rotor is only half of that of the rotor with surface-permanent magnets.

The induced back EMF of the PMSMs shown in Figure 1.9 (n = 1500 rpm, N_{ph} = 48) is illustrated in Figure 1.10.

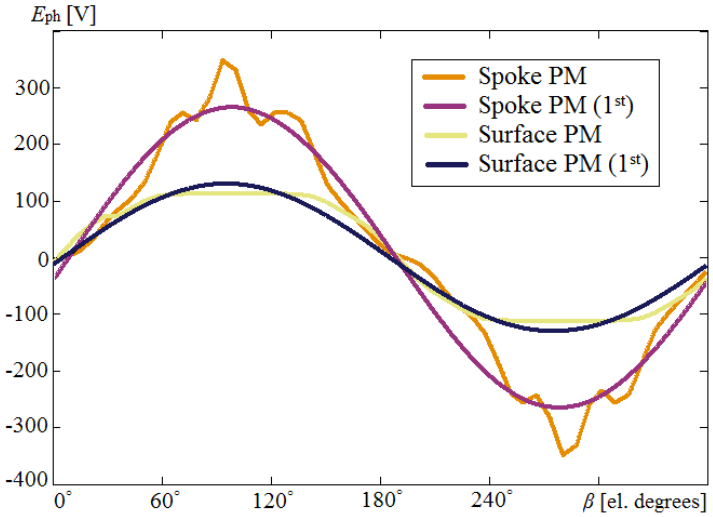

Figure 1.10: Back-EMF curves of the two machines illustrated in Figure 1.9 at 1500 rpm, and their fundamental (1st) harmonics.

Figure 1.10 illustrates that the fundamental back EMF in the rotor surface PMSM is approximately half of that of the spoke-type rotor PMSM. This means that there can still be a significant increase in the air gap flux density in the spoke-type PM, even though the permanent magnet flux density is significantly lower than in the rotor surface-magnet PMSM.

It should be noted that in the case of the spoke-type rotor it is possible to use totally open slots, as it is shown in Figure 1.8 (b), because the flux concentration takes place on the rotor side, whereas in the rotor with surface PMs, semi-closed slots should be used.

As a conclusion of the studies on possible flux concentration, we may state that it is possible to achieve a significant air gap flux density boost if the rotor with embedded permanent magnets is used, and if there are no mechanical restrictions on the inner rotor radius to reserve this place for additional permanent magnet material. However, in this case, the stator should also be redesigned to avoid significant oversaturation in the stator steel lamination. Further, it should be noted that in the studied cases with embedded magnets, the steel supporting bridges in the rotor were not considered. In practice, they produce a significant permanent magnet flux leakage, and can considerably reduce the total air gap flux density, even though it can be still higher than in the rotor surface PMSM. Again, the air gap flux density can have an influence on the synchronous inductance of a machine because of the different number of turns required for achieving a particular voltage level. This aspect is described in more detail in Section 1.4.

Another approach to increase the torque and power density of a machine with ferrite magnets is to use a larger air gap radius. Without increasing the machine outer dimensions, this can be achieved with an outer rotor or axial-flux structure. In this case, the stator flux linkage increases as a result of the larger surface area of the permanent magnet that faces the air gap, as it is shown in Figure 1.11, where a conventional inner rotor PMSM and an outer rotor PMSM are shown in the same scale.

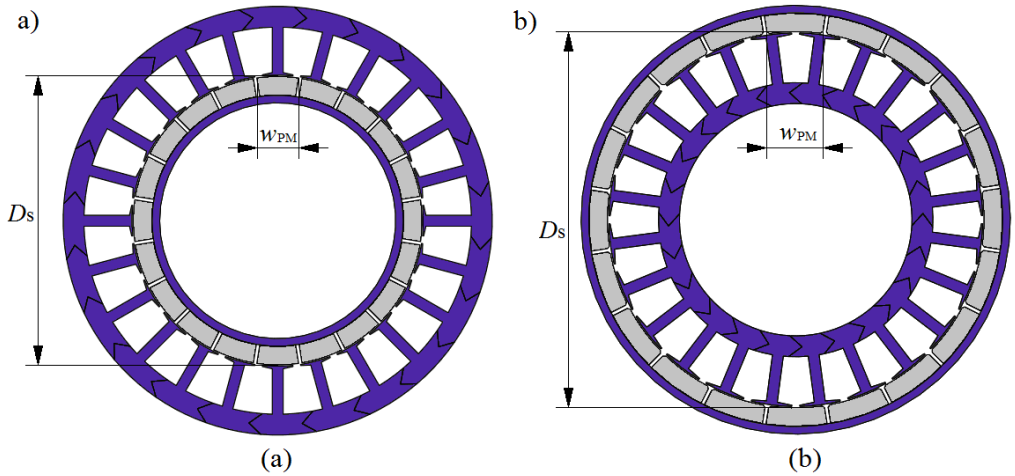

Figure 1.11: a) Conventional inner rotor PMSM. b) Outer rotor PMSM. The external dimensions of the machines are the same. The slot area is kept constant in both machines. The relatively high thickness of the stator yoke can be explained by the segmented structure, which requires additional room in the stator yoke for connecting it to the frame of the machine. Ferrite magnets are used in both cases.

Figure 1.11 shows that the permanent magnet width w_{PM} of the PMSM with the inner rotor is lower compared with the outer rotor topology. This reduces the value of permanent magnet flux linkage, which is estimated by (if it is assumed that there is no PM flux leakage) the permanent magnet flux density B_{PM}, the number of winding turns in the stator N_S and the PM surface S_{PM} as

$$\Psi_{PM} = k_w S_{PM} B_{PM} N_S = k_w l_{PM} w_{PM} B_{PM} N_S \tag{1.5}$$

Therefore, in the inner rotor PMSM, the back-EMF value and the torque performance are also lower compared with the outer rotor topology, if the slot space factor and the current density are kept the same. This advantage of the outer rotor PMSMs was one of the main reasons that encouraged the author to start studying this type of electrical machines, especially for industrial applications, where inexpensive and robust constructions are required. Thus, the focus of the work has been on low-cost materials and manufacturing of PMSMs while keeping their performance at a competitive level. The work addresses the outer rotor topology, the use of ferrite permanent magnets, tooth-coil winding, segmented construction, and different design optimizations to enhance torque performance (Petrov and Pyrhönen, 2013; Petrov et al., 2013; Petrov et al., 2014a; Petrov et al., 2014c; Petrov et al., 2014b; Ponomarev et al., 2014a; Ponomarev et al., 2014b; Ponomarev et al., 2014c)

The tooth-coil winding arrangement, which is often referred to as fractional slot non-overlapping winding, has been a “hot topic” in the literature over the last decade. This can be explained by the constructional and electromagnetic advantages of the winding arrangement, a shorter end-winding length, cheaper and simpler assembly, better field-weakening characteristics, a lower cogging torque, and a lower torque ripple. All of these constructional features of TCW PMSMs extensively discussed in the literature (EL-Refaie et al., 2008; Alberti et al., 2014; Petrov and Pyrhönen, 2013; Barcaro and Bianchi, 2012).

We may conclude that outer rotor surface TCW PMSMs combine the above listed advantages from different aspects. This leads to a simplified and lower-cost manufacturing process without compromising the machine performance. However, these electrical machines (with rotor surface ferrite permanent magnets) are not very extensively studied in the higher power range ($\geq$ 50 kW), and thus, the objective of this work is to bridge this research gap. Chapter 2 describes this type of a machine in more detail, with challenges and limitations that these PMSMs may face.

1.2 PMSMs with rotor embedded permanent magnets

The concentration of magnetic flux is an advantageous technique to increase the torque or power density of an electrical machine. Together with the flux concentration, an inductance saliency can be achieved. According to (Bianchi et al., 2000), inductance saliency can be successfully used to increase the maximum torque of a PMSM and to improve its field-weakening performance by means of reluctance torque. Reluctance

torque can be produced in a machine having different d- and q-axis inductances L_d and L_q. The influence of the difference in inductance (along d- and q-axis) on the reluctance torque can be expressed as:

$$T_{rel} = (L_d - L_q) i_d i_q \tag{1.6}$$

Therefore, the use of ferrite magnets together with the inductance saliency technique has been intensively studied over the last few years (Barcaro and Bianchi, 2014; Vartanian et al., 2012; Morimoto et al., 2014b). These types of machines are often called PM-assisted synchronous reluctance motors (PMASynRM). Usually, the main purpose of ferrite magnets in these machines is to improve their power factor. In order to roughly compare the performances of a synchronous reluctance machine (SRM) and a PMASynRM, vector diagrams of the machines with similar d- and q-axis inductances are shown in Figure 1.12 (a, b) (Bianchi, 2013). The phase stator resistance is often not shown in vector diagrams, and it is assumed to be negligible if it is lower than 0.02 p.u., which is usually the case for middle- and large-size industrial electrical machines. Therefore, from here onwards, the phase resistance is not taken into account when presenting the machine performance by the vector theory (except the cases when $R_s \geq$ 0.02 p.u.).

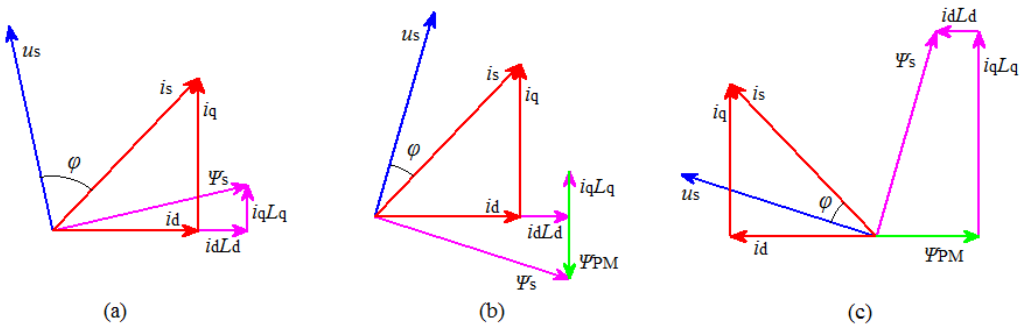

Figure 1.12: a) Vector diagram of the SRM: u_S = 0.97 p.u., i_S = 1 p.u., i_d = 0.7 p.u., i_q = 0.7 p.u., Ψ_S = 0.97 p.u., Ψ_{PM} = 0 p.u., i_dL_d = 0.95 p.u. i_qL_q = 0.21 p.u., φ = 58°. b) Vector diagram of the PMASynRM, q-axis is in the permanent magnet flux direction: u_S = 1 p.u., i_S = 1 p.u., i_d = 0.7 p.u., i_q = 0.7 p.u., Ψ_S = 1 p.u., Ψ_{PM} = 0.5 p.u., i_dL_d = 0.95 p.u., i_qL_q = 0.21 p.u., φ = 28°. c) Vector diagram of the same PMASynRM as in (b), but represented by a different logic (as a permanent magnet machine), the d-axis is in the permanent magnet direction . The stator resistance is assumed negligible.

Comparing the vector diagrams in Figure 1.12 (a, b), we may see that by insertion of permanent magnet flux linkage, which is only 0.5 p.u., it is possible to "compensate for" the armature reaction and improve the power factor of the machine. In Figure 1.12 (c), the same PMASynRM is illustrated, but with a different logic of presentation (the d- and q-axes are switched and the machine is treated as a permanent magnet machine with saliency). A conventional PMSM is usually represented so that the permanent magnet flux linkage is along the d-axis. However, there is no difference between the machines shown in Figure 1.12 (b and c), the difference is only a matter of terminology. In the

case of Figure 1.12 (b), the machine can be called a synchronous reluctance PM assisted machine, and in the case of Figure 1.12 (c), it can be called a permanent magnet synchronous reluctance machine. As this doctoral dissertation is not dedicated to purely synchronous reluctance machines, from here onwards the d-axis is the one that is along the permanent magnet flux linkage. A division between the PMASynRM and the PMSynRM could be made based on the torque components. A machine producing mostly PM torque is a PMSynRM while a machine producing mostly reluctance torque is a PMASynRM.

It should be noted that the use of permanent magnets in an electrical machine not only leads to an additional source of flux linkage which produces an excitation torque component (Nerg et al., 2014), but it also has an influence on the saturation behaviour of different iron paths, especially on the rotor side (Tokuda et al., 2009). This leads to different saturation levels of the iron bridges in the rotor, and consequently, to a variation in the synchronous inductance. Therefore, the performance and behaviour of the machine after insertion of even a small amount of magnets may be quite different from a purely synchronous reluctance machine.

The variation in the synchronous inductance in different load points of a PMSM with inner rotor permanent magnets should be analysed carefully, because saturation and cross-saturation phenomena are especially significant in most of these machine types (Ponomarev et al., 2014b; Ruuskanen et al., 2014b). This means that at the nominal power, the inductance saliency can be different and the maximum performance can be lower than expected. This phenomenon can also have an influence on the controllability of the machine if the control estimates the position of the rotor based on its inductance saliency (Ponomarev et al., 2014b).

PMSMs with inner rotor permanent magnets can also be subject to significant torque ripple, and a special arrangement should be implemented to reduce the torque ripple (Alberti et al., 2014; Barcaro and Bianchi, 2012). Especially, the torque ripple can be very significant in deep field weakening area (in percentage of the applied torque). According to the author's understanding, this is partially explained by the fact that in the field weakening area, a large demagnetization current component is applied to reduce the magnetic flux on the stator side, which makes the inductance variation very sensitive to the rotor position and stator current uncertainties. However, not very much was found in the literature to support these assumptions.

A PMSM with inner rotor permanent magnets is a promising arrangement in terms of torque and power density. In addition, if the mechanical assembly is considered, the rotor lamination that covers permanent magnets protects them from detachment at high speeds (in the case of an inner rotor) and other external mechanical influences. Insertion of rare-earth permanent magnets inside the rotor can significantly reduce the eddy current losses in them, because the iron layer above them serves as a path for magnetic flux variations and reduces the alternating magnetic flux from the armature to penetrate through the magnet. The rare-earth permanent magnet eddy current losses may have a

high value, because the typical resistivity of NeFeB is between 0.9 − 1.8 μΩm (Ruoho et al., 2009; Neorem Magnets, 2015). Therefore, the influence of possible eddy current losses on the thermal state of the rare-earth permanent magnet should be carefully analysed to prevent possible demagnetization faults.

At high loads, the reluctance torque component in a PMSM with inner rotor embedded permanent magnets can reach a very high value, which depends on the machine structure and can be larger than the excitation torque. For example, in the Toyota Prius II motor, the reluctance torque component can be even half of the total torque (Cai et al., 2014). This shows the importance of keeping the inductance saliency ratio as high as possible in that type of machines.

Concentration of the magnetic flux on the rotor side significantly complicates the rotor structure, because laminated rotor steel should usually be used in this case. Further, mechanical issues related to the robustness of the construction have to be solved. For example, there is a trade-off between the permanent magnet flux leakage (through iron bridges in the rotor) and its mechanical reliability when the thickness of the iron bridge is varied. Therefore, many approaches have been suggested in the literature to reduce or to get rid of iron bridges (EL-Refaie et al., 2014; Lindh et al., 2013; Sampathirao and Baylon, 2014; Cirani et al., 2014).

In the case of rotor surface ferrite PMSMs, it is not necessary to use a laminated rotor yoke, because the relatively large effective air gap significantly suppresses the alternating magnetic flux components caused by the armature reaction. The rotor surface ferrite permanent magnets do not suffer from eddy currents either, because they have a very high electric resistivity (Petrov and Pyrhönen, 2013). This means that an outer rotor can be advantageous in applications that require a low-cost and robust PMSM construction and that have a higher efficiency compared with asynchronous machines.

Even though the reluctance torque can significantly impact the total torque achieved in distributed winding PMSMs (Obata et al., 2014), it is very challenging to get any competitive reluctance torque in the case of TCW PMSMs, because of the significant leakage inductance, which decreases the difference in the d- and q-axis inductances (Barcaro and Bianchi, 2011). Further, because of the large leakage inductance in TCW PMSMs (Ponomarev et al., 2014a), the field weakening can be achieved easier if such a load mode is required by the application, even in the surface rotor permanent magnets. Therefore, the surface rotor topology seems to be more feasible when the TCW PMSM is used, owing to its lower permanent magnet flux leakages and simpler construction.

We may conclude that two main torque density increase approaches in TCW PMSMs that apply ferrite magnets are embedded permanent magnet technology (mainly for the flux concentration) and outer rotor topology with rotor surface PM. However, it is also interesting to discuss the possibility of using embedded permanent magnet technology together with outer rotor topology. This is discussed in the following section.

1.3 Comparison of the outer rotor surface PMSM with the outer rotor embedded permanent magnet PMSM

In (Petrov and Pyrhönen, 2013) it was shown that an outer rotor PMSM with rotor surface ferrite magnets can have higher power density compared with the inner rotor PMSM because of the larger air gap radius and the larger active permanent magnet surface. However, if a PMSM with embedded permanent magnets is considered, it can be used in order to achieve permanent magnet flux concentration and also to bring some benefits in terms of additional reluctance torque. For this reason, it is necessary to analyse and compare the following types of electrical machines: an outer rotor PMSM with surface ferrite magnets and an outer rotor PMSM with embedded permanent magnets.

The use of embedded magnets can change the rotor thickness (which includes rotor steel and permanent magnets) regardless of the magnetic circuit reluctance. It means that in the case of an outer rotor construction with the particular external dimensions, the use of embedded magnets instead of surface PMs can decrease the air gap diameter, as it is shown in Figure 1.13. Therefore, if the size of the machine and the electric loading remain the same, the air gap flux density should be inversely proportional to the decreasing radius squared in order to be able to reach the same torque density in an outer rotor PMSM with embedded magnets as in a rotor surface PMSM.

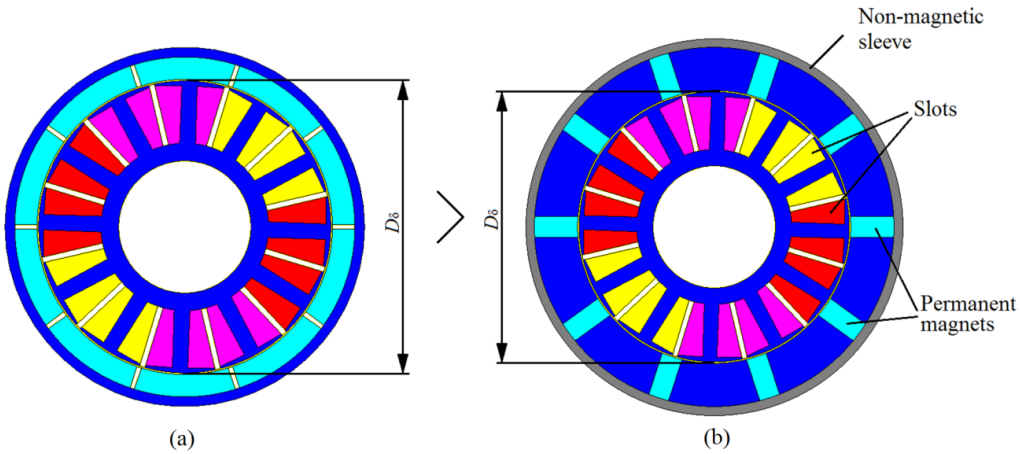

Figure 1.13: Outer rotor PMSMs with the same external diameter of the active elements a) with rotor surface PMs and b) with embedded PMs.

It should be noted that the torque of the machine with embedded magnets also contains reluctance torque, which is not the case with the rotor surface PMs. However, if tooth-coil winding is considered (e.g. 12-slot 10-pole machine construction) the reluctance torque has a lower impact on the total torque than a machine with a distributed winding (Barcaro and Bianchi, 2011; Tangudu et al., 2009). It means that in this case, it is

reasonable to only consider the torque produced by the permanent magnets and the armature current.

In order to have the same permanent magnet flux in an outer rotor PMSM with embedded permanent magnets (spoke rotor type) as in a PMSM with rotor surface permanent magnets, it is necessary to have a double permanent magnet height and half of its width as it shown in Figure 1.14.

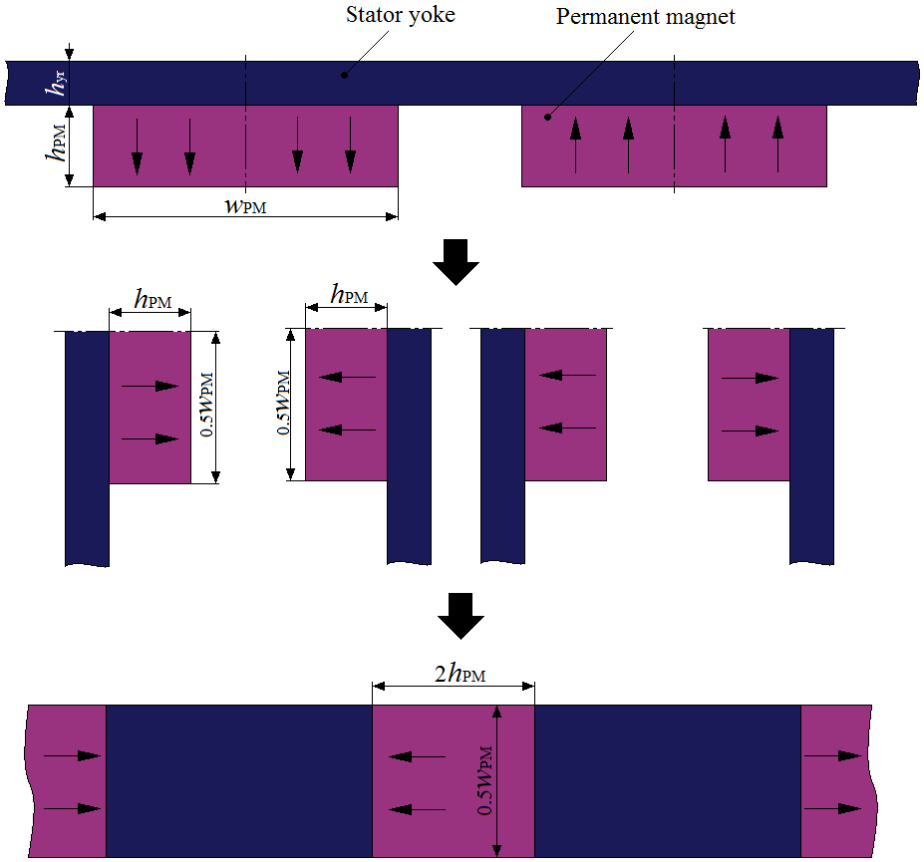

Figure 1.14: Permanent magnet reconfiguration where the magnets are transferred from the rotor-surface-magnet to embedded-magnet rotor (spoke type).

Analytically, the ratio of the external rotor diameters owing to the permanent magnet reconfiguration from the rotor-surface-magnet to embedded-magnet (for the outer rotor PMSM) can be estimated as

$$\frac{D_{\text{er.emb}}}{D_{\text{er.surf}}} = \frac{w_{\text{PM}} + D_{\delta}}{2h_{\text{PM}} + 2h_{\text{yr}} + D_{\delta}} \tag{1.7}$$

whereas the permanent magnet width in the rotor surface type is written as

$$w_{\mathrm{PM}} = \alpha_{\mathrm{PM}} \frac{\pi(D_\delta + h_{\mathrm{PM}})}{2p} \tag{1.8}$$

Combining Eq. (1.7) with Eq. (1.8), the ratio of the external rotor diameters (embedded and surface rotor types) can be estimated by

$$\frac{D_{\mathrm{er.emb}}}{D_{\mathrm{er.surf}}} = \alpha_{\mathrm{PM}} \frac{\pi(D_\delta + h_{\mathrm{PM}})}{2p\left(2h_{\mathrm{PM}} + 2h_{\mathrm{yr}} + D_\delta\right)} + \frac{D_\delta}{2h_{\mathrm{PM}} + 2h_{\mathrm{yr}} + D_\delta} \tag{1.9}$$

In Eq. (1.9) we can see that the ratio of the external rotor diameters of the embedded and surface permanent magnet rotor types depends on the air gap diameter D_δ, the permanent magnet height h_{PM}, the rotor yoke height h_{yr}, the relative permanent magnet width α_{PM}, and the number of pole pairs p. An example of a comparison of external rotor diameters with different permanent magnet heights and pole pair numbers is shown in Figure 1.15.

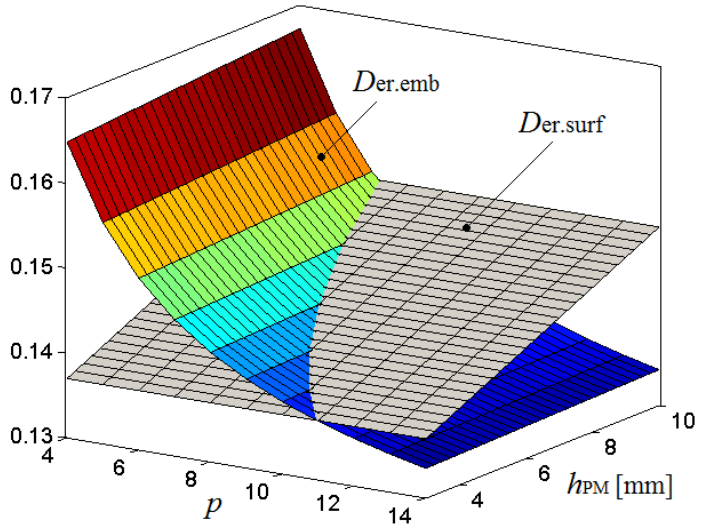

Figure 1.15: Comparison of outer rotor external diameters with rotor surface permanent magnets ($D_{\mathrm{er.surf}}$) and with rotor embedded permanent magnets ($D_{\mathrm{er.emb}}$). The rotor yoke height is h_{yr} = 5 mm, the permanent magnet height is h_{PM} = 10 mm, the air gap diameter is D_δ = 121 mm, and the relative permanent magnet width is α_{PM} = 0.9.

Figure 1.15 demonstrates that if the number of pole pairs is relatively low, it is not advantageous to use embedded permanent magnets in the outer rotor topology. However, even at a high number of pole pairs (e.g. p = 10) there is not much gain in the external dimensions of the machine, especially, if the additional non-magnetic supporting unit (non-magnetic sleeve) is taken into account. Further, the embedded magnets make the rotor construction more complicated from the manufacturing point of view, which requires the use of laminated iron (to reduce iron losses), and there are higher requirements regarding the precision of component dimensions.

It should be noted that in the case of embedded magnets, it is possible to increase the permanent magnet width, which also increases the external rotor diameter. Therefore, it is possible to increase the flux produced by the permanent magnets, and consequently, the air gap flux density by having a larger external rotor diameter, which can be determined by

$$D_{\mathrm{er}} = D_{\delta} + w_{\mathrm{PM}} \tag{1.10}$$

whereas if it is assumed that no saturation occurs in the stator, the air gap flux density can be estimated as

$$B_{\delta} = \frac{2pw_{\mathrm{PM}}B_{\mathrm{PM}}}{\pi D_{\delta}} \tag{1.11}$$

Assuming that the linear current density is not changed with the flux density variation (if the steel permeability is assumed to be linear), it is possible to increase the tangential stress by producing a higher air gap flux density. In this case, the tangential stress and torque are directly proportional to the air gap flux density, and they can be defined by

$$\sigma_{F_{\tan}} = \frac{\hat{A}\hat{B}_{\delta}\cos\zeta}{2} \tag{1.12}$$

$$T = \sigma_{F_{\tan}} l\pi \frac{D_{\delta}^2}{2} \tag{1.13}$$

Combining Eqs (1.10)–(1.14), the final torque expression for the outer rotor PMSM with embedded permanent magnets (spoke type) is given as

$$T = l\frac{D_{\delta}}{2}Ap(D_{\mathrm{er}} - D_{\delta})B_{\mathrm{PM}}\cos\zeta \tag{1.14}$$

In Eq. (1.14) it can be seen that the torque depends on both the air gap diameter and the difference between the external rotor diameter and the air gap diameter. Figure 1.16 shows a comparison of the torque estimated by Eq. (1.14) and the torque of the outer rotor surface permanent magnet PMSM with the same parameters.

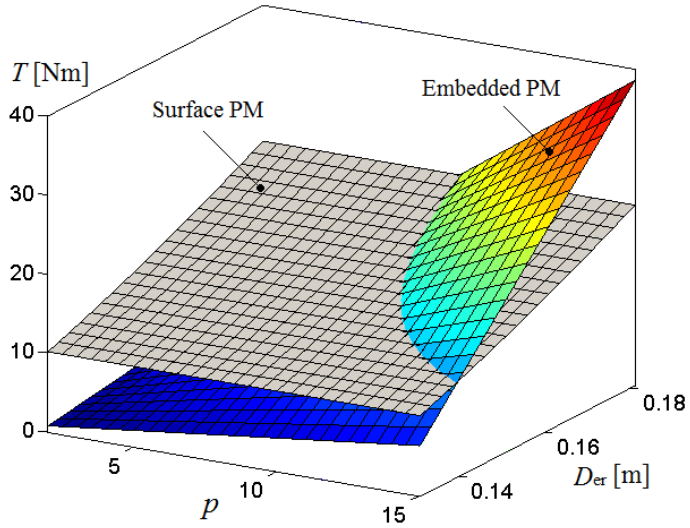

Figure 1.16: Torque as a function of pole pair numbers p and external rotor diameter D_{er} of the outer rotor PMSM with embedded permanent magnets (spoke type) and of the rotor surface PMSM. The permanent magnet height is h_{PM} = 10 mm, the rotor yoke height is h_{yr} = 5 mm, the air gap diameter of the PMSM with embedded magnets is D_{δ} = 121 mm, the machine length is l = 110 mm, the permanent magnet flux density is B_{PM} = 0.28 T, the linear current density is A = 46 kA/m, and the relative permanent magnet width in the rotor surface PMSM is α_{PM} = 0.9. It is assumed that the permeability of the stator does not change as a function of air gap flux density.

Figure 1.16 shows that with a moderate number of pole pairs, the outer rotor PMSM with rotor surface permanent magnets has a higher power density than a similar PMSM with embedded permanent magnets (spoke type). However, with high numbers of pole pairs and with a large difference between the air gap diameter and the external rotor diameter, it is possible to achieve a higher torque density with a spoke-type rotor.

Concluding the discussion about the rotor surface permanent magnet and embedded permanent magnet approaches, we may state that in most of the outer rotor PMSM cases, a rotor surface permanent magnet is more advantageous because of its simpler construction and smaller external dimensions (at a moderate number of pole pairs). However, embedded permanent magnets can be successfully applied to concentrate the permanent magnet flux and increase the air gap flux density. In this section, it was assumed that the air gap flux density does not have an influence on the electrical loading (A) of the machine, because the saturation factor is not taken into account. Therefore, the resultant torque is directly proportional to the achieved air gap flux density. However, it is not completely valid if the saturation is taken into account as it described in the following section.

1.4 Comparison of rotor surface PMSMs with different air gap flux densities

Rare-earth permanent magnets have a relatively high remanent flux density compared with ferrite permanent magnets. Therefore, the air gap flux density in a machine with rare-earth permanent magnets should be larger than in the machine with ferrite magnets, if these two magnet types are used in similar rotor surface PMSMs and have the same PM height. According to Maxwell's stress tensor the air gap flux density has a direct influence on the overall tangential stress, and consequently, on the torque of the machine:

$$\sigma_{F_{\tan}} = \frac{B_{\mathrm{t}} B_{\mathrm{n}}}{\mu_0} \tag{1.15}$$

Therefore, the machine with a higher air gap flux density (produced by permanent magnets) is expected to have a higher power density. However, this argument is not completely valid for PMSMs, as it shown below.

The steel used in the electrical machine (usually silicon steel) has a non-linear *BH* curve. This means that it has a particular limit of flux density after which the permeability of the steel starts to decrease rapidly (Pyrhönen et al., 2014). Therefore, the geometry of the machine steel parts should be selected according to the maximum magnetic flux to avoid oversaturation regions, otherwise it would lead to a reduction in the magnetic circuit permeability. It means that in a PMSM with a particular air gap flux density, the stator teeth width, the stator yoke width, and the rotor yoke width should be optimized to keep the peak flux density in the permitted range, which usually does not exceed 1.8 T (Pyrhönen et al., 2008).

It should be noted that the flux density in the tooth depends on its magnetic flux and cross-sectional area. It means that with lower flux values, the flux density decreases (if the cross sectional area of the tooth remains the same). In this case, in order to use steel and permanent magnets efficiently, the tooth cross-sectional area should be optimized so that the flux density reaches the point close to the steel saturation level (1.5 − 1.8 T). If it is assumed that the machine has the same geometry along its length in the axial direction, it can be solved as a 2D problem. In this case, the flux density in the tooth can be increased only by reducing its width (with a constant air gap flux density). This means that if all other parameters remain the same (air gap radius, slot height), the slot area increases with the reduction in the tooth width. Therefore, with a larger slot area it is possible to increase the electrical loading and to some extent, compensate for the reduction in magnetic loading, which is a result of the lower air gap flux density.

According to Eq. (1.5), the flux linkage is a result of the product of the flux density, the surface area, and the number of winding turns. In an electrical machine with a moderate

saturation level, the main flux path takes place in the steel region. Therefore, the flux linkage in TCW PMSM of the winding with N_s turns can be written as

$$\hat{\Psi} = k_w \hat{B}_d b_d l N_s \tag{1.16}$$

The number of winding turns in Eq. (1.16) is usually selected such that the desirable voltage level (and consequently the flux linkage) at the nominal load is reached. However, with a particular number of winding turns, the wire area is directly proportional to the slot area.

In conclusion, based on the fact that the number of turns can be reduced if the air gap flux density increases, which leads to a larger armature tooth width, and the fact that the larger armature tooth width leads to a smaller slot area (if the external machine dimensions remain the same), we may state that the higher air gap flux density reduces the electrical loading (A) of the machine. Thus, achieving a machine with the maximum power density is not a straightforward task. Instead, it means that a very high air gap flux density does not necessarily yield the machine with the highest possible power density.

Analytically, the trade-off between the air gap flux density and the electrical loading of an outer rotor PMSM can be expressed by the phase current (with a constant current density in the conductor) as function of air gap flux density (with a constant tooth flux density) as follows

$$\hat{\Phi} = \frac{2}{\pi} \hat{B}_\delta \tau_p l \tag{1.17}$$

$$b_d = \frac{\hat{\Phi}}{\hat{B}_d l} \tag{1.18}$$

$$h_{ys} = \frac{\hat{\Phi}}{\hat{B}_{ys} l} \tag{1.19}$$

$$h_d = (r_\delta - h_1 - h_2 - h_3) - \left(r_{in.st} + h_{ys} + h_3\right) \tag{1.20}$$

$$N_s = \frac{\hat{E}}{\hat{\Phi} \omega k_w} \tag{1.21}$$

$$S_{\mathrm{u}} = \frac{\pi(r_\delta - h_1 - h_2 - h_3)^2 - \pi(r_\delta - h_1 - h_2 - h_3 - h_{\mathrm{d}})^2}{Q_{\mathrm{s}}} - b_{\mathrm{d}}h_{\mathrm{d}} - 2h_3h_{\mathrm{d}} - b_{\mathrm{c}}h_{\mathrm{d}} \tag{1.22}$$

$$z_{\mathrm{Q}} = \frac{2N_{\mathrm{s}}m}{Q_{\mathrm{s}}} \tag{1.23}$$

$$S_{\mathrm{c}} = \frac{S_{\mathrm{u}}k_{\mathrm{Cu}}}{z_{\mathrm{Q}}} \tag{1.24}$$

$$R_{\mathrm{ph}} = \frac{N_{\mathrm{s}}l_{\mathrm{ew}}}{\sigma_{\mathrm{Cu}}S_{\mathrm{c}}} \tag{1.25}$$

$$I_{\mathrm{ph}} = JS_{\mathrm{c}} \tag{1.26}$$

The outer rotor PMSM described in (Petrov and Pyrhönen, 2013) was studied as an example to determine the phase current (with a constant current density) and the phase resistance as function of air gap peak flux density. Further, the influence of other parameters such as the inner stator radius, the stator tooth peak flux density and the stator yoke peak flux density on the optimized solution was considered.

Figure 1.17 presents the phase current and the phase resistance as a function of air gap peak flux density and inner stator radius (with all the other parameters constant) derived from Eqs. (1.17)−(1.26).

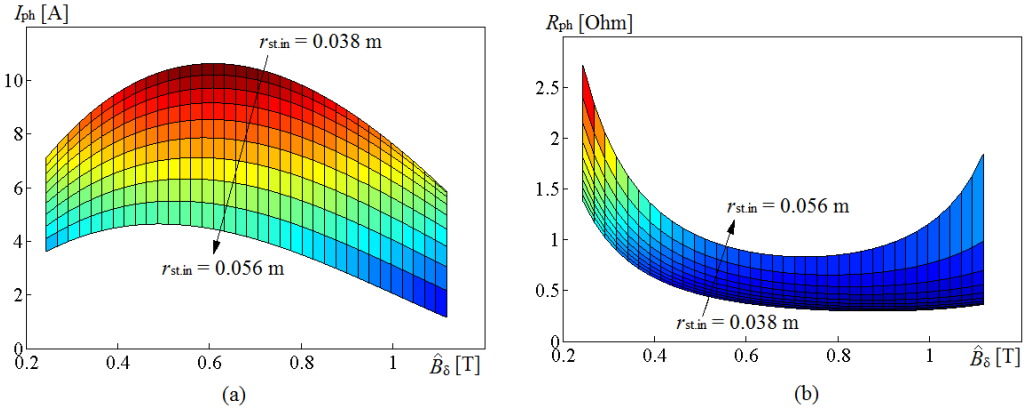

Figure 1.17: a) Maximum phase current and b) phase resistance as function of air gap peak flux density and inner stator radius ($r_{\mathrm{st.in}}$). The current density is J = 3.6 mm^2, the stator tooth peak flux density is $\hat{B}_{\mathrm{d}} = 1.6$ T, and the stator yoke peak flux density is $\hat{B}_{\mathrm{ys}} = 1.3$ T.

Figure 1.17 shows that if the inner stator radius has to be larger in order to reserve inner space for some other needs, the maximum phase current can be achieved at a relatively low air gap peak flux density, which is approximately $\hat{B}_\delta = 0.5$ T. However, the phase resistance, and consequently, the Joule losses in the stator winding with a larger inner stator radius increase, because of the limited slot space, which leads to a lower wire area.

Figure 1.18 depicts the phase current and the phase resistance as a function of air gap flux density, stator tooth peak flux density, and stator yoke peak flux density (with all the other parameters constant) derived from Eqs. (1.17)–(1.26).

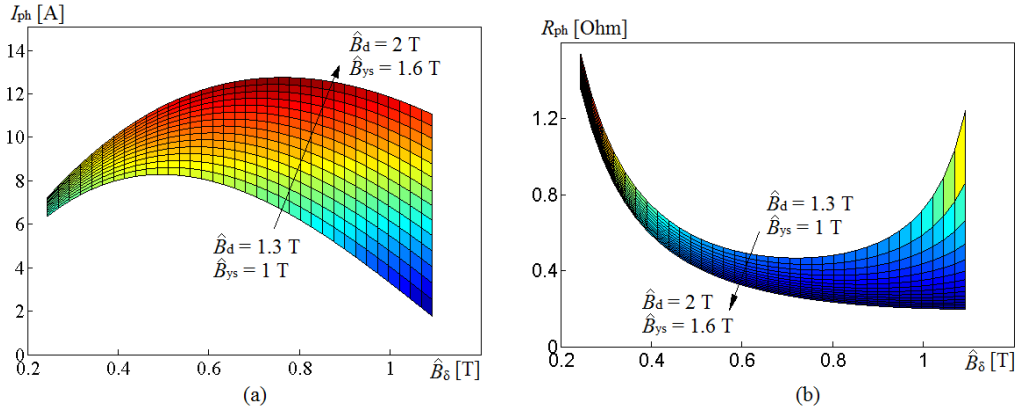

Figure 1.18: a) Maximum phase current and b) phase resistance as a function of air gap flux density, stator tooth peak flux density ($\hat{B}_d$), and stator yoke peak flux density $\hat{B}_{ys}$. The current density is $J = 3.6$ mm^2 and the inner stator radius is $r_{st.in} = 0.04$ m.

Figure 1.18 shows that with lower values of stator tooth and stator yoke peak flux density, the maximum current (with constant inner stator radius and current density) can be achieved at a relatively low air gap flux density ($\hat{B}_\delta = 0.45$ T). Often, in high-speed machines (with a high electrical frequency), the flux density in the stator yoke and in the stator tooth is selected to be below the saturation point to avoid excessive iron losses in the machine (Uzhegov et al., 2014). Therefore, in this case, the air gap flux density can be selected lower than the value that the modern rare-earth magnets can provide with the conventional air gap height.

Figure 1.19 shows a scaled view of three PMSMs with different air gap flux densities, and with the same tooth flux density, yoke flux density, phase current, and current density. The PMSMs in Figure 1.19 (a) and (c) have the highest possible and the lowest possible air gap flux densities if other machine parameters are constant, whereas the machine in Figure 1.19 (b) is the original PMSM with ferrite magnets and an air gap peak flux density $\hat{B}_\delta = 0.37$ T. We can see that the original machine has the lowest external dimensions compared with its counterparts with the utmost (the lowest possible and the highest possible) air gap flux densities. However, if other parameters of the machine can be changed (e.g. the stator tooth peak flux density and the stator yoke peak

flux density) the external dimensions of the machine with a higher air gap flux density will be lower.

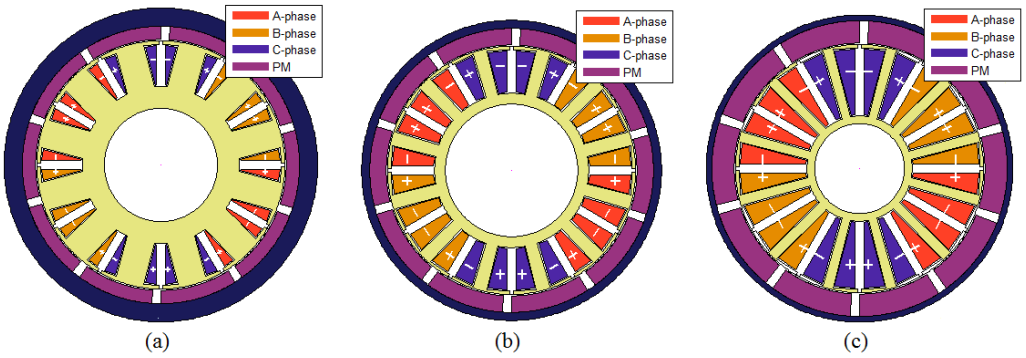

Figure 1.19: Scaled view of the analytically evaluated outer rotor PMSMs with different permanent magnet remanences (different air gap peak flux densities) and with the constant stator tooth peak flux density $\hat{B}_{\mathrm{d}} = 1.6$ T and the stator yoke flux density $\hat{B}_{\mathrm{ys}} = 1.3$ T. a) The air gap peak flux density is $\hat{B}_{\delta} = 0.9$ T, b) the original geometry of the PMSM with the air gap flux density is $\hat{B}_{\delta} = 0.37$ T, and c) the air gap flux density is $\hat{B}_{\delta} = 0.27$ T.

In the previous analysis the value of the phase current was chosen as the main input parameter. However, it does not necessarily guarantee a constant power for all three cases shown in Figure 1.19 because of different synchronous inductances. As it is mentioned above, the peak air gap flux density at the required voltage level has a direct influence on the number of turns, whereas the magnetizing inductance can be calculated by

$$L_{\mathrm{m}} = \frac{m}{2}\frac{2}{\pi}\mu_0 \frac{1}{2p}\frac{4}{\pi}\frac{\tau_{\mathrm{p}}}{\delta_{\mathrm{eff}}} l'(k_{\mathrm{w}}N_{\mathrm{s}})^2 \tag{1.27}$$

In Eq. (1.27) we can see that the magnetizing inductance is proportional to the number of winding turns squared. Therefore, at a very low air gap flux density (where a high number of turns are required to reach a certain voltage level), the magnetizing inductance can have a large value. Again, the synchronous inductance, which contains the magnetizing inductance and other inductance components, as it is described in Section (2.2), has a direct influence on the maximum torque at a particular speed, and if the inductance saliency is not considered, it can be estimated as (Salminen et al., 2005)

$$T_{\max} = \frac{mp}{\omega_s^2}\frac{EU}{L_{\mathrm{s}}} \tag{1.28}$$

According to Eqs. (1.27) and (1.28), it can be concluded that apart from the nominal current and the phase resistance, the maximum torque also varies as a function of air gap flux density as a result of the synchronous inductance variation. Therefore, when the air gap flux density is selected in the machine design optimization process, the

maximum torque should be taken into account in order to achieve feasible overload capabilities.

A more detailed analysis of the influence of the slot geometry on the synchronous inductance and on the nominal power variation (as a function of synchronous inductance) is given in Section 2.2.

In summary, we may state that the maximum air gap flux density does not necessarily provide the highest tangential stress, because with limited external machine dimensions there is often a trade-off between the magnetic and electrical loadings of the PMSM. Therefore, in order to find the optimal solution with the highest power density it is necessary to analyse the maximum electrical loading as a function of air gap flux density with the given machine constraints.

1.5 Outline of the work

The main objective of the doctoral dissertation is to develop PMSM structures suitable for industrial applications in terms of performance characteristics and manufacturing cost. The challenges faced in the work were related to the inevitable reduction in the machine performance if low-cost solutions are implemented. However, two PMSM structures with a competitive performance and low manufacturing costs were developed. The first PMSM structure included the use of low-cost and abundant ferrite magnets with the outer rotor and tooth-coil winding topology. The manufacturing process of the second PMSM structure could be simplified by using a segmented stator structure with a halved number of stator coils, lower stator steel waste during the lamination manufacturing, and a simpler winding routine. However, the paper about PMSM with segmented stator structure is not published yet. Therefore, the paper is not included in this dissertation. Its contents is briefly referred in Chapter 3.

The doctoral dissertation contains four chapters and eight original papers. The discussions in the dissertation are related to the limitations and advantages of the proposed PMSM topologies, with the focus on tangential stress, synchronous inductance, torque ripple, solid rotor losses, demagnetization risk, economical aspects, dynamic performance, overload capability, and fault conditions. The discussion is supported by simulated and measured results. The directions for future work are suggested at the end of the dissertation.

Publication I describes the benefits of using an outer rotor surface ferrite permanent magnets synchronous machine topology in an industrial application. The machine topology was compared with conventional asynchronous machines in the range of a few kilowatts. The main idea of the torque density increase by implementing the outer rotor structure in the case of ferrite permanent magnets was suggested by Prof. Pyrhönen. Mr. Petrov showed the feasibility of the concept by FEM simulations and measurement results.

Publication II describes one of the limiting factors of using ferrite magnets in PMSMs, which is the demagnetization risk. Further, the performance characteristics of the designed PMSM were analysed at different permanent magnet temperatures. A non-uniform permanent magnet cooling factor was taken into account, which allowed observing the permanent magnet parts that are mostly subjected to the demagnetization risk. Mr. Petrov estimated the loss distribution in the PMSM and its performance characteristics. Dr. Polikarpova evaluated the thermal state of the permanent magnets. Prof. Pyrhönen was in charge of the supervision of the project and the revision of the paper.

Publication III shows alternative methods of synchronous inductance evaluation in a tooth-coil winding PMSM. The conventional method of analytical synchronous inductance computation was compared with the proposed one, which does not take iron saturation into account and with a magnetic equivalent circuit model. The importance of saturation on the stator side for correct machine performance estimation was highlighted. The drawbacks of analytical approaches compared with FEM were described. Mr. Petrov developed the proposed analytical approaches of synchronous inductance estimation and compared them with the FEM results. Dr. Ponomarev thoroughly reviewed the paper. Prof. Shirinskii gave valuable feedback on the paper considering the magnetic equivalent circuit model. Prof. Pyrhönen was in charge of the supervision of the project and thorough revision of the paper.

Publication IV shows one of the possible reasons for a torque ripple increase in rotor surface PMSMs at higher loads. A non-uniform peak flux density in the stator teeth of a 12-slot 10-pole PMSM was shown. An analytical approach of the synchronous inductance variation caused by the described phenomena was evaluated and compared with the FEM analysis. This synchronous inductance variation was considered the main reason for the 6^{th} torque ripple harmonic in the rotor surface magnet 12-slot 10-pole PMSM. Mr. Petrov developed an analytical method for the evaluation of the synchronous inductance variation and the torque ripple. Dr. Ponomarev thoroughly reviewed the paper. Prof. Pyrhönen was in charge of the supervision of the project and revision of the paper.

Publication V describes a possible way to reduce torque ripple and cogging torque in TCW PMSMs. It was shown that skewing alone is not capable of eliminating torque ripple and can even cause an increase in the torque ripple in some load conditions. Different stator teeth widths were suggested to achieve the same peak flux density in them in a particular load point. This approach was implemented together with stepped skewing of the rotor. Three TCW PMSMs in different power ranges were simulated to verify the feasibility of the concept. Mr. Petrov found the reason for synchronous inductance variation in rotor surface magnet TCW PMSMs, and developed a method to reduce its negative effects. Dr. Ponomarev modelled a 18-slot 16-poles PMSM with the proposed method and took part in reviewing the paper. Dr. Alexandrova modelled a large power wind generator with the proposed method. Prof. Pyrhönen was in charge of the supervision of the project and revision of the paper.

Publication VI reviews different analytical methods of synchronous inductance evaluation in TCW PMSMs, which can be implemented at early design stages. The paper describes a method of harmonic air-gap leakage factor computation and its influence on the synchronous inductance. Methods of synchronous inductance component evaluation were considered and compared with each other. Four different TCW PMSMs were simulated by the FEM and measured to verify the correctness of the analytical synchronous inductance evaluation with a reasonable error between the measured and analytical results. Dr. Ponomarev was the principal author and investigator of the paper. He was responsible for the theoretical analysis of the paper, explanation of the suggested synchronous inductance evaluation principles, and verification of the analytical results by FEM computations. Dr. Alexandrova took part in reviewing of the paper. Mr. Petrov implemented the analytical equations described in the paper to estimate the inductance of the 12-slot 10-pole machine and verified the results by the FEM and measurements. Dr. Lindh implemented the analytical equations described in the paper to estimate the inductance of an inner rotor TCW PMSM and verified the results by the FEM and measurements. Prof. Lomonova reviewed the paper. Prof. Pyrhönen was in charge of the supervision of the project and revision of the paper.

Publication VII describes the importance of correct synchronous inductance evaluation in the case of sensorless control, when iron saturation is taken into account. The origin of torque ripple on the rotor side was described for TCW PMSMs. Possible solutions for torque ripple reduction were suggested. Dr. Ponomarev was the principal author and investigator of the paper. He modelled an 18-slot 16-pole PMSM by the FEM to estimate the inductance variation in different load conditions. Mr. Petrov thoroughly reviewed the paper. Prof. Pyrhönen was in charge of the supervision of the project and revision of the paper.

Publication VIII implements the method described in Publication IV for an 18-slot 16-pole TCW PMSM. It was shown that this method can be successfully used for other type of tooth-coil winding topologies than the 12-slot 10-pole TCW PMSM. Dr. Ponomarev was the principal author and investigator of the paper. He modelled the 18-slot 16-pole PMSM by the FEM at the nominal load with different stator teeth widths to reduce the torque ripple. Mr. Petrov was the investigator of the method. Prof. Pyrhönen was in charge of the supervision of the project and revision of the paper.

1.6 Scientific contribution of the doctoral dissertation

The main target of the doctoral dissertation is to study the technical and economic feasibility of rotor-surface ferrite magnet PMSMs with an outer rotor topology for typical industrial applications in the power range of 0.75 − 90 kW. The research hypothesis is that such machines are feasible and can compete with other solutions, at least in special cases.

The study involves knowledge from different engineering areas that are used as boundary conditions in the optimization of the PMSM. Mechanical, thermal, and

electro-magnetic analyses are combined to find the practical optimum. The optimization comprises continuous iteration of the machine design to find a suitable solution that can satisfy all the requirements regarding the mechanical assembly, safety during the machine operation, proper cooling capability and reliable electro-magnetic performance in order to provide high efficiency with a sufficient torque reserve and a low torque ripple.

The electro-magnetic optimization process developed in the work has several stages:

- The first stage covers a fast analytical design optimization, which does not take the steel saturation into account. It was developed for outer rotor topology, which leads to different geometrical rearrangements during the optimization process compared with a conventional inner rotor electrical machine.
- The second stage contains an analytical model, which takes the steel saturation into account. It is used for the verification of the results estimated by the first stage. This analytical model was developed in order to have a clearer picture of the flux distribution in a magnetic circuit and to analyse the influence of steel saturation conditions on the machine performance as a function of speed and torque. The model includes a control algorithm, which, according to the synchronous inductance, phase resistance, and iron losses, generates the optimum current and voltage vectors for the maximum efficiency operating point. Therefore, together with the electrical machine design solution found by this approach, a viable control strategy can be achieved. It provides an opportunity to implement an appropriate fast design optimization at the early design stage without consuming an excessive amount of time.
- The third stage concerns the verification of the analytical results by the finite element method and an analysis of the local demagnetization risk in the permanent magnets at the nominal load and in fault conditions (e.g. short-circuit). A quasi 3D FEM modelling is implemented for the consideration of non-equal temperature distribution in the permanent magnets along the axial length. The generated FEM model can include the control algorithm generated in the second stage, thereby reducing the time required for tuning of the current and voltage vectors in a particular load condition.

The sequential use of the above-described stages can significantly reduce the time required for the optimization of a radial-flux rotor-surface ferrite magnet PMSM, still considering the most important phenomena related to the electro-magnetic processes of the machine.

An outcome of the machine optimization at the second stage was the discovery of local stator regions in a TCW PMSM, which face an asymmetric over-saturation condition (higher flux density compared with the one preliminary selected by the designer) at the nominal load, resulting from the permanent magnet flux density interaction with the armature reaction. It was discovered that the inherent asymmetry of over-saturated regions leads to an additional low-order torque ripple harmonic. The methods for

elimination of such an effect were proposed and verified by enhanced modelling of different TCW PMSM topologies by the FEM. The advantages and limitations of this method were analysed and the following hints for further research are given.

The methodology for permanent magnet and armature teeth design optimization, which was applied to the machine design process, also considers the local demagnetization risk, caused by the stator tooth tip flux leakage. The difference of the local demagnetization risk from the conventional one is that the stator tooth tip leakage flux penetrates through the air gap to the permanent magnet region, and with a strong armature reaction, can cause a local demagnetization risk. This phenomenon was thoroughly investigated by FEM simulations, and the results were taken into account in the design optimization process.

1.7 Engineering contribution of the thesis

The outer rotor TCW PMSM with rotor surface ferrite permanent magnets in the range suitable for most of industrial applications (0.75 − 90 kW) has not been extensively studied before. The PMSMs examples with a similar structure, found by the author, were intended for powers not higher than a few kilowatts because of the challenges to keep the ferrite magnets in the safe region from the demagnetization risk, especially if fault conditions are considered. Further, the relatively low tangential stress can be a major drawback of these electrical machines compared with rare-earth PMSMs.

The design of a 50 kW PMSM with a relatively simple structure for commercial competitiveness was proposed by applying non-conventional optimization methodology in order to take into account the "weakness" of ferrite magnets in terms of the demagnetization risk and compensation of the low magnetic energy product by constructional means (e.g. tooth-coil winding, outer rotor construction). The main challenges were identified as the demagnetization risk of the ferrite magnets, losses in the solid rotor, the impact of synchronous inductance on the PMSM performance, additional AC losses in the stator winding, and the influence of these losses on the thermal condition of the stator winding.

The demagnetization risk was analysed in detail, and actions to reduce the risk of irreversible demagnetization were suggested. The impact of temperature on the PMSM performance, including permanent magnet characteristics, was considered within the design optimization process of the rotor surface PMSM. The demagnetization risk in fault conditions (e.g. short-circuit) was estimated taking into account the different magnet characteristics in the axial direction of the machine. It was found that the classical risk evaluation of two-directional demagnetization is not suitable for the studied machine because of the uneven cooling capability along the axial length, which has an influence on the permanent magnet thermal conditions, and consequently, on the magnet properties. Contrary to rare-earth permanent magnets, the most critical part of the ferrite magnets subjected to the demagnetization risk was found in the coldest magnet region. This phenomenon was the primary reason for directing the main stator

heat dissipation through the air gap, because the permanent magnet close to the air gap faces the strongest armature reaction (as it was found in the design process).

The influence of tooth tip flux leakage on the magnetic state of the permanent magnets was analysed at different machine loads. Possible challenges caused by this phenomenon (including the maximum limit for armature reaction determined by the permanent magnet demagnetization risk) were considered in the design of medium- and large- power industrial rotor surface ferrite magnet PMSMs. In the TCW PMSMs with rotor surface permanent magnets these challenges can be expressed by an electrical loading limit set by the risk of demagnetization, even if very thick magnets are used; this risk is due to the inherent tooth tip flux leakages in TCW PMSMs. The effectiveness of the proposed actions to minimize the effect in order to achieve the maximum possible electrical loading was analysed, and advice for the design of similar machines were given.

The influence of stator slot leakages on the circulating currents in the stator windings (which leads to additional AC losses) was investigated. It was found that the reasons for the relatively high stator slot leakage seem to inherently correlate with the use of "weak" ferrite magnets because of the need for high stator slots and a large number of winding turns. The influence of the winding structure (straight parallel strands with different numbers of parallel strands in a coil, Llitz wires) on the additional AC losses was investigated. The impact of heat caused by the additional AC losses on the thermal condition of the winding and the possible reduction in the lifetime of the insulation were estimated; the issue should be taken into account in the optimization of the cooling arrangement. Therefore, the cooling arrangement should be optimized to have a reserve capability to dissipate heat with additional losses such as circulating current losses.

The losses in the solid rotor were analysed for different PMSM structures. The influence of the permanent magnet geometry and the pole pair number on the losses in the solid rotor was examined. The main reason for rotor losses, that is, the current linkage sub-harmonics, was found and investigated. The proposed approaches to reduce these losses were analysed and verified by FEM simulations.

The second part of the research is related to a novel stator winding arrangement in segmented TCW PMSMs. The impact of the optimized segmented stator structure on the machine performance was evaluated. The proposed optimization approaches to minimize the reduction in the PMSM performance when the machine is rearranged to a segmented TCW PMSM were discussed and analysed.

The performance and economic advantages of the proposed PMSM structures were discussed. It was shown that these types of electrical machines can successfully compete with induction motors commonly used in industrial applications.

2 Outer rotor PMSM

According to Section 1.1, it is possible to achieve a higher air gap flux density with embedded permanent magnets in the inner rotor topology, if the inner rotor area is used for the magnetic flux concentration technique (e.g. the use of a spoke-type PM rotor). This section shows that the outer rotor can also be successfully exploited to enhance the performance of the PMSMs having ferrite magnets. However, in the case of an outer rotor instead of permanent magnet flux concentration, the slot area is increased. Therefore, we may conclude that the inner rotor PMSM with embedded magnets and the outer rotor PMSM apply a similar technique to increase the power density of the machine; that is, the efficient use of the inner space of the PMSM. However, in the case of permanent magnet flux concentration, the magnetic loading increases, whereas in the case of an outer rotor PMSM and a large slot area, the electric loading and the air gap radius can be increased. In general, both of these methods can be efficiently applied to improve the power density of a PMSM. However, the electric loading (unlike the magnetic loading) may often be limited by different factors such as thermal conditions, Joule losses and synchronous inductance. Therefore, these factors should be considered if the outer rotor topology is selected. The thermal condition of the winding depends on the Joule losses and the cooling capability of the machine, and it can be improved after the electromagnetic machine components are designed. However, the synchronous inductance should be considered in the PMSM design. The effect of the synchronous inductance on the machine performance is discussed in Section 2.2.

As it was described in the first chapter, permanent magnet technology is successfully applied to rotating electrical machines. Numerous new interesting topologies have been developed by using permanent magnets such as flux switching machines (Zhu et al., 2005; Ilhan et al., 2012), dual-rotor or dual-stator axial flux PMSMs (Baun et al., 2013; Parviainen et al., 2004), and PMSMs with segmented rotor and stator structures (Chino et al., 2011; Heins et al., 2013). Many PMSM solutions described in the literature have been developed for a particular application; however, their wide-scale use is not economically feasible. Therefore, if the target is to harvest the benefits of permanent magnet technology without a significant increase in manufacturing costs, some new machine design should be found. One of the above described approaches is to use an outer rotor ferrite PMSM, Figure 1.11 (b). In this case, the air gap radius can be much larger compared with the inner rotor topology, Figure 1.11 (a), when the same external diameter D_e is used. A larger air gap diameter together with a larger magnetic flux produced by the permanent magnets should partly compensate for the low magnetic energy density of ferrite magnets. However, also other parameters of the machine are different from the conventional inner rotor topologies such as synchronous inductance, number of phase turns, moment of inertia, cooling arrangement, and thermal condition of the winding. Therefore, it is important to thoroughly analyse the influence of the rotor topology on the machine main characteristics. In this chapter, an outer rotor ferrite PMSM in the typical power range for an industrial application is assessed and the feasibility of this machine is examined. As an example, a 50 kW, 3000 rpm PMSM

designed for a bus vehicle generator is described. The simplified structure of the PMSM is shown in Figure 2.1.

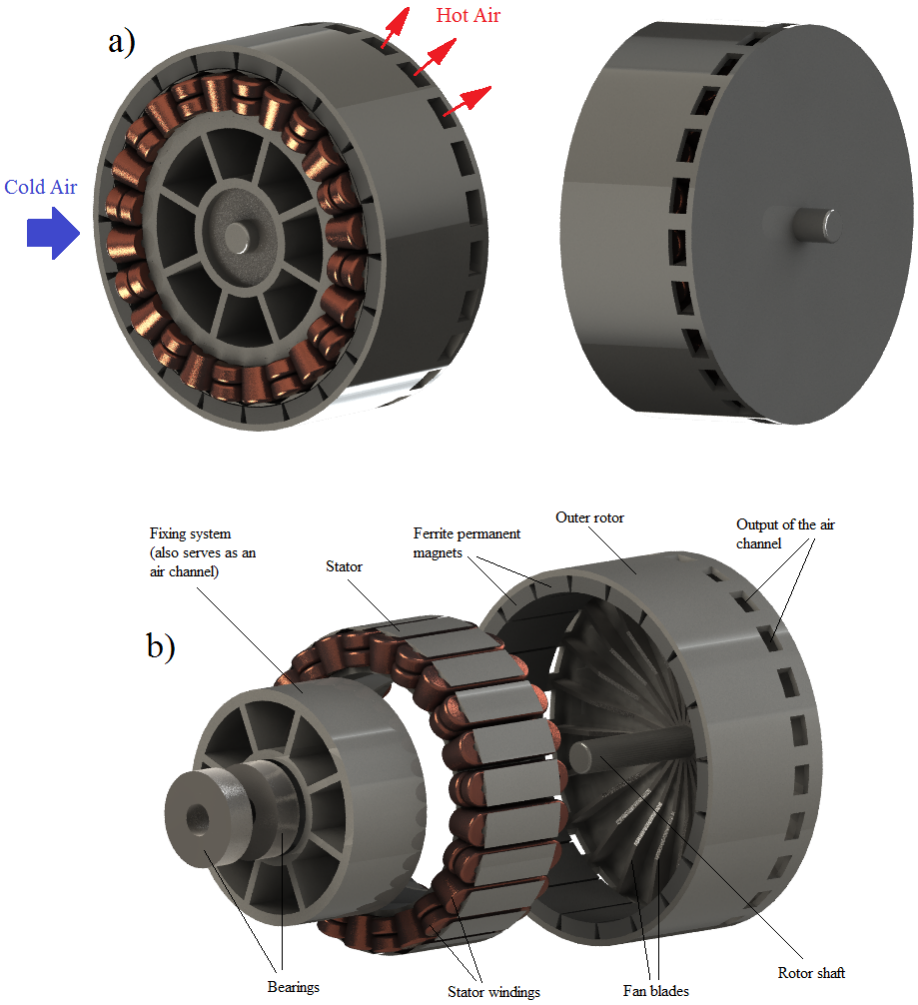

Figure 2.1: Simplified construction of the PMSM studied in the doctoral dissertation. The PMSM constructional elements are: outer rotor, tooth-coil winding, rotor surface ferrite magnets, and integrated fan. a) Assembled PMSM, b) PMSM components.

The PMSM studied in the dissertation was designed to achieve the required power (50 kW at 3000 rpm) for the electrical power generation in a hybrid bus. In the design, no tight limit were set for the machine size. Therefore, it was possible to achieve a relatively low tangential stress in the machine. In this case, the manufacturing costs can be reduced significantly if inexpensive ferrite magnets are used instead of rare-earth magnets. The main challenges in the design of this machine were possible partial magnet demagnetization, stator winding cooling arrangement, synchronous inductance minimization, validation of the possible advantages to use an outer rotor construction,

torque ripple analysis, and additional AC losses in the stator winding. These aspects are described in more detail below.

First of all, it is important to analyse the torque and power density variation in two machines that apply similar active electromagnetic materials and have the same external dimensions but have different rotor topologies (inner vs. outer rotor). This variation may have an influence on the final decision on the rotor topology used. An example of such a rearrangement is illustrated in Figure 1.11. The figure shows that a significant torque density improvement can be reached if an outer rotor arrangement is used, even if the tangential stress is kept the same. This can be explained by the larger active surface of the outer rotor structure, which together with the air gap radius has a direct influence on the torque achieved by the machine (Pyrhönen et al., 2008):

$$T = \sigma_{F_{\tan}} r_{\mathrm{r}} S_{\mathrm{r}} = \sigma_{F_{\tan}} 2\pi r_{\mathrm{r}}^2 l' \tag{2.1}$$

In Eq. (2.1) we can see that the torque of the machine with the same tangential stress is a function of radius squared. This means that increasing the air gap radius by 10 % can improve the torque by more than 20 %.

The increase in the air gap diameter by rearranging the PMSM from an inner rotor machine to an outer rotor structure can be estimated if the following component dimensions are known: stator tooth height, permanent magnet height, stator yoke height, and rotor yoke height. These dimensions are shown in Figure 2.2.

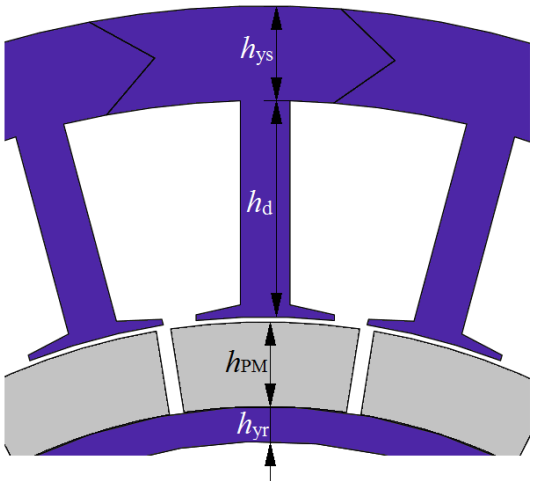

Figure 2.2: PMSM component dimensions that determine the increase in the air gap diameter if the machine is rearranged to an outer rotor structure.

The increase in the air gap diameter when the inner rotor PMSM is rearranged into an outer rotor PMSM can be estimated by

$$\Delta D_\delta = 2 \cdot \left(h_\mathrm{d} + h_\mathrm{ys}\right) - 2 \cdot \left(h_\mathrm{PM} + h_\mathrm{yr}\right) \tag{2.2}$$

The air gap radius can be increased if the stator tooth height and the stator yoke height are larger than the rotor permanent magnet height and the rotor yoke height. According to Eq. (2.2), the ratio of the air gap increase (ΔD_δ) to the inner rotor PMSM air gap is

$$\frac{\Delta D_\delta}{D_\delta} = \frac{2 \cdot \left(h_\mathrm{d} + h_\mathrm{ys}\right)}{D_\delta} - \frac{2 \cdot \left(h_\mathrm{PM} + h_\mathrm{yr}\right)}{D_\delta} \tag{2.3}$$

This means that the potential torque capability difference between the inner rotor and outer rotor PMSMs depends on the tooth height h_d, the stator yoke height h_ys, permanent magnet height h_PM and the rotor yoke height h_yr in proportion to the inner rotor diameter of the PMSM. An example of the ratio of the air gap diameter increase to the inner rotor PMSM air gap diameter ($\Delta D_\delta/D_\delta$) as a function of tooth height is shown in Figure 2.3. This PMSM has a fixed stator yoke height, rotor yoke height, and permanent magnet height, which were estimated for the original machine (with the stator tooth height ~45 mm) according to the algorithm presented in (Pyrhönen et al., 2008). Moreover, in Figure 2.3, a potential torque increase is shown if the tangential stress is kept constant. We can see that a significant torque improvement can be achieved in a PMSM with a larger stator tooth height when it is rearranged into an outer rotor structure. In Figure 2.4, inner rotor and outer rotor PMSMs are shown for two outermost stator tooth height points (Figure 2.3). In Figure 2.4 (a) it can be seen that the stator tooth height is hardly realizable, because there is almost no space for the stator winding in the slots. However, even in this case the torques achievable with the outer rotor and inner rotor PMSMs are approximately the same, and the difference starts to increase in favour of the outer rotor PMSM with a larger stator tooth height.

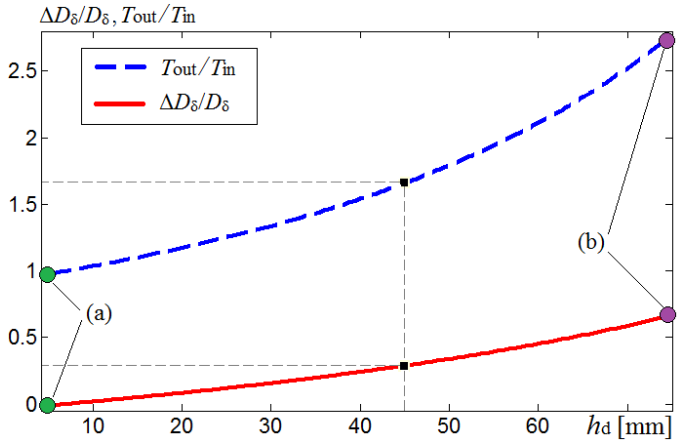

Figure 2.3: Ratio of the air gap increase to the air gap of inner rotor PMSM ($\Delta D_\delta/D_\delta$) and torque increase ($T_\mathrm{out}/T_\mathrm{in}$) when an inner rotor PMSM is rearranged into an outer rotor PMSM with the same external dimensions as a function of tooth height (h_d). T_out is the torque of the PMSM with the outer rotor topology, and T_in is the torque of the PMSM with the inner rotor topology. Points (a) and (b) refer to the different designs illustrated in Figure 2.4.

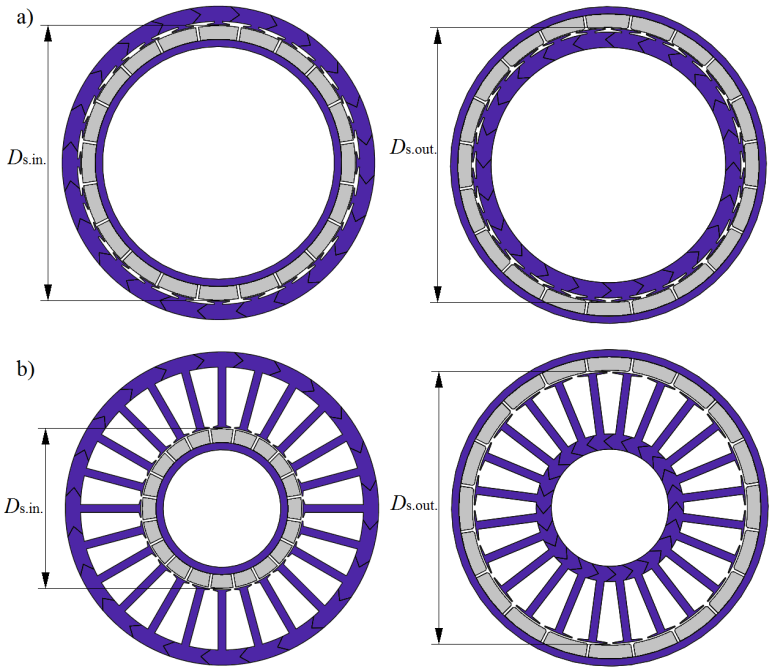

Figure 2.4: Scaled view of PMSMs with the same external dimensions. a) The inner rotor and outer rotor PMSMs are related to Figure 2.3 (a). b) The inner rotor and outer rotor PMSMs are related to Figure 2.3 (b).

It should be noted that PMSMs that apply rotor surface ferrite permanent magnets instead of rare-earth permanent magnets have a lower magnetic flux produced by these magnets. Therefore, they have to use a higher number of winding turns, which leads to a larger phase resistance (if the current density remains the same). It means that in order to reduce the phase resistance, the wire area has to be increased, which may result in increase the stator tooth height. In the case of an outer rotor PMSM, if there is no need to reserve inner stator space for other purposes, the stator tooth height can be increased without increasing external radius of the machine.

In the previous comparison of inner rotor and outer rotor PMSMs, it was assumed that the tangential stress is the same in both cases. However, with the same external size of the machines, the slot area in an outer rotor PMSM is somewhat lower than in a corresponding inner rotor case (if the tooth height is the same in both cases). This is due to the fact that with the outer rotor construction the active stator area is lower than in the inner rotor construction. Therefore, with the same stator tooth width and stator tooth height (that takes the same space in the active stator area), there is consequently lower space for the stator slot. The ratio of the outer rotor PMSM slot area ($S_{u.out}$) to the inner rotor PMSM slot area ($S_{u.in}$) is

$$\frac{S_{\mathrm{u.out}}}{S_{\mathrm{u.in}}} = \frac{\left(\pi\left(D_{\mathrm{e}}-2\left(h_{\mathrm{yr}}+\delta+h_{\mathrm{PM}}\right)\right)^2/4-\pi\left(D_{\mathrm{e}}-2\left(h_{\mathrm{yr}}+\delta+h_{\mathrm{PM}}+h_{\mathrm{d}}+h_1/2\right)\right)^2/4-Q_{\mathrm{s}}h_{\mathrm{d}}b_{\mathrm{d}}\right)/Q_{\mathrm{s}}}{\left(\pi(D_{\mathrm{e}}-2h_{\mathrm{ys}})^2/4-\pi\left(D_{\mathrm{e}}-2\left(h_{\mathrm{ys}}+h_{\mathrm{d}}+h_1/2\right)\right)^2/4-Q_{\mathrm{s}}h_{\mathrm{d}}b_{\mathrm{d}}\right)/Q_{\mathrm{s}}} \quad (2.4)$$

The numerator in Eq. (2.4) represents the slot area in an outer rotor PMSM, whereas the denominator in Eq. (2.4) represents the slot area in an inner rotor PMSM. According to Eq. (2.4), the reduction in the slot area depends mainly on the permanent magnet height h_{PM}, the air gap length δ, the height of the teeth h_{d}, the width of the teeth b_{d}, the height of the tooth tip h_1 relative to the external PMSM diameter D_{e}, and the number of slots Qs. However, in the machine under study, the external diameter is relatively large, which means that there is no significant reduction in the slot area, as it is shown in Figure 2.5.

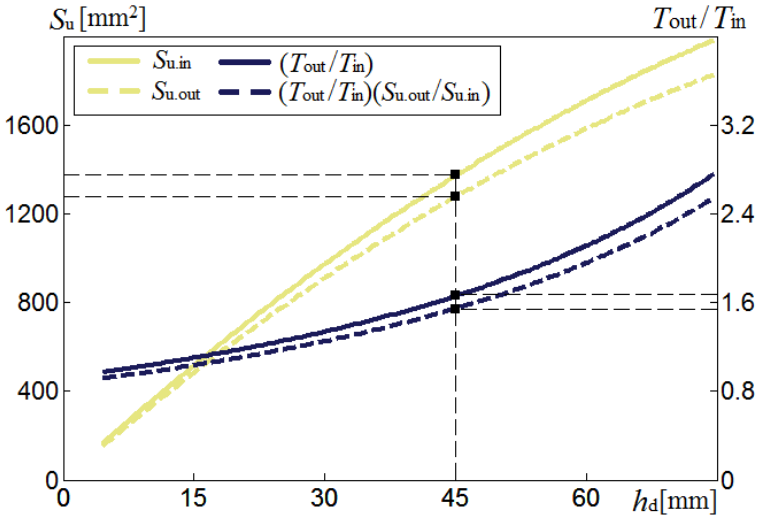

Figure 2.5: Actual slot areas S_{u} in the inner and outer rotor PMSMs and the torque ratios with the assumption that there is no difference in the slot areas, i.e., the slot areas of the inner and outer rotor PMSMs are the same (continuous lines) and taking this difference into account (dashed lines). The external diameter is kept constant. The torque ratio with the unchanged slot areas (continuous line) is the same as illustrated in Figure 2.3.

Figure 2.5 shows that even with a reduced slot area (i.e. reduced tangential stress) there is still a significant torque improvement when the outer rotor topology is used.

2.1 Tangential stress

Tangential stress is an important parameter of an electrical machine. This parameter shows how efficiently the air gap surface is used. For example in high power wind generators, it is crucial to keep the dimensions of the active electromagnetic machine parts as small as possible. Therefore, a very high tangential stress is required, especially

in high-power direct drive wind generators (Alexandrova et al., 2012). The tangential stress depends on the linear current density A, the air gap normal flux density B_δ and the phase shift ζ between the distributions of A and B_δ as it is shown in Eq. (1.12). Therefore, if the permanent magnet flux density cannot be regulated, as in the case of rotor surface permanent magnets (when permanent magnets are already selected), the only way to adjust the tangential stress is to apply a different sum of current in the slot. The sum of current in the slot means the phase current multiplied by the number of conductors z_Q in a slot. If the number of conductors in a slot is estimated (based on back-EMF, synchronous inductance, and applied voltage), the sum of current in the slot can be adjusted by applying a different phase current value.

There are several factors that limit the maximum phase current to be applied. One of the most important factors is the thermal state of the winding. In the case of high losses in the stator winding, the windings can be subjected to faults resulting from their relatively poor insulation characteristics against high temperatures. According to (Montsinger, 1930) the life time of an insulator is halved by each 10° C of its temperature increase. In (Dakin, 1948), it was claimed that insulation deterioration caused by a temperature influence can be estimated by the Arrhenius chemical rate equation. However, no significant difference was found between these two approaches (Brancato, 1992). Therefore, the rule concerning halving of the insulation life time by each 10° C increase is often used in practice.

The thermal state of the winding depends on the power losses (heat) produced in the machine as well as on the cooling arrangement chosen to reduce the overall temperature in the critical parts of the machine. In electrical machines designed for industrial applications, an air cooling arrangement is often used because of its robustness and simplicity, and because industrial applications usually do not have strict requirements for size limit. However, the cooling capability of air is much worse compared with liquid cooling or direct liquid cooling arrangements (Alexandrova Y., 2014). Therefore, it is important to keep the current density in an allowable range to avoid excessive temperature in the stator winding if air cooling is implemented (Pyrhönen et al., 2008).

In addition to the stator winding thermal conditions, the linear current density A (which is proportional to the tangential stress), can have a negative impact on the permanent magnet magnetic state. It is well known that permanent magnets can be subjected to irreversible demagnetization if the operating flux density in the magnets decreases below the critical point. This critical point together with the remanent flux density varies at different temperatures as it is shown in Figure 2.6.

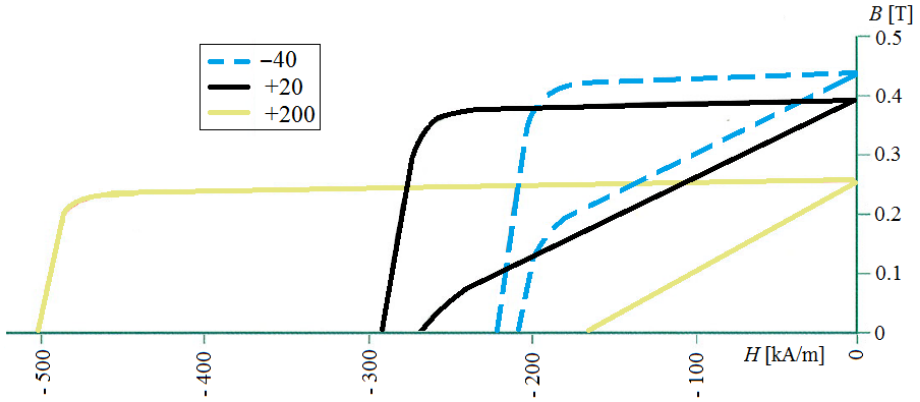

Figure 2.6: *BH* curves of a BM9 type hard ferrite magnetic material by Bakker Magnetics at +200° C, +20° C and −40° C (Bakker Magnetics, 2015; Petrov and Pyrhönen, 2013).

Figure 2.6 illustrates the polarization and demagnetization curves with their knee areas at different temperatures. For the magnetic material at the temperatures of +20° C and −40° C, the knee areas of the demagnetization curves are located in the second quadrant. This means that at these temperatures the flux density of the permanent magnets should not decrease below 0.2 T at −40° C or 0.1 T at 20° C, because otherwise irreversible demagnetization is inevitable. According to Figure 2.6, if a PMSM operates at different loads and ambient temperatures, its performance and demagnetization risk should be evaluated. For example, in the case of the studied PMSM, the remanent flux density decreases at a higher temperature. However, in this case it is possible to increase the linear current density without reaching the point with a demagnetization risk.

Figure 2.7 shows the normal component of the flux density in the permanent magnet surface close to the air gap for three different temperatures. The nominal power is kept constant in all three cases. Therefore, as a result of the higher remanent flux density at the lower temperature, the stator current can be reduced in order to get the same output power as at the higher temperature (where the permanent magnet remanent flux is lower). In Figure 2.7 it is shown that there is no demagnetization risk at the nominal load even if the temperature of the permanent magnet decreases to −40° C. However, in the design of a similar surface rotor PMSM, one should keep the tangential stress relatively low in order to avoid the risk of demagnetization at a short-circuit, overload conditions, and especially at the nominal load.

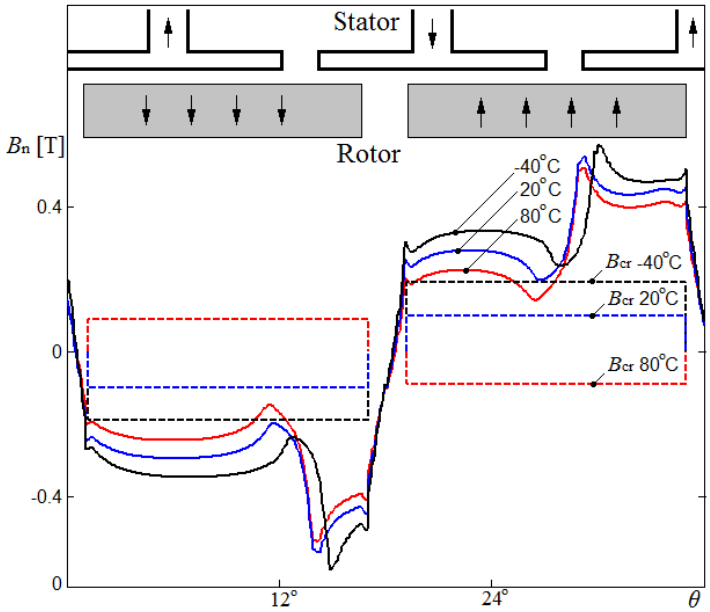

Figure 2.7: Normal component of the flux density at different magnet temperatures and the corresponding limit values for the PM material. The PMSM is operating at the nominal load power. The magnet is located close to the stator slot where the peak current is conducting.

Figure 2.7 reveals that in part of the PM material the remanent flux density is exceeded at the rated load because of the influence of the armature reaction. This causes an extra problem in the design as a permanent magnet hysteresis loss may occur if the PM material flux density varies below and above the remanent flux density (Pyrhönen et al., 2015). This condition results from the target of reaching as high air gap flux density as possible, and because of large magnet height h_{PM} selected for the magnet material. Further, the high armature linear current density typical for low flux density machines allows high enough armature reaction thereby this kind of a disadvantageous situation possible.

A short-circuit fault in a rotor surface magnet PMSM can cause a high initial peak current because of the two current components in the transient condition. The first current component consists of current in the steady state during the short-circuit, the peak value of which is inverse to the inductive reactance (ωL) and the phase resistance, while the second current component is exponential which decreases over time towards zero; its initial value depends on the instant current value when the short-circuit occurs. Therefore, the sum of both components at the very beginning during the short circuit gives the highest peak current value, as it is seen in Figure 2.8, and this current value should be considered in the demagnetization analysis.

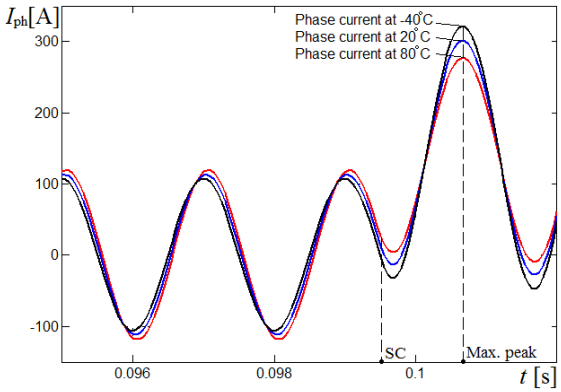

Figure 2.8: Phase current in a short-circuit at 80° C, 20° C and -40° C. Three-phase short-circuit occurs at $t = 0.0995$ s.

Figure 2.8 shows that a short-circuit at the lowest permanent magnet temperature gives the highest peak of phase current. Thus, knowing also that at lower temperatures the knee point of the ferrite permanent magnet *BH* curve goes towards a higher value of flux density, we may expect that during a three phase short-circuit at a lower permanent magnet temperature, irreversible demagnetization may occur with a higher probability. In order to verify these expectations, the flux density was measured at different depths of permanent magnets from the air gap (in the FEM model) at a short-circuit at 80° C and −40° C permanent magnet temperatures. The resultant flux densities were compared with the critical value of the flux density for a particular temperature. The comparative graphics are shown in Figure 2.9 and in Figure 2.10.

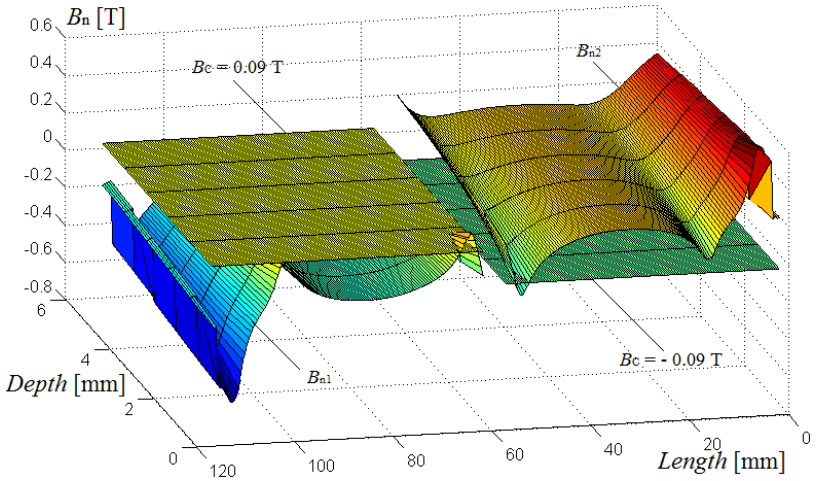

Figure 2.9: Permanent magnet flux density at different depths from the air gap during a short-circuit peak current for the temperature of 80° C. The magnet is located close to the stator slot where the peak current is conducting. The flat surfaces represent the critical values B_c for the permanent magnets at 80° C. If the actual flux density exceeds the critical flux density, local irreversible demagnetization may occur. In the figure, this takes place at the magnet surface (0 mm depth) and edges (about 70 mm length).

Figure 2.9 shows that the resultant flux density in the permanent magnets at a short circuit is almost entirely in the safe zone (without the risk of irreversible demagnetization) even close to the air gap region. Therefore, we may conclude that if the temperature of the permanent magnets is high enough, it is possible to avoid irreversible demagnetization even in the worst operating condition (nominal speed, three-phase short-circuit, permanent magnet is close to the slot with the peak phase current).

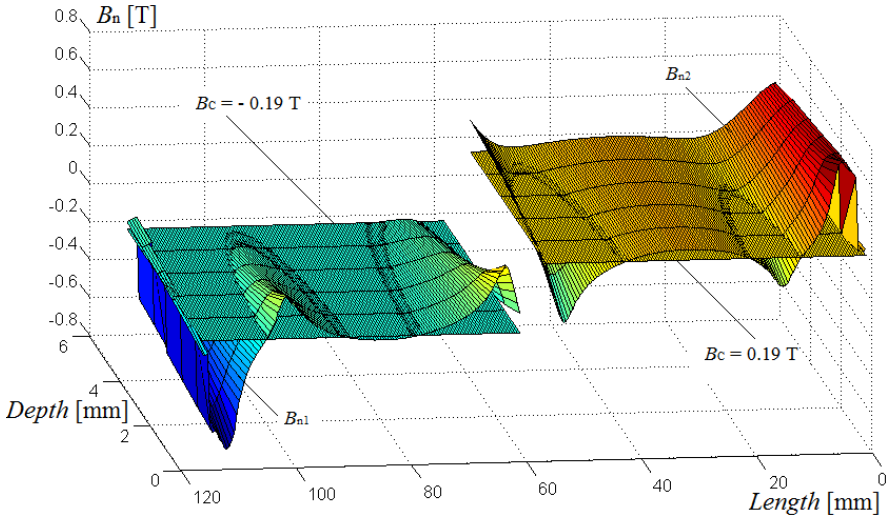

Figure 2.10: Permanent magnet flux density at different distances from the air gap during a short-circuit peak current for the temperature of −40° C. The magnet is located close to the stator slot where the peak current is conducting. The flat surface represents the critical value for the permanent magnets at −40° C. If the actual flux density exceeds the critical flux density B_c, local irreversible demagnetization may occur.

Figure 2.10 demonstrates that if a three-phase short-circuit occurs at the permanent magnet temperature of −40° C, a large proportion of the resultant flux density in the permanent magnets exceeds the critical value. However, if a further distance from the air gap is considered, the influence of the armature reaction is partially damped, because of the low magnetic permeability of the permanent magnets, and the risk of irreversible demagnetization is reduced. This means that only the permanent magnet skin close to the air gap can be subjected to partial demagnetization, as it can be seen in Figure 2.10.

Another limiting factor for the maximum tangential stress is the synchronous inductance with the maximum voltage applied. This effect can be seen in Figure 2.11, where equivalent circuits of a PMSM in the d- and q-axes are shown. If a rotor surface magnet PMSM is considered with $i_d = 0$, the applied voltage in the q-axis should be proportional to the flux linkage in the d-axis, which equals the permanent magnet flux linkage ($i_d = 0$). This means that the q-axis voltage equals the back-EMF at no-load. However, the voltage in the d-axis is proportional to the flux linkage in the q-axis, which equals the multiple of the q-axis inductance and the q-axis stator current.

Therefore, in higher load conditions the d-axis voltage will increase until the total voltage reaches the maximum limit, after which field weakening starts. The total voltage in a vector representation can be estimated as

$$u = \sqrt{u_{\mathrm{d}}^2 + u_{\mathrm{q}}^2} \tag{2.5}$$

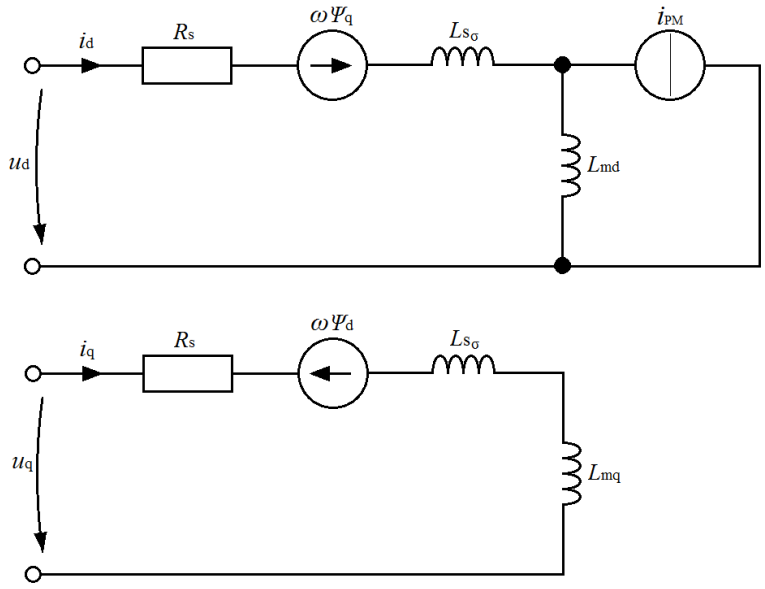

Figure 2.11: Equivalent circuits of a PMSM in the d- and q-axes (More et al., 2008).

Figure 2.12 shows two vector diagrams for the same PMSM, assuming that the synchronous inductance remains constant (it does not depend on the load). The vector diagrams represent two load points: $i_{\mathrm{d}} = 0$, and the maximum theoretically achievable torque at the nominal speed ($\omega = 1$ p.u.) with the rated voltage ($u_{\mathrm{s}} = 1$ p.u.).

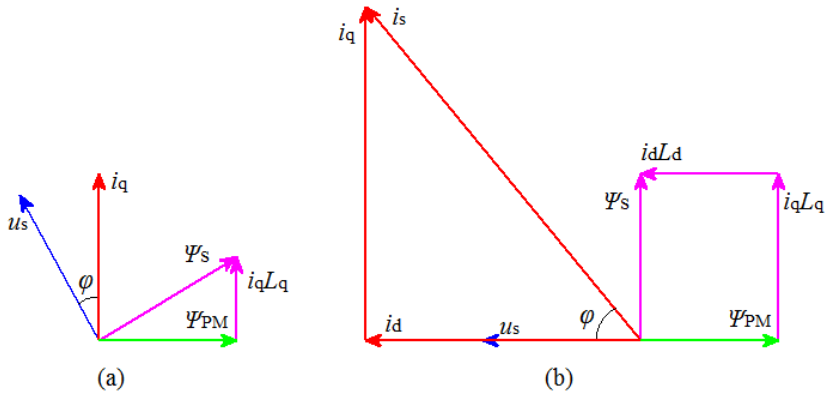

Figure 2.12: Vector diagram of a PMSM with a) $i_d = 0$ control ($u_s = 1$ p.u., $i_s = 1$ p.u., $i_d = 0$ p.u., $i_q = 1$ p.u., $\Psi_s = 1$ p.u., $\Psi_{PM} = 0.87$ p.u., $i_dL_d = 0$ p.u. $i_qL_q = 0.5$ p.u., $\varphi = 30°$) and b) maximum theoretically achievable torque at the nominal speed ($u_s = 1$ p.u., $i_s = 2.65$ p.u., $i_d = -1.74$ p.u., $i_q = 2$ p.u., $\Psi_s = 1$ p.u., $\Psi_{PM} = 0.87$ p.u., $i_dL_d = -0.87$ p.u., $i_qL_q = 1$ p.u., $\varphi = 49°$). The stator resistance is assumed negligible.

Figure 2.12 (b) shows that there is a limit for the maximum electrical loading that can be achieved at a particular speed and voltage. This limit comes from the fact that it is not possible to get rid of the armature reaction by a field weakening control as it is done with the permanent magnet flux linkage. Therefore, when the flux linkage caused by the armature reaction in the q-axis reaches the value corresponding to the voltage available, the torque cannot be increased any further. It means that the tangential stress is limited not only by the thermal state of the stator winding and the risk of permanent magnet irreversible demagnetization, but also by the electromagnetic factors such as synchronous inductance, rotational speed, and maximum terminal voltage available. The maximum theoretically achievable torque in a PMSM without inductance saliency ($L_d = L_q$) at the nominal speed can be estimated by:

$$T_{max} = \Psi_{PM} i_{q.max} = \Psi_{PM} \left(\frac{u_s}{\omega L_q} \right) \tag{2.6}$$

The limiting factors of the tangential stress described above make it challenging to construct a PMSM with rotor surface ferrite permanent magnets at high power levels because of the low magnetic flux produced by the ferrite permanent magnets. It should be compensated for by a larger slot area and a higher number of winding turns N_s. These parameters have a direct influence on the synchronous inductance, which is described in the following section.

2.2 Synchronous inductance

Synchronous inductance is one of the most important parameters in an electrical machine. Because of the non-linear *BH* curve of the material used to assist the magnetic flux conduction such as silicon steel (Abeywickrama et al., 2008), soft magnetic

composite (Okada et al., 2010; Maloberti et al., 2014), or cobalt-iron lamination (Cossale et al., 2014), it is challenging to analytically evaluate the variation in synchronous inductance as a function of load point in an electrical machine. Usually, a thorough FEA is needed to evaluate synchronous inductance for the whole load range (Ruuskanen et al., 2014a). The importance of correct inductance evaluation can be justified by control requirements (especially, if a sensorless control is implemented) and by the performance variation of the machine with different synchronous inductances. It should be noted that in the vector theory there are two inductances, viz. along the d-axis (L_d) and the q-axis (L_q). If these inductances are not equal (especially in PMSMs with embedded magnets), there is saliency in the electrical machine. This saliency ratio may contribute to the total torque of the machine. However, the main focus of the dissertation is on rotor surface magnet PMSMs, which have saliency only because of the local saturation in the iron. Usually, this saliency does not essentially contribute to any significant additional torque. Therefore, no special attention is given to the reluctance torque, and it is assumed that $L_d \approx L_q$.

Despite the fact that the synchronous inductance is not constant in different operating points, a "classical" analytical method is often adopted at early design stages (Ponomarev et al., 2014a; Pyrhönen et al., 2014). The drawback of this approach is that it does not take into account the armature reaction when the synchronous inductance is evaluated. Therefore, analytical methods have been introduced that take the armature reaction into account in every load mode by means of iterative evaluation of an equivalent magnetic circuit (Hsieh and Hsu, 2012; Petrov et al., 2014c). They require a more complicated structure compared with only analytical formulas (Prieto et al., 2014), but they are still not as computationally heavy as the FEM. Therefore, it is more advantageous to use an equivalent magnetic circuit (also known as a lumped model) to precisely evaluate the influence of the armature reaction on the magnetic state of the iron parts in different load points. An example of an algorithm used in the lumped model is shown in Figure 2.13.

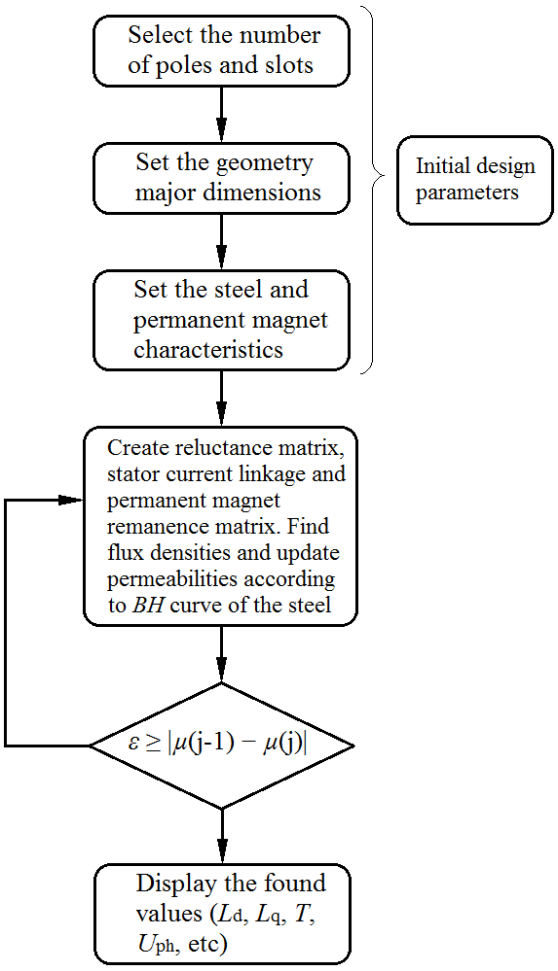

Figure 2.13: Algorithm for the identification of the electric machine parameters with the saturation effect.

Figure 2.13 shows that iteration is an inherent part of an algorithm to take into account the non-linear steel behaviour. The precision of the inductance evaluation depends on the threshold error accepted in the algorithm, which also has an influence on the computational time of the model.

The inductance L indicates how much flux linkage Ψ a magnetic circuit can accumulate with current. The energy W associated with the circuit is directly proportional to its inductance. It is not possible to transform one form of energy into another one immediately. Therefore, it takes time to transform electrical energy into the magnetic energy and vice versa; this is called a transient process. Because of this transient process in the case of sinusoidal quantities, the current sine waveform lags behind the voltage sine waveform. The angle between voltage and current is represented by a power factor. The power factor shows the electrical power component that contributes to the electro-

mechanical conversion and the electrical power component that only fluctuates between the stator winding and back to the network. Therefore, often in the design of PMSMs some actions are taken to keep the synchronous inductance within a reasonable range, except for the cases when a PMSM should work in a deep field weakening mode. In this case, a high synchronous inductance can assist in reducing the permanent magnet flux linkage in the stator winding by means of armature reaction. When going into field weakening, the d-axis negative current is used to demagnetize the stator d-axis flux with the armature reaction $I_d L_s$.

As it was mentioned above, exact evaluation of the synchronous inductance is a very challenging task in rotating electrical machines. Additional complexity comes from the non-homogeneous stator and rotor surfaces close to the air gap. This leads to a synchronous inductance variation in different rotor positions in relation to the stator. Finally, we may conclude that there are two main parameters that have an influence on the synchronous inductance of an already designed PMSM: the stator current vector (value, direction) and the rotor position. However, this does not mean that the synchronous inductance variation has a strong influence on the deviation of the current waveform from the sine waveform (in the case of a sine voltage supply), because the current in an electrical machine has a very inertial behaviour and does not significantly change as a result of synchronous inductance variation. Instead, the voltage waveform in the case of current supply may change noticeably if the saturation in the magnetic circuit takes place, as it can be seen in Figure 2.14.

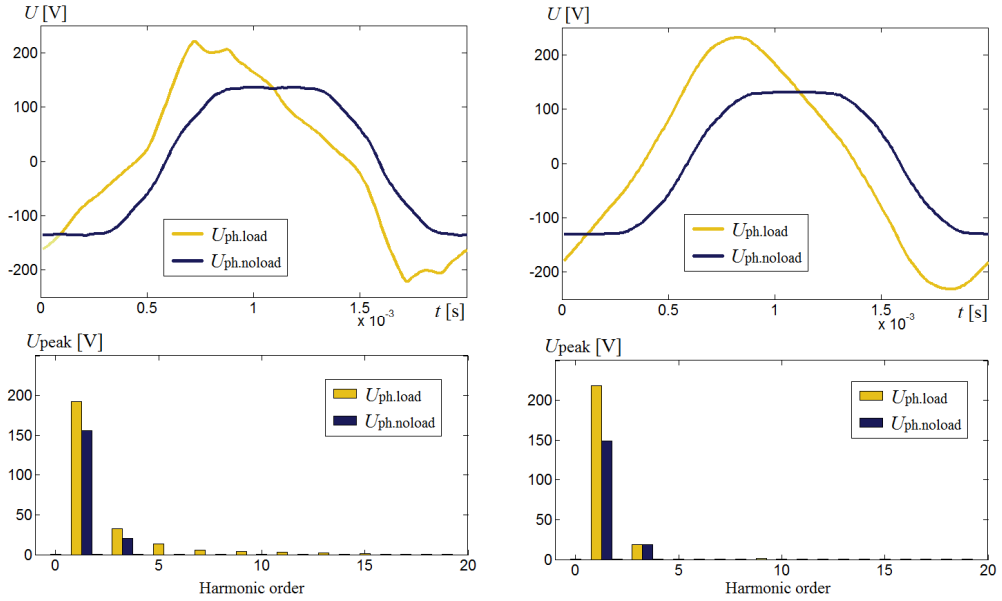

Figure 2.14 a) Voltage waveforms of the PMSM under study at no-load and at the nominal load and their harmonic spectra, saturation is taken into account (steel has the *BH* curve of M270-35A). b) Voltage waveforms at no-load and at the nominal load and their harmonic spectra,

saturation is not taken into account (steel has a constant relative permeability μ_r = 500). The results were attained from the outer rotor PMSM with the current supply (Flux 2D) studied in this chapter.

Figure 2.14 shows that the PMSM with a linear *BH* curve does not have additional harmonic components in the voltage spectrum at the nominal load compared with the no-load back-EMF. However, if an actual steel *BH* curve is used, the harmonic spectrum of the nominal load voltage is different compared with the no-load back EMF. For better understanding, let us consider a simple circuit shown in Figure 2.15.

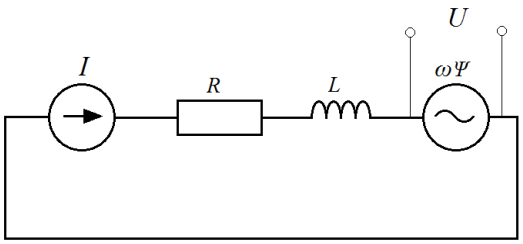

Figure 2.15: Simple circuit with current supply, back-EMF ($\omega\Psi$), constant resistance, and variable inductance.

If saturation is taken into account, the inductance in Figure 2.15 varies. Therefore the voltage value at the terminals of the current source can be found by

$$\begin{aligned}\boldsymbol{u_s} &= R\boldsymbol{i_s} + \mathrm{j}\omega\boldsymbol{\Psi_s} = R\boldsymbol{i_s} + \mathrm{j}\omega(\boldsymbol{\Psi_{PM}} + \boldsymbol{i_s}L_s) \\ &= R\boldsymbol{i_s} + \mathrm{j}\omega\boldsymbol{\Psi_{PM}} + \boldsymbol{i_s}\frac{\mathrm{d}L_s}{\mathrm{d}t} + L_s\frac{\mathrm{d}\boldsymbol{i_s}}{\mathrm{d}t}\end{aligned} \tag{2.7}$$

In the case of constant inductance, if a machine with a linear *BH* curve is considered, there are no voltage disturbances at the terminals of the machine in the case of current supply. However, if saturation is taken into account, inductance variation leads to some voltage disturbance.

It should be noted that in the case of a voltage supply (sinusoidal voltage waveform), the synchronous inductance variation is often not enough to significantly affect the current waveform, which mainly represents the torque quality in an electrical machine. For example, in the machine, if a voltage supply is implemented, the phase current is usually sinusoidal and does not contain significant harmonics in both cases (with the linear and non-linear *BH* curves of the steel, as it can be seen in Figure 2.16). According to the author's understanding this is due to the inertial current behaviour, which prevents the phase current instant change. Therefore, other reasons for the occurrence of torque ripple must be found. These reasons are addressed in Section 2.3.

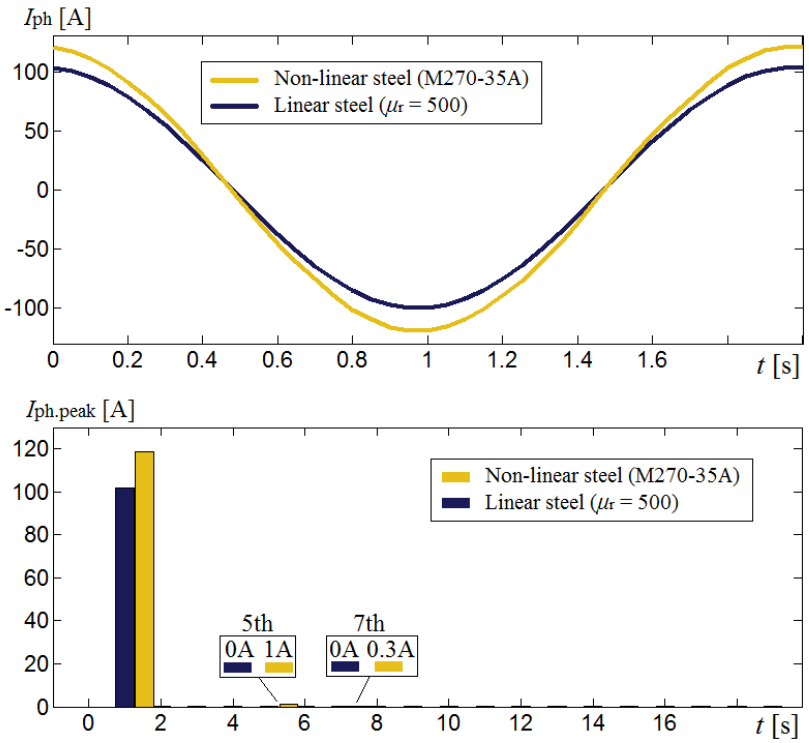

Figure 2.16: Current waveforms of the PMSM under study at the nominal load for two different cases: saturation is taken into account (steel has *BH* curve of M270-35A), saturation is not taken into account (steel has a constant relative permeability μ_r = 500), and the harmonic spectra of the current waveforms, highlighting the 5th and 7th harmonics.

In addition to the non-linear behaviour, the synchronous inductance in a PMSM can significantly affect its torque and power characteristics at the edge of the maximum voltage or current applied, as it can be seen in Figure 2.17, where the maximum achievable torque and power values of two similar PMSMs are shown with the same permanent magnet flux linkage, current, and voltage limits, but with different synchronous inductances (L_s = 0.6 p.u. and L_s = 0.9 p.u.).

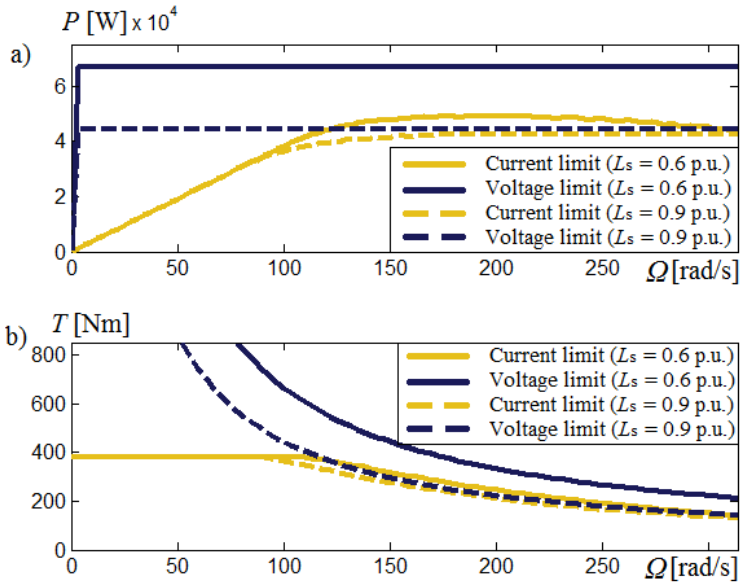

Figure 2.17: Maximum achievable powers and torques as a function of speed for two rotor surface magnet PMSMs with different synchronous inductances: L_s = 0.6 p.u. and L_s = 0.9 p.u.. The permanent magnet flux linkage is Ψ_{PM} = 0.8 p.u., the maximum voltage and phase currents are the same for both machines (in absolute values). The power and torque are limited by the maximum allowable current and voltage in the machine. The field weakening region starts at 105 rad/s for the machine with L_S = 0.6 p.u. and at 87 rad/s for the machine with L_S = 0.9 p.u.

Figure 2.17 shows that in the case of L_s = 0.9 p.u. the PMSM cannot achieve the same maximum power as the similar PMSM but with L_s = 0.6 p.u., despite the fact that they have the same maximum torque until the field weakening (with the limited current and voltage values up to 1 p.u.). This is because of the voltage limitation, which reduces the voltage vector in the deep field weakening region (MTPV control), does not allow to get the unity power factor in a point where both the current and voltage vectors are equal to 1 p.u. In the case of L_s = 0.6 p.u. instead, the unity power factor is reached at ~200 rad/s, when both the voltage and current vectors are equal to 1 p.u. This means that if these PMSMs are used in the HEV, the one with L_s = 0.6 p.u. can have a better performance at particular vehicle speeds.

This effect can be analysed by the vector theory. In Figure 2.18 (a, b), two PMSMs are represented by vector diagrams. In the case of Figure 2.18 (a), the PMSM has a relatively small synchronous inductance L_s = 0.5 p.u., which allows achieving the unity power factor at the angular speed ω = 1.4 p.u., when both the current and voltage vectors are at maximum, Figure 2.18 (c), whereas in the case of Figure 2.18 (b), the PMSM has a relative large synchronous inductance L_s = 0.9 p.u., which prevents from achieving the unity power factor with the maximum voltage and current vectors. In such a PMSM, the maximum achievable power is at the angular speed ω = 4 p.u., where the

MTPV control begins and the voltage vector starts to decrease at higher speeds, Figure 2.18 (d).

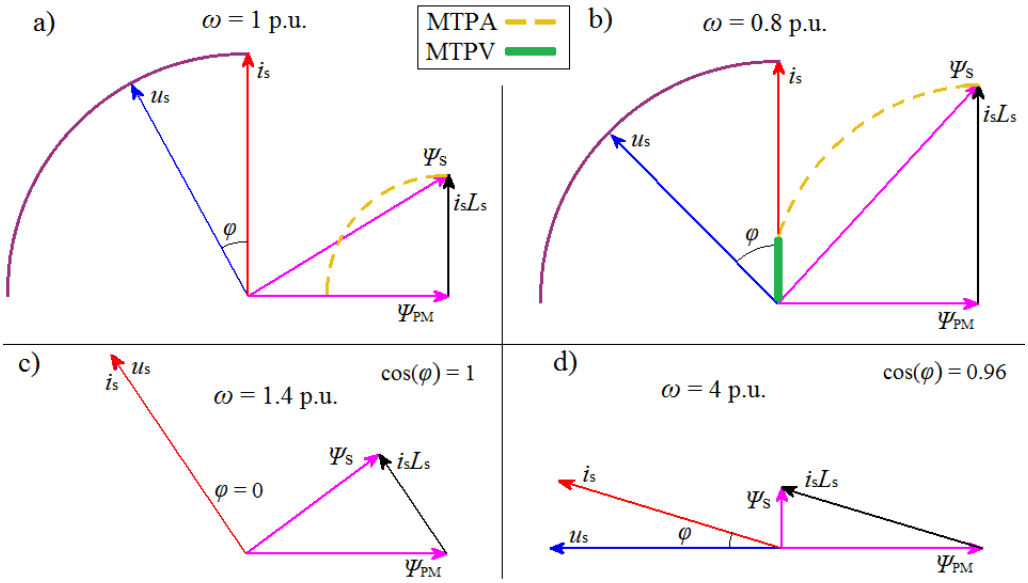

Figure 2.18: a) Vector diagram of a PMSM with the $i_d = 0$ control and $L_s = 0.5$ p.u. ($u_s = 1$ p.u., $i_s = 1$ p.u., $i_d = 0$ p.u., $i_q = 1$ p.u., $\Psi_s = 1$ p.u., $\Psi_{PM} = 0.87$ p.u., $i_dL_d = 0$ p.u. $i_qL_q = 0.5$ p.u., $\varphi = 30°$) and the field weakening path of the stator flux linkage. b) Vector diagram of a PMSM with the $i_d = 0$ control and $L_s = 0.9$ p.u. ($u_S = 1$ p.u., $i_s = 1$ p.u., $i_d = 0$ p.u., $i_q = 1$ p.u., $\Psi_S = 1$ p.u., $\Psi_{PM} = 0.87$ p.u., $i_dL_d = 0$ p.u., $i_qL_q = 0.9$ p.u., $\varphi = 46°$) and the field weakening path of the stator flux linkage. c) Maximum achieved power of the PMSM shown in (a). d) Maximum achieved power of the PMSM shown in (b). In the PMSM shown in (a), only the MTPA is applied, whereas in the PMSM shown in (b), both the MTPA and MTPV should be applied.

The permanent magnet flux linkage naturally has a direct influence on the vector diagram of a PMSM and can be selected so that the current and voltage vector angles are shifted closer to the desired positions with a better PMSM performance in the operating point. However, the flux linkage was kept constant in described examples in order to highlight the impact of the synchronous inductance on the PMSM characteristics in the whole speed range (including the field weakening mode).

As a conclusion, while considering the role of synchronous inductance in a PMSM, two main features should be highlighted: the non-linear behaviour as a function of current vector, and the impact of armature reaction on the stator flux linkage. Usually, a lower synchronous inductance is better for high dynamic performance; however, a very low synchronous inductance can reduce the field weakening capability of a PMSM and increase the current ripple because of the PWM control topology.

Synchronous inductance is composed of several inductance components, each for a particular PMSM element. These inductances are the magnetizing inductance L_m, the

end-winding inductance L_{ew}, the slot leakage inductance L_u, the tooth tip leakage inductance L_{tt}, the air gap leakage inductance L_δ, and the skew inductance L_χ.

The sum of these inductances gives the total synchronous inductance (Ponomarev et al., 2014a):

$$L_s = L_m + L_{ew} + L_u + L_{tt} + L_\delta \tag{2.8}$$

Analytical equations for each inductance element in Eq. (2.8) are developed and introduced in the literature (Ponomarev et al., 2013; EL-Refaie and Jahns, 2005; Tapia et al., 2013). However, for the sake of completeness classical analytical equations for inductance evaluation are given below:

$$L_m = \tau_p l' \frac{\mu_0}{\delta_{ef}} \frac{4q}{Q_s} \left(\frac{m}{\pi} k_{wp} N_s\right)^2 \tag{2.9}$$

$$L_{ew} = \frac{4m}{Q_s} \mu_0 N_s^2 q l_w \lambda_{ew} \tag{2.10}$$

$$L_u = \frac{4m}{Q_s} \mu_0 N_s^2 l' \lambda_u \tag{2.11}$$

$$L_{tt} = \frac{4m}{Q_s} \mu_0 N_s^2 l' k_2 \lambda_{tt} \tag{2.12}$$

$$L_\delta = \sigma_\delta L_m \tag{2.13}$$

$$\sigma_\delta = \sum_{\substack{v=1 \\ v \neq p}}^{v=+\infty} \left(p \frac{k_{wv}}{v \cdot k_{wp}}\right)^2 \tag{2.14}$$

From Eqs. (2.9)−(2.14) we can see that there is no principal difference between the inner rotor and outer rotor PMSMs if the rest of the constructional parameters are kept the same, except for the slot leakage inductance L_u, where the coefficient λ_u represents the geometry of a slot (Chevailler et al., 2007) by

$$\lambda_u = k_1 \frac{h_4 - h'}{3b_4} + k_2 \left(\frac{h_3}{b_4} + \frac{h_1}{b_1} + \frac{h_2}{b_4 - b_1} \ln \frac{b_4}{b_1}\right) + \frac{h'}{4b_4} \tag{2.15}$$

The slot dimensions related to Eq. (2.15) can be found in Figure 2.19.

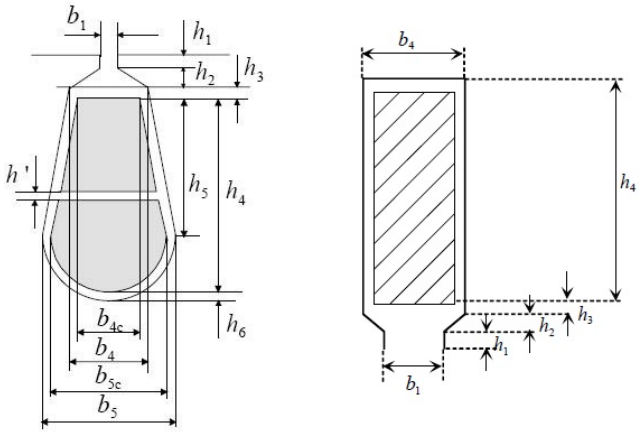

Figure 2.19: Slot dimensions. (Pyrhönen et al., 2008)

In a PMSM with an inner rotor and a fixed stator, the height of the slot has a direct influence on the external diameter of the machine. However, in the case of an outer rotor, an increase in the slot height only sacrifices the inner diameter of the active PMSM part. This means that if the inner diameter of the machine is not used, increasing the slot height in an outer rotor topology can improve the torque density of a machine. In this case, the slot leakage flux linkage is the only important parameter that is affected by the stator slot variation. If the slot leakage flux linkage is too high, it can increase the total synchronous inductance to an impractical value, which may degrade the performance of a PMSM, as it is shown in Figure 2.17.

In order to estimate the slot leakage inductance, Eq. (2.11) can be used. However, the total synchronous inductance should be a final output of the computation in order to determine a PMSM performance. The synchronous inductance as a function of stator slot height was evaluated by using the analytical equations (2.8)−(2.15) and validated by the FEM. The results of analytical and FEM computations are shown in Figure 2.20 (a). It can be seen that the synchronous inductance estimated analytically and by the FEM are close to each other. However, the synchronous inductance estimated by the FEM has a non-linear curve as a function of slot height and is flattened at large stator height values. Figure 2.20 (a) shows that the stator slot leakage inductance can have a significant impact on the total synchronous inductance. Therefore, it is not feasible to adopt a very high stator slot height if the synchronous inductance is already large. In the case of the machine studied in this doctoral dissertation, the tooth and the slot total height was selected h_d = 45 mm, which leads to the synchronous inductance L_S = 0.63 p.u.

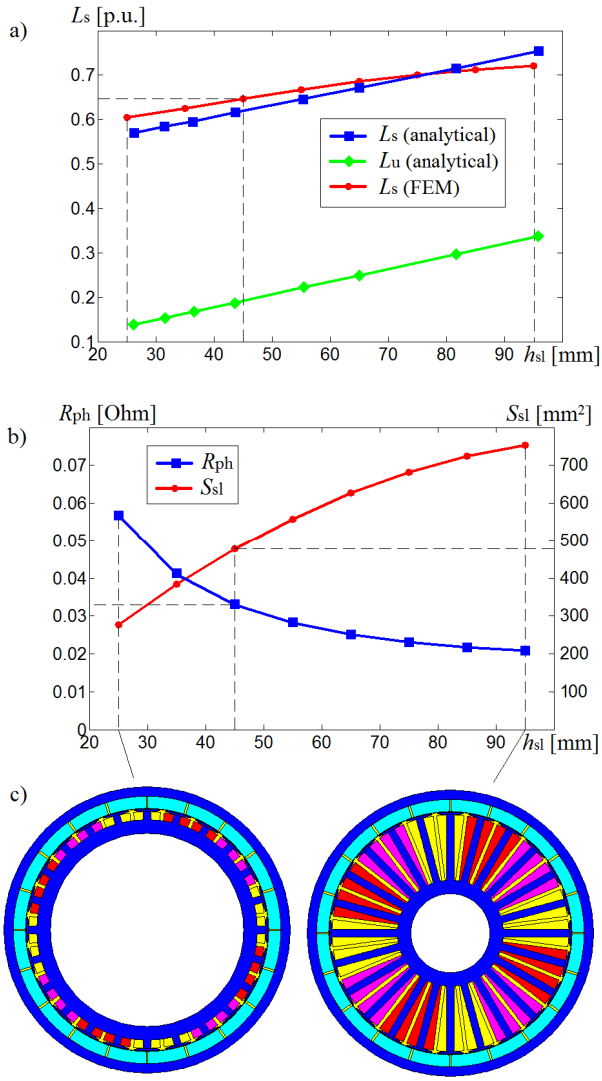

Figure 2.20: a) Synchronous inductance and slot leakage inductance as a function of slot height. The synchronous inductance is computed analytically and verified by the FEM. The end-winding leakage inductance is kept constant, which is estimated by Eq. (2.10). The slot leakage inductance is computed analytically. b) Stator slot area and phase resistance as a function of slot height. The copper space factor is kept constant (k_{Cu}). c) Schematic views of the studied machine in two utmost points of the slot height in (a, b).

Naturally, a suitably higher stator height is better, because it has a direct link with the slot area. Therefore, it is possible to increase the copper area, and consequently, reduce the phase resistance, Figure 2.20 (b). However, in the case of a high electrical frequency, there are also significant AC losses along with the DC ones in a PMSM. The AC losses can be caused by the strand-level and bundle level circulating currents, which depends on the slot leakage flux. Therefore, it is not a direct solution to only increase

the stator slot height to reduce copper losses, because a reduction in the DC losses can lead to an increase in the AC losses. Moreover, the iron losses increase in the case of high teeth. These AC losses are described in Section 2.4 in more detail.

In conclusion, it should be noted that the synchronous inductance is important and one of the most complicated characteristics in an electrical machine. It has an impact on three main parameters of a PMSM: power factor, overload capability, and field weakening. Further, it has an indirect impact on the torque ripple of a PMSM, as it is described below. The synchronous inductance can be evaluated analytically with and without taking into account the saturation caused by armature reaction. It is advantageous, even at the early design stages, to consider the impact of armature reaction on saturation, because this factor can significantly influence the resulting machine performance (Petrov et al., 2014c). The synchronous inductance should be verified by the FEM. The importance of correct synchronous inductance evaluation is illustrated in Figure 2.17, which shows that if the synchronous inductance value is underestimated, it may lead to a machine design that cannot achieve the required power.

2.3 Torque ripple

The challenge of torque ripple reduction is often associated with inner rotor PMSMs or SRM (Bianchi et al., 2009; Barcaro et al., 2012; Azar et al., 2012). This can be explained by the lower equivalent air gap, which in the case of rotor surface magnet PMSMs prevents a significant influence of armature reaction on the rotor steel saturation level. In the case of an asynchronous machine, the low equivalent air gap is compensated for by the rotor cage winding, which has a very high time constant. However, in a TCW PMSM, it is not practically possible to have a damping winding, because it would lead to excessive circulating current losses caused by the stator winding current linkage harmonics (EL-Refaie et al., 2008). Therefore, inner rotor PMSMs or SRMs are often subjected to high torque ripple harmonics. Based on the recent literature on the torque ripple reduction in PMSMs, it can be concluded that there are still no particular guidelines for the minimization of this torque ripple, but only some tips are given that can be applied and thoroughly modelled by a trial and error method to find the design with the minimum torque ripple (Bianchi et al., 2009; Zheng et al., 2011; Sizov et al., 2010; Lindh et al., 2014).

In principle, in rotor surface magnet PMSMs, the rotor yoke saturation (and its variation) should not have a significant influence on the torque ripple, because surface permanent magnets produce a relatively large reluctance in the magnetic circuit; consequently the possible variation in the rotor yoke reluctance (caused by the different saturation level if the flux density in the rotor yoke changes because of armature reaction) is not significant. In inner rotor PMSMs instead, the torque ripple generated by reluctance variation on the rotor side can be quite large.

Usually, with different rotor topologies, skewing is a good solution for cogging torque elimination and significant reduction in the current-linkage-induced torque ripple

(Güemes et al., 2011). Further, permanent magnet or rotor shaping can be optimized to improve the performance characteristics of a PMSM and to reduce cogging torque and torque ripple (Wang et al., 2014a; Wang et al., 2014b). However, even in rotor surface magnet PMSMs there are not always clear explanations for the occurrence of some torque ripple harmonics (Shin and Kwon, 2009), except for those which are caused by a non-sinusoidal back EMF, cogging torque or electronic controller nonlinearities (Islam et al., 2011). When there is torque ripple caused by different saturation levels in the magnetic circuit, which cause the reluctance variation, some trial and error methods are usually applied to optimize the stator tooth and rotor geometries close to the air gap to get the desired torque performance (Bianchi and Bolognani, 2002). However, in the literature there is no clear information where particularly these saturations take place and how these phenomena impact the total magnetic circuit reluctance, and only some assumptions are made (Islam et al., 2011). Therefore, it is important to understand where the saturation variation occurs in TCW PMSMs to focus the design efforts on this part of the magnetic circuit.

In (Petrov et al., 2014a; Ponomarev et al., 2014c) it was shown that in the TCW PMSM, the peak flux density in the stator teeth is not equally distributed, but with a particular periodicity. Therefore, some of the stator teeth can be subjected to a higher saturation compared with the others. This phenomenon produces additional periodicity in the magnetic circuit that has a lower frequency compared with the cogging torque (Petrov et al., 2014a). Therefore, torque ripple that is generated by saturation in the stator teeth has the lowest order harmonic component in the TCW PMSM. It was shown that the lowest-order torque ripple harmonic components are the most harmful to the mechanical structure of the whole system (Sopanen et al., 2011). Therefore, in (Petrov et al., 2014a), as a solution, it was proposed to reduce and even cancel the torque ripple caused by unequal saturation distribution on the stator side by selecting unequal teeth widths. However, it works well only for a particular loading point, whereas at other loads the saturation distribution in the stator teeth is not equal because of different armature reactions in various load modes. Therefore, this invention does not solve the problem but highlights the behaviour of tooth-coil machines.

The influence of magnetic circuit saturation on the torque ripple can be observed in Eq. (2.7), where the inductance variation, caused by the saturation effect, can have an influence on the current waveform if a voltage supply is applied. However, no significant high-order harmonics in the current waveform at the voltage supply were observed. Therefore, other reasons for the influence of saturation on the torque ripple should be found in the TCW PMSM.

The permanent magnet flux depends on the coercive force, permanent magnet permeability, permanent magnet geometry, permanent magnet magnetization direction, air gap height, and iron reluctance. If it is assumed that permanent magnets are magnetized in the radial direction, the permanent magnet flux can be found by

$$\Phi_{\mathrm{PM}} = \frac{H_{\mathrm{c}} l_{\mathrm{m}}}{R_{\mathrm{PM}} + R_{\mathrm{Fe}} + R_{\delta}} \tag{2.16}$$

whereas the iron reluctance R_{Fe} is inversely proportional to the iron permeability μ_{Fe}. Iron permeability is not linear, and can significantly decrease in highly saturated conditions. Therefore, the permanent magnet flux is not constant at different electrical loadings (armature reactions), which increase the flux through the magnetic circuit, and consequently, leads to its higher saturation. This permanent magnet flux variation is considered the main reason for the torque ripple caused by the saturation of the magnetic circuit in rotor surface TCW PMSMs.

Another significant source of torque ripple with an order lower than the least common multiple (LCM) between the slot number Q_{s} and the pole number 2p (Zhu et al., 2014) can be the mechanical uncertainties in the production process (Zhu et al., 2008). This factor is very harmful in series production machines (Qian et al., 2014; Gasparin et al., 2009) and in prototype manufacturing, and can spoil the geometry optimization results. Possible manufacturing errors lead to unreliable simulated data (for an idealized model) if torque ripple is regarded as a clue parameter. Therefore, this factor should be carefully considered, different manufacturing uncertainties should be determined, and their possible impact on the torque quality simulated, especially, if not only permanent magnet and rotor uncertainties are taken into account, but also stator segments are considered in the case of segmented stator structures similar to the one described in Chapter 3.

It should be mentioned that much effort has been put into torque ripple reduction by means of control methods (Islam et al., 2011). However, torque ripple reduction associated with power electronics is out of the scope of this work. Therefore, only PMSM design methods for torque ripple reduction were studied.

To sum up, we may state that it is still very challenging (or almost impossible) to fully eliminate torque ripple in PMSMs in every loading condition. This is mainly due to the non-linear behaviour of steel and non-ideal manufacturing conditions. One of the possible solutions is to design a machine where the flux density in the lamination remains fairly far from the saturation region. However, in this case, steel would not be used very efficiently, and the size of the machine would increase together with its manufacturing costs.

2.4 AC losses

If low manufacturing costs are the target, the winding arrangement should also be observed, because the number of winding coils, the winding type, and its production process significantly impact the total manufacturing cost of the stator. The winding process can be simplified if the stator has totally open slots and pre-processed windings are used (Jack et al., 2000). In this case, it is possible to achieve a high copper space factor. However, with an open slot construction, the air gap flux density in the normal

direction is distorted, and the permanent magnet flux linkage is significantly lower, because part of permanent magnets that do not directly face the stator teeth have a relatively high reluctance. Therefore, if a higher permanent magnet flux linkage is required, a semi-closed slot construction is preferred.

Another option to simplify the stator winding manufacturing routine in TCW PMSMs is to use a segmented stator structure, which allows to wind a coil around the stator tooth (segment) relatively easily, as it is shown in Figure 2.21.

Figure 2.21: Photo of a tooth (stator segment) that contains the stator coil with parallel strands.

If a simple winding arrangement is required with a high copper space factor, it is advantageous to make a coil of straight (not twisted) parallel strands. The need to divide a large-area coil into separate parallel strands can be explained by mechanical limitations, that is, the relatively low bending radius of the coil when it is wound around a narrow stator tooth, as it can be seen in Figure 2.21. However, the division of a coil into separate parallel strands also has an influence on its electromagnetic characteristics. For example, the use of a high number of strands allows reducing skin effect in the coil (Reddy and Jahns, 2010).

In addition to the skin effect, proximity effect can have a significant impact on the total additional AC losses in the stator winding if a machine operates at a high electrical frequency (Reddy et al., 2009). These losses are also called bundle proximity losses that are caused by circulating currents in the parallel strands of the same coil (Reddy et al., 2009). It is possible to avoid or significantly reduce these losses if winding transposition is implemented in such a way that each strand faces the same magnetic flux as the other strands of the coil. However, the use of twisting strands or Litz wire can increase the cost of the winding and reduce the copper space factor. It can also be challenging to

bend the coil around the teeth if the twisting pitch is very small. Therefore, sometimes it is advantageous to choose a simple straight arrangement of the coil strands. Further, in the case of a high-frequency PMSM, it is necessary to arrange some kind of transposition of parallel strands to reduce excessive circulating current losses. However, in the case of the PMSM studied in this dissertation, there was a misunderstanding between the author of the dissertation and the winding manufacturer, which led to the manufacturing of the stator winding coils of straight (not twisted) parallel strands. Therefore, there are significant additional AC losses in the stator winding, which clearly degrade the overall efficiency of the machine. Nevertheless, the cooling of the stator was sufficient to dissipate the heat caused by these losses, and the stator winding did not reach the thermal limits specified by the winding insulation.

In the literature there are some other suggestions, in addition to strand transposition, regarding the reduction of AC losses in the winding (van der Geest et al., 2013; Mellor et al., 2006; Popescu and Dorrell, 2013; Reddy et al., 2008). However, most of the proposed techniques to reduce additional winding AC losses degrade the performance of the machine at a low speed (low electrical frequency), at least to some extent, which might be not acceptable for some applications, for instance vehicle traction systems. Therefore, it is important to estimate in advance the negative effects of additional AC losses on the PMSM characteristics if the losses cannot be avoided. One of the natural effects of additional losses is extra heat in the machine, and if it is not dissipated properly, it can cause a significant reduction in the lifetime of the winding insulation.

As it was mentioned above, the stator winding of the PMSM under study contains straight parallel strands wound around the teeth. This together with the fact that the use of ferrite permanent magnets in the PMSM inevitably increases its slot area (because of the low air gap flux density, which should be compensated for by a higher number of winding turns) leads to a case where the stator slot flux leakage causes a high circulating current in the coil. An example of the circulating currents caused by the slot flux leakage, known as bundle proximity losses, for a non-twisted straight winding is shown in Figure 2.23 (a) and in Figure 2.24 (a) at two different time instants (when the total phase current is zero and when the phase current has the peak value). Again, Figure 2.23 (b) and Figure 2.24 (b) show the current density distribution for the same load when the windings are twisted at the end as it is shown in Figure 2.22.

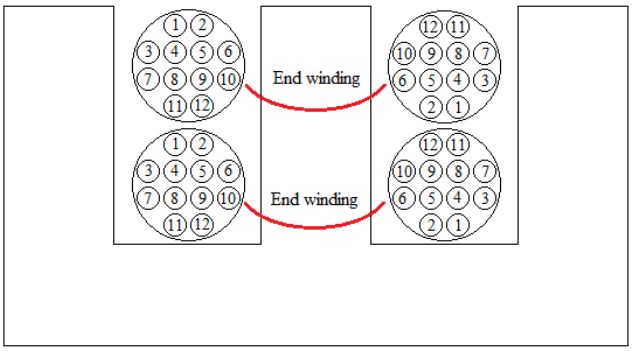

Figure 2.22: Winding connection with twisting of the winding end. Two strands with the same number in different slot represent one turn. The twisting is carried out so that a strand position switches from the top to the bottom.

The winding transposition should be carried out in such a way that the slot flux leakage that one strand turn faces is the same as for other strand turns. In this case, generation of circulating current can be minimized or even avoided, as it can be seen in Figure 2.23 (b).

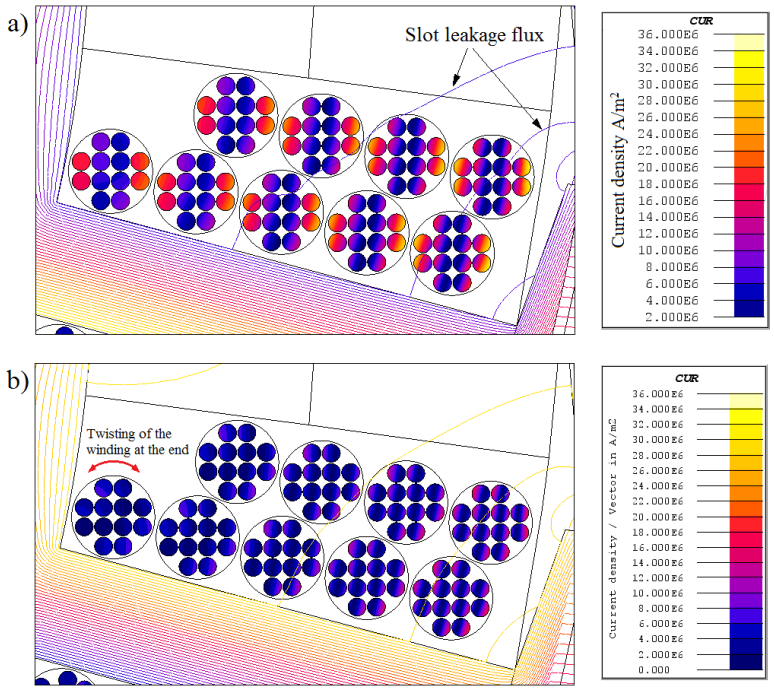

Figure 2.23: Current density distribution in the winding at the nominal load of the PMSM under study. The coil contains twelve parallel strands. The current distribution is shown at the moment when the total current of the phase is zero. The end winding resistance is not taken into account. a) Straight strands without transposition at the winding end. b) Twisted winding at the end as shown in Figure 2.22.

Figure 2.23 shows that the slot leakage flux is relatively low compared with the case illustrated in Figure 2.24, because the total mean current (which does not include circulating current) in the coil is zero.

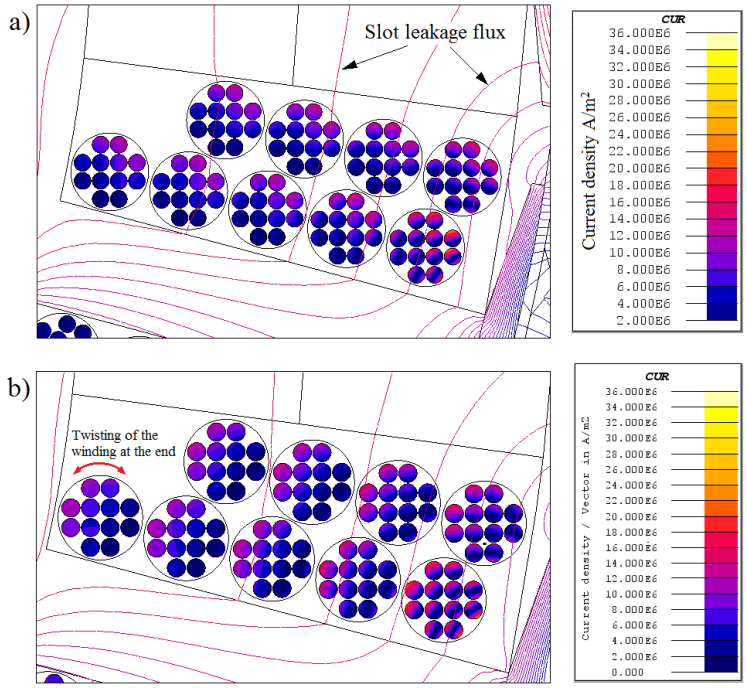

Figure 2.24: Current density distribution in the winding at the nominal load of the PMSM under study. The coil contains twelve parallel strands. The current distribution is shown at the moment when the total current of the phase has the peak value. The end winding resistance is not taken into account. a) Straight strands without transposition at the winding end. b) Twisted winding at the end as shown in Figure 2.22.

The leakage flux in the slot shown in Figure 2.24 (at the time instant when the phase current has the peak value) is much more intense compared with the case of Figure 2.23, because this flux leakage in the slot is caused not only by the permanent magnets, but also by the mean phase current (peak value). Therefore, by observing the two figures above, we may conclude that there is an alternating flux leakage in the slot with its maximum and minimum values. According to Faraday's induction low, alternating flux induces a back-EMF

$$e = -\frac{\mathrm{d}\Psi}{\mathrm{d}t} \tag{2.17}$$

The induced back EMF lags behind the slot leakage flux linkage by 90 electrical degrees. Therefore, if the resistance is dominating compared with the reactance in the circuit, the vector of the induced circulating current should also lag behind the slot leakage flux linkage by approximately 90 electrical degrees. Consequently, in the

observed case shown in Figure 2.23 and in Figure 2.24, the circulating current is mainly resistance limited and not inductance limited. The Joule losses in the stator winding as a function of torque and speed of the PMSM are shown in Figure 2.25.

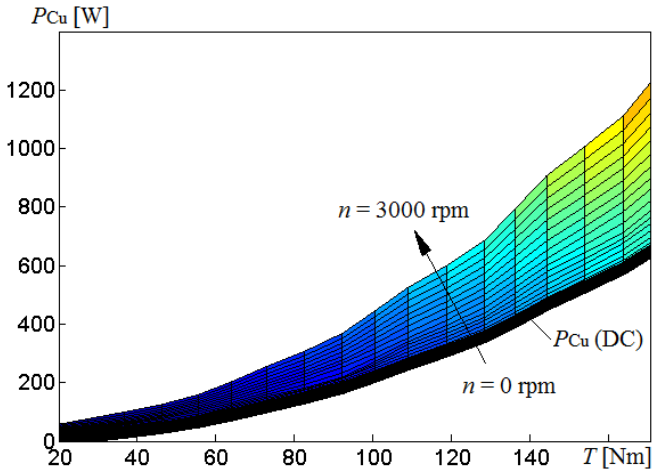

Figure 2.25: Joule stator winding losses at different torques and angular speeds of the studied PMSM.

Figure 2.25 shows that at the nominal load (n = 3000 rpm, T = 170 Nm). The estimated losses in the winding at nominal torque and at low (zero) speed can be half of that at nominal torque and nominal speed.

It should be noted that the position of the coils shown in Figure 2.23 does not precisely follow the actual location of coils in the machine. Further, the number of parallel strands in the coil is different, which is 27 in reality. However, the total coil area is the same in the simulation and in the actual machine (~23 mm^2). The objective of this simulation was not to precisely estimate the additional AC losses caused by circulating currents, but to evaluate an approximate proportion of these losses in the total machine losses. It was found that these losses can be very high in the PMSM, and significantly reduce its efficiency. Thus, it is necessary to apply parallel strand transposition or to use Litz wire to prevent the performance deterioration in a PMSM having a high electrical frequency and significant stator slot leakages.

2.5 Measurement results

The outer rotor ferrite permanent magnet PMSM studied in this doctoral dissertation was designed in collaboration between the Departments of Mechanical Engineering and Electrical Engineering. The main electro-magnetic design of the machine was carried out within the Department of Electrical Engineering. However, the development of the cooling arrangement (size and geometry of the rotor fan) was performed by Professor Jaakko Larjola from the Department of Energy Technology and by the Department of Mechanical Engineering. They also provided their advice regarding the mechanical

reliability of the construction. Therefore, from the author's point of view, the main risk of the PMSM manufacturing was the overheating of the stator winding at the nominal load resulting from the possible underestimation of the machine losses and mistakes made in the cooling arrangement assessments.

This chapter provides the information about the measurement results of the electro-magnetic part of the PMSM, such as the back-EMF, current at the nominal load and efficiency map of the machine for different operating points. Importantly, also the thermal state of the stator winding was evaluated in several places close to the hottest spots of the PMSM (in the stator winding).

The measured and estimated back-EMFs are shown in Figure 2.26. We can see that there is a good correlation between the estimated and measured back-EMFs. The difference between the estimated and measured EMF peak values is 3 %. However, the actual back-EMF is not constant in different load points, because the permanent magnet temperature has a direct influence on its remanent flux density, as it can be seen in Figure 2.6. Therefore, the remanent flux density used in the FEM simulations was B_r = 0.34 T, which is the estimated remanent flux density for the magnet used at the temperature T = 80° C. However, uniform distribution of this particular temperature in the permanent magnets might be not the case in the actual PMSM at the nominal load. This could cause the difference between the average values of the actual and evaluated back-EMFs, as it is seen in Figure 2.26.

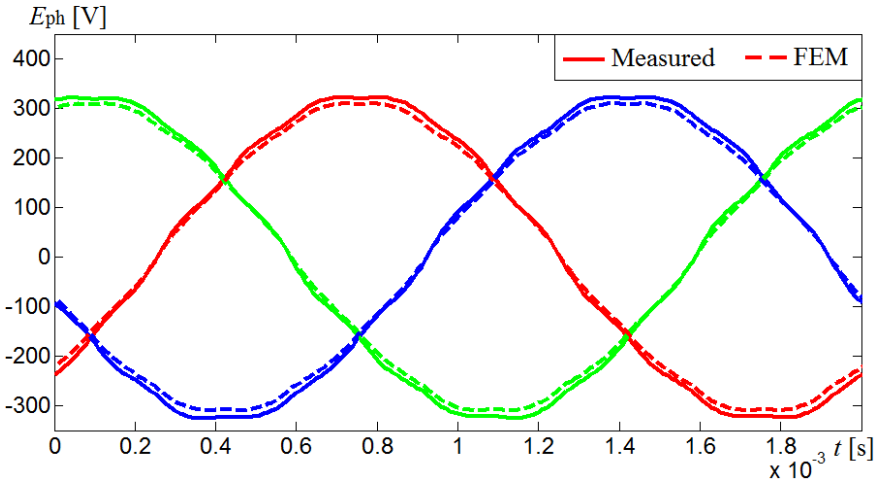

Figure 2.26: Measured and estimated back-EMFs of the PMSM under study. The remanent flux density used in the FEM is B_r = 0.34 T. The back-EMF of the actual machine was measured instantaneously after it had worked for several hours at the nominal load in order to reach the steady-state temperature in the permanent magnets.

The voltage supply applied in the simulation has a purely sinusoidal waveform. However, the actual voltage waveform of the electrical machine supplied by a frequency converter, usually has a discontinuous character, which causes some ripple in

the current waveform. The measured current waveform at the nominal load and the voltage waveform of the PMSM under study is shown in Figure 2.27.

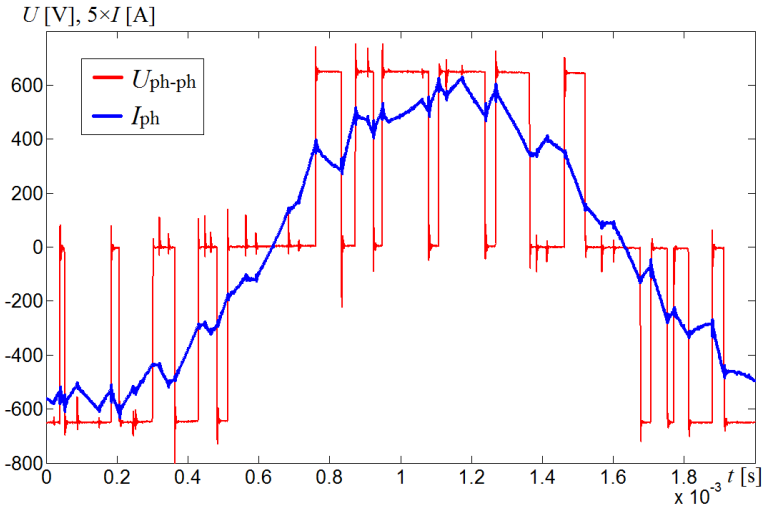

Figure 2.27: Measured phase-to-phase voltage and phase current at the nominal load. The switching frequency is not constant, because the PMSM was controlled by the DTC.

According to (Iwasaki et al., 2009), this current ripple can cause additional losses in the stator winding. However, the FEM simulation with the same current supply shown in Figure 2.27 indicated that this was not the case in the PMSM under study.

As it was mentioned above, the additional AC losses in the PMSM significantly impact its total losses, especially at higher speeds. Therefore, the measured efficiency was much lower compared with the expected one, as can be seen in Figure 2.28. Together with the proximity losses, one possible reason for this efficiency drop can be the additional hysteresis losses in the permanent magnets (Pyrhönen et al., 2015). However, this hypothesis is under study at the moment, and the permanent magnet samples, which were used in the prototype, are tested in order to evaluate any hysteresis losses.

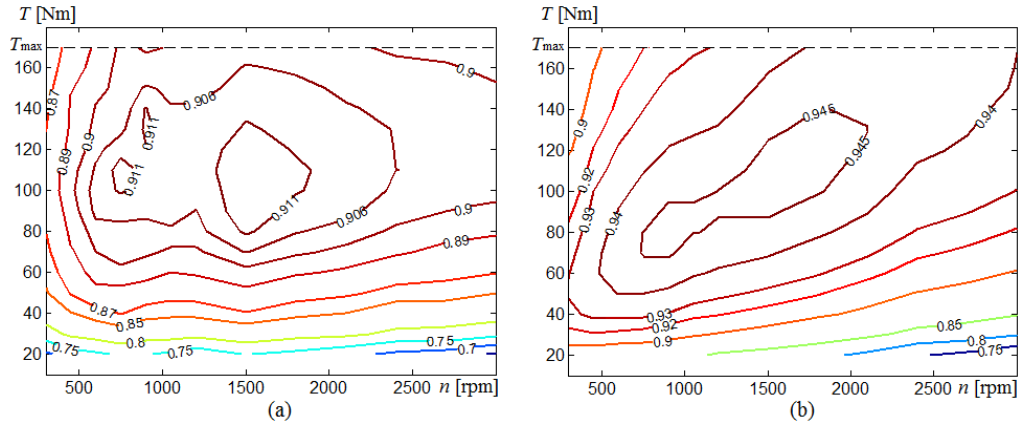

Figure 2.28: Efficiency maps of the PMSM a) measured and b) estimated efficiency map with measured no-load losses (iron + mechanical friction losses).

The efficiency shown in Figure 2.28 (a) is the measured one. In addition to the electromagnetic losses it includes mechanical losses (friction, windage). Figure 2.28 (b) illustrates the efficiency map estimated with consideration of stator copper losses (with no proximity effect taken into account), eddy current losses in the solid rotor (FEM), and measured no-load losses (that includes iron losses and mechanical friction losses). We can see that the measured efficiency map and estimated efficiency map (with no proximity effect taken into account and with no AC additional losses), are too different, and an acceptable correlation between the efficiency maps is only found in the high-torque and low-speed area. In this region, the power to frequency ratio is at maximum, which means that the impact of additional AC losses on the overall PMSM efficiency is at minimum. However, at higher frequencies the additional AC losses can have a significant effect on the total losses. This effect is shown in Figure 2.29, which shows the proportion of losses in the PMSM as function of speed.

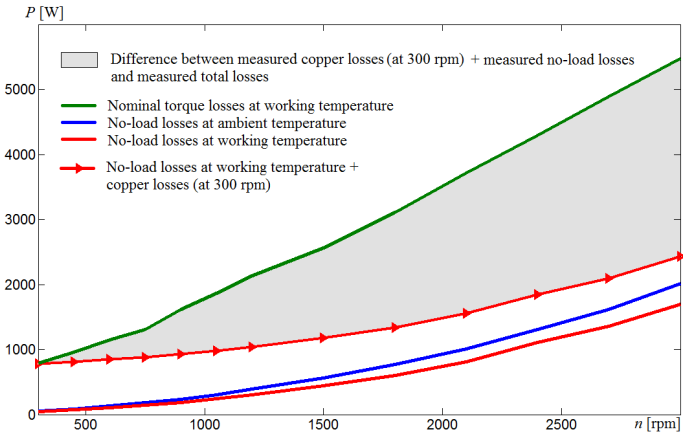

Figure 2.29: Proportion of losses in the PMSM as a function of rotational speed. Additional AC losses (which are added to the DC copper losses and no-load losses) are highlighted by grey colour.

Figure 2.29 shows that at a higher angular speed of the PMSM, the additional AC losses can account for the largest proportion of the total losses. Therefore, this aspect should be carefully analysed in the design process and some actions, for instance strand transposition, should be taken.

Together with additional AC losses due to proximity effect, there remains an option that the extra losses are caused by hysteresis in the permanent magnet rotor. As it was shown in Section 2.1, the armature reaction in this type of a machine is high as the flux density is low, and a high linear current density has to be used to compensate for the low flux density. Despite the considerable magnet height, the magnets are prone to hysteresis loss because the armature reaction drives parts of the magnets above the remanent flux density of the material. However, when preparing the prototype, the possible hysteresis losses were ignored. They were later studied for instance in (Pyrhönen et al., 2015). Recently, we have also measured the hysteresis behaviour of the magnet material used in this case.

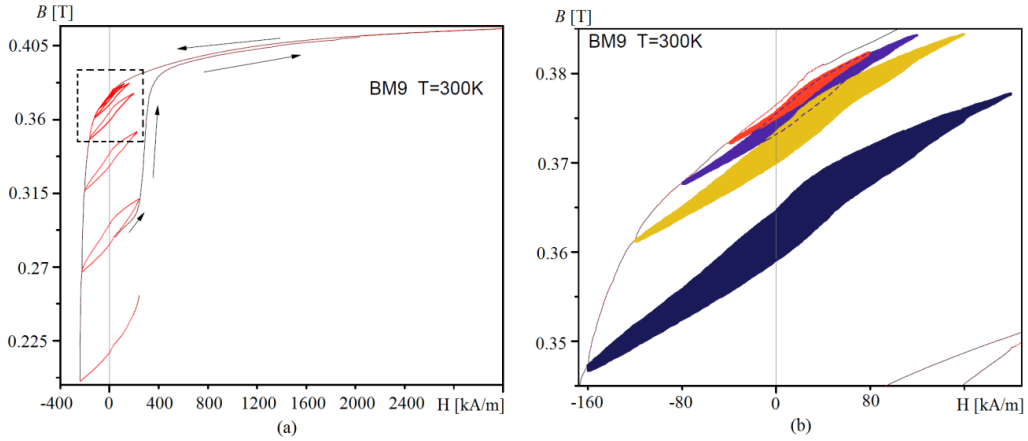

Figure 2.30: a) Measured hysteresis loops of the ferrite permanent magnet used in the PMSM at different applied field strengths. b) Zoomed view of the hysteresis loops in the point close to the remanent flux density (Loops courtesy Raivo Stern Tallinn).

Figure 2.30 shows that the hysteresis loops appear in the magnets when the operating point switches from the first quadrant (where the PM flux density is below the remanent flux density) to the second quadrant (where the PM flux density is above the remanent flux density). These hysteresis loops can lead to additional AC losses in actual PMSMs if the armature reaction acts in such a way that the *BH* curve crosses the *J*-axis (zero magnetic field strength) (Pyrhönen et al., 2015).

As it can be seen in Figure 2.7, in the case of the studied PMSM (at the nominal load), the armature reaction is strong enough to make the permanent magnet flux density fluctuate so that it crosses the remanent flux density. Therefore, it can be assumed that the hysteresis losses can take place in the ferrite magnets. A preliminary estimation of this loss gives the following results

$$\Delta B \approx 1.8 \text{ mT} \tag{2.18}$$

$$\Delta H \approx 150 \text{ kA} \tag{2.19}$$

$$\Delta B \Delta H \approx 270 \text{ J/m}^3 \tag{2.20}$$

According to the rough estimation based on Figure 2.7 and Figure 2.30, we may conclude that at the nominal load, the permanent magnets generate additional losses $\Delta B \Delta H \approx 270$ J/m^3 for one cycle. At 3000 rpm in the 24-slot 20-pole TCW PMSM, the frequency of this cycle in one permanent magnet is 1200 Hz. The volume of one magnet is $V_{\text{PM}} = 8.9\times10^{-5}$ m^3. If it is assumed that the flux density distribution along the permanent magnet height is the same (except spikes that are generated by the tooth tip flux leakage and that do not penetrate deep in the magnet height), the total loss can be found as

$$P_{\text{PM}} = \Delta B \Delta H \times f \times 2p \times V_{\text{PM}} = 580 \text{ W} \tag{2.21}$$

The resultant hysteresis loss in the ferrite magnets found in Eq. (2.21) partially explains the additional AC losses in the PMSM at the nominal load. However, it still has to be more carefully estimated as a function of speed and torque in order to grasp its influence on the efficiency map of the PMSM.

The losses in the PMSM turn into heat, which should be dissipated in order not to reach the maximum permitted temperature limit of the PMSM components. Usually in PMSMs, the stator windings have the highest temperatures, whereas the winding insulation life time is very sensitive to the temperature variation. There are different insulation classes which, in addition to the different mechanical and electrical properties (e.g. partial discharge strength) have different maximum temperatures to be able to operate for a certain amount of time (Pyrhönen et al., 2008). The insulation of the PMSM studied in this dissertation has a thermal class 200, which means that its maximum permitted temperature is 200° C.

In principle, the inner stator arrangement brings additional challenges to the stator winding cooling, because in this case the stator losses should be dissipated through the rotational part of the machine. However, in the case of the PMSM under study, this challenge was solved by using an integrated fan in the rotor, which forces the air flow to pass through the stator slots and cool the stator windings.

Nine temperature sensors were installed in the PMSM stator winding to follow its temperature state at different working loads. The locations of the temperature sensors installation for one phase are shown in Figure 2.31.

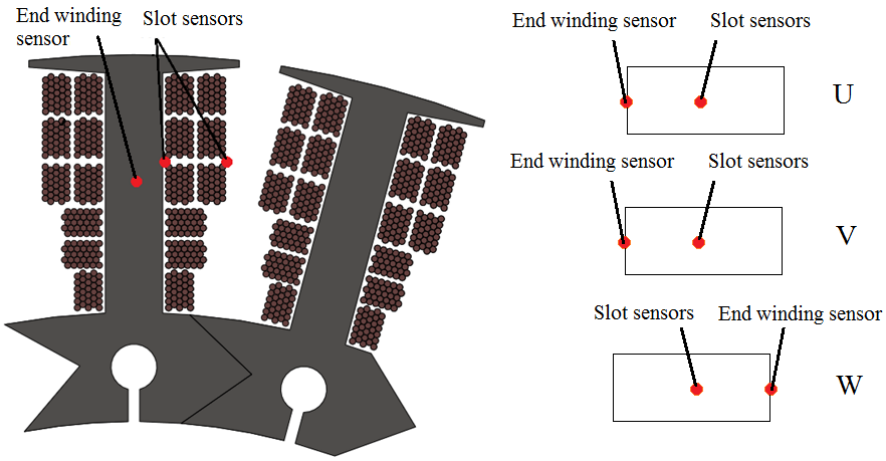

Figure 2.31: Location of the temperature sensors in the stator windings. All the slot sensors are located approximately in the middle of the machine length. However, the end-winding sensors are located at the edge of the stator stack. Two phases (U, V) have end-winding sensors on the same side, and phase W has the end-winding sensors on the opposite side.

Figure 2.31 depicts the locations of the temperature sensors. These sensors were installed for each phase in the same locations. However, the end-winding sensor for one phase (W) has an opposite location compared with the end-winding sensors for the two other phases (U, V). The end-winding sensor of phase W is located close to the input cooling air in the stator. Therefore, it is expected that it has the lowest temperature compared with the other stator winding sensors, as can be seen in Figure 2.32.

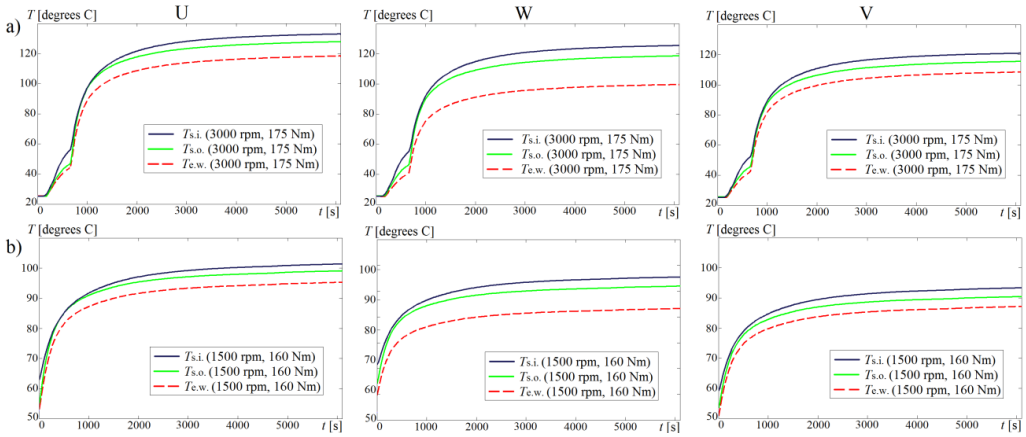

Figure 2.32: Measured temperature in the end winding (end-winding sensor) and in the slot (slot sensors). a) Temperature at the nominal power (3000 rpm, 175 Nm) b) Temperature at the nominal torque and at half the nominal speed (1500 tpm, 160 Nm). U, W and V are the phases where the sensors are installed. In phase W, the end winding sensor is installed on the side close to the air input, and in phases U and V the end winding sensors are installed on the side close to the air output. $T_{e.w.}$ is the temperature in the end-winding area, $T_{s.i.}$ is the temperature inside the slot winding, and $T_{s.o.}$ is the temperature on the surface of the slot winding.

The temperature of the stator winding in different locations was measured for two different loads. These temperatures are shown in Figure 2.32. The loads are 3000 rpm, 175 Nm and 1500 rpm, 160 Nm. The hottest temperature can be observed inside the slot between the winding and the stator lamination stack. It was expected, because there are two main sources of heat; the stator lamination and the stator winding. Further, the air flow that passes through the stator slot mainly cools the surface of the winding. Therefore, the temperature of the winding surface ($T_{s.o.}$) is lower than the temperature between the stator winding and the lamination stack. The lowest winding temperature is in the end-winding especially in phase (W), where the temperature sensor is located on the side close to the air input.

We may conclude that the air flow is sufficient to keep the winding temperature below the thermal limit of the insulation.

3 Segmented stator PMSM

The studies on segmented stator arrangements can be justified by the opportunity to simplify the manufacturing process. Segmented stator arrangement should lead to a fast and very simple winding routine, and therefore a simple automatization system. However, some challenges and drawbacks can be found if electromagnetically insulated segments are used. A PMSM with segmented stator structure was analysed and the results were verified by measurements. This chapter shows the main aspects which should be considered if a machine with similar structure is designed. The analysis results in more detailed can be found in a future journal article.

The stator segmentation can be divided into two main types. The first type resembles a conventional electrical machine, the only difference being the additional air gaps between the stator segments, which may cause some performance deterioration if the height of these air gaps is significant enough (Zhu et al., 2012). In the second segmentation type, the stator segments are electromagnetically insulated from each other, which may significantly change the flux pattern of the whole machine (Li et al., 2014; Heins et al., 2013; Dajaku and Gerling, 2012). Therefore, the parameters of a PMSM with a segmented stator can differ from those with a monolithic stator. An example of the flux pattern variation in two similar PMSMs but with different stator structures (monolithic and segmented), is shown in Figure 3.1.

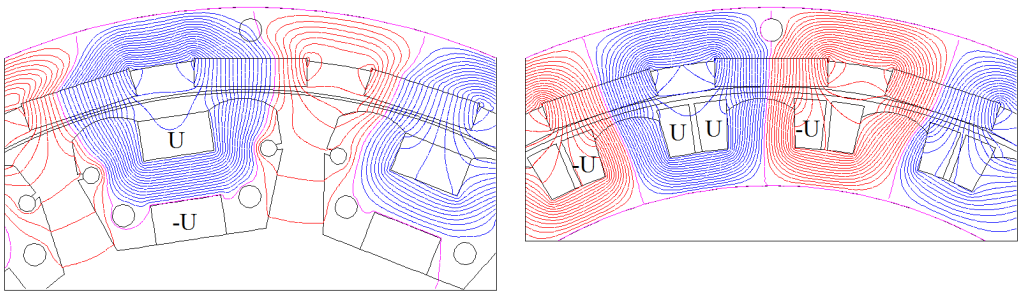

(a) (b)

Figure 3.1: Flux patterns at the no-load operation of a) the segmented stator PMSM under study and b) a similar PMSM but with a monolithic stator. The non-symmetric flux behaviour in the rotor yoke (the flux does not flows in the shortest path) of the segmented PMSM is due to the fact that the rotor yoke is modelled as a solid structure, where eddy currents prevent its immediate change.

Figure 3.1 shows that in the segmented stator structure, the flux pattern is highly asymmetric. It causes additional flux harmonics in the air gap and in the rotor yoke. However, the back-EMF is not subjected to significant disturbances and it is kept almost purely sinusoidal, as can be seen in Figure 3.5, where the back-EMFs of the two PMSMs shown in Figure 3.1 are illustrated.

The segmented PMSM under study is originally a 24-slot 20-pole TCW PMSM, rearranged in such a way that there is a cut between the stator teeth pairs. The stator

teeth pairs contain the winding of only one phase. Therefore, the winding routine can be significantly simplified, as it is shown in Figure 3.2. In this case, it is relatively easy to wind a coil around the stator segment, especially if open slots are used.

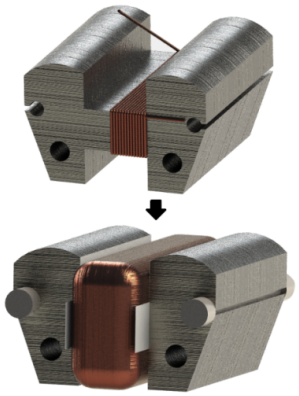

Figure 3.2: Winding process of the rearranged stator segment. The coil can be wound relatively easily around the stator segment especially if open slots are used.

Each segment is equivalent to two stator teeth of a conventional (monolithic) TCW PMSM. However, as can be seen in Figure 3.2, it requires only one winding operation. It means that the duration of the winding manufacturing process can be reduced. It should be noted that the number of coil turns should be approximately the same in both the monolithic stator and segmented stator structures.

The principal difference between the winding processes of the conventional TCW PMSM and the proposed one is the end-winding length. Figure 3.3 shows that the end-winding length in a conventional TCW PMSM is related to its slot width (b_4), whereas in the segmented PMSM it depends on the winding height (h_4). It means that in the proposed segmented PMSM, the axial length of the end winding depends on the selected stator slot height, which should be kept within a reasonable range.

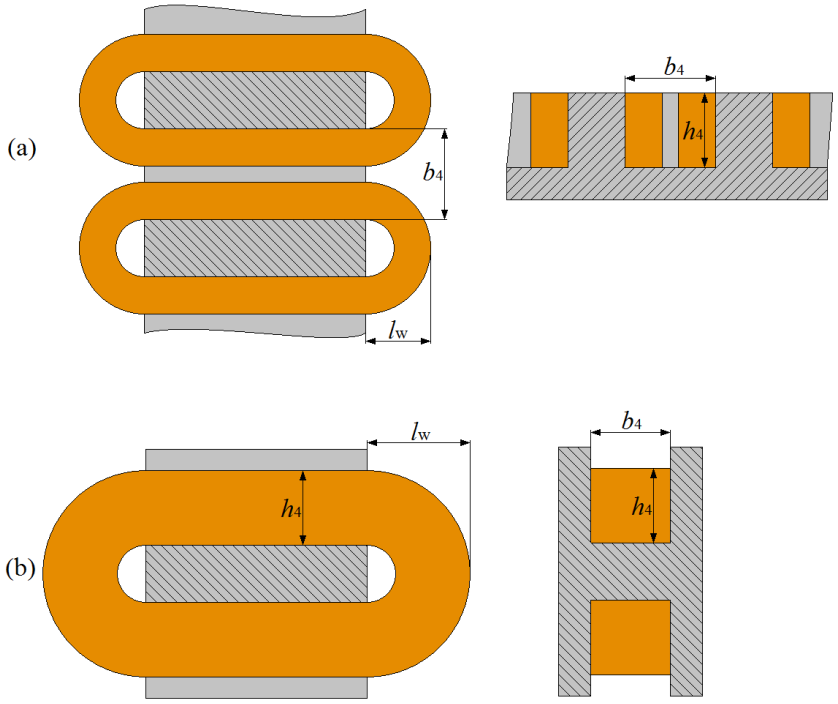

Figure 3.3: a) Conventional TCW PMSM winding arrangement. b) Proposed segmented PMSM winding arrangement.

The simplified structure of the generator is shown in Figure 3.4. According to the application, the generator should be integrated into the hook block of a hoist. Each stator segment is attached to a special supporting unit, which keeps the segments in their position. As it is described below, the position of each stator segment should be symmetrical, and no mechanical uncertainties are allowed if cogging torque is a critical parameter.

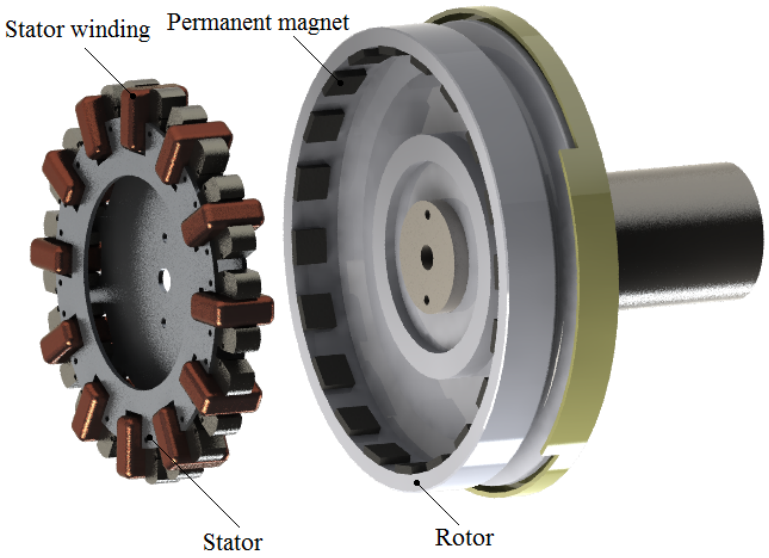

Figure 3.4: Simplified construction of the segmented PMSM under study. The PMSM constructional elements are: outer rotor, segmented stator structure, and the new winding arrangement.

The back-EMF of the proposed PMSM is lower than that of the analogous conventional TCW PMSM, as can be seen in Figure 3.5. It means that if the same back-EMF has to be achieved, the number of winding turns in the segmented PMSM structure should be increased.

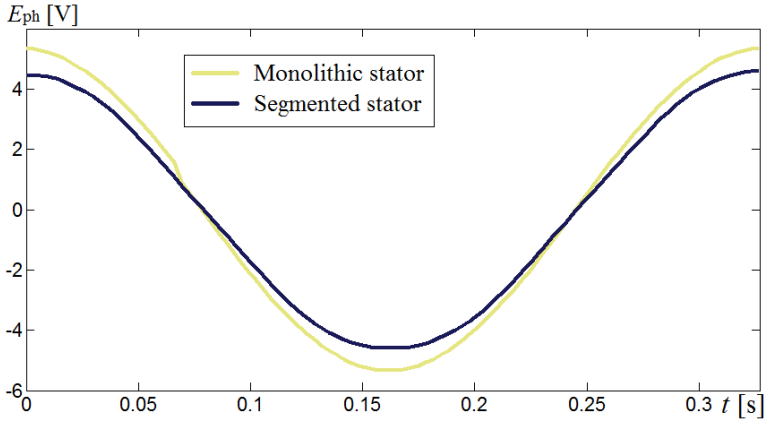

Figure 3.5: Back-EMF of the similar PMSMs (rotor geometry, number of winding turns, and air gap length are the same in both PMSMs) the only difference being in the stator structure.

The back-EMF shown in Figure 3.5 for the PMSM with the segmented stator structure is lower (13 %) compared with the PMSM with the monolithic stator. It can be explained by observing the PMSMs flux patterns, Figure 3.1. The PMSMs have such rotor positions that the permanent magnet flux in phase U is at maximum. In the case

with the segmented stator, the flux leakage between the segments does not contribute to the generation of back-EMF, which decreases the overall EMF. This, however, does not apply to the monolithic stator, because it has only the slot flux leakage.

To sum up, based on the small difference between the EMF values of the monolithic and segmented stator structures, we may assume that the performance characteristics of the PMSMs shown in Figure 3.1 do not differ significantly, especially if actions are taken to reduce flux leakages between the segments. However, because of the heavily distorted permanent magnet flux linkage in the rotor yoke of the PMSM with the segmented stator, it is very sensitive to the material used in the rotor yoke. For instance, if the rotor yoke is made of solid steel, it can cause significant losses in the rotor as a result of eddy currents. This phenomenon is explained in detail in the following section.

3.1 Influence of the stator segmentation arrangement on rotor-surface permanent magnet losses and rotor yoke losses

As it was mentioned above, if the stator yoke is not monolithic but discontinuous as a result of segmentation, it can cause a highly asymmetric flux pattern, which tends to vary in every rotor position. In order to study the nature of this phenomenon the reluctance variation of the PMSM magnetic circuit has to be observed as a function of rotor position. Figure 3.6 shows the flux maps of the PMSM with a segmented stator in different rotor positions.

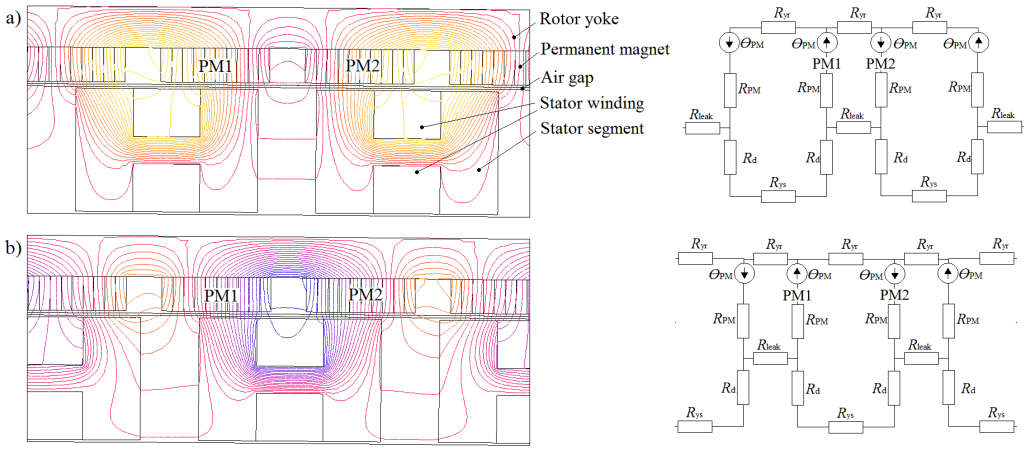

Figure 3.6: Flux pattern variation in different rotor positions. a) Rotor position when the common flux between permanent magnets PM1 and PM2 is at minimum. b) Rotor position when the common flux between permanent magnets PM1 and PM2 is at maximum.

Figure 3.6 shows that there is a significant flux variation in the rotor yoke in different rotor positions. This magnetic flux variation may cause significant eddy current losses in the rotor if it is made of a solid material with a high permeability. However, the flux density fluctuation in permanent magnets is in the same range as in the similar PMSM

with a monolithic stator, because the main flux path in permanent magnets does not vary as in the rotor yoke.

The variation of the flux in the rotor yoke can be explained by the magnetic circuit variation in different rotor positions as can be seen in Figure 3.6. In this type of the PMSM (with the segmented stator), it produces a negative effect because of the additional losses in the rotor yoke. However, the similar principle is used in the flux switching machine described in (Sarlioglu et al., 1994; Zhu, 2011), where the windings are located on the same side as the permanent magnets. Because of different flux paths produced by permanent magnets in different rotor positions, EMF is induced in the windings. In order to avoid excessive rotor losses caused by eddy currents, the rotor yoke has to be made of laminated steel.

The flux density variation in the rotor yoke has the same frequency as the flux density variation in the stator yoke, or in other words, as the back EMF frequency. If we assume that the rotor yoke contains the winding with the same number of turns as the stator winding, the peak value of the fundamental (first) harmonic of the permanent magnet flux linkage in the rotor yoke would be approximately half of one in the stator yoke, as can be seen in Figure 3.7, where the flux linkages in the stator yoke and in the rotor yoke are shown as a function of rotor position in electrical degrees.

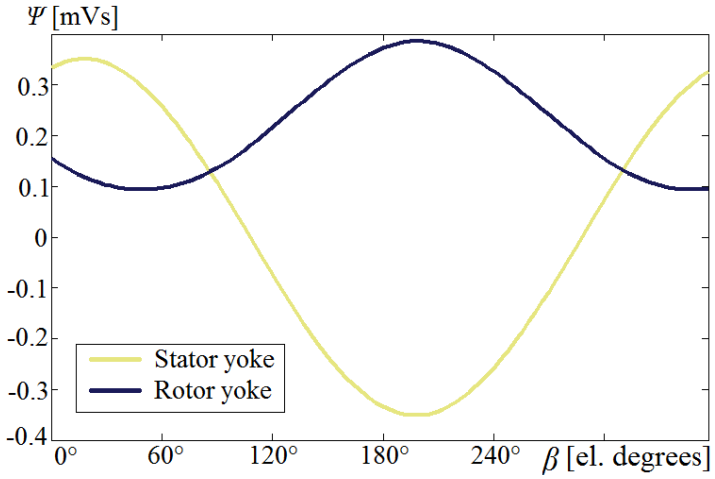

Figure 3.7: Flux linkage in the stator and rotor yokes of the PMSM (Figure 3.6) at no load. The axial length of the machine is 50 mm, and the rotor and stator yoke thicknesses are 12 mm and 8 mm, respectively.

According to Figure 3.7, even if the rotor yoke is made of a lamination stack the iron losses are comparable with those in the stator steel. Therefore, in PMSMs having a stator structure with discontinuities, additional losses can be expected in the rotor yoke, especially if it is made of solid steel.

The segmented PMSM studied in this thesis has a solid rotor yoke, because it significantly simplifies the PMSM structure. The PMSM was designed as a generator for a low-speed and very low-power application (18 rpm, 0.5 W). Therefore, even though the solid rotor significantly reduces the machine efficiency, the total absolute value of the input mechanical power is not increased dramatically.

The influence of the solid rotor losses on the total input power as a function of rotational speed at the nominal current (I_{ph} = 1 A) is shown in Figure 3.8. The figure shows that at a low speed, the rotor losses have a small contribution to the total input power. However, at a higher speed (> 100 rpm) the rotor losses caused by eddy current start to increase to a non acceptable value, which would require the use of laminated steel.

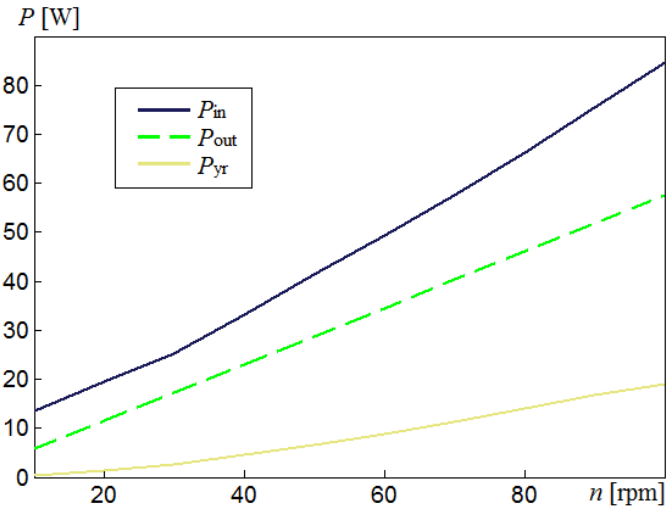

Figure 3.8: Solid rotor yoke losses as a function of rotational speed at the nominal torque (FEM). PMSM is operating in the motoring mode.

Figure 3.8 demonstrates that the proportion of solid rotor losses at low rotational speeds is small. However, in a low-power machine at a low rotational speed, the phase resistance can have a significant influence on the machine performance as described in the following section.

3.2 Influence of stator phase resistance on the machine performance

Figure 3.8 shows the output power that can be achieved at 18 rpm (P_{out} = 10 W) in the motoring mode. However, according to the application, the PMSM has to operate in the generator mode to supply measurement electronics inside of the hook block of hoist and generate electrical power P_{out} = 0.5 W with the phase voltage U_{ph} = 3 V_{rms}. In the design of the machine, the wire area was selected to be much larger than the thermal winding condition would require. In the consideration on the machine for industrial application (0.75 − 90 kW), it was assumed that the phase resistance does not have any influence on

the machine performance because the phase resistance value was lower than 0.02 p.u. However, for a very low-power machine (at a low speed), the phase resistance should be taken into account. The vector diagrams that consider the phase resistance of the studied machine for the required power (0.5 W at 18 rpm) and for the higher power (114 W at 262 rpm) are shown in Figure 3.9.

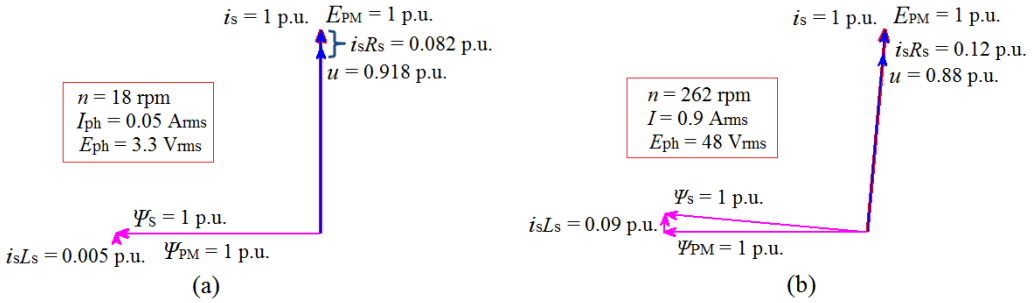

Figure 3.9: Vector diagrams of the studied machine with a segmented stator a) at the power required by the application and, b) at a higher power at a higher rotational speed and phase current.

In the vector diagram shown in Figure 3.9 (a) we can see that the phase resistance together with the applied phase current has a direct influence on the terminal voltage of the generator. Therefore, the phase resistance should be selected such that the required terminal voltage is achieved at the nominal power.

Usually, the terminal voltage is a fixed parameter, which is provided by the application. Therefore, the back EMF of the generator should be designed so that at the nominal load, the terminal voltage does not decrease below the permitted value. It means that in a machine with a higher phase resistance at the same load (current), the back-EMF should be larger. This is achieved by a higher number of turns, which, in turn, further increase the phase resistance. An algorithm that can be used for the evaluation of the phase resistance and the back-EMF is shown in Figure 3.10.

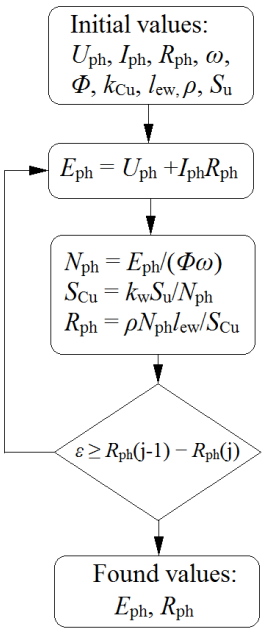

Figure 3.10: Algorithm for the evaluation of the back-EMF and phase resistance of the generator with the given slot area (S_u), phase voltage (U_{ph}), phase current (I_{ph}), angular speed (ω), permanent magnet flux (Φ), and copper space factor (k_{Cu}). It is assumed that the synchronous inductance is negligible and the power factor is $\cos(\varphi) = 1$.

Figure 3.10 shows that the phase resistance is proportional to the back-EMF squared if other parameters remain the same. Therefore, if a machine with a low terminal voltage and a low power is designed, apart from the conventional design method (Pyrhönen et al., 2008), the phase resistance can be artificially reduced. Otherwise, the voltage drop in the generator phase resistance at a particular current may prevent reaching the required phase voltage. An example of the back-EMF and phase resistance characteristics as a function of generated power and stator slot area is shown in Figure 3.11.

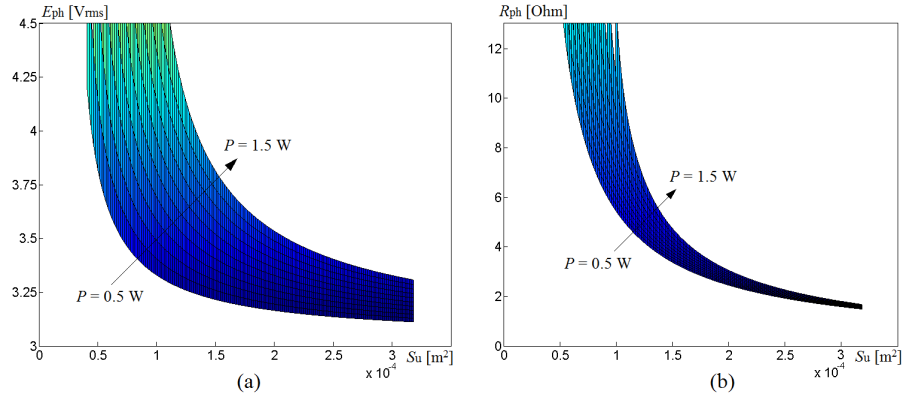

Figure 3.11: a) Back-EMF and b) phase resistance as a function of slot area and generated power. The parameters are similar to the studied machine with a segmented stator: U_{ph} = 3 V, ω = 18.85 s^{-1}, l_{ew} = 108 mm, k_{Cu} = 0.37, Φ = 2.68e-4 Vs. It is assumed that the synchronous inductance is negligible and the power factor is cos(φ) = 1. The machine operates in the generator mode.

Figure 3.11 shows that it is impossible to achieve the generated power P = 1.5 W with a slot area smaller than 1e-4 m^2 because of significant voltage drop in the armature winding, even though the induced current does not cause any thermal issues. Therefore, the slot area should be increased to increase the wire area, and consequently, reduce the phase resistance.

3.3 Challenges in segmented stator PMSMs

The studied segmented stator PMSM has a unique stator winding arrangement, which was developed after the constructional rearrangement of the TCW PMSM with q = 0.4, as shown in Figure 3.12. It can be seen that the number of windings was reduced (in a conventional TCW PMSM there are 24 windings, whereas in the redesigned machine there are 12 windings). However, the electrical frequency and number of phase winding turns remains the same as in the original machine. It should be noted that as a result of the lower peak flux linkage in the rearranged PMSM with the same number of turns, the back-EMF is lower than in the conventional TCW PMSM, as it is shown in Figure 3.5

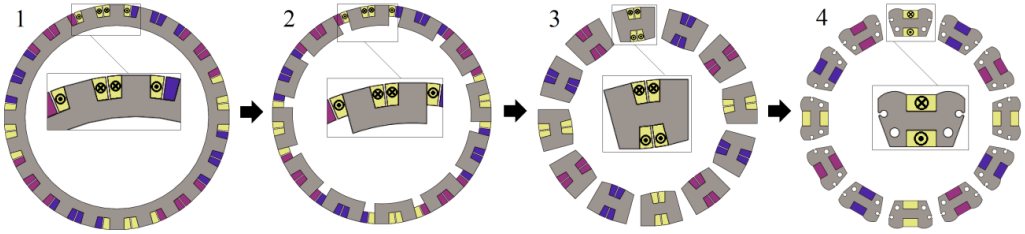

Figure 3.12: Geometry transformation of a TCW PMSM q = 0.4, 24 slots (1) into a modular stator with 12 segments (2). The construction in (3) is analogous to the stator construction in (2) but with rearranged windings. The final geometry in (4) includes the stator segment roundings in the stator structure and an increased slot width of the segment.

The challenges related to a PMSM with a segmented stator arise from its constructional features. First of all, segmentation leads to flux pattern variation in different rotor positions, as it is shown in Figure 3.6. Therefore, some additional rotor losses (Figure 3.8) and cogging torque can be expected. As it was mentioned above, the additional rotor losses can be eliminated if a laminated rotor is implemented. Again, cogging torque and torque ripple can be reduced if for instance some methods mentioned in (Bianchi et al., 2009; Alotto et al., 2011; Aydin et al., 2003) are applied. However, in reality, a significant cogging torque (which includes low harmonic components) can occur in a segmented stator PMSM as a result of mechanical uncertainties, which include a non-symmetrical stator segment position in relation to other segments. Non-symmetrical stator and rotor positions were analysed, and it was shown that even a small asymmetry can lead to a significant cogging torque, as can be seen in Figure 3.13.

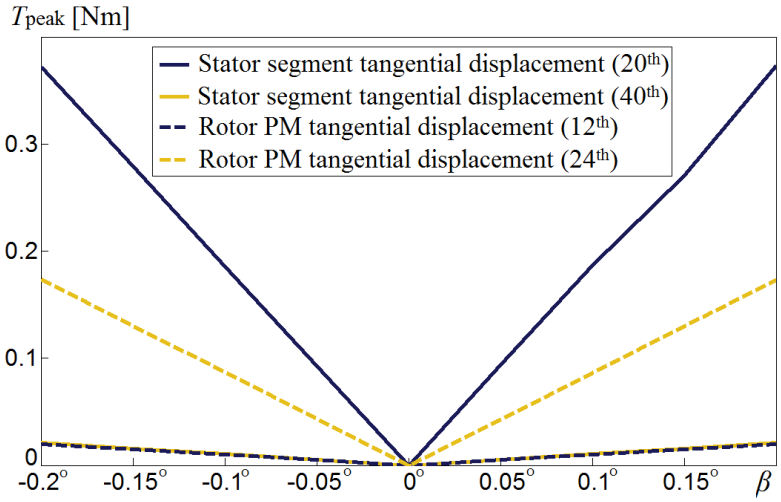

Figure 3.13: Additional cogging torque harmonics as a function of tangential displacement of the stator segment and the rotor permanent magnet. β is the mechanical angle of the displacement in the tangential direction (FEM). The harmonics (20^{th}, 40^{th}, 24^{th} and 24^{th}) are shown for a mechanical period (e.g. the 20^{th} harmonic for a mechanical period is $20^{th}/p = 2^{th}$ for the electrical period).

Figure 3.13 shows that low order harmonics (20^{th} and 40^{th}) of the cogging torque occur in the machine with one stator segment asymmetry. If another stator segment is also displaced, the torque cogging harmonics are added up. Therefore, the importance of precise tooling and assembly is emphasized in the manufacturing.

The actual cogging torque of the designed machine was estimated by the method described in (Zhu, 2009). The photo of the test setup is shown in Figure 3.14.

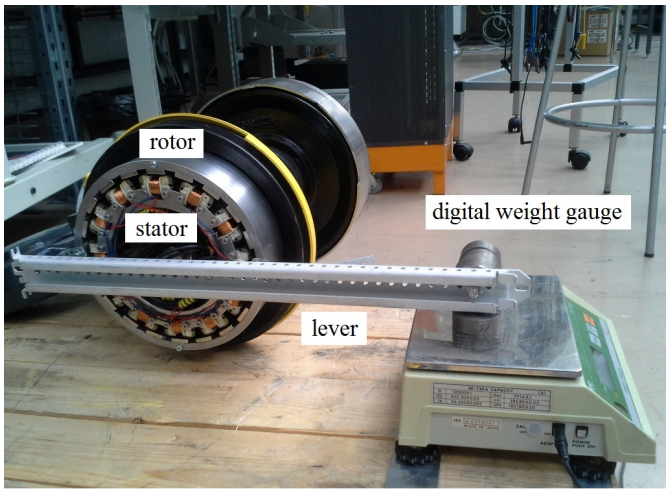

Figure 3.14: The test setup for the estimation of the real cogging torque.

The measured cogging torque and the cogging torque estimated by the FEM are shown in Figure 3.15

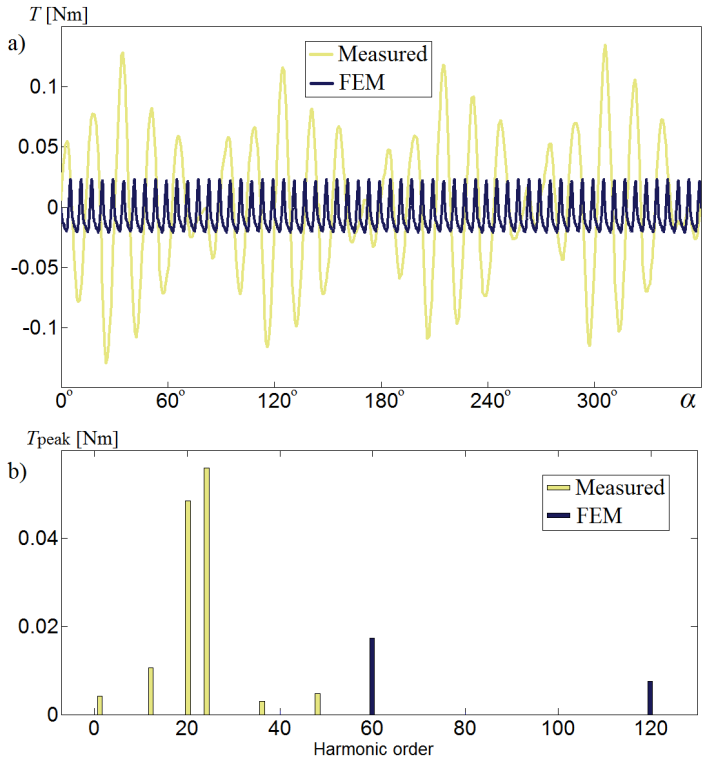

Figure 3.15: a) Waveforms of the cogging torque measured and estimated by the FEM. b) Harmonic spectra of the cogging torque measured and estimated by the FEM. α is the mechanical angle.

Figure 3.15 shows that there are large low-order harmonic components in the cogging torque waveform, which can be explained by some mechanical uncertainties in the assembly. However, according to Figure 3.13, even a small displacement of a segment or a permanent magnet leads to a significant additional cogging torque.

In summary we may state that also in a conventional TCW PMSM, a precise permanent magnet position and the even air gap along the machine length are required to eliminate an additional cogging torque caused by mechanical uncertainties. However, in a segmented PMSM, this task is more challenging, because the stator lamination does not consist of one unit, but several magnetically insulated segments separated from each other. Therefore, they also require a precise assembly routine to prevent some displacement if a low cogging torque is required.

3.4 Suggestions for further research

Figure 3.5 shows that the back-EMF of the proposed PMSM structure is lower than the back-EMF of the analogous conventional TCW PMSM. However, as we can see in Figure 3.4, the inner generator area is not used by any means. Therefore, if an additional rotor with permanent magnets is used in the inner PMSM area, thereby constituting a double rotor structure, it is possible to significantly increase the induced back-EMF by keeping the number of turns the same. Such an arrangement can provide some advantages compared with a conventional single-stator double-rotor construction, as it shown in Figure 3.16.

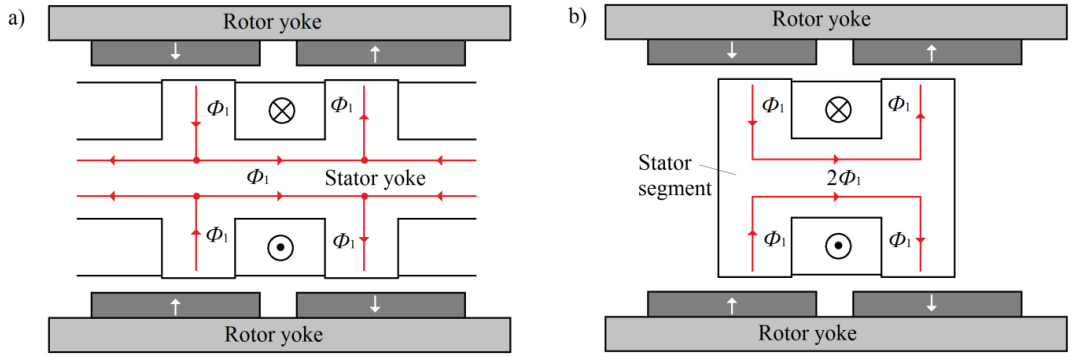

Figure 3.16: Flux paths in the 2D plane for the slotted TORUS machine (a) North-North type magnet arrangement and (b) segmented stator North-North type magnet arrangement.

Figure 3.16 (a) shows that in the conventional stator construction, the permanent magnet flux that penetrates into the stator flows in two directions and covers two coils. However, in the segmented PMSM, Figure 3.16 (b), the flux is concentrated and flows through only one coil. This means that the number of winding turns in the last arrangement can be significantly decreased; in an ideal case, the number of winding turns of the proposed motor is half compared with the original one, which reduces the copper losses and simplifies the construction. Therefore, the stator winding can be used

more efficiently, which leads to a smaller size and lower winding Joule losses. Currently, this PMSM arrangement is studied in the laboratory of Lappeenranta University of Technology.

4 Conclusion

The main objective of the doctoral dissertation was to develop the cost reduction of permanent magnet synchronous machines. The actions aiming at cost reduction are associated with both the simplicity of manufacturing and the use of inexpensive materials.

To this end, the characteristics of a PMSM and features related to its machine topology have to be analysed in detail to gain comprehensive understanding of the topic. Some aspects related to the PMSM performance were considered such as air gap flux density, synchronous inductance, slot geometry, local saturation, rotor topology, additional AC losses, solid rotor losses, and the risk of permanent magnet demagnetization. It was shown that the designed PMSM that applies rotor surface ferrite magnets instead of rare-earth magnets can be used in a typical industrial application with the required power, P = 50 kW, and even higher (at 3000 rpm). At the same time, the designed PMSM can be competitive in terms of efficiency and manufacturing cost with typical asynchronous machines used in industrial applications.

The limiting factors that the designers of similar machines may face are the permanent magnet demagnetization risk, the thermal condition of the stator winding, and an excessive armature reaction caused by a large synchronous inductance. The latter makes the rotor surface ferrite magnet vulnerable to hysteresis losses, which have to be taken into account when using high-power ferrite magnet machines. The ferrites must be protected from an excessive armature reaction by constructional means.

All the above mentioned features are related to the low magnetic energy of ferrite magnets. In the doctoral dissertation, some hints are given to extend these limits such as implementation of embedded permanent magnets (with flux concentration), optimization of the stator slot and tooth geometry, the use of outer rotor topology, and placing the permanent magnet region having a higher demagnetization risk in a hot environment.

Because of the permanent magnet characteristic variation as a function of temperature, the PMSM performance and its partial demagnetization risk should be evaluated with all the possible permanent magnet temperatures. In the case of a hybrid vehicle application, the lowest permanent magnet temperature (e.g. -40° C) can provide the highest air gap flux density by permanent magnets. However, at the same time, it results in the most risky case from the viewpoint of permanent magnet, especially if a short-circuit at the nominal speed is considered. The solution implemented in the cooling design was to dissipate the heat generated in the stator winding and the stator steel partially through the air gap, which leads to an increase in the temperature of the permanent magnet surface close to the air gap, where the influence of the armature reaction on the permanent magnet flux density is at strongest.

In the work, a design optimization algorithm was developed based on an analytical method that takes saturation into account. This method can be successfully applied at the early design stages and in the in-depth analysis of the machine behavior, which also covers local saturation regions. With this algorithm, it was found that asymmetrical local saturation can be observed in the TCW PMSM, caused by the interaction of the armature reaction with the permanent magnet flux. An optimization method was developed to avoid local saturation of this kind in a particular load point.

It was observed that the manufactured 50 kW, 3000 rpm PMSM had a much lower efficiency than what was expected in the design stage. This was partly explained by the additional AC losses in the stator winding, caused by circulating currents. At the time of the writing of the doctoral dissertation, some suggestions about the possible sources of these losses are being studied. For example, permanent magnet hysteresis losses can contribute to the total losses at higher loads. This phenomenon is considered to be a topic of further research, which could reveal the origin of additional losses in a PMSM.

For low-speed and extremely low-power mobile applications (where a high air gap flux density is required to reduce the drop voltage in the winding resistance at the nominal load), another manufacturing simplification was developed, which incorporates the use of a segmented stator with an unique winding structure. With this approach, the winding routine can be simplified, because of the lower winding number and the segment geometry favouring a low-cost automatic winding routine. The opportunity to use a double-rotor structure makes this machine even more advantageous than a conventional double-rotor PMSM in terms of stator winding Joule losses and torque density. Further research can be related to the optimization of the double-rotor structure (e.g. axial flux topology) and its comparison with conventional machines.

It is difficult to evaluate the actual benefits (manufacturing cost reduction) obtained by the proposed techniques because of the continuous variation in material prices in the market (e.g. rare-earth elements and copper). However, the use of rare-earth-free high-performance electrical machines can provide a less risky electrical machine manufacturing business, still keeping the performance characteristics of the produced machines at a competitive level. This can be a good motivation to continue the study of rare-earth-free PMSM design solutions even for weight- and volume- critical applications such as hybrid electric vehicles or wind turbines.

References

Abeywickrama, K.G.N.B., Daszczynski, T., Serdyuk, Y.V., and Gubanski, S.M. (2008), "Determination of Complex Permeability of Silicon Steel for Use in High-Frequency Modeling of Power Transformers," *IEEE Transactions on Magnetics*, vol.44, no.4, pp. 438–444.

Alberti, L., Barcaro, M., and Bianchi, N. (2014), "Design of a Low-Torque-Ripple Fractional-Slot Interior Permanent-Magnet Motor," *IEEE Transactions on Industry Applications*, vol.50, no.3, pp. 1801–1808.

Alberti, L. and Bianchi, N. (2013), "Theory and Design of Fractional-Slot Multilayer Windings," *IEEE Transactions on Industry Applications*, vol.49, no.2, pp. 841–849.

Alexandrova Y., S.R.S..P.J. (2014), "Permanent magnet synchronous generator design solution for large direct-drive wind turbines: Thermal behavior of the LC DD-PMSG," *Applied Thermal Engineering*, pp. 554–563.

Alexandrova, Y., Semken, S., Polikarpova, M., and Pyrhonen, J. (2012), "Defining proper initial geometry of an 8 MW liquid-cooled direct-drive permanent magnet synchronous generator for wind turbine applications based on minimizing mass," *in 2012 XXth International Conference on Electrical Machines (ICEM)*, pp. 1250–1255.

Alotto, P., Barcaro, M., Bianchi, N., and Guarnieri, M. (2011), "Optimization of Interior PM Motors With Machaon Rotor Flux Barriers," *IEEE Transactions on Magnetics*, vol.47, no.5, pp. 958–961.

Aoyama, M. and Noguchi, T. (2014), "Mathematical model of novel wound-field synchronous motor self-excited by space harmonics," *in 2014 International Power Electronics Conference (IPEC-Hiroshima 2014 - ECCE-ASIA)*, pp. 1405–1411.

Aydin, M., Qu, R., and Lipo, T.A. (2003), "Cogging torque minimization technique for multiple-rotor, axial-flux, surface-mounted-PM motors: alternating magnet pole-arcs in facing rotors," *in Industry Applications Conference, 2003. 38th IAS Annual Meeting.*, vol.1, pp. 555–561.

Azar, Z., Zhu, Z.Q., and Ombach, G. (2012), "Influence of Electric Loading and Magnetic Saturation on Cogging Torque, Back-EMF and Torque Ripple of PM Machines," *IEEE Transactions on Magnetics*, vol.48, no.10, pp. 2650–2658.

Bakker Magnetics (2015), *Magnetic materials and components*, [Online], [Accessed 25 March 2015], available at http://www.bakkermagnetics.com/.

Barcaro, M. and Bianchi, N. (2011), "Torque components in integral- and fractional-slot IPM machines," *in 2011 IEEE International Electric Machines & Drives Conference (IEMDC)*, pp. 1340–1345.

Barcaro, M. and Bianchi, N. (2012), "Torque ripple reduction in fractional-slot Interior PM machines optimizing the flux-barrier geometries," *in 2012 XXth International Conference on Electrical Machines (ICEM)*, pp. 1496–1502.

Barcaro, M. and Bianchi, N. (2014), "Interior PM Machines Using Ferrite to Replace Rare-Earth Surface PM Machines," *IEEE Transactions on Industry Applications*, vol.50, no.2, pp. 979–985.

Barcaro, M., Bianchi, N., and Magnussen, F. (2012), "Remarks on Torque Estimation Accuracy in Fractional-Slot Permanent-Magnet Motors," *IEEE Transactions on Industrial Electronics*, vol.59, no.6, pp. 2565–2572.

Baun, M., Krotsch, J., Ulm, J., and Piepenbreier, B. (2013), "Multi-Criteria Comparison of External and Dual-Rotor PMSM Topologies with Non-Overlapping Windings," *in GMM/ETG Symposium Innovative Small Drives and Micro-Motor Systems, 2013.*, pp. 1–6.

Bianchi, N. (2013), "Synchronous reluctance and interior permanent magnet motors," *in 2013 IEEE Workshop on Electrical Machines Design Control and Diagnosis (WEMDCD)*, pp. 75–84.

Bianchi, N. and Bolognani, S. (2002), "Design techniques for reducing the cogging torque in surface-mounted PM motors," *IEEE Transactions on Industry Applications*, vol.38, no.5, pp. 1259–1265.

Bianchi, N., Bolognani, S., Bon, D., and Dai Pre, M. (2009), "Rotor Flux-Barrier Design for Torque Ripple Reduction in Synchronous Reluctance and PM-Assisted Synchronous Reluctance Motors," *Industry Applications, IEEE Transaction on*, vol.45, no.3, pp. 921–928.

Bianchi, N., Bolognani, S., and Chalmers, B.J. (2000), "Salient-rotor PM synchronous motors for an extended flux-weakening operation range," *IEEE Transactions on Industry Applications*, vol.36, no.4, pp. 1118–1125.

Bianchi, N., Bolognani, S., and Corda, J. (2002), "Tubular linear motors: a comparison of brushless PM and SR motors," *in International Conference on (Conf. Publ. No. 487) Power Electronics, Machines and Drives.*, pp. 626–631.

Boldea, I., Tutelea, L.N., Parsa, L., and Dorrell, D. (2014), "Automotive Electric Propulsion Systems With Reduced or No Permanent Magnets: An Overview," *IEEE Transactions on Industrial Electronics*, vol.61, no.10, pp. 5696–5711.

Brancato, E.L. (1992), "Estimation of lifetime expectancies of motors," *IEEE Electrical Insulation Magazine*, vol.8, no.3, pp. 5–13.

Cai, H., Guan, B., and Xu, L. (2014), "Low-Cost Ferrite PM-Assisted Synchronous Reluctance Machine for Electric Vehicles," *IEEE Transactions on Industrial Electronics*, vol.61, no.10, pp. 5741–5748.

Chevailler, S., Feng, L., and Binder, A. (2007), "Short-circuit faults in distributed and concentrated windings of PM synchronous motors," *in 2007 European Conference on Power Electronics and Applications*, pp. 1–10.

Chiba, K., Takemoto, M., Ogasawara, S., and Yim, W.G. (2013), "Ferrite-magnet spoke-type IPMSM with W-shaped magnet placement," *in IECON 2013 - 39th Annual Conference of the IEEE Industrial Electronics Society*, pp. 2869–2874.

Chino, S., et al. (2011), "Fundamental characteristics of a ferrite permanent magnet axial gap motor with segmented rotor structure for the hybrid electric vehicle," *in 2011 IEEE Energy Conversion Congress and Exposition (ECCE)*, pp. 2805–2811.

Cirani, M., Eriksson, S., and Thunberg, J. (2014), "Innovative Design for Flux Leakage Reduction in IPM Machines," *IEEE Transactions on Industry Applications*, vol.50, no.3, pp. 1847–1853.

Cossale, M., et al. (2014), "Practical Investigations on Cobalt-Iron Laminations for Electrical Machines," *in 2014 XXIth International Conference on Electrical Machines (ICEM)*.

Dajaku, G. and Gerling, D. (2012), "A novel 12-teeth/10-poles PM machine with flux barriers in stator yoke," *in 2012 XXth International Conference onElectrical Machines (ICEM)*, pp. 36–40.

Dakin, T.W. (1948), "Electrical Insulation Deterioration Treated as a Chemical Rate Phenomenon," *Transactions of the American Institute of Electrical Engineers*, vol.67, no.1, pp. 113–122.

de Almeida, A., Ferreira, F.J.T.E., and Quintino Duarte, A. (2014), "Technical and Economical Considerations on Super High-Efficiency Three-Phase Motors," *IEEE Transactions on Industry Applications*, vol.50, no.2, pp. 1274–1285.

Dorrell, D.G. (2014a), "A Review of the Methods for Improving the Efficiency of Drive Motors to Meet IE4 Efficiency Standards," *Journal of Power Electronics*, pp. 842-851. ISBN 978-1-4338-0559-2.

Dorrell, D.G. (2014b), "The challenges of meeting IE4 efficiency standards for induction and other machines," *in 2014 IEEE International Conference on Industrial Technology (ICIT)*, pp. 213–218.

EL-Refaie, A., et al. (2014), "Advanced High-Power-Density Interior Permanent Magnet Motor for Traction Applications," *IEEE Transactions on Industry Applications*, vol.50, no.5, pp. 3235–3248.

EL-Refaie, A.M. and Jahns, T.M. (2005), "Optimal flux weakening in surface PM machines using fractional-slot concentrated windings," *IEEE Transactions on Industry Applications*, vol.41, no.3, pp. 790–800.

EL-Refaie, A.M., Zhu, Z.Q., Jahns, T.M., and Howe, D. (2008), "Winding Inductances of Fractional Slot Surface-Mounted Permanent Magnet Brushless Machines," *in IEEE Industry Applications Society Annual Meeting, 2008. IAS '08.*, pp. 1–8.

Gasparin, L., Cernigoj, A., Markic, S., and Fiser, R. (2009), "Additional Cogging Torque Components in Permanent-Magnet Motors Due to Manufacturing Imperfections," *IEEE Transactions on Magnetics*, vol.45, no.3, pp. 1210–1213.

Güemes, J.A., Iraolagoitia, A.A., Del Hoyo, J.J., and Fernández, P. (2011), "Torque Analysis in Permanent-Magnet Synchronous Motors: A Comparative Study," *IEEE Transactions on Energy Conversion*, vol.26, no.1, pp. 55–63.

Heins, G., Ionel, D., and Thiele, M. (2013), "Winding factors and magnetic fields in permanent magnet brushless machines with concentrated windings and modular stator cores," *in 2013 IEEE Energy Conversion Congress and Exposition (ECCE)*, pp. 5048–5055.

Hsieh, M.-F. and Hsu, Y.-C. (2012), "A Generalized Magnetic Circuit Modeling Approach for Design of Surface Permanent-Magnet Machines," *IEEE Transactions on Industrial Electronics*, vol.59, no.2, pp. 779–792.

Ilhan, E., et al. (2012), "Sensitivity analysis for phase inductances in Flux-Switching PM machines," *2012 XXth International Conference on Electrical Machines (ICEM)*, pp. 763–768.

Islam, M.S., Islam, R., and Sebastian, T. (2011), "Experimental Verification of Design Techniques of Permanent-Magnet Synchronous Motors for Low-Torque-Ripple Applications," *IEEE Transactions on Industry Applications*, vol.47, no.1, pp. 88–95.

Iwasaki, S., et al. (2009), "Influence of PWM on the Proximity Loss in Permanent-Magnet Brushless AC Machines," *IEEE Transactions on Industry Applications*, vol.45, no.4, pp. 1359–1367.

Jack, A.G., et al. (2000), "Permanent-magnet machines with powdered iron cores and prepressed windings," *IEEE Transactions on Industry Applications*, vol.36, no.4, pp. 1077–1084.

Kim, S.-I., et al. (2014), "Investigation and Experimental Verification of a Novel Spoke-Type Ferrite-Magnet Motor for Electric-Vehicle Traction Drive Applications," *IEEE Transactions on Industrial Electronics*, vol.61, no.10, pp. 5763–5770.

Kiyota, K., Kakishima, T., and Chiba, A. (2014), "Comparison of Test Result and Design Stage Prediction of Switched Reluctance Motor Competitive With 60-kW Rare-Earth PM Motor," *IEEE Transactions on Industrial Electronics*, vol.61, no.10, pp. 5712–5721.

Lindh, P., et al. (2014), "Design of a Traction Motor With Tooth-Coil Windings and Embedded Magnets," *IEEE Transactions on Industrial Electronics*, vol.61, no.8, pp. 4306–4314.

Lindh, P.M., et al. (2013), "Electrical and mechanical design of a PM traction motor with tooth coils," *in 2013 15th European Conference on Power Electronics and Applications (EPE)*, pp. 1–8.

Li, G.J., et al. (2014), "Influence of Flux Gaps on Electromagnetic Performance of Novel Modular PM Machines," *IEEE Transactions on Energy Conversion*, vol.29, no.3, pp. 716–726.

Maloberti, O., et al. (2014), "3-D–2-D Dynamic Magnetic Modeling of an Axial Flux Permanent Magnet Motor With Soft Magnetic Composites for Hybrid Electric Vehicles," *IEEE Transactions on Magnetics*, vol.50, no.6, pp. 1–11.

Mellor, P.H., Wrobel, R., and McNeill, N. (2006), "Investigation of Proximity Losses in a High Speed Brushless Permanent Magnet Motor," *in Industry Applications Conference, 2006. 41st IAS Annual Meeting.*, vol.3, pp. 1514–1518.

Montsinger, V.M. (1930), "Abridgment of loading transformers by temperature," *Journal of the A.I.E.E.*, vol.49, no.4, pp. 293–297.

More, D.S., Kalluru, H., and Fernandes, B.G. (2008), "Comparative analyis of Flux Reversal machine and Fractional slot concentrated winding PMSM," *in 34th Annual Conference of IEEE Industrial Electronics. IECON 2008.*, pp. 1131–1136.

Morimoto, S., Asano, Y., Kosaka, T., and Enomoto, Y. (2014a), "Recent technical trends in PMSM," *in 2014 International Power Electronics Conference (IPEC-Hiroshima 2014 - ECCE-ASIA)*, pp. 1997–2003.

Morimoto, S., Ooi, S., Inoue, Y., and Sanada, M. (2014b), "Experimental Evaluation of a Rare-Earth-Free PMASynRM With Ferrite Magnets for Automotive Applications," *IEEE Transactions on Industrial Electronics*, vol.61, no.10, pp. 5749–5756.

Neorem Magnets (2015), *NdFeB Physical Properties*, [Online], [Accessed 25 March, 2015], avaliable at http://www.neorem.fi.

Nerg, J., et al. (2014), "Direct-Driven Interior Magnet Permanent-Magnet Synchronous Motors for a Full Electric Sports Car," *IEEE Transactions on Industrial Electronics*, vol.61, no.8, pp. 4286–4294.

Obata, M., Morimoto, S., Sanada, M., and Inoue, Y. (2014), "Performance of PMASynRM With Ferrite Magnets for EV/HEV Applications Considering Productivity," *IEEE Transactions on Industry Applications*, vol.50, no.4, pp. 2427–2435.

Okada, Y., Dohmeki, H., and Konushi, S. (2010), "Proposal of 3D-stator structure using soft magnetic composite for PM motor," *in 2010 XIX International Conference on Electrical Machines (ICEM)*, pp. 1–6.

Parasiliti, F., et al. (2004). "Three-phase induction motor efficiency improvements with die-cast copper rotor cage and premium stee,". *In Proceedings of SPEEDAM'04 Symposium*,.

Parviainen, A., Niemela, M., and Pyrhonen, J. (2004), "Modeling of axial flux permanent-magnet machines," *IEEE Transactions on Industry Applications*, vol.40, no.5, pp. 1333–1340.

Petrov, I., Polikarpova, M., and Pyrhönen, J. (2013), "Rotor surface ferrite magnet synchronous machine for generator use in a hybrid application — Electro-magnetic and thermal analysis," *in 39th Annual Conference of the IEEE, Industrial Electronics Society, IECON 2013*, pp. 3090–3095.

Petrov, I., Ponomarev, P., Alexandrova, Y., and Pyrhönen, J. (2014a), "Unequal Teeth Widths for Torque Ripple Reduction in Permanent Magnet Synchronous Machines With Fractional-Slot Non-Overlapping Windings," *IEEE Transactions on Magnetics*, pp. 1–9.

Petrov, I., Ponomarev, P., and Pyrhönen, J. (2014b), "Torque Ripple Reduction in 12-slot 10-pole Fractional Slot Permanent Magnet Synchronous Motors with Non-Overlapping Windings by Implementation of Unequal Stator Teeth Widths," *in 2014 International Conference on Electrical Machines (ICEM)*, pp. 1455–1460.

Petrov, I., Ponomarev, P., Shirinskii, S., and Pyrhönen, J. (2014c), "Inductance evaluation of fractional slot permanent magnet synchronous motors with non-overlappingwinding by analytical approaches," *in 2014 16th European Conference on Power Electronics and Applications (EPE'14-ECCE Europe)*, pp. 1–10.

Petrov, I. and Pyrhönen, J. (2013), "Performance of Low-Cost Permanent Magnet Material in PM Synchronous Machines," *IEEE Transactions on Industrial Electronics*, vol.60, no.6, pp. 2131–2138.

Ponomarev, P., et al. (2014a), "Inductance Calculation of Tooth-Coil Permanent-Magnet Synchronous Machines," *IEEE Transactions on Industrial Electronics*, vol.61, no.11, pp. 5966–5973.

Ponomarev, P., Lindh, P., and Pyrhönen, J. (2013), "Effect of Slot-and-Pole Combination on the Leakage Inductance and the Performance of Tooth-Coil Permanent-Magnet Synchronous Machines," *IEEE Transactions on Industrial Electronics*, vol.60, no.10, pp. 4310–4317.

Ponomarev, P., Petrov, I., and Pyrhönen, J. (2014b), "Influence of Travelling Current Linkage Harmonics on Inductance Variation, Torque Ripple and Sensorless Capability of Tooth-Coil Permanent-Magnet Synchronous Machines," *IEEE Transactions on Magnetics*, vol.50, no.1, pp. 1–8.

Ponomarev, P., Petrov, I., and Pyrhönen, J. (2014c), "Torque Ripple Reduction in Double-Layer 18/16 TC-PMSMs by Adjusting Teeth Widths to Minimize Local Saturation," *2014 International Conference on Electrical Machines (ICEM)*, pp. 1461–1467.

Popescu, M. and Dorrell, D.G. (2013), "Proximity Losses in the Windings of High Speed Brushless Permanent Magnet AC Motors With Single Tooth Windings and Parallel Paths," *IEEE Transactions on Magnetics*, vol.49, no.7, pp. 3913–3916.

Prieto, B., Martinez-Iturralde, M., Fontan, L., and Elosegui, I. (2014), "Analytical calculation of the slot leakage inductance in fractional-slot concentrated-winding machines," *IEEE Transactions on Industrial Electronics*.

Puranen, J. (2006), "Induction motor versus permanent magnet synchronous motor in motion control applications: a comparative study,". Dissertation (Acta Universitatis Lappeenrantaensis), Lappeenranta University of Technology.

Pyrhönen, J., Jokinen, T., and Hrabovcová, V. (2008). *Design of Rotating Electrical Machines*. New York: John Wiley & Sons, Ltd.

Pyrhönen, J., Jokinen, T., and Hrabovcová, V. (2014). *Design of Rotating Electrical Machines, 2nd Edition*. New York: John Wiley & Sons, Ltd.

Pyrhönen, J., et al. (2015), "Hysteresis Losses in Sintered NdFeB Permanent Magnets in Rotating Electrical Machines," *IEEE Transactions on Industrial Electronics*, vol.62, no.2, pp. pp.857–865.

Qian, H., Guo, H., Wu, Z., and Ding, X. (2014), "Analytical Solution for Cogging Torque in Surface-Mounted Permanent-Magnet Motors With Magnet Imperfections and Rotor Eccentricity," *IEEE Transactions on Magnetics*, vol.50, no.8, pp. 1–15.

Reddy, P.B. and Jahns, T.M. (2010), "Analysis of bundle losses in high speed machines," *in 2010 International Power Electronics Conference (IPEC)*, pp. 2181–2188.

Reddy, P.B., Jahns, T.M., and Bohn, T.P. (2009), "Transposition effects on bundle proximity losses in high-speed PM machines," *in IEEE Energy Conversion Congress and Exposition. ECCE 2009.*, pp. 1919–1926.

Reddy, P.B., Jahns, T.M., and EL-Refaie, A.M. (2008), "Impact of Winding Layer Number and Slot/Pole Combination on AC Armature Losses of Synchronous Surface PM Machines Designed for Wide Constant-Power Speed Range Operation," *in IEEE Industry Applications Society Annual Meeting, 2008. IAS '08*, pp. 1–8.

Ruoho, S., Santa-Nokki, T., Kolehmainen, J., and Arkkio, A. (2009), "Modeling Magnet Length In 2-D Finite-Element Analysis of Electric Machines," *IEEE Transactions on Magnetics*, vol.45, no.8, pp. 3114–3120.

Ruuskanen, V., et al. (2014a), "Design and drive-cycle based analysis of direct-driven permanent magnet synchronous machine for a small urban use electric vehicle," *in 2014 16th European Conference on Power Electronics and Applications (EPE'14-ECCE Europe)*, pp. 1–10.

Ruuskanen, V., et al. (2014b), "Drive Cycle Analysis of a Permanent Magnet Traction Motor based on Magnetostatic Finite Element Analysis," *IEEE Transactions on Vehicular Technology*.

Salminen, P., Niemela, M., Pyrhonen, J., and Mantere, J. (2005), "High-torque low-torque-ripple fractional-slot PM-motors," *in 2005 IEEE International Conference on Electric Machines and Drives*, pp. 144–148.

Sampathirao, S. and Baylon, F. (2014), "A Low-cost Semi-Modular Dual-Stack PM BLDC Motor for a PV based Bore-well Submersible Pump," *2014 XXIth International Conference on Electrical Machines (ICEM)*, pp. 24–30.

Sarlioglu, B., Zhao, Y., and Lipo, T.A. (1994), "A novel doubly salient single phase permanent magnet generator," *in Industry Applications Society Annual Meeting, 1994., Conference Record of the 1994 IEEE*, vol.1, pp. 9–15.

Sergeant, P. and Van den Bossche, A.P.M. (2014), "Influence of the Amount of Permanent-Magnet Material in Fractional-Slot Permanent-Magnet Synchronous Machines," *IEEE Transactions on Industrial Electronics*, vol.61, no.9, pp. 4979–4989.

Shin, D.-j. and Kwon, B.-I. (2009), "Multi-objective optimal design for in-wheel permanent magnet synchronous motor," *in International Conference on Electrical Machines and Systems, 2009. ICEMS 2009.*, pp. 1–5.

Silventoinen, P., Salo, J., Tolsa, K., and Pyrhonen, J. (1999), "Dynamic tests with a switched reluctance motor drive," *IEEE Aerospace and Electronic Systems Magazine*, vol.14, no.1, pp. 25–28.

Sizov, G.Y., Ionel, D.M., and Demerdash, N.A.O. (2010), "Modeling and design optimization of PM AC machines using computationally efficient - finite element analysis," *in 2010 IEEE Energy Conversion Congress and Exposition (ECCE)*, pp. 578–585.

Sopanen, J., Ruuskanen, V., Nerg, J., and Pyrhonen, J. (2011), "Dynamic Torque Analysis of a Wind Turbine Drive Train Including a Direct-Driven Permanent-Magnet Generator," *IEEE Transactions on Industrial Electronics*, vol.58, no.9, pp. 3859–3867.

Takeno, M., et al. (2011), "Power and efficiency measurements and design improvement of a 50kW switched reluctance motor for Hybrid Electric Vehicles," *in 2011 IEEE Energy Conversion Congress and Exposition (ECCE)*, pp. 1495–1501.

Tangudu, J.K., Jahns, T.M., El-Refaie, A.M., and Zhu, Z.Q. (2009), "Segregation of torque components in fractional-slot concentrated-winding interior PM machines using frozen permeability," *in Energy Conversion Congress and Exposition, 2009*, pp. 3814–3821.

Tapia, J.A., et al. (2013), "Optimal Design of Large Permanent Magnet Synchronous Generators," *IEEE Transactions on Magnetics*, vol.49, no.1, pp. 642–650.

Tokuda, T., Sanada, M., and Morimoto, S. (2009), "Influence of rotor structure on performance of permanent magnet assisted synchronous reluctance motor," *in International Conference on Electrical Machines and Systems, 2009. ICEMS 2009*, pp. 1–6.

Uzhegov, N., Nerg, J., and Pyrhönen, J. (2014), "Design of 6-slot 2-pole high-speed permanent magnet synchronous machines with Tooth-Coil windings," *in 2014 International Conference on Electrical Machines (ICEM)*, pp. 2537–2542.

van der Geest, M., Polinder, H., Ferreira, J.A., and Zeilstra, D. (2013), "Stator winding proximity loss reduction techniques in high speed electrical machines," *in 2013 IEEE International Electric Machines & Drives Conference (IEMDC)*, pp. 340–346.

Vartanian, R., Toliyat, H.A., Akin, B., and Poley, R. (2012), "Power factor improvement of synchronous reluctance motors (SynRM) using permanent magnets

for drive size reduction," *in 2012 Twenty-Seventh Annual IEEE Applied Power Electronics Conference and Exposition (APEC)*, pp. 628–633.

Vrenken, R.H.S., et al. (2013), "Switched reluctance motor drive for full electric vehicles - Part I: Analysis," *in 2013 8th International Conference and Exhibition on Ecological Vehicles and Renewable Energies (EVER)*, pp. 1–7.

Wang, K., Zhu, Z.Q., and Ombach, G. (2014a), "Torque Enhancement of Surface-Mounted Permanent Magnet Machine Using Third-Order Harmonic," *IEEE Transactions on Magnetics*, vol.50, no.3, pp. 104–113.

Wang, K., Zhu, Z.Q., Ombach, G., and Chlebosz, W. (2014b), "Average Torque Improvement of Interior Permanent-Magnet Machine Using Third Harmonic in Rotor Shape," *IEEE Transactions on Industrial Electronics*, vol.61, no.9, pp. 5047–5057.

Zheng, P., et al. (2011), "Torque ripple reduction in an interior permanent-magnet synchronous motor for servo applications," *in 2011 International Conference on Electrical Machines and Systems (ICEMS)*, pp. 1–5.

Zhu, Z.Q. (2009), "A simple method for measuring cogging torque in permanent magnet machines," *in IEEE Power & Energy Society General Meeting, 2009. PES '09*, pp. 1–4.

Zhu, Z.Q. (2011), "Switched flux permanent magnet machines — Innovation continues," *in 2011 International Conference on Electrical Machines and Systems (ICEMS)*, pp. 1–10.

Zhu, Z.Q., Azar, Z., and Ombach, G. (2012), "Influence of Additional Air Gaps Between Stator Segments on Cogging Torque of Permanent-Magnet Machines Having Modular Stators," *IEEE Transactions on Magnetics*, vol.48, no.6, pp. 2049–2055.

Zhu, Z.Q., Chen, J.T., Wu, L.J., and Howe, D. (2008), "Influence of Stator Asymmetry on Cogging Torque of Permanent Magnet Brushless Machines," *IEEE Transactions on Magnetics*, vol.44, no.11, pp. 3851–3854.

Zhu, Z.Q. and Liu, X. (2014), "Novel stator electrically field excited synchronous machines without rare-earth magnet," *in 2014 Ninth International Conference on Ecological Vehicles and Renewable Energies (EVER)*, pp. 1–13.

Zhu, Z.Q., et al. (2005), "Analysis of electromagnetic performance of flux-switching permanent-magnet Machines by nonlinear adaptive lumped parameter magnetic circuit model," *IEEE Transactions on Magnetics*, vol.41, no.11, pp. 4277–4287.

Zhu, Z.Q., Wu, L.J., and Mohd Jamil, M.L. (2014), "Influence of Pole and Slot Number Combinations on Cogging Torque in Permanent-Magnet Machines With Static and Rotating Eccentricities," *IEEE Transactions on Industry Applications*, vol.50, no.5, pp. 3265–3277.

Publication I

Petrov, I., Pyrhönen, J., "Performance of Low-Cost Permanent Magnet Material in PM Synchronous Machines," *IEEE Transactions on Industrial Electronics*, vol.60, no.6, pp.2131−2138, June 2013

Performance of Low-Cost Permanent Magnet Material in PM Synchronous Machines

Ilya Petrov and Juha Pyrhönen, *Member, IEEE*

***Abstract*—Permanent magnet synchronous machines (PMSM) are considered a viable option in various types of applications. However, particularly in consumer and low-power industrial applications, the price may be a factor that limits the use of PMSMs. In addition to a different technology, the main reason for the high price of PMSMs is the use of expensive neodymium or samarium-cobalt magnets. Their use is necessary only if a high motor torque T to linear current density A ratio (T/A) is required. Ferrite permanent magnets are low cost, abundant, and have negligible eddy current losses in low-frequency applications such as motor drives. They have a much lower energy product $(BH_{\max})$ than the most modern magnets. Because of the high prices of rare earth magnets, many parties are seeking for opportunities to use ferrites instead. In the case of rotor surface ferrite magnets, the air gap flux density remains low. The air gap torque producing tangential Maxwell stress is proportional to the product of the air gap flux density B_δ[Vs/m^2] and the linear current density A [A/m]. If the flux density is low and A cannot be increased, the rotor has to be made larger than in machines having a high air gap flux density. In the case of multiple pole machines, the outer rotor approach, with its low rotor yoke height, offers an interesting alternative. The air gap diameter of these machines can be made larger than in conventional inner rotor type motors without increasing the machine outer dimensions. In this paper, an outer rotor PMSM with ferrite magnets is analyzed and tested. The machine characteristics in a fan drive are compared with an induction machine of the same power.**

***Index Terms*—Fans, ferrite magnets, permanent magnet machines.**

I. Introduction

In DEVELOPED countries, the majority of generated electrical energy is consumed by electric motors. There is a large variety of electric drives available. Their power range varies from fractional kilowatts to several megawatts. Over the latest few decades, one of the main targets in the development of electrical machines has been to produce variable-speed motor drives with easy adaptability to different operating conditions. In the recent years the most essential design target has been to reach high drive efficiencies [1]. This explains the rapid development of permanent magnet synchronous machines (PMSMs) and their applications. Nevertheless, it is seen that PMSMs still cannot compete with the economics of induction motors (IM) in most of the industrial applications. Typically, permanent magnet machines are used in the low or medium power range or in special applications such as wind power generators, where the benefits of permanent magnet machines are greatest. The main reason is that the construction of modern PMSM contains expensive rare earth magnets. Therefore, several projects have been started to develop rare-earth-free PMSMs which should be technically and economically competitive [2]–[4].

There are many studies that describe and compare different configurations of tooth-coil-winding (TCW) and traditional rotating field windings in PMSMs [5]–[9].

The aim of this paper is to analyze a TCW synchronous PM machine drive and to determine its competitiveness with conventional industrial motor drives when, instead of rare earth magnets, much weaker and cheaper ferrite magnets are used in the design. A motor with ferrite magnets will have about 30–50% of the power density of rare earth motors [10]. However, by using the outer rotor construction, it is possible to increase the electromagnetic torque and to improve the overall performance of the motor. In the case of semiclosed slots and tooth coil windings, an outer rotor machine is significantly easier to wind than an inner rotor counterpart while the conductors can be inserted from outside to the slots of the armature [11]. The outer rotor configuration also solves one inherent problem of PMSMs with surface magnets—the risk of the ejection of magnets from the rotor at high speeds.

Section II studies the general properties of PMSMs. Section III shows the possible advantages and drawbacks associated with an outer rotor. Section IV compares the external rotor PMSM drive with a commercial internal rotor IM drive and shows the possible application fields, where the advantages of the studied motor drive type can be competitive in comparison with a traditional frequency converter IM drive.

II. General Properties of Conventional PMSMs

Fast dynamic response requirements and the demand for high efficiency have made PMSM drives popular. Research effort has been put into the development of appropriate permanent magnet machine constructions and their control for different application requirements [12]–[18].

In the literature, permanent magnet machines are usually divided into brushless DC motors (BLDC) and PMSMs. The main differences between them are the control and the back electromotive force (EMF) waveform. BLDC motors should have a trapezoidal back EMF and rectangular phase currents in the steady state. This allows using the simplest possible control technique and a position feedback that monitors the rotor position only six times per revolution. An ideal PMSM

Manuscript received November 29, 2011; revised February 7, 2012; accepted March 6, 2012. Date of publication March 22, 2012; date of current version February 6, 2013.

The authors are with the Department of Electrical Engineering, Lappeenranta University of Technology, 53850 Lappeenranta, Finland (e-mail: ilya.petrov@lut.fi; juha.pyrhonen@lut.fi).

Digital Object Identifier 10.1109/TIE.2012.2191757

TABLE I
COMPARISON OF THE CHARACTERISTICS OF PRESENT-DAY HARD MAGNETIC MATERIALS [19], [20]

Characteristic	NdFeB	SmCo	Ferrites
Remanence, B_r [T]	1.44	1.12	0.41
Coercivity, H_c [kA/m]	1115	730	240
Energy density, $(BH)_{max}$ [kJ/m^3]	400	240	32
Max cont. Temperature, T_{max} [C°]	80	300	250
Resistivity, Ω [(ohm·m)×10^{-6}]	1.1-1.7	0.65-0.9	10^9
Relative permeability, μ	1.04-1.1	1.04-1.12	1.1-1.3

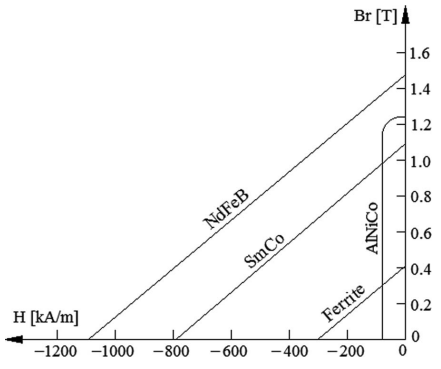

Fig. 1. Second quadrant B–H characteristics of PMs [16].

has a sinusoidal back EMF and consequently sinusoidal phase currents in the steady state.

The characteristics of the PMSMs strongly depend on the rotor constructions. The types of PMSM rotor constructions can be divided into two main branches; rotors with surface magnets and rotors with buried (embedded) magnets.

The location of the permanent magnets can be chosen according to the requirements of the application. Usually, in applications with a fast dynamic response and a high overload-torque requirement, surface magnets are a good choice. In other applications where a field weakening mode should be obtained, buried magnets may have advantages over rotor surface magnets [16].

III. CHARACTERISTICS THAT CAN BE OBTAINED BY AN OUTER ROTOR IN THE PMSM

The properties of a PMSM are greatly influenced by the permanent magnet type and its characteristics. Table I shows the characteristics of the latest neodymium (NdFeB), samarium-cobalt (SmCo), and ferrite magnets.

Table I shows that NdFeB magnets have the lowest allowed operating temperature.

The demagnetization BH curves of different permanent magnets in the room temperature are shown in Fig. 1.

Normally, the operating points of permanent magnets in motors are found in the second quadrant of the BH curves. Fig. 1 and Table I indicate that the remanent flux density of ferrite magnets are about 30–40% of the flux densities in rare

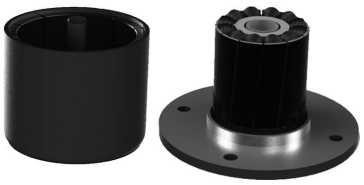

Fig. 2. Rotor and stator of the PMSM studied. The stator with semiclosed slots is skewed to avoid cogging. The stator winding is a double-layer tooth coil winding containing two coil sides in each slot.

earth magnets. However, the prices of ferrite magnets are only 5–10% of the prices of rare earth magnets [11], [21]. Another essential feature of ferrites is their high electrical resistivity. It can be particularly useful in electrical machines, where the influence of harmonics can degrade the thermal condition of the rotor, for instance, in fractional slot machines or high-speed motor drives, where the influences of harmonics are greatest. This provides an opportunity to consider machines with ferrite magnets in the aforementioned application fields.

The outer rotor TCW synchronous machine construction with rotor surface ferrite magnets studied here is shown in Fig. 2.

In an outer rotor machine, it is natural to use rotor surface magnets, which guarantees the largest possible air gap diameter for the machine. Embedding the magnets in an outer rotor should diminish the air gap diameter [11].

The winding type of the studied machine is a three-phase concentrated tooth winding with the number of slots per pole and phase $q \leq 0.5$. Each coil is wound around one tooth, and the end windings are shortest possible. This provides the capability to reduce the conductive material use compared with integer slot windings and decrease copper losses, which are the dominant losses in small- and medium-power machines at low speeds [7]. The insulation and manufacturing systems are also easier to implement in the fractional slot windings as the end windings are not overlapping each other [5]. In addition, tooth coil PM machines have, with an appropriate design, low cogging and ripple torques and an ability to achieve a significantly higher copper slot fill factor compared with conventional stator structures, which also have an impact on the machine power density [8]. In this paper, two possible approaches to increase the power to volume ratio of the machines with relatively weak ferrite magnets are introduced: an outer rotor and a tooth coil windings.

As it can be seen in Fig. 2, the studied motor has 12 slots, three-phase stator windings, and five rotor pole pairs, which means that $q = 0.4$. In the range of fractional slot PM machines, it seems that the $q = 0.4$ construction is one of the best choices because of its low cogging and ripple torques, a high operating harmonic winding factor, and high pull-out torque [5], [22]. A double-layer concentrated winding is used, as it has a shorter axial length and thus better potential to be more compact than the single-layer winding. It should be noted that such a machine operates at the (-)fifth stator harmonic, not the fundamental component of the armature created flux density. The (-)fifth harmonic of the machine is dominating. The first

harmonic could also be regarded as a subharmonic of the order $-1/5$ [6].

The essential drawbacks of tooth coil wound motors are the significant amplitudes of harmonics, which can cause extra heating and eddy current losses in the rotor. This is one of the main challenges of fractional-slot concentrated winding configurations, owing to various sub- and super-space-harmonic components, which are not in synchronism with the rotor [8]. The slot harmonics have the biggest impact on the current linkage harmonic spectrum in TCW synchronous PM machines [23]. To reduce the losses, the rotor can be made of electrical sheet steel. However, in the case of rotor surface ferrites, the thickness of the magnets must be selected high to get an air gap flux density close to the low remanent flux density. Therefore, the armature reaction harmonics are heavily suppressed before entering the rotor yoke, which can be made of solid material in this case; however, it is difficult to arrange bulky permanent magnets in such a way that they do not interact with the stator harmonics. At high speeds, rotor surface NdFeB magnets, experiencing stator-current- and permeance-variation-generated harmonic fields, must be made of small pieces to avoid excessive eddy current losses, which are the biggest losses in the rotor generated from current linkage harmonic spectrum [23]. Because of their high resistivity, ferrite magnets do not have such a restriction and can be used as bulky magnet blocks on the rotor surface. As it can be seen in Table I, the resistivity of ferrite magnets is the highest compared with other PM materials (about 10^9 times the resistivity of NdFeB and SmCo). This means that in ferrite magnet machines, eddy currents should not have a significant influence on the motor performance.

The magnetic pole arc width has a significant influence on the TCW synchronous PM machine cogging torque when no skewing is used [24]. In this case, the machine is, however, skewed, and the pole arc has been chosen on the base of getting the highest possible flux linkage with the weak magnets.

One of the strongest present-day ferrite magnets found in the European Standard IEC 60404-8-1 is HF 32/22, which can be used on the rotor surface. The characteristics of this magnet type are introduced in Table I. It should be noted that ferrite magnets are chemical compounds consisting of ceramic materials. Thus, they are relatively hard and brittle. This means that they cannot be used in applications with essential mechanical stresses.

An expression for the main dimensions of the machine can be derived by the definition of the torque through the tangential Maxwell stress including also the Esson's law utilizing the machine constant C_{mec} [25]

$$T = \sigma_{\mathrm{Ftan}} r_\delta S_{\mathrm{r}} = 2\sigma_{\mathrm{Ftan}} \pi r_\delta^2 l' = \frac{2}{\pi} C_{\mathrm{mec}} r_\delta^2 l \qquad (1)$$

where r_δ is the airgap radius of the machine, S_{r} is the rotor surface area, l' is effective core length, and σ_{Ftan} is the average tangential stress, which is equal to

$$\sigma_{\mathrm{Ftan}} = \frac{\hat{A}\hat{B}_\delta \cos\varphi}{2} \qquad (2)$$

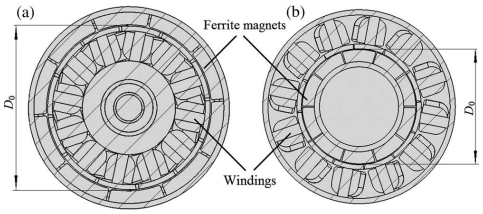

Fig. 3. Sectional drawing of the 10-pole, 12-slot PMSMs. (a) With an outer rotor construction. (b) With a conventional inner rotor.

where $\hat{A}$ is the amplitude of the linear current density fundamental, $\hat{B}_\delta$ is the amplitude of the operating harmonic flux density, and φ is the angle between $\hat{A}$ and $\hat{B}_\delta$. As the remanence of the HF 32/22 is low, the load line of the magnet in the second quadrant of the BH demagnetization chart is selected almost vertical to reach as high air-gap flux density as possible. This results in a relatively high PM thickness. In this case, the thickness of the magnet $h_{\mathrm{pm}} = 11.5$ mm while the machine air gap $\delta = 0.8$ mm being only 7% of the magnet thickness. As the iron parts produce some magnetic voltage, the analytical calculations of the magnetic circuit of the machine show that the peak value of the air gap flux density is approximately equal to $\hat{B}_\delta = 0.37$ T being about 90% of the remanent flux density, and the main flux peak $\widehat{\Phi}_\delta = 0.985 \cdot 10^{-3}$ Vs. The large magnet material volume is the price one has to pay when using rotor surface ferrite magnets. The peak linear current density $\hat{A} = 65$ kA/m. Because of (2), if $\cos(\varphi) \approx 1$, the average tangential stress with these values is equal to $\sigma_{\mathrm{Ftan}} = 12$ kPa. The tangential stress of the motor is only about 30–50% of the average value of the ordinary totally enclosed fan-cooled PMSMs with NdFeB magnets [25].

According to [25] in low-power multiple-pole synchronous or asynchronous machines, the C_{mec} typically reaches values in the range of 80–120 kWs/m^3. Despite the fact that in those traditional machines, the fundamental air gap flux density reaches values in the range of 0.8 T and in a case of using rotor surface ferrite magnets the air gap flux density remains below 0.4 T, the machine constant still gets quite a high value (118 kWs/m^3), which proves that machine volume is used well.

As a result of the low permanent magnet flux density, the height of the rotor yoke can be small. In our case, $h_{\mathrm{ys}} = 5$ mm, which results in the peak flux density in the rotor yoke $\hat{B}_{\mathrm{yr}} = 1.6$ T. Because of the requirements set for torque and the outer machine dimensions in the blower application, the air gap diameter and the effective core length were chosen $D_{\mathrm{s}} = 0.121$ m and $l' = 0.11$ m, respectively. Thus, under the condition $\cos(\varphi) = 1$, the torque of $T = 30$ Nm can be reached.

In Fig. 3, the difference between the air gap diameter of the outer and inner rotor machines can be seen.

In the case of an external rotor, wider ferrite magnets are needed, and as a consequence, significantly more flux can be produced in an outer rotor machine.

TABLE II
PARAMETERS OF THE PMSM WITH THE OUTER ROTOR CONSTRUCTION

Main dimensions of the machine	Air gap diameter D_s [mm]	121
	Equivalent length of the core l' [mm]	110
	Rotor outer diameter, D_o [mm]	156
	Air gap length, δ [mm]	0.8
Number of stator slots, Q		12
Number of rotor poles, $2p$		10
Linear current density RMS value, A [kA/m]		45.96
Tangential stress, σ_{Ftan} [kPa]		12
Air gap flux density peak, $\hat{B}_\delta$ [T]		0.37
Fundamental winding factor, k_W		0.924
Number of turns per phase, N_{ph}		380
Current density, J [A/m^2×10^6]		5.6
Machine constant, C_{mec} [kWs/m^3], calculated with D_s		118

The induced voltage $\hat{E}_{\text{ph}}$ depends on the number of turns in series N_{ph} angular frequency and winding factor k_w as [25]

$$\widehat{E}_{\text{ph}} = N_{\text{ph}}\omega k_{\text{w\_tot}}\widehat{\Phi}_\delta \tag{3}$$

$$k_{\text{w\_tot}} = k_{\text{pv}}k_{\text{dv}}k_{\text{sq}} \tag{4}$$

$$\omega = 2\pi\frac{n}{60}p \tag{5}$$

where $k_{\text{w\_tot}}$ is the total winding factor of the operating harmonic, which consists of the pitch factor $k_{\text{pv}} = 0.966$, the distribution factor $k_{\text{dv}} = 0.966$, and the skewing factor $k_{\text{sq}} = \sin(\alpha/2)/(\alpha/2)$. In the 12-slot 10-pole (12/10) machine without skewing, the winding factor is equal to $k_w = 0.933$ [11], [12] and the total winding factor of the machine is equal to $k_{\text{w\_tot}} = k_{\text{pv}}k_{\text{dv}}k_{\text{sq}} = 0.924$, ω is the flux angular frequency, $n = 1500$ rpm is the rated speed of the rotor, and p is the number of pole pairs.

Combining (3)–(5), the number of turns per series N_{ph} can be found by

$$N_{\text{ph}} = \frac{\widehat{E}_{\text{ph}}}{\omega k_{\text{w\_tot}}\widehat{\Phi}_\delta}. \tag{6}$$

The number of turns per phase connected in series $N_{\text{ph}} = 380$. In a 10-pole, 12-slot PMSM, it is also possible to get unity distribution factor by using a six-phase winding instead of a three-phase winding [26]. Thus, the average torque could be further increased.

The main dimensions and parameters of the machine shown in Fig. 2 are given in Table II.

A test setup was constructed to determine the real characteristics of the machine. The motor is connected via a torque transducer to a DC-machine. First the DC-machine was used as a motor to find out PM-motor no load properties. The test setup is shown in Fig. 4.

The measured phase-to-phase EMF waveform of the motor is shown in Fig. 5. The motor was forced to rotate by an external machine at $\Omega = 62.8$ [rad/s] to produce a 50-Hz terminal voltage output.

Fig. 5 shows that the back EMF of the motor has an almost purely sinusoidal shape. At nominal motor speed $\Omega = 157$ [rad/s], the RMS value of phase-to-phase back EMF is 332.6 V.

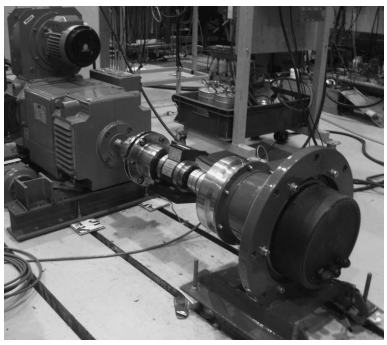

Fig. 4. Testing the 12/10 outer rotor PMSM in laboratory.

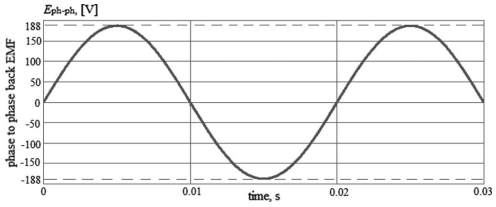

Fig. 5. Phase-to-phase EMF $E_{\text{ph}-\text{ph}}$ of the drive (the frequency is 50 Hz).

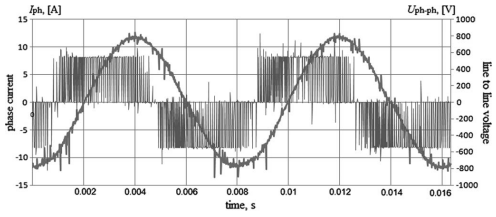

Fig. 6. Phase current and phase-to-phase supply voltage of the PMSM at the rated torque operation.

To determine the most essential properties of the motor, an experiment was made at the nominal load and the nominal frequency, according to thermal and maximum voltage level restrictions. The motor was controlled by a frequency converter ASCM1 by ABB. The motor is driven without any position or speed sensor. The supply voltage and current waveforms are shown in Fig. 6.

The measured motor drive parameters at the rated power are shown in Table III.

Taking into account the fact that the permanent magnet losses in the machine are negligible and current density in the stator is in the range of typical value of PMSM machines, no accurate thermal measurements were implemented. However, during the rated loading of the machine in the test bench at ambient temperature $t = 20$ °C, the rotor outer surface temperature was measured to be 54 °C.

High efficiency is the most essential advantage favoring the use of the low-power PMSM instead of an IM. Can we reach

TABLE III
MOTOR DATA IN THE NOMINAL POINT

Torque, [Nm]	Speed, [n/rpm]	Output Power, [W]	Phase to phase EMF, [V_{rms}]	Current, [A_{rms}]	Rated frequency, f [Hz]
29.9	1500	4700	332.6	8.38	125
Motor input power, [W]	cosφ	Eff., [%]	Phase resistance, R[Ω]	Equivalent stator inductance, L[mH]	Number of phases, m
5032	0.87	93.4	0.98 (0.04 p.u.)	17 (0.57 p.u.)	3

TABLE IV
MACHINE MEASUREMENTS WITH THE FAN LOAD TYPE

№	Mechanical load		Output power	Motor current	Motor phase voltage	Power factor	Eff.
	n [rpm]	T [Nm]	P_{out} [W]	I_{Mrms} [A]	U_{Mrms} [V]	cosφ	η [%]
1	1500	29.9	4696	8.38	230	0.87	93.4%
2	1270	21.7	2886	6.08	184	0.92	93.6%
3	1078	15.3	1727	4.3	150	0.96	93%
4	866	9.9	898	2.84	117	0.98	91.6%

TABLE V
MACHINE MEASUREMENTS WITH A CONSTANT LOAD TORQUE

№	Mechanical load		Output power	Motor current	Motor phase voltage	Power factor	Eff.
	n [rpm]	T [Nm]	P_{out} [W]	I_{Mrms} [A]	U_{Mrms} [V]	cosφ	η [%]
1	1500	29.9	4696	8.38	230	0.87	93.4%
2	1270	29.9	3977	8.40	196	0.87	92.8%
3	1078	29.9	3375	8.38	167	0.87	92.3%
4	866	29.9	2712	8.39	136	0.87	90.9%

a competitive efficiency with a machine equipped with rotor surface ferrite magnets? To see the motor efficiency at different load conditions, several experiments were made. The motor measurements with the fan load ($T \cong n^2$) at different velocities are shown in Table IV.

Next, let us investigate the performance of the machine connected to a constant torque at the same velocities as in Table IV. The experimental results are shown in Table V.

The measurements introduced in Tables IV and V show that the efficiency of the PMSM remains high even though the low-flux-density ferrite magnets are used instead of the rare earth NdFeB, which have already become a typical solution in permanent magnet machines.

The loss distribution was found by the finite-element analysis (FEA). The finite-element computations were performed with Cedrat's Flux2D software. The sketch of the machine is shown in Fig. 7.

The machine dimensions are introduced in Tables II and IX. The iron of the modeled machine has the similar properties as the electric sheet M400-65A. The resistivity and permeability of the permanent magnets are introduced in Table I. The mesh of the model contains of 14 972 first-order elements and 30 067 nodes. The mesh was composed with 99.45% of excellent

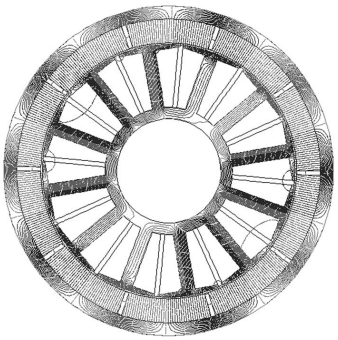

Fig. 7. Flux routes at no-load for 12-slot 10-pole surface magnet machine.

TABLE VI
LOSS DISTRIBUTION IN THE PMSM

Type of losses	Distribution, [%]	Value of losses, [W]
Copper loss stator	62	206
PM eddy current loss	~ 0	~ 0
Iron loss, stator	18.1	60
Iron loss, rotor yoke	11.4	38
Total iron loss	29.5	98
Mechanical loss and Additional loss	8.4	28
Total losses	100	332

quality elements. The FEA results of the motor in the nominal operating point are given in Table VI.

The mechanical and additional losses in Table VI were not estimated by FEM analysis, but they were found by elimination approach.

Table VI shows that the losses in the permanent magnets caused by eddy currents calculated in the model have negligible values.

Flux2D estimates the stator laminated iron losses by the following equation:

$$\frac{1}{T}\int_0^T P_{\mathrm{Fe}}(t)\,dt = k_{\mathrm{h}}\hat{B}^2 f k_{\mathrm{f}} + \frac{1}{T}\int_0^T k_{\mathrm{f}}\left[\sigma_{\mathrm{Fe}}\frac{d^2}{12}\left(\frac{dB(t)}{dt}\right)^2 + k_{\mathrm{e}}\left(\frac{dB(t)}{dt}\right)^{1.5}\right]dt \quad (7)$$

where P_{Fe} is the iron losses, $\hat{B}$ is the maximum flux density in the element concerned, B is the instantaneous flux density, f is the frequency, σ_{Fe} is the conductivity, d is the lamination sheet thickness, k_{h} is the coefficient of the hysteresis loss, k_{e} is the coefficient of excess loss, and k_{f} is the stacking factor. The factors depend on the steel material applied [7], [11].

However, this algorithm does not work with not laminated solid iron. Therefore, the rotor losses of the machine were represented as Joule losses and calculated by the same 2-D FEA software. It was noticed that this value is quite significantly influenced by operating mode of the machine. With lower torque and speed of the machine, the rotor losses decrease.

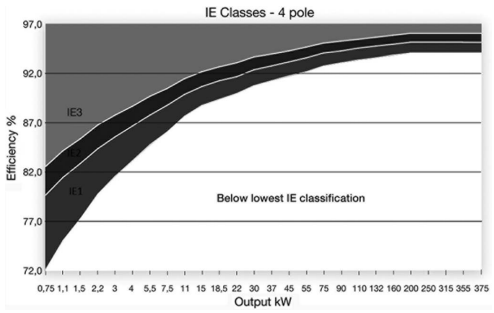

Fig. 8. Power-to-efficiency curves for IE3, IE2, and IE1 classes for four-pole asynchronous motor [28].

TABLE VII
MINIMUM EFFICIENCY VALUES DEFINED IN IEC 60034-30:2008 STANDARD [28]

Output power, P [kW]	IE1 4 pole	IE2 4 pole	IE3 4 pole
5.5	84.7	87.7	89.6

It should be, also, noted that the skewing of the stator slots was not implemented in the model, therefore the real rotor losses may differ from the one which was got by modeling. The aim of the data in Table VI is not to precisely determine the losses distribution in the machine, but to show the factors which give the possibility to get higher efficiency by using the PMSM instead of a conventional asynchronous machine. A similar table that shows the distribution of the induction machine losses is provided in Section IV. In addition, the efficiencies are compared in the following section.

A drawback in the outer rotor constructions is that the cooling of the stator winding is somewhat difficult. Outer rotor machines are, however, often used in fan applications, and in such cases, the work tool, (i.e., the fan) very efficiently cools the rotor, which also helps the cooling of the stator.

The motor data and the characteristics of the outer rotor machine described above provide an opportunity to consider the competitiveness of the outer rotor permanent magnet machine magnetized by ferrite magnets, when compared with standard industrial machines.

IV. COMPARISON OF THE OUTER ROTOR PERMANENT MAGNET SYNCHRONOUS MOTOR WITH AN INDUCTION MOTOR OF THE SAME POWER

Currently, at least 90% of industrial drive systems employ IMs [27]. There are three minimum efficiency values defined in IEC 60034-30:2008. They are shown in Fig. 8.

Table VII shows efficiencies for the four-pole machine power $P = 5.5$ kW for IE1, IE2, and IE3 efficiency classes.

For comparison, a low-voltage general performance IM M2BA 132 SMB, which is a part of IE2 efficiency class according to IEC 60034-30; 2008, manufactured by ABB was selected. Taking into account that the comparison of the machine performances should be made with a blower drive, a flange-mounted motor was chosen. Table VIII shows the parameters of the machine.

TABLE VIII
M2BA 132 SMB INDUCTION MOTOR CHARACTERISTICS IN A SINUSOIDAL SUPPLY

Output power, P[kW]	Speed, n[rpm]	Nom. Current, I_N [A]	Nom. torque, T_N [Nm]
5.5	1460	11.1	35.9
Moment of inertia, J[kgm^2]	Efficiency		
	Full load, 100%	¾ load, 75%	½ load, 50%
0.033	89	89.8	88.9

TABLE IX
OUTER DIMENSIONS OF THE M2BA 132 SMB INDUCTION MOTOR AND THE STUDIED PMSM

Dimension	IM	PMSM
Length of the machine, L [mm]	533	190
Diameter of the motor, D [mm]	230	158
Length of the shaft, l_E [mm]	80	0

Let us first consider the outer dimensions of the induction machine. The most essential dimensions of the drives are listed in Table IX.

It should be noted that in Table IX, the diameters of the mounting flanges, which are larger than the motor outer diameter, are not taken into account in the machine dimensions.

The fact that the IM is longer than the PMSM can be explained by the additional length of the shaft in the IM. However, from the extra material point of view, it has only a minor influence. Further, in the stand-alone IM, there is a cooling fan attached to the machine, whereas the PMSM is made without a special cooling system. This is because of the specific nature of the blower application, where the motor is cooled automatically by the work tool. Also, the end windings contribute to the additional length of the IM, which requires much more material in a conventional asynchronous machine with a low number of poles and an integer value of slots per phase per pole than in a PMSM with concentric windings. Thus, the conductive material cost savings may compensate some of the costs of the additional permanent magnets in the PMSMs. Moreover, the production method of concentrated windings can be easier to implement than the production of distributed conventional slot windings [5].

A problem in the use on an outer rotor machine may arise from the fact that almost the whole machine surface is rotating. This is another reason for the choice of the blower application when comparing the IM and the external rotor PMSM. In a fan drive, the outer rotor machines, as it is shown further, may have a great advantage compared with inner rotor types.

Next, let us investigate the efficiencies of the motors. The efficiencies of the IM in direct-on-line use are shown in Table VIII in different load conditions. If the speed control of the machine is implemented by a frequency converter, the efficiency of the IM is somewhat lower. It is stated that the additional losses in the motor caused by the frequency converter may increase the total motor losses up to 15–20% compared with direct-on-line operation [29]. This leads to a decrease in the machine efficiency by 2% in the rated point. The results of the PMSM experiments in different load conditions are given

TABLE X
TYPICAL LOSS DISTRIBUTION IN AN INDUCTION MACHINE IN THE POWER RANGE 5.5 kW [25]

Type of losses	Distribution, [%]	Value of losses, [W]
Mechanical loss	3	20
Copper loss stator	48	326
Copper loss rotor	26	177
Iron loss stator	15	102
Iron loss rotor	5	34
Total iron loss	20	136
Additional loss	3	20
Total losses	100	680

in Tables IV and V. The measurement results show that the efficiency does not drop under 90% even at one one-fifth of the rated power, and in the rated point, it is equal to 93.4%. Such a high efficiency in this power range compared with the induction machine can be explained by the absence of the copper rotor losses in the PMSM and also by the fact that in the permanent magnet machines, no magnetization current is needed in the stator windings. In contrast, in an asynchronous motor, in addition to the losses in the stator, there are also significant Joule losses in the rotor. The approximated loss distribution of a conventional induction machine with four poles and 5.5-kW power range is given in Table X.

The difference between the two investigated motor efficiencies in the rated point is

$$\Delta\eta = \eta_{\mathrm{PMSM}} - \eta_{\mathrm{IM}} = 93.4\% - (89.0 - 2.0)\% = 6.4\% \quad (8)$$

where η_{PMSM} is the efficiency of the PMSM at the rated power, supplied by the frequency converter, η_{IM} is the efficiency of the IM at the nominal power including losses caused by a frequency converter. If it is assumed that the motors operate the whole year without breaks, at the nominal power, the difference in the consumed power would be

$$P_{\mathrm{out}}\left(\frac{1-\eta_{\mathrm{IM}}}{\eta_{\mathrm{IM}}} - \frac{1-\eta_{\mathrm{PMSM}}}{\eta_{\mathrm{PMSM}}}\right)\cdot(365\ \mathrm{days}\cdot 24\ \mathrm{h}) = 3800\ \mathrm{kWh}. \quad (9)$$

Equation (9) shows that the energy consumption can be reduced as much as by 3800 kWh annually by a PMSM with a ferrite magnet rotor construction instead of an IM in the 5.5-kW range.

PMSMs are typically not connected directly on line, but a frequency converter is needed. Thus, it seems to be a more expensive solution when compared with the initial cost of an IM without speed control. However, a convincing argument in favor of the speed control of the blower drive is that it has a large potential for saving energy and reducing noise. In fans, the opportunity of setting the operating point as required by pressure difference provides a great advantage compared with noncontrolled motor drives from the energy consumption point of view. Apart from the efficiency aspect, the noise and vibration in the partial load range can also be reduced by speed variation.

An essential drawback of the PMSMs with rotor surface magnets is problems related to the implementation of the field weakening mode in cases it is needed. The low synchronous inductance (in this case $L_{\mathrm{s}} = 0.57$ p.u.) is caused by the large equivalent air gap. Such a value of synchronous inductance results in a limited field weakening range.

In the IMs instead, the magnetic field can be easily weakened. However, in the field weakening mode, the load torque should have a lower value with a higher speed. It is not the option of the blower drives as their torque rises in square with the speed.

The outer rotor construction in a fan drive offers a very compact design compared with the traditional stand-alone motor drive, Fig. 9.

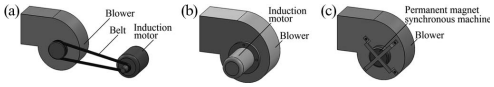

Fig. 9. Possible coupling of the electrical machine to the fan. (a) Indirect coupling with the induction motor by a belt transmission. (b) Direct coupling of the induction motor to the fan. (c) Direct coupling of the outer rotor to the fan blades.

TABLE XI
PROS AND CONS OF AN INTEGRATED DRIVE

Factor	Integration of power electronics with the electrical machine	Integration of a fan with the electrical machine	Separately composed system
Efficiency	+	+	–
Accuracy	+	+	–
Size	+	+	–
Additional mounting	+	+	–
Reliability	+	+	–
Price	depends on situation	depends on situation	depends on situation
Cable oscillations	±	no effect	–
Other electromagnetic compatibility (EMC) problems	±	no effect	–
Option of replacing parts of the construction	–	–	+
Operating in harsh environments	–	–	+

Fig. 9 shows three coupling types of the fan to the machine. IM usually, coupled by a belt transmission (a) or directly by a muff (b). In the first case, the belt transmission efficiency should be taken into account. It varies typically in the range of 90–98%, and therefore, it further reduces the competitiveness of the IM drive. The direct coupling does not have such a drawback; however, it still takes more place and requires more mounting than the case of the integrated machine drive to the blower as shown in Fig. 9(c). Table XI compares the characteristics of a fully integrated system with a conventional blower construction.

Table XI shows the possible advantages of an integrated system. The only essential drawbacks of such a system are the impossibility to replace individual parts of the construction by new ones and vulnerability to harsh environments where acid gases may corrode the integrated design.

TABLE XII
PARAMETERS OF THE IM AND THE PMSM

Specification	Induction machine	PMSM
Number of slots per pole per phase, q	Integer	Fractional ($q \leq 5$)
End winding geometry	Overlapping winding, long end winding	Single tooth coil winding, short end winding
Efficiency	Inherent efficiency limitation	Capability to reach very high efficiency
Coupling of fan blades	Additional mechanical units for coupling	Fan blades can be directly attached to the outer rotor (facilitating the use of the fully integrated system)
Power to volume ratio	Quite standardized value	Higher than in the IM
Production process	Well developed technological process	Slot tooth winding and permanent magnets located on the surface of the outer rotor may lead to the simplification of the production process
Pole number	High pole numbers are limited by the risk of having a low magnetization inductance and therefore a poor power factor	Within the wide array of possible pole numbers, only a few arrangements have a desirable performance

For the final comparison purpose, the most essential differences between the IM and the studied fractional slot permanent magnet synchronous motor with ferrite magnets are shown in Table XII.

V. CONCLUSION

The characteristics of the outer rotor permanent magnet machine with ferrite magnets were investigated. The main target of the proposed motor construction is not to compete with a PMSM that uses NdFeB magnets, but to compete with an IM in an industrial fan application. In particular, the application of outer rotor PMSMs to blower drives looks very promising. The prices of motors with ferrite magnets should remain in the same range as the prices of conventional IMs. However, the efficiency and power consumption of the PMSM are much more competitive even when compared with induction machines in the high efficiency classes IE3 and IE4. This can be the main reason for the substitution of industrial asynchronous motors by permanent magnet machines with ferrite magnets in blower applications

REFERENCES

[1] H. B. Ertan, M. Y. Üçtug, R. Colyer, and A. Consoli, *Modern Electrical Drives*. New York: Springer-Verlag, 2000.

[2] A. Chiba, Y. Takano, M. Takeno, T. Imakawa, N. Hoshi, M. Takemoto, and S. Ogasawara, "Torque density and efficiency improvements of a switched reluctance motor without rare-earth material for hybrid vehicles," *IEEE Trans. Ind. Appl.*, vol. 47, no. 3, pp. 1240–1246, May/Jun. 2011.

[3] S. Chino, S. Ogasawara, T. Miura, A. Chiba, M. Takemoto, and N. Hoshi, "Fundamental characteristics of a ferrite permanent magnet axial gap motor with segmented rotor structure for the hybrid electric vehicle," in *Proc. IEEE ECCE*, Sep. 17–22, 2011, pp. 2805–2811.

[4] S. Ooi, S. Morimoto, M. Sanada, and Y. Inoue, "Performance evaluation of a high power density PMASynRM with ferrite magnets," in *Proc. IEEE ECCE*, Sep. 17–22, 2011, pp. 4195–4200.

[5] H. Jussila, P. Salminen, M. Niemelä, and J. Pyrhönen, "Guidelines for designing concentrated winding fractional slot permanent magnet machines," in *Proc. Int. Conf. POWERENG*, Apr. 12–14, 2007, pp. 191–194

[6] P. Salminen, J. Pyrhönen, H. Jussila, and M. Niemelä, "Concentrated wound permanent magnet machines with different rotor designs," in *Proc. Int. Conf. POWERENG*, Apr. 12–14, 2007, pp. 514–517.

[7] H. Jussila, "Concentrated winding multiphase permanent magnet machine design and electromagnetic properties—Case axial flux machine," Ph.D. dissertation, Dept. Elect. Eng., Lappeenranta Univ. Technol., Lappeenranta, Finland, 2009.

[8] A. M. EL-Refaie, "Fractional-slot concentrated-windings synchronous permanent magnet machines: Opportunities and challenges," *IEEE Trans. Ind. Electron.*, vol. 57, no. 1, pp. 107–121, Jan. 1, 2010.

[9] J. Cros and P. Viarouge, "Synthesis of high performance PM motors with concentrated windings," *IEEE Trans. Energy Convers.*, vol. 17, no. 2, pp. 248–253, Jun. 2002.

[10] A. R. Tariq, C. E. Nino-Baron, and E. G. Strangas, "Consideration of magnet materials in the design of PMSMs for HEVs application," in *Proc.IEEE Power Energy Soc. Gen. Meeting*, Jul. 24–29, 2011, pp. 1–6.

[11] F. Meier, "Permanent-magnet synchronous machines with non-overlapping concentrated windings for low speed direct-drive applications," Ph.D. dissertation, Royal Inst. Technol. School Elect. Eng. Elect. Mach. Power Electron., Stockholm, Sweden, 2008.

[12] T. Heikkilä, "Permanent magnet synchrnous motor for industrial applications—Analisis and design," Ph.D. dissertation, Dept. Elect. Eng, Lappeenranta Univ. Technol., Lappeenranta, Finland, 2002.

[13] R. Krishnan, *Permanent Magnet Synchronous and Brushless DC Motor Drives*, 1st ed. Boca Raton, FL: CRC Press, 2010.

[14] A. Emadi, *Energy-Efficient Electric Motors*, 3rd ed. Boca Raton, FL: CRC Press, 2004.

[15] T. J. E. Miller, *Brushless Permanent-Magnet and Reluctance Motor Drives*. London, U.K.: Oxford Univ. Press, 1989.

[16] J. Puranen, "Induction motor versus permanent magnet synchronous motor in motion control applications: A comparative study," Ph.D. dissertation, Dept. Elect. Eng., Lappeenranta Univ. Technol., Lappeenranta, Finland, 2006.

[17] L. Ferraris, P. Ferraris, E. Pošković, and A. Tenconi, "Theoretic and experimental approach to the adoption of bonded magnets in fractional machines for automotive applications," *IEEE Trans. Ind. Electron.*, vol. 59, no. 5, pp. 2309–2318, May 2012.

[18] F. Magnussen and C. Sadarangani, "Winding factors and Joule losses of permanent magnet machines with concentrated windings," in *Proc. IEEE IEMDC*, Jun. 1–4, 2003, vol. 1, pp. 333–339.

[19] 2011, Nov. [Online]. Available: http://www.vacuumschmelze.de

[20] A. Goldman, *Modern Ferrite Technology*, 2nd ed. Pittsburgh, PA: Springer-Verlag, 2006.

[21] 2011, Nov. [Online]. Available: http://www.intemag.com

[22] G. S. Liew, C. Tang, W. L. Soongand, N. Ertugrul, and D. B. Gehlert, "Finite-element analysis and design of a radial-field brushless PM machine utilizing soft magnetic composites," in *Proc. IEEE IEMDC*, May 15–18, 2011, pp. 930–935.

[23] E. Fornasiero, N. Bianchi, and S. Bolognani, "Slot harmonic impact on rotor losses in fractional-slot permanent magnet machines," *IEEE Trans. Ind. Electron.*, vol. 59, no. 6, pp. 2557–2564, Jun. 2012.

[24] W. Fei and P. C. K. Luk, "Torque ripple reduction of a direct-drive permanent-magnet synchronous machine by material-efficient axial pole pairing," *IEEE Trans. Ind. Electron.*, vol. 59, no. 6, pp. 2601–2611, Jun. 2012.

[25] J. Pyrhönen, T. Jokinen, and V. Hrabovcová, *Design of Rotating Electrical Machines*. New York: Wiley, 2008.

[26] M. Barcaro, N. Bianchi, and F. Magnussen, "Faulty operations of a PM fractional-slot machine with a dual three-phase winding," *IEEE Trans. Ind. Electron.*, vol. 58, no. 9, pp. 3825–3832, Sep. 2011.

[27] A. M. Trzynadlowski, *Control of Induction Motors*. Waltham, MA: Academic, 2001.

[28] 2011, Nov. [Online]. Available: http://www.abb.com

[29] L. Aarniovuori, "Induction motor drive energy efficiency—Simulation and analysis," Ph.D. dissertation, Dept. Elect. Eng., Lappeenranta Univ. Technol., Lappeenranta, Finland, 2010.

Authors' photographs and biographies not available at the time of publication.

Publication II

Petrov, I., Polikarpova, M., and Pyrhönen, J., "Rotor surface ferrite magnet synchronous machine for generator use in a hybrid application — Electro-magnetic and thermal analysis," *in 39th Annual Conference of the IEEE Industrial Electronics Society, IECON 2013* , pp.3090−3095, 10−13 Nov. 2013

Rotor surface ferrite magnet synchronous machine for generator use in a hybrid application – electro-magnetic and thermal analysis

Ilya Petrov, Maria Polikarpova Juha Pyrhönen

***Abstract*—To reach a particular tangential stress in a PMSM the magnetic loading and the electric loading should have corresponding values. This means that if the magnetic loading is restricted by the characteristics of cheap and relatively weak ferrite permanent magnets, the electric loading should be increased to keep the tangential stress at desirable value. However, the latter is also limited because of the demagnetization risk of the permanent magnets by a high armature reaction. Therefore, surface ferrite PMSMs should have a low tangential stress in order to avoid the demagnetization risk, which consequently leads to a low torque density. This is one of the main drawbacks of ferrite magnets used in electric motor drives. This paper describes some possibilities for improving the torque density with surface ferrite PMSMs, describes the restrictions which one can meet while designing this type of the electric machines and observe the influence of temperature variation in the magnets on the electric machine performance. An example is done with the analytical and the FEM analyses of a 50 kW, 3000 rpm, permanent magnet generator for a series hybrid electric vehicle application.**

***Index Terms*—Permanent magnet machines, ferrite magnets, TC-PMSM, tooth-coil winding.**

I. Introduction

Permanent magnet technology is constantly developing and the use of permanent magnet is increasing, due to the benefits they can provide. An additional boost of the progress of permanent magnet synchronous machines (PMSMs) was got after establishing of the interior magnet rotor structure (which assists sensorless controls and is more advantageous for working in a field weakening mode) [1], [2] and with the development of tooth-coil winding approaches (with pole/slot ratios which suit best for particular applications) [3], [4]. However, due to the high price of the rare earth elements in the modern magnets, it is sometimes not economically feasible to use such technology in the applications which should have a relatively high power (starting from dozens of kilowatts) and high speed range (starting from dozens of rad/s). At this power and speed areas conventional asynchronous machines should have similar performance characteristics as PMSMs with the slightly smaller peak efficiency in the static efficiency map [5], less torque density and lower power factor [6].

After the rapid increase of the neodymium magnets' price in 2010, there appeared many companies and organizations which try to find appropriate designs for so called "rare earth free" electric machines. The main purpose of the "rare earth free" electric machines is to reach almost the same torque density as in commercially available neodymium PMSMs, without efficiency deterioration [7]–[14]. Major part of these attempts was done for hybrid electric vehicle applications [7]–[11]. Common measures in order to increase the power density of PMSMs are high angular speeds [15], increase the number of pole pairs (in order to reduce the stator yoke height), increase the tangential stress (by use of stronger permanent magnets or higher electric loading) [16], use tooth coil winding [3], reluctance torque implementation [17] and increase the air gap diameter of the PMSM with the same outer dimensions [14].

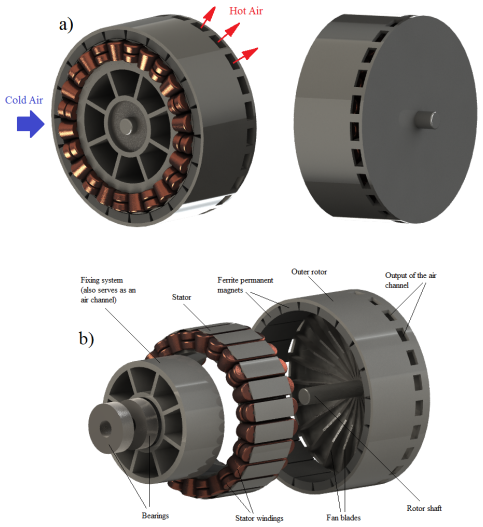

Fig. 1. 50 kW, 3000 rpm generator for the series hybrid electric vehicle a) assembled view b) units of the generator

One of the possible solutions, which was offered by the authors in [14], was to use the outer rotor construction, which in the case of a PMSM with relatively weak ferrite magnets, significantly increases the machine overall torque density by means of enlargement the air gap diameter.

However, the proposed electric machine had a 5 kW nominal power, and in this case there was not demagnetization risk even at overload conditions and at a short circuit, due to the

TABLE I
GENERATOR PARAMETERS

Parameter	Value
Stack (physical) iron length l_{Fe} [mm]	102
Stator inner diameter D_{si} [mm]	244
Stator outer diameter D_{so} [mm]	338
Rotor outer diameter D_{ro} [mm]	388
Rotor tangential tension δ_{tan} (at rated torque) [kPa]	8.6
Number of stator slots Q_{s}	24
Number of pole pairs p	10
Permanent magnet height [mm]	17
Permanent magnet Bakker Magnetics BM9 remanence B_{r} at rated temperature (+80° C)	0.34
Effective coil-turns in half-slot $z_{\mathrm{Q}}/2$ [mm]	10
Winding factor k_{w1} [mm]	0.933
Winding connection	star
Stator core material	M270-35A
Rated speed n_{N} [rpm]	3000
Rated torque T [Nm]	159
Rated terminal phase voltage U_{ph} [Vrms]	230
Rated phase back-emf (at no load) E_{ph} [Vrms]	205
Rated stator current I_{S} [Arms]	83.8
Stator resistance R_{s} [ohm]	0.025

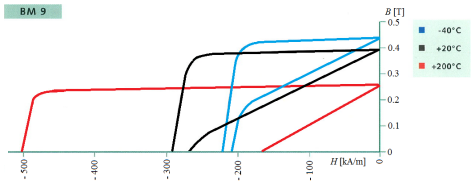

Fig. 2. BH curve of BM9 type hard ferrite magnetic material by Bakker Magnetics at different temperatures [18]

low armature current influence on the magnetic state of the magnets.

In this paper an analysis of using ferrite permanent magnets in electric machines in a higher power range and with the same approach for increasing the torque density (enlarge the air gap diameter by using an outer rotor construction) is, again, proposed. The details which should be considered during the design of this type of electric machines are described. An example of 50 kW, 3000 rpm ferrite magnet rotor surface PMSM (FRSPMSM) is introduced. First, the design and an optimization was made analytically by the method described in [19]. Then a verification of the analytical results was done by the FEM analysis in Flux2D$^{\mathrm{TM}}$. The meshed sketch of the generator is shown in Fig. 3. The 2D FEM model contains of 39510 first order elements and 79335 nodes. The mesh was composed with 98.3 % of excellent quality elements. The achieved results of the design routine are represented in the paper.

The application of the proposed FRSPMSM is a generator for a series hybrid electric bus. However, in a power range of such an application, the demagnetization risk is of special concern, because of the much higher armature reaction influence on the magnetic state of the ferrite permanent magnets. Therefore, in this case the main questions are:

- Which are the real demagnetization risks at nominal load, at overload condition and at short circuit?
- What measures can be implemented to decrease the demagnetization effect and how these measures might affect on the performance of the PMSM?

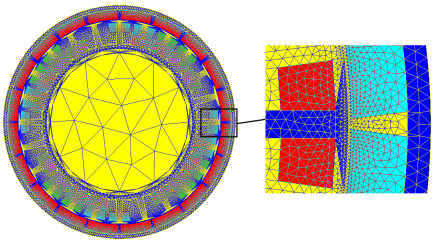

Fig. 3. Meshed sketch of the FRSPMSM

Parameters of the designed ferrite PMSM are introduced in Table I. The electric machine geometry is shown in Fig. 1

II. VARIATION CHARACTERISTICS OF THE FERRITE PMSM WITH TEMPERATURE CHANGE

Analytically the FRSPMSM was designed for one particular temperature which is +80° C. However, it is known that ferrite magnets are quite sensitive to temperature variation. This fact with the aspect that in the bus application the ambient temperature might vary significantly, makes it necessary to analyze the generator at the boundaries of possible ambient temperature change.

The permanent magnet material used in the generator is BM 9 hard ferrite magnetic material by Bakker Magnetics [18]. The demagnetization BH curves of the magnets at different temperatures are shown in Fig. 2. In the figure it is seen that with a higher magnet temperature the remanent flux density of the magnet reduces. This feature is similar to a property of neodymium magnets. However, the difference between rare-earth magnets and ferrite magnets is that neodymium magnets at higher temperature are more vulnerable to a demagnetization risk, whereas higher temperature of the ferrite magnets makes them more withstanding from the demagnetization point of view. Therefore, it can be concluded that it is needed to keep the magnets at a relatively high temperature to be able to implement the higher electric loading or in other words the higher linear current densities without a demagnetization risk.

In order to observe the demagnetization risk and performance change with temperature variation the following temperature points were chosen: -40° C, +20° C and +80° C. Therefore, it is assumed that the lowest possible temperature of the magnets is -40° C, which is a potential ambient temperature in winter time in Finland (the place where the vehicle is going to be tested), and the average magnet temperature is +80° C at the nominal load and at +50° inlet cooling air (which is possible in summer time). Estimation of the magnet temperature at the nominal load is described in Section IV.

By taking into account the above mentioned information, it is obvious that the temperature variation should have a

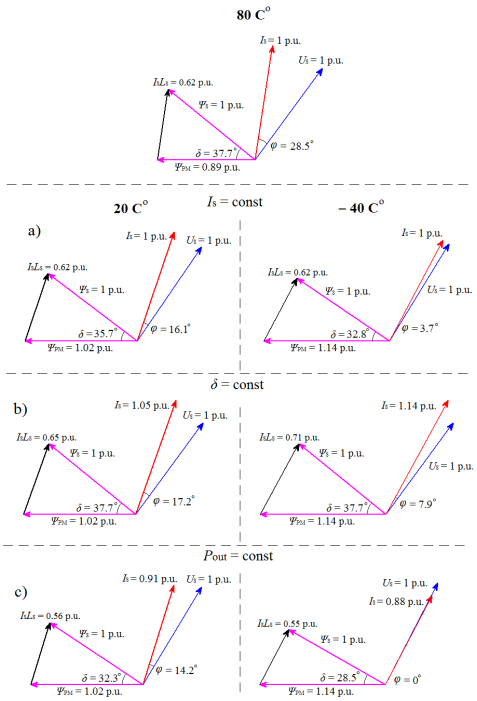

Fig. 4. Vector diagram of the PMSM in nominal working point (+80° C) and its variation for +20° C and -40° C at a) constant stator current, b) constant load angle and c) constant output power

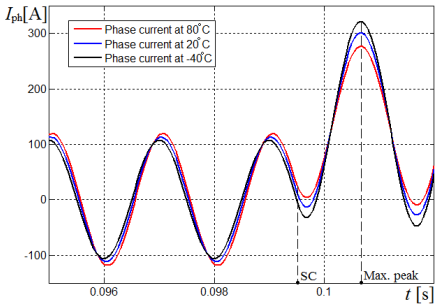

Fig. 5. Phase current at different magnet temperatures. The three-phase short circuit is launched at t = 0.0995 s

significant influence on the FRSPMSM performance. Fig. 4 shows how the vector diagram of the generator changes if the (a) stator current, (b) the load angle or (c) the power/torque is kept constant with temperature reduction. However, because the power/torque at the nominal working point is restricted by internal combustion engine (ICE) rating the output power of the generator should be kept constant. Therefore, the analysis of the demagnetization risk at different temperatures is made for constant output power.

Absolute values of the currents of the electric machine at different magnet temperatures (different remanent flux densities) are estimated by 2D FEM analysis and introduced in Fig. 5. The output power is kept constant ($P_{\text{out}} = 50$ kW). A three-phase short circuit occurs at t = 0.0995 s.

Estimated current, load angle and power factor by analytical approach and by FEM at different magnet temperatures are introduced in Table II (the output power is kept constant). According to the table it can be concluded that with the temperature decrease, the current and load angle also decrease, whereas the power factor increases. The difference between FEM and analytical values is small, because of not significant saturation effect in these types of electric machine. However, the saturation still has some influence on the synchronous inductance change, which can be concluded due to more rapid load angle decrease with higher remanent flux density (lower temperature), whereas the analytical approach uses constant synchronous inductance.

TABLE II
GENERATOR PARAMETER VARIATIONS AT DIFFERENT TEMPERATURES

Magnet temperature	+80° C	+20° C	-40° C
FEM			
Stator phase current, I_{ph} [Arms]	83.8	77	74.6
Power factor, $\cos(\varphi)$	0.88	0.96	0.99
Load angle, δ	38.5°	32.5°	26.7°
Analytical			
Stator phase current, I_{ph} [Arms]	85.6	77.7	75.4
Power factor, $\cos(\varphi)$	0.88	0.97	1
Load angle, δ	37.7°	32.3°	28.5°

III. EVALUATION OF DEMAGNETIZATION RISK IN FRSPMSMS

At different electric states of the PMSM (nominal load, overload, short circuit) it is needed to evaluate if there is a demagnetization risk due to armature reaction.

According to [20] the influence of both normal and tangential field strengths can lead to irreversible demagnetization of the permanent magnets. However, based on FEM analysis in [20] if a multi-pole surface PMSM is considered there is no significant impact on the demagnetization by the tangential field strength, therefore in this paper only the normal component of the flux density (parallel to the magnetization direction) is considered and based on these results the demagnetization risk is evaluated.

Normal components of the flux density in the permanent magnet at different temperatures are illustrated in Fig. 6. As it is mentioned above the phase current also changes with the temperature variation. This means that the real flux density in the magnets is a result of the remanent flux density and the armature reaction, which are functions of temperature. The flux densities are shown for the time instant when the peak

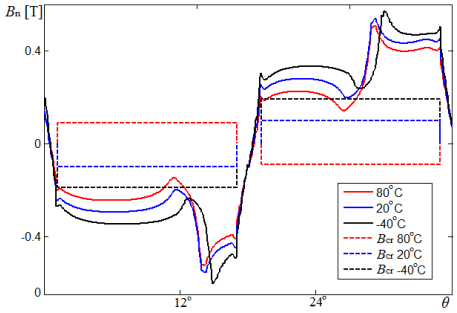

Fig. 6. Normal component of the flux density at different magnet temperatures and corresponding limiting values for the PM material. The PMSM is at nominal load power. The magnet is located just near to the stator slot where the peak current is flowing.

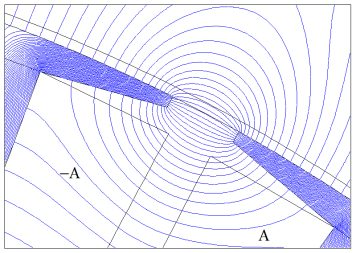

Fig. 7. Effect of the tooth tip flux leakage on the permanent magnet state. The permanent magnet is replaced by vacuum. Therefore the flux lines are only resulting from the armature current.

current is in the slot which is near by the magnet. This is the worst condition from the demagnetization point of view. The flux densities are shown at 0.1 mm depth in the magnets.

Fig. 6 also shows the critical values of flux density for each temperature B_{cr}. The critical value represents the minimum point for particular temperature above of which there is no demagnetization risk. As it can be seen in the figure the flux densities of the permanent magnet do not decrease to the critical value which means that there is no demagnetization risk at the nominal load.

In Fig. 6 the drops of the normal components of the flux density in the middle of each magnets can be seen. These drops are due to tooth tip flux leakage which might have a significant impact on demagnetization risk especially at high armature currents. The effect of the tooth tip flux leakage is shown in Fig. 7.

Fig. 7 shows that the flux lines are more intense close to the edge of the tooth tip. This means that the influence of armature reaction on the magnetic state of the magnets is essentially due to tooth tip flux linkage. Therefore, there is no reason to significantly increase the permanent magnet width, because this approach will not help to avoid the partial demagnetization by the tooth tip flux leakage.

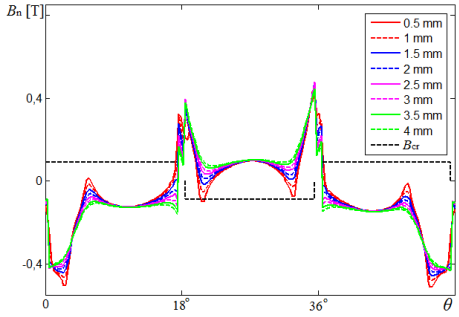

Fig. 8. Normal component of the flux density at +80° C with the critical limit. B_{cr} is the critical limit for the demagnetization risk at +80°. When the normal component of the magnet flux density crosses the critical value, partial demagnetization can occur. For +80° C the critical value is $B_{\mathrm{cr}} = -0.09$ T.

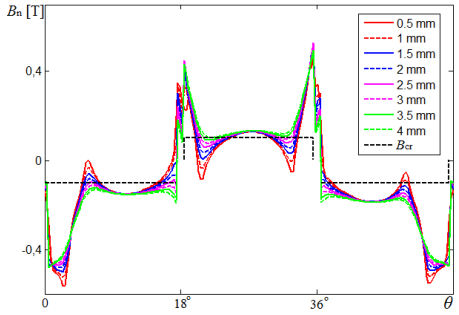

Fig. 9. Normal component of the flux density at +20° C with the critical limit. B_{cr} is the critical limit for the demagnetization risk at +20°. When the normal component of the magnet flux density crosses the critical value, partial demagnetization can occur. For +20° C the critical value is B_{cr} = 0.1 T.

The algorithm in the hybrid vehicle is made in such a way that the generator does not work at the power higher than its nominal power. Therefore, an overload condition cannot be implemented for the generator. However, an observation of the demagnetization risk at the short circuit with the different magnet temperatures should be made.

Fig. 8 – Fig. 10 show the normal component of the magnet flux densities at different temperatures (+80° C, +20° C and -40° C) at the three-phase short circuit (Fig. 5 – Max.peak). The flux densities are shown at different magnet depths from the air gap (from 0.5 mm to 4 mm).

It can be seen that if a generator experiences a short circuit at a low temperature (until magnets are not heated up to +80° C due to the losses), it can lead to a demagnetization risk at a three-phase short circuit.

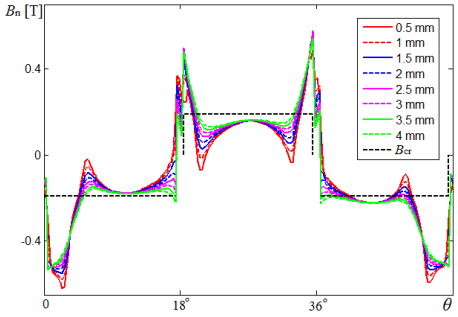

Fig. 10. Normal component of the flux density at -40° C with the critical limit. B_{cr} is the critical limit for the demagnetization risk at -40°. When the normal component of the magnet flux density crosses the critical value, the partial demagnetization occurs. For -40° C the critical value is B_{cr} = 0.19 T.

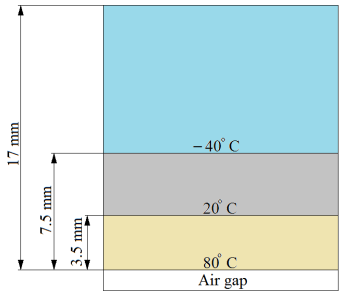

Fig. 11. Required temperature at different magnet depth for preventing the demagnetization risk at three phase short circuit.

IV. Possible Approaches to Avoid the Demagnetization Risk

In Figs. 8 – 10 it can be seen that a highest demagnetization risk is at the small depth in permanent magnets, due to the reasons described above. Therefore, each magnet depth has its particular safe temperature to prevent the demagnetization risk at the three-phase short circuit. The picture with the three depth points (0 mm, 3.5 mm and 7.5 mm) which should have the highlighted temperature in order to prevent the partial demagnetization risk at the short circuit is illustrated in Fig. 11.

At the first thought it seems that the required temperature at small magnet depths should be reached fast at nominal working point, because most of the losses are in the copper and the stator steel, the part of which go through the air gap to the magnets and heat them up. However, due to the cooling methods implemented in the generator (Fig. 1), in reality the magnet temperature is not constant along the magnet length because the input air is heated as it passes through the generator and consequently has different temperatures along the air gap length. In order to verify the

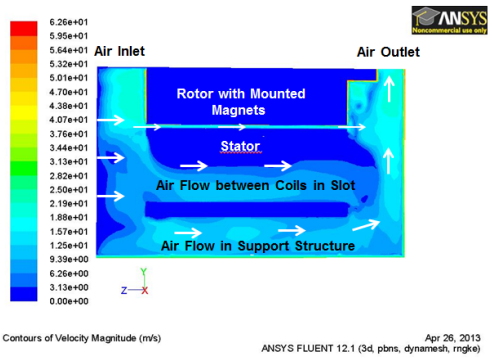

Fig. 12. CFD analysis of the active part of the PMSM. The air speed distribution in the generator.

assumption, a CFD model was created, which shows the real heat distribution in the magnet at nominal load and nominal angular speed (nominal air cooling speed in the generator). The geometry and mesh with approximately 100000 nodes were created in Gambit software. A sector of the machine which includes only one permanent magnet is selected for modeling because of the limited computational resources. The discussed machine model is solved by using energy and $\kappa - \xi$ modes of ANSYS multi-physical software. The inlet and outlet boundary conditions (air velocity and inlet air temperature), materials properties, volumetric heat losses and rotor rotation were determined for reliable thermal modeling. The convection coefficients on the stator and the rotor back surfaces are 80 and $140 \mathrm{W/m^2K}$ correspondingly. The air cooling speed distribution in the generator is shown in Fig. 12.

The temperature distributions in the magnet at nominal load, at air speed distribution shown in Fig. 12 with inlet air temperature +50° and -40° are illustrated in Figs. 13 and 14.

In Figs. 13 and 14 it is seen that the bottom part of the magnet is heated more than the upper part. Therefore the losses generated by FRSPMSM are in favor of demagnetization risk preventing. However, due to different temperature distribution in the magnet, demagnetization risk at the front part of the magnet is higher compared to the rear part. After comparing the CFD simulation results with Fig. 11, it can be seen that the front part of the magnets is still under demagnetization risk at three-phase short circuit, even if the inlet temperature is high.

V. Conclusion

Some hints concerning the design of FRSPMSM are made. It was shown that the performance of such type of electric machines are highly depended on the magnet temperature. This especially might be noticeable in hybrid electric vehicle applications.

It was shown that there is no demagnetization risk at

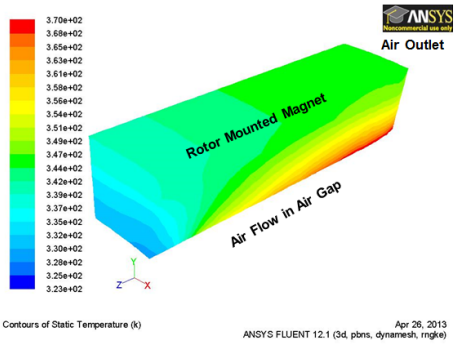

Fig. 13. CFD analysis of the active part of the PMSM. Temperature distribution in the magnet at nominal power and input air temperature +50°. The magnet does not have any practical losses, therefore it is heated up by the losses in the rotor yoke, and losses in the stator through the air gap.

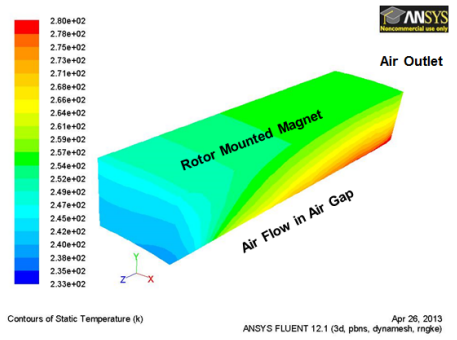

Fig. 14. CFD analysis of the active part of the PMSM. Temperature distribution in the magnet at nominal power and input air temperature -40°. The magnet does not have any practical losses, therefore it is heated up by the losses in the rotor yoke, and losses in the stator through the air gap.

the nominal load of the electric machine at least for the temperature range between +80° C to -40° C. Also the demagnetization risk at the short circuit can be prevented if the magnet temperature is +80° C or higher. This temperature is not necessary in the whole magnet depth, but just for the particular magnet depth (0 mm for +80° C, 3.5 mm for +20° C and after 7.5 mm -40° C can be kept).

Also another approach can be implemented to prevent the partial demagnetization risk, the increase of the synchronous inductance by means of the leakage inductance. The increase of the leakage inductance can be easily done by the semi-closed slot width variation or by use of semi-magnetic wedges with a particular relative permeability μ_r = 2–10. However, this paper does not contain an analysis of such the approach.

REFERENCES

[1] N. Bianchi and S. Bolognani, "Influence of rotor geometry of an ipm motor on sensorless control feasibility," *Industry Applications, IEEE Transactions on*, vol. 43, no. 1, pp. 87–96, 2007.

[2] R. Dutta, L. Chong, and M. Rahman, "Design and experimental verification of an 18-slot/14-pole fractional-slot concentrated winding interior permanent magnet machine," *Energy Conversion, IEEE Transactions on*, vol. 28, no. 1, pp. 181–190, 2013.

[3] A. EL-Refaie, "Fractional-slot concentrated-windings synchronous permanent magnet machines: Opportunities and challenges," *Industrial Electronics, IEEE Transactions on*, vol. 57, no. 1, pp. 107–121, 2010.

[4] P. Ponomarev, P. Lindh, and J. Pyrhonen, "Effect of slot and pole combination on the leakage inductance and the performance of tooth-coil permanent-magnet synchronous machines," pp. 1–1, 2012.

[5] A. Bazzi and P. Krein, "Comparative evaluation of machines for electric and hybrid vehicles based on dynamic operation and loss minimization," in *Energy Conversion Congress and Exposition (ECCE), 2010 IEEE*, 2010, pp. 3345–3351.

[6] R. Lateb, N. Takorabet, F. Meibody-Tabar, A. Mirzaian, J. Enon, and A. Sarribouette, "Performances comparison of induction motors and surface mounted pm motor for pod marine propulsion," in *Industry Applications Conference, 2005. Fourtieth IAS Annual Meeting. Conference Record of the 2005*, vol. 2, 2005, pp. 1342–1349 Vol. 2.

[7] M. Obata, S. Morimoto, M. Sanada, and Y. Inoue, "Characteristic of pmasynrm with ferrite magnets for ev/hev applications," in *Electrical Machines and Systems (ICEMS), 2012 15th International Conference on*, Oct., pp. 1–6.

[8] K. Chiba, S. Chino, M. Takemoto, and S. Ogasawara, "Fundamental analysis for a ferrite permanent magnet axial gap motor with coreless rotor structure," in *Electrical Machines and Systems (ICEMS), 2012 15th International Conference on*, Oct., pp. 1–6.

[9] D. Dorrell, M.-F. Hsieh, and A. Knight, "Alternative rotor designs for high performance brushless permanent magnet machines for hybrid electric vehicles," *Magnetics, IEEE Transactions on*, vol. 48, no. 2, pp. 835–838, Feb. 2012.

[10] S. Chino, S. Ogasawara, T. Miura, A. Chiba, M. Takemoto, and N. Hoshi, "Fundamental characteristics of a ferrite permanent magnet axial gap motor with segmented rotor structure for the hybrid electric vehicle," in *Energy Conversion Congress and Exposition (ECCE), 2011 IEEE*, Sept., pp. 2805–2811.

[11] M. Paradkar and J. Boecker, "Design of a high performance ferrite magnet-assisted synchronous reluctance motor for an electric vehicle," in *IECON 2012 - 38th Annual Conference on IEEE Industrial Electronics Society*, Oct., pp. 4099–4103.

[12] Y.-H. Jeong, K. Kim, Y.-J. Kim, B.-S. Park, and S.-Y. Jung, "Design characteristics of pma-synrm and performance comparison with ipmsm based on numerical analysis," in *Electrical Machines (ICEM), 2012 XXth International Conference on*, Sept., pp. 164–170.

[13] P. Sekerak, V. Hrabovcova, J. Pyrhonen, S. Kalamen, P. Rafajdus, and M. Onufer, "Comparison of synchronous motors with different permanent magnet and winding types," *Magnetics, IEEE Transactions on*, vol. 49, no. 3, pp. 1256–1263, March 2013.

[14] I. Petrov and J. Pyrhonen, "Performance of low-cost permanent magnet material in pm synchronous machines," *Industrial Electronics, IEEE Transactions on*, vol. 60, no. 6, pp. 2131–2138, June 2013.

[15] D. Gerada, A. Mebarki, and C. Gerada, "Optimal design of a high speed concentrated wound pmsm," in *Electrical Machines and Systems, 2009. ICEMS 2009. International Conference on*, 2009, pp. 1–6.

[16] R. Semken, M. Polikarpova, P. Roytta, J. Alexandrova, J. Pyrhonen, J. Nerg, A. Mikkola, and J. Backman, "Direct-drive permanent magnet generators for high-power wind turbines: benefits and limiting factors," *Renewable Power Generation, IET*, vol. 6, no. 1, pp. 1–8, 2012.

[17] M. Barcaro, N. Bianchi, and F. Magnussen, "Remarks on torque estimation accuracy in fractional-slot permanent-magnet motors," *Industrial Electronics, IEEE Transactions on*, vol. 59, no. 6, pp. 2565–2572, 2012.

[18] http://www.bakkermagnetics.com.

[19] J. Pyrhönen, T. Jokinen, and V. Hrabovcová, *Design of Rotating Electrical Machines*. New York: John Wiley Sons, 2008.

[20] S. Ruoho and A. Arkkio, "Partial demagnetization of permanent magnets in electrical machines caused by an inclined field," *Magnetics, IEEE Transactions on*, vol. 44, no. 7, pp. 1773–1778, 2008.

Publication III

Petrov, I., Ponomarev, P., Shirinskii, S., and Pyrhönen, J., "Inductance evaluation of fractional slot permanent magnet synchronous motors with non-overlapping winding by analytical approaches," *in 16th European Conference on Power Electronics and Applications (EPE'14-ECCE Europe), 2014* , pp.1−10, 26−28 Aug. 2014

Inductance Evaluation of Fractional Slot Permanent Magnet Synchronous Motors with non-overlapping Winding by Analytical Approaches

Ilya Petrov, Pavel Ponomarev, Sergey Shirinskii, Juha Pyrhönen
Laboratory of Electrical Drives Technology, LUT Energy, Lappeenranta University of Technology
Skinnarilankatu 34 53850
Lappeenranta, Finland
Phone: +358465517885
E-mail: ilya.petrov@lut.fi
URL: http://www.lut.fi

Keywords

<<Electrical machine>>, <<FSPMSM>>, <<Tooth-coil winding>>, <<Inductance>>, <<Permanent magnet machines>>.

Abstract

Fractional slot permanent magnet synchronous machines with non-overlapping winding (FSPMSM) also known as tooth coil winding permanent synchronous machines (TCW PMSM) have gained intensive attention during the latest decade. Therefore, their design methods are constantly developed and improved. Numerical solution, i.e. finite element analysis (FEA), is still computationally heavy and time consuming, which makes it problematic to use this method in an optimization process. For this reason it is advantageous to use an analytical design method, for searching a design, which satisfies the needed characteristics of a PMSM, during the optimization process.

Synchronous inductance is the major parameter of TCW PMSMs, which defines the overload capability of an electrical machine as well as its field weakening characteristics. Armature reaction, together with the permanent magnet flux linkage, specifies the voltage level, which is required for particular operating condition. Therefore, it is important to estimate this parameter as precisely as possible at early design stages. Low armature reaction should be favourable concerning the maximum reachable torque at the nominal speed. However, together with the reduction of the armature reaction, there is decrease of permanent magnet flux linkage, which is undesirable and in order to prevent it, the permanent magnet material amount must be increased.

Here, the classical analytical approach of the inductance estimation is used, and a simple alternative to it is presented and evaluated. Also, a lumped model (LM) taking saturation into account has been created. The comparison and verification of the models are done by FEA and by the practical test setup of a 12-slot 10-pole TCW PMSM.

Introduction

Preliminary design of an electrical machine by using an iterative analytical approach [2] with an optimization algorithm remains quite a strong and convenient tool. It helps to significantly shorten the time for finding the parameters and geometry of a PMSM, which fulfil all the requirements and give the optimized results in a limited time. The analytical computation can be used in the similar way as it is done in [1], where particular parameters of a TCW PMSM are iterated and a solution which gives the most promising results is highlighted. However, other optimization algorithms are also utilized in the design of a FSPMSM such as Differential Evolution Optimization Algorithm [2], or Artificial Neural Network [3].

An inductance estimation of an electrical machine by the analytical approach is considered as one of the most complicated and important design aspects. The complexity of the inductance evaluation can be explained by a non-linear BH-curve of steel used in electric motor drives. Therefore, at different rotor speeds and load torques, some inductance components of a PMSM can vary, due to armature reaction [14]. However, in order to simplify the machine design process, permeability of steel is often assumed to

be constant, whereas there are many applications, which require using electric motor drives at variable operating conditions with different steel saturation level. The correct evaluation of the inductance in every working point is important because this parameter determines the dynamic performance of the electric motor drive, its overload capability and the performance of the machine in a field weakening mode [10].

The popularity of TCW PMSMs can be explained by the simple and compact mechanical construction of the winding arrangement, short end windings (which brings less amount of copper material used in the FSPMSM and consequently lower Joule losses in the stator windings) [8], low cogging torque, fault tolerance, wide constant power speed range (CPSR), possibility to reach a high slot space factor [9], and cheaper armature manufacturability [7].

There are several analytical approaches, which can be used to estimate a phase inductance. According to one of the methods, it is needed, firstly, to find the magnetizing inductance, and, then, this parameter is used for estimation of the air-gap leakage inductance. This approach is inherently dedicated for distributed rotating-field slot winding PMSMs (DW PMSM), which differs from TCW PMSM ($q \leq 0.5$) by the fact that in rotating-field slot winding the working (fundamental) current linkage harmonic can be easily observed from the current linkage waveform, whereas in TCW PMSM the current linkage waveform has a pulsating character. However, there are several examples of using this method for TCW PMSM [6, 5]. Another algorithm determines the phase inductance by means of self and mutual inductances of the phases, e.g. as it is done for a TCW PMSM in [18]. The drawback of these approaches is the fact that they do not consider the armature current influence on the steel saturation level of the designed machine. This drawback can be avoided if the magnetic circuit is represented as a lumped model with variable resistances, which take into account the non-linear steel behaviour [16].

Conventional algorithm for phase inductance estimation in PMSM

Commonly used equations for inductance evaluation of PMSMs can be found in [4]. A similar algorithm was used in the design of FSPMSM in a number of papers, of which some examples are [8-10].

The main component of the synchronous inductance evaluation in a PMSM is widely thought to be the magnetizing inductance L_{m}. Which, usually, has the highest impact on the total value of the synchronous inductance in DW PMSMs. Magnetizing inductance is associated with the accumulated magnetic energy by the synchronous (operational) armature current linkage harmonic. This characteristic indeed is quite an important in most of the DW PMSMs and in induction machines (IM). In IMs the magnetizing inductance value represents the current component which is needed to be involved to create the magnetizing flux linkage in the electric machine. Therefore, the power factor in this type of electric machines is highly dependent on the value of the magnetizing inductance. For example, the power factor of an IM can be improved by a higher value of the magnetizing inductance. Usually, the magnetizing inductance in induction motor drives is the highest component of the total synchronous inductance.

In a PMSM the magnetizing inductance is also an important characteristic. Despite the fact that during the design of a PMSM with high torque density and severe dynamic performance, the magnetizing inductance is tried to be made as small as possible (in order to reduce the armature reaction) [19], it, usually, has the highest contribution in the total synchronous inductance, whereas the leakage inductance has a less significant share in the total inductance.The magnetizing inductance of a single-phase winding can be estimated by [4]

$$L_{\mathrm{p}} = \frac{4\mu_0}{\pi}\frac{\tau_{\mathrm{p}}}{p\pi\delta_{\mathrm{eff}}} l_{\mathrm{i}} (k_{\mathrm{W}} N_{\mathrm{ph}})^2, \tag{1}$$

where μ_0 is the permeability of the vacuum, τ_{p} is the pole pitch, p is the number of pole pairs, δ_{eff} is the equivalent air gap, l_{i} is the effective length of the stator stack, k_{W} is the winding factor, N_{ph} is the number of phase winding turns in series. However, in order to take into account the mutual coupling in a m-phase machine the magnetizing inductance of single-phase machine is multiplied by $m/2$, which gives

$$L_{\mathrm{m}} = \frac{2m\mu_0}{\pi}\frac{\tau_{\mathrm{p}}}{p\pi\delta_{\mathrm{eff}}} l_{\mathrm{i}} (k_{\mathrm{W}} N_{\mathrm{ph}})^2, \tag{2}$$

It means that the magnetizing inductance of a 3-phase symmetrical winding system is $3/2$-times the magnetizing inductance developed in a corresponding single-phase winding system, due to the influence of the mutual magnetic coupling between phases. This phenomenon can be seen in Fig. 1 (b, c) in case of DW PMSM with number of slots per phase per pole $q = 1$. For the simplification purposes the values of the variables in Fig. 1 are in per units (i.e. 1 p.u. current linkage means that there is 1 p.u. current flows in the winding and there is one coil in the slot).

Fig. 1(d, e) shows the synchronous harmonic of a 12-slot 10-pole FSPMSM at single-phase supply and at three phase supply. This synchronous harmonic represents a magnetizing inductance of the electrical

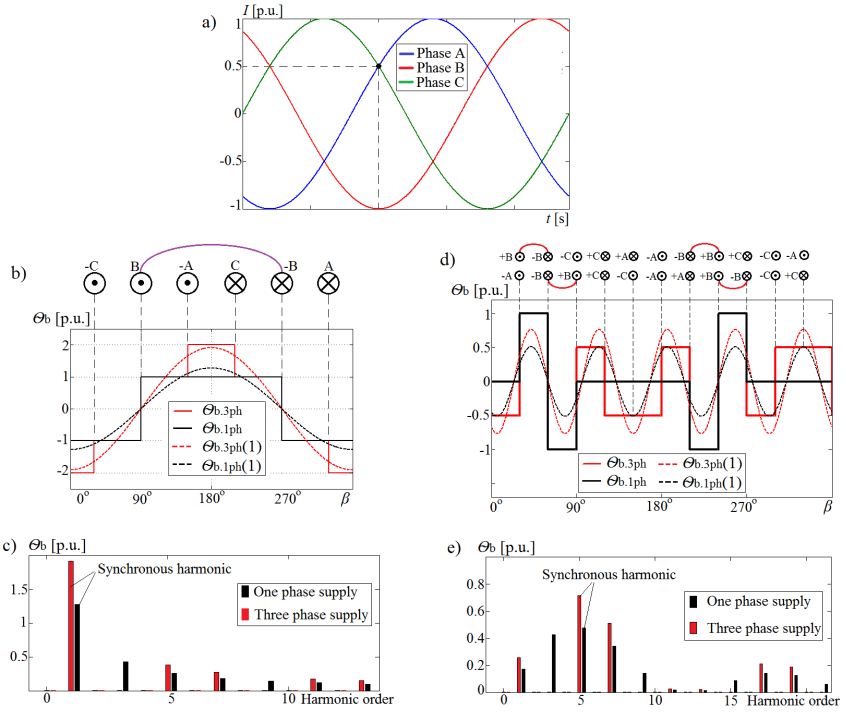

Fig. 1: Three phase supply with one conductor per slot and peak current $I_{\text{peak}} = 1$p.u. a) Three phase current b) Current linkage (θ) waveforms with fundamental harmonics at three- and single-phase supply, when currents in phases A and C are 0.5 p.u. and current in phase B is 1 p.u. in tooth coil winding ($q = 0.4$) c) Current linkage harmonic content at three- and single-phase supply (peak values) in tooth coil winding ($q = 0.4$) d) Current linkage waveform with fundamental harmonics at three- and single-phase supply, when currents in phases A and C are 0.5 p.u. and current in phase B is 1 p.u. in integral slot winding ($q = 1$) c) Current linkage harmonic content at three- and single-phase supply (peak values) in integral slot winding ($q = 1$).

machine. Comparing Figs. 1 (c) and 1 (e) it can be seen that the synchronous harmonic share in the total air gap inductance of the TCW PMSM is much less significant compared to the DW PMSM.

Similarly to DW PMSM, in a TCW PMSM all the current linkage harmonics increase by 50 % at three-phase supply compared to single-phase supply, except the third-order harmonics, which are cancelled. However, if the TCW PMSM does not have mutual inductance (e.g. 12-slot 10-pole PMSM), in the ideal case (without taking into account end winding leakage, slot leakage and tooth-tip leakage inductances), there is no difference between the phase inductance at single- or three-phase supply. Therefore, it is possible to analyze only a single phase or even just one stator slot in order to estimate the phase inductance for the three-phase supply, with the assumptions described above.

Fig. 2 shows the magnetic fluxes in a 12-slot 10-pole electrical machine with a smooth rotor (without permanent magnets), and with such a slot geometry, which minimizes the slot and tooth-tip leakage inductance, in order to have a minimum impact of the leakages on the total inductance. In this figure it is seen that the TCW PMSM might have different flux paths at single- and at three-phase supply. It can be even thought that there is some mutual inductance in the electrical machine at three-phase supply, because each phase have common magnetic flux with other phases. However, flux connection is only in the rotor side, and not in the stator side, which means that indeed a magnetic state of one phase does not depend on other phases, with negligible flux leakages and with constant steel permeability.

Based on the magnetic flux map illustrated in Fig. 2 it might be assumed that the stator of a 12-slot 10-pole FSPMSMs can be made of six segmented pieces totally isolated from each other as it is described and done in [13]. However, despite that the magnetic fluxes of each phase are totally insulated from each other, they have common flux linkage, due to the permanent magnets. The contours of the magnetic flux lines created by the permanent magnets differ from the magnetic flux contours created by the armature winding, which requires that the stator yoke has a continuous structure without any cuts. It means that if a cut in the stator side is made, the air gap flux density created by the permanent magnets is degraded by the permeance variations at different rotor positions. This would lead to high order back EMF harmonics, lower fundamental back EMF value, torque ripples, higher permanent magnet eddy current losses and

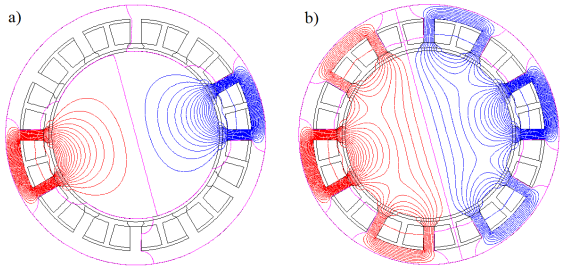

Fig. 2: Magnetic flux lines of an electrical machine with $q = 0.4$ (12-slot 10-pole machine) and the smooth laminated rotor (without permanent magnets) a) at single-phase supply b) at three-phase supply.

rotor yoke losses. Therefore, despite the apparent independence of each phase (segment) the magnetic insulation between them in the stator side is not recommended.

Alternative phase inductance evaluation by using only a slot geometry

In the previous section it was shown that if the PMSM does not have a mutual inductance, at symmetric three phase supply, the phase inductance remains the same as in singe-phase supply. Therefore, the FSPMSM can be virtually divided into several parts. Each part consists of one phase segment. For example, a 12-slot 10-pole electric machine can be divided into 6 separate identical segments, where each segment can be arranged in a way as it is illustrated in Fig. 3.

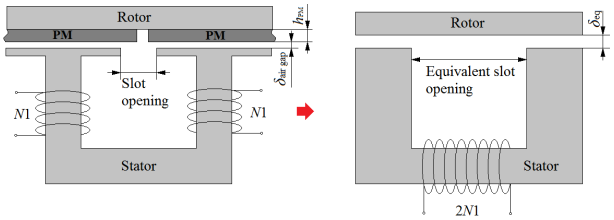

Fig. 3: Segment modification of 12-slot 10-pole FSPMSM to a simple magnetic circuit. Two windings around the stator teeth can be replaced by one winding with the same amount of turns.

In Fig. 3 it is seen that, if the steel permeability is assumed to be constant, a separate segment of the FSPMSM can be considered as a simple magnetic circuit with an equivalent air gap and equivalent slot opening. Equivalent air gap takes into account physical air gap, reluctance of permanent magnets, reluctance of stator and rotor iron. Whereas, equivalent slot opening can be estimated by [4]

$$b_{\mathrm{eq}} = k \cdot b_1, \tag{3}$$

$$k = \frac{2}{\pi}\left(\arctan\frac{b_1}{2\delta} - \frac{2\delta}{b_1}\ln\sqrt{1+\left(\frac{b_1}{2\delta}\right)^2}\right), \tag{4}$$

where b_1 is the physical slot opening, δ is the physical air gap. The inductance which is determined by the magnetic flux which crosses the air gap of the simple magnetic circuit, shown in Fig. 3, can be estimated by

$$L_\delta = \frac{{N_{\mathrm{ph}}}^2}{R_\delta}, \tag{5}$$

$$R_\delta = \frac{\delta}{\mu_{\mathrm{o}} A} = \frac{\delta_{\mathrm{eq}}}{\mu_{\mathrm{o}} l_{\mathrm{i}}\left(\frac{2r\pi}{Q_{\mathrm{s}}} - b_{\mathrm{eq}}\right)}, \tag{6}$$

where L_δ is the air-gap leakage inductance, R_δ is the air gap reluctance, r is the air gap radius, Q_s is the number of stator slots. By using (5) and (6) it is possible to easily estimate the inductance which is corresponding to the flux linkage in the air gap at particular phase current of the FSPMSM. The proposed approach can be a simple alternative for the phase inductance estimations of TCW PMSM.

The total synchronous inductance of TCW PMSM contains all the inductances. In the classical inductance evaluation method, the total air gap inductance includes the air-gap harmonic leakage inductance and the magnetizing inductance. Other inductance components such as slot leakage inductance, end winding inductance and tooth-tip leakage inductance can be estimated by the equations listed in [5]. These equations are repeated here for the sake of completeness

$$L_{\mathrm{u}} = \frac{4m}{Q_{\mathrm{s}}}\mu_0 N_{\mathrm{ph}}^2 l_{\mathrm{i}} \lambda_{\mathrm{u}}, \tag{7}$$

$$L_{\mathrm{tt}} = \frac{4m}{Q_{\mathrm{s}}}\mu_0 N_{\mathrm{ph}}^2 l_{\mathrm{i}} \lambda_{\mathrm{tt}}, \tag{8}$$

$$L_{\mathrm{e.w.}} = \frac{4m}{Q_{\mathrm{s}}}\mu_0 N_{\mathrm{ph}}^2 q l_{\mathrm{ew}} \lambda_{\mathrm{ew}}. \tag{9}$$

The proposed analytical approach of synchronous inductance estimation, which might be a good alternative to the classical one, is suitable for TCW PMSMs with negligible mutual inductance. However, in order to avoid large errors in the inductance estimation the saturation level of the steel should stay approximately the same in all load conditions, which is not always the case of TCW PMSMs [**?**].

TCW PMSM inductance evaluation by lumped model

Another alternative to the analytical inductance evaluation is the lumped parameter model, which takes into account the non-linear steel behaviour.

Similar methods for PMSMs performance estimation were used in several papers. Some of the examples can be found in [16, 12]. However, in this paper some limitations of a PMSM performance analysis by using the lumped model are investigated, particularly the torque ripple evaluation capability. The proposed in the paper model has minimum components number, in order to reduce the computational time, but which is still enough for the synchronous inductance and the some torque ripple low order harmonics evaluation.

The example of a TCW PMSM lumped model is shown in Fig. 4. It consists of an equivalent magnetic circuit with constant and variable reluctance components. Fig. 5 shows the locations of each reluctance in the magnetic circuit.

The lumped model illustrated in Fig. 4 contains radial branches at each tooth pitch, which represent stator tooth and implement stator winding current linkage and permanent magnet current linkage. The value of the stator winding current linkage at each tooth is described by sine function of time, while sinusoidal current waveform is assumed. The stator tooth current linkage of the phase A in the lumped model can be found as

$$\theta_{\mathrm{wA}} = \frac{N_{\mathrm{ph}}}{4} I_{\mathrm{phA}} \sqrt{2} \sin(wt), \tag{10}$$

where I_{ph} is the phase current. Permanent magnet current linkage in the same radial direction determines the flux in corresponding tooth, created by permanent magnet.

It is possible to implement any permanent magnet current linkage waveforms in the model during the rotation of the PMSM. However, it is usually advisable to design a PMSM which has sinusoidal no-load back EMF and consequently the current linkage of the permanent magnets during the rotation should induce the flux linkage in the stator teeth with sinusoidal shape. Therefore, the permanent magnet current linkage should be represented by sine function

$$\theta_{\mathrm{pmN}} = H_{\mathrm{c}} h_{\mathrm{pm}} \sin\left(wt + \alpha N - \frac{\pi}{2}\right), \tag{11}$$

where $H_{\mathrm{c}} h_{\mathrm{pm}}$ is the peak value of the permanent magnet current linkage and N is permanent magnet number. The first permanent magnet (which was selected in advance) does not have an angle shift.

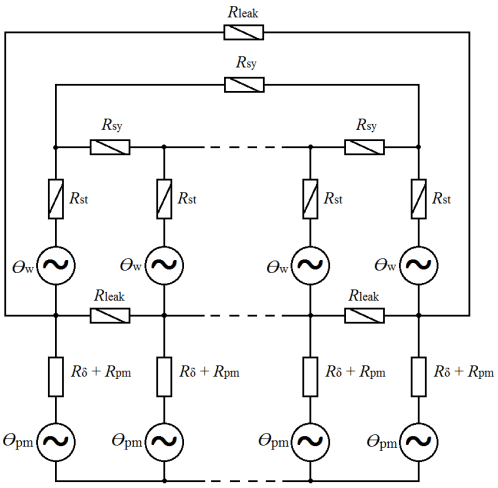

Fig. 4: Lumped model of a FSPMSM magnetic circuit (Rotor yoke is neglected). R_{leak} is the total slot leakage reluctance, R_{sy} is the stator yoke reluctance, R_{st} is the stator tooth reluctance, R_{pm} is the permanent magnet reluctance.

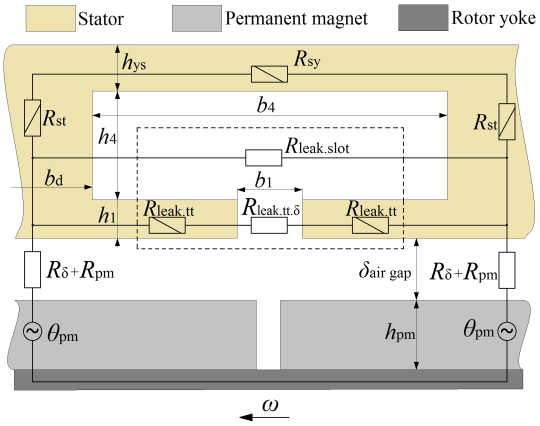

Fig. 5: Replacements of the electrical machine active parts by equivalent elements of the lumped model (Rotor yoke is neglected).

Therefore, it has permanent magnet number $N = 0$ and the last permanent magnet has permanent magnet number $N = Q_{\text{s}} - 1$. It should be noted that the real number of a permanent magnet can differ from the virtual number (where it is always equal to the stator slot number). However, at the armature side, the virtual rotor has the same behaviour as the real one. It is achieved by a proper selection of the shift angle α. The shift angle α shows the sine function shift between two neighboring virtual permanent magnet current linkages. The shift angle depends on the number of slots and poles, and can be calculated by

$$\alpha = p(\frac{2\pi}{p} - \frac{2\pi}{Q_{\text{s}}}), \tag{12}$$

In order to obtain the maximum torque per ampere control (MTPA) in PMSMs with surface permanent magnets, it is needed to have 90° angle shift (load angle) between the armature current linkage value along the stator tooth and the permanent magnet current linkage value along the same tooth as function of time. This is arranged by adding $\frac{\pi}{2}$ angle shift of the permanent magnet current linkage compared to the armature current linkage as it is seen in (11).

The model illustrated in Fig. 4 is dedicated for the analysis of surface PMSMs. However, it is possible to rearrange the model for evaluation of embedded PMSMs. In this case the constant permanent magnet

reluctance should be replaced by a variable reluctance. The geometry (flux path), for the evaluation of this reluctance, changes at different rotor positions, which also should be taken into account. However, the model for inner rotor PMSMs is out of the scope of this paper.

Experimental verification of the analytical methods of the inductance evaluation

The verification of the classical and proposed two alternative analytical methods is performed with an outer rotor ferrite TCW PMSM which is described in [11]. Additional model was created which has higher flux density in the stator teeth and stator yokes, in order to observe the influence of steel saturation on the inductance evaluation by different methods. Higher flux densities were achieved by thinner stator teeth and yokes. Magnetic flux density plots of the FSPMSMs are shown in Fig. 6. Hereafter, these two electrical machines are called FSPMSM1 (original) and FSPMSM2 (with thinner stator teeth and stator yokes).

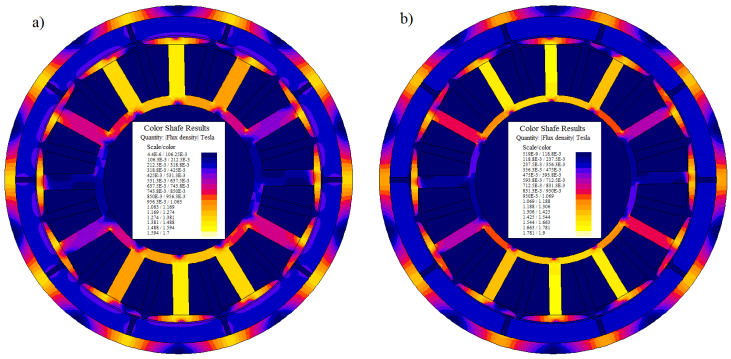

Fig. 6: Outer rotor FSPMSM a) FPSMS1 with 1.45 T peak flux density in the teeth b) FPSMS2 with 1.65 T peak flux density in the teeth.

The objective of the analysis is to observe the influence of the saturation on the distinction between the classical analytical method, the alternative analytical model, the lumped model and the FEM results. The main parameters of the electrical machines are introduced in Table I.

Table I: FSPMSMs parameters

Parameter	FSPMSM1	FSPMSM2
Number of winding turns per phase N_{ph}	184	184
Air gap length δ [mm]	0.8	0.8
Stack (physical) iron length l_{Fe} [mm]	120	120
Physical slot opening b_1 [mm]	3.2	3.2
Rotor outer diameter D_{re} [mm]	181.5	181.5
Stator outer diameter D_{se} [mm]	149.2	149.2
Stator yoke thickness h_{ys} [mm]	5.2	3.7
Stator tooth width w_{ys} [mm]	8.4	6.4
Permanent magnet height h_{PM} [mm]	10	10
Permanent magnet remanence B_r at the rated temperature (80 C)	0.34	0.34
Peak flux density in the tooth B_{peak} at rated temperature (80 C)	1.45	1.65
Stator core material	M400-50A	M400-50A

Table II shows the values of the synchronous inductance estimated by the above described analytical models and by the FEM analysis at a low load mode, at the nominal load and at double load. The total synchronous inductance contains all the inductance elements of the electrical machine.
Table II shows that the inductance estimation results found by the first and the second analytical model is very close to the FEA results and to the experimental results, at low load torque, because the electrical machines are not heavily saturated. However, if a PMSM is designed in such a way that the flux density in the stator tooth/yoke reaches high values (1.65 – 2 T), it might cause a significant error in the inductance

Table II: Inductance estimation

Method	L_S at low torque [mH]	
	FSPMSM1	FSPMSM2
Classical analytical method	13.71	12.97
Simplified analytical method	13.79	13.05
Lumped model	13.5	12.34
FEM	14.3	13.1
Experiments	13.7	–
	L_S at nominal torque [mH]	
Classical analytical method	13.71	12.97
Simplified analytical method	13.79	13.05
Lumped model	12.5	10.8
FEM	12.5	10.8
Experiments	12.9	–
	L_S at double nominal torque [mH]	
Classical analytical method	13.71	12.97
Simplified analytical method	13.79	13.05
Lumped model	10.5	8.5
FEM	10.5	8.5
Experiments	–	–

estimation by the analytical methods. Conversely, the lumped model, which takes the saturation into account, very precisely follows the results of FEA in terms of inductance evaluation.

From the obtained results shown in Table II, it is seen that if the application requires usage of the machine at different working points (e.g. traction motor), it is preferable to use the lumped model for the geometry optimization of the PMSM, because in this case it is possible to get adequate results of the synchronous inductance and, consequently, to analyze the electrical machine performance at any working point. Whereas, the classical analytical method can give overestimated performance if the TCW PMSM is highly saturated.

The lumped model can be used in order to preliminarily estimate the teeth and yokes flux densities of the electrical machine at any load condition. Therefore, it can help to tune the stator slot geometry at early design stages, or to use the model for a geometry optimization of the PMSM.

Comparison of FEA and lumped model stator flux linkages along d- and q-axes, and output power versus q-axis armature current (maximum torque per current control) are shown in Fig. 7 (a).

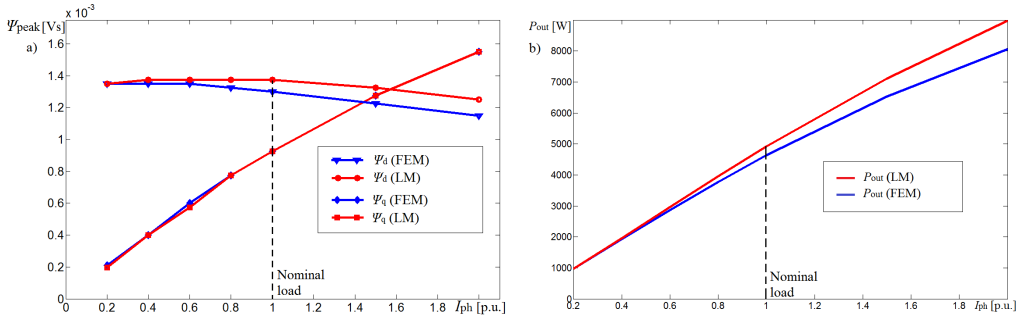

Fig. 7: a) d- and q-axes flux linkages versus armature current of FSPMSM1, b) electromagnetic power of FSPMSM1, by lumped model and FEA ($I_d = 0$).

Good agreement between the numerical model and the lumped model can be seen in Figs. 7. However, the lumped model overestimates the machine performance at high load conditions. This can be explained by the fact that the saturation of the tooth tip of the lumped model does not have any influence on the permanent magnet flux linkage. Whereas, in reality the saturation of the tooth tip increases the reluctance of the magnetic circuit which consequently leads to lower d-axis flux linkage (permanent magnet flux linkage). Due to this reason the output power is also overestimated, as it can be seen in Fig. 7 (b). It

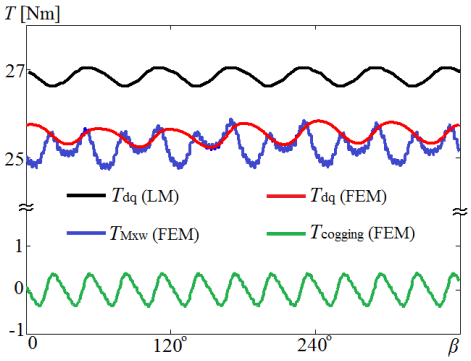

Fig. 8: Electromagnetic torque curves of FSPMSM1 during one electric rotation, estimated by FEM and by LM.

should be noted that the lumped model q-axis flux linkage almost totally coincides with the FEA results. Therefore, the lumped model can be a good tool for evaluation of the synchronous inductance at different working points.

According to [15], in the synchronous $d-q$ reference frame the electromagnetic torque is computed as

$$T = \frac{3}{2} p(\psi_{\mathrm{d}} i_{\mathrm{q}} - \psi_{\mathrm{q}} i_{\mathrm{d}}) + \frac{\partial W_{\mathrm{m}}}{\partial \theta_{\mathrm{m}}}. \tag{13}$$

where both terms together represent Maxwell's stress tensor, the first term alone represents the torque by the vector theory, and the second term alone represents the torque by the coenergy variation.

Fig. 8 shows the nominal torque of FSPMSM1 estimated by LM through the use of vector theory $T_{\mathrm{dq}}(\mathrm{LM})$, by FEM through the use of vector theory $T_{\mathrm{dq}}(\mathrm{FEM})$, by FEM through the use of Maxwell stress tensor $T_{\mathrm{Mxw}}(\mathrm{FEM})$, and no-load (cogging) torque estimated by FEM through the use of coenergy variation $T_{\mathrm{cogging}}(\mathrm{FEM})$.

In Fig. 8 it is seen that estimation of the torque by vector theory does not give the information about the cogging torque, which together with the torque estimated by vector theory gives the real torque value [15]. The torque estimated by LM has 5 % higher average value than was estimated by FEM. However, both of them has sixth harmonic component with the similar amplitude. According to [14] this torque harmonic component is due to the local saturation, which is caused by the interaction of the armature flux linkage harmonics and PM flux linkage synchronous harmonic. Therefore, the LM can be used for the adjustment of the PMSM geometry, in order to get the value of the sixth torque harmonic within tolerable magnitude.

Conclusion

In this paper several analytical approaches for the estimation of the synchronous inductance in TCW PMSMs have been described and compared. The analytical methods are verified with FEA and measurement results.

In TCW PMSMs, which are designed with high flux density in stator teeth and yoke, inductance value significantly depends on the load condition, which must be taken into account while machine analysis.

It was shown that using the classical approaches (with frozen steel permeability) might cause an unpractical error at the nominal load and at overload conditions in rotor surface magnet PMSMs with highly saturated stator teeth and yokes.

A simple alternative method to the classical analytical inductance evaluation was described. It has been proven that the synchronous inductance of TCW PMSMs with negligible mutual inductance, can be estimated by the presented method with the same accuracy as in the classical approach.

The lumped model (which takes the saturation effect into account) for the TCW PMSM was described. It was shown that it can be a fast and adequate tool for synchronous inductance evaluation of FSPMSMs. It also estimates the torque ripples caused by local saturation, which can be useful for the reduction or elimination of some harmonics in the electromagnetic torque.

References

[1] Sergeant, P. and Van den Bossche, A.: Influence of the amount of permanent magnet material in fractional-slot permanent magnet synchronous machines, Industrial Electronics, IEEE Transactions on pp. 1-8, 2013

[2] Sizov, G.Y. and Zhang, P. and Ionel, D.M. and Demerdash, N.A.O and Rosu, M.: Automated Multi-Objective Design Optimization of PM AC Machines Using Computationally Efficient- FEA and Differential Evolution, Industrial Electronics, IEEE Transactions on pp. 1-8, 2013

[3] Wang, A. and Jinbo Wang and Biao Wu and Chenglong Shi: Structural Optimization of the Permanent Magnet Drive Based on Artificial Neural Network and Particle Swarm Optimization, Intelligent Human-Machine Systems and Cybernetics (IHMSC), 2011 International Conference on Vol 2, pp. 70-74, 2011

[4] Juha Pyrhönen and Tapani Jokinen and Valéria Hrabovcová: Design of Rotating Electrical Machines, John Wiley Sons, 2008

[5] Hanne Jussila: Structural Optimization of the Permanent Magnet Concentrated Winding Multiphase Permanent Magnet Machine Design and Electromagnetic Properties – Case Axial Flux Machine, Dept.Elect.Eng., Lappeenranta University of Technology, Ph.D dissertation, 2009

[6] Ponomarev, P. and Lindh, P. and Pyrhonen, J.: Effect of Slot-and-Pole Combination on the Leakage Inductance and the Performance of Tooth-Coil Permanent-Magnet Synchronous Machines, Industrial Electronics, IEEE Transactions on Vol 60 pp. 4310-4317, 2013

[7] Montonen, J. and Lindh, P. and Pyrhonen, J.:Design process of traction motor having tooth coil windings, Electrical Machines (ICEM), 2012 XXth International Conference on pp. 1264-1268, 2012

[8] Alberti, L. and Barcaro, M. and Bianchi, N.: Design of a low torque ripple fractional-slot interior permanent magnet motor, Energy Conversion Congress and Exposition (ECCE), 2012 IEEE pp. 509-516, 2012

[9] EL-Refaie, A.M.: Fractional-Slot Concentrated-Windings Synchronous Permanent Magnet Machines: Opportunities and Challenges, Industrial Electronics, IEEE Transactions on Vol 57 pp. 107-121, 2010

[10] Dutta, R. and Rahman, M. F. and Chong, L.: Winding Inductances of an Interior Permanent Magnet (IPM) Machine With Fractional Slot Concentrated Winding, Magnetics, IEEE Transactions on Vol 48 pp. 4842-4849, 2012

[11] Petrov, I. and Pyrhonen, J.: Performance of Low-Cost Permanent Magnet Material in PM Synchronous Machines, Industrial Electronics, IEEE Transactions on Vol 60 pp. 2131-2138, 2013

[12] Bracikowski, N. and Hecquet, M. and Brochet, P. and Shirinskii, S.V.: Multiphysics Modeling of a Permanent Magnet Synchronous Machine by Using Lumped Models, Industrial Electronics, IEEE Transactions on Vol 59 pp. 2426-2437, 2012

[13] Dajaku, G. and Gerling, D.: A novel 12-teeth/10-poles PM machine with flux barriers in stator yoke, Electrical Machines (ICEM), 2012 XXth International Conference on pp. 36-40, 2012

[14] Ponomarev, P. and Petrov, I. and Pyrhonen, J.: Influence of Travelling Current Linkage Harmonics on Inductance Variation, Torque Ripple and Sensorless Capability of Tooth-Coil Permanent Magnet Synchronous Machines, Magnetics, IEEE Transactions on pp. 1-8, 2013

[15] Barcaro, M. and Bianchi, N. and Magnussen, F.: Remarks on Torque Estimation Accuracy in Fractional-Slot Permanent-Magnet Motors, Industrial Electronics, IEEE Transactions on Vol 59 pp. 2565-2572, 2012

[16] Tangudu, J.K. and Jahns, T.M. and EL-Refaie, A. and Zhu, Z.Q.: Lumped parameter magnetic circuit model for fractional-slot concentrated-winding interior permanent magnet machines, Energy Conversion Congress and Exposition, 2009. ECCE 2009. IEEE pp. 2423-2430, 2009

[17] EL-Refaie, A.M. and Jahns, T.M.: Optimal flux weakening in surface PM machines using fractional-slot concentrated windings, Industry Applications, IEEE Transactions on Vol 41 pp. 790-800, 2005

[18] Jussi Puranen: Induction Motor Versus Permanent Magnet Synchronous Motor in Motion Control Applications: a Comparative Study, Dept.Elect.Eng., Lappeenranta University of Technology, Ph.D dissertation, 2006

[19] Pavel Ponomarev: Tooth-Coil Permanent Magnet Synchronous Machine Design for Special Applications, Dept.Elect.Eng., Lappeenranta University of Technology, Ph.D dissertation, 2013

Publication IV

Petrov, I., Ponomarev, P., and Pyrhönen, J., "Torque Ripple Reduction in 12-slot 10-pole Fractional Slot Permanent Magnet Synchronous Motors with Non-Overlapping Windings by Implementation of Unequal Stator Teeth Widths," *in XIX International Conference on Electrical Machines (ICEM), 2014*, vol., no., pp.1−6, 2−5 Sept. 2014

Torque Ripple Reduction in 12-slot 10-pole Fractional Slot Permanent Magnet Synchronous Motors with Non-Overlapping Windings by Implementation of Unequal Stator Teeth Widths

Ilya Petrov, Pavel Ponomarev Juha Pyrhönen

***Abstract*—This paper describes an optimization of the stator geometry in a way that the torque ripple at particular load is reduced.**

The principle applied to the torque ripple reduction is based on the synchronous inductance variation suppression, caused by the non-linear steel saturation, which might be significant even in permanent magnet synchronous motors (PMSMs) with rotor surface permanent magnets.

The design optimization, described in this paper, aims in reducing the armature reaction influence on the local steel saturation in fractional slot permanent magnet synchronous machines (FSPMSM) by rearranging of the stator teeth widths.

The optimization was defined by means of magnetic equivalent circuit model (lumped model), and verified with finite element method (FEM).

***Index Terms*—Permanent magnet machines, FSPMSM, tooth-coil winding, fractional slot PMSM.**

I. Introduction

Electrical vehicles (EV) and hybrid electrical vehicles (HEV) more and more often appear in the market. Even working and utility vehicles start to take advantages of electrical and hybrid-electric drivetrain topologies. Essential part of these vehicles is using permanent magnet synchronous motors (PMSMs) in traction applications and in electricity generation. At the same time, FSPMSMs are considered and already used in numerous other applications [1].

Fractional slot permanent magnet synchronous machines with non-overlapping windings also known as tooth coil winding permanent magnet synchronous machines (TCW PMSM) have gained intensive attention during the latest decade. These types of electrical machines have found a wide range of applications, including traction motors, integrated devices, wind generators and industrial applications (fans, pumps). Some of the applications are very critical in terms of torque ripple.

Popularity of TCW PMSMs can be explained by their constructional advantages, which reduce the end winding length, facilitate cheaper and simpler assembling, and in some configurations increase the synchronous inductance for better field weakening [2]–[5]. Therefore, it is important to investigate the details of this type of electrical machines, in order to improve their performance even further. In this article a 12-slot 10-pole TCW PMSM is analyzed. It has only one sub-harmonic, relatively high winding factor and balanced magnetic pull.

Despite the fact that with particular slot/pole combination TCW PMSMs might have significantly lower torque ripple and cogging torque compared to distributed rotating-field slot winding permanent magnet synchronous machines (DW PMSM) with integer number of slot per pole per phase [6], intensive research is continued in order to further reduce the torque ripple, because it allows using the electrical machines in applications, which require extremely low torque ripples relative to the nominal torque, e.g. direct-driven permanent magnet wind generators [7].

Some techniques for the torque ripple reduction in TCW PMSMs can be found in [8]–[13]. In [8]–[10] the torque ripple reduction, together with the rotor iron losses minimization, were carried out by using more complex armature winding with multiple-layer stator structure. However, this technique leads to a smaller winding factor of the synchronous harmonic, as well as to more complicated end winding connections, which is undesirable, especially in high power electrical machines, where it is difficult to implement bending and connections of the coils with a relatively large diameter.

In [8] and [11] the torque ripple reduction is presented for interior-permanent magnet synchronous machines, by adjusting flux barriers in the rotor. However, there is no division between the reduction of the 6^{th} and 12^{th} order torque ripple harmonics during the optimization, but just the difference between the minimum torque and the maximum torque is considered. Also it can be observed that even after the rotor optimization in [11], essential torque ripples appeared in the working conditions close to the nominal load and in the field weakening area.

In [12] it was concluded that a significant part of torque ripples in TCW PMSMs is caused by local over-saturation, due to the presence of non synchronous harmonics, which with some periodicity interact with the synchronous harmonic and create these local over saturations in the rotor with embedded magnets. It was suggested to adjust the control algorithm in order to suppress these torque ripples. However, the proposed method might be difficult and not cost efficient in practice, because it requires an extensive analysis of the synchronous inductance variation of each particular electrical machine.

A torque ripple reduction of 12-slot 10-pole TCW PMSM was achieved by permanent magnet shape adjustment in [13]. Instead of a permanent magnet, which creates a rectangular flux density waveform in the air gap, a permanent magnet

978-1-4799-4389-0/14/$31.00 ©2014 IEEE

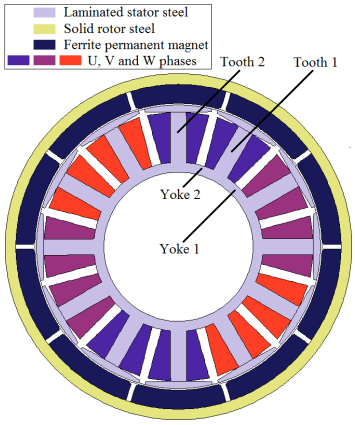

Fig. 1. Geometry layout of TCW PMSM with outer rotor.

shape with a sinusoidal flux density waveform with 3^{rd} order harmonic was suggested, in order to eliminate some torque ripple harmonics. However, this technique might also increase the total price of the permanent magnets, due to more complex manufacturing process. Also the total flux linkage is decreased by using the magnets with the proposed shapes compared to the rectangular shape, which leads to smaller back EMF.

This paper describes the reduction of the 6^{th} torque ripple order harmonic in a 12-slot 10-pole PMSM with rotor surface permanent magnets. It is the lowest possible order torque ripple harmonic presented in the electrical machine. It should be noted that the low order torque ripple harmonics are more harmful compared to higher order harmonics, because the low order torque ripple harmonics with higher probability cause undesirable vibrations in the system compared to other torque ripple harmonics [14].

The torque ripple reduction is implemented by adjusting the stator geometry, which should not lead neither to additional costs nor performance deterioration. The stator geometry optimization is carried out by a lumped model and it is verified by FEM. The commercial FEM software package was applied in the calculations.

Section II explains the reasons of the 6^{th} order torque ripple harmonic in TCW PMSMs with rotor surface permanent magnets and introduces the lumped model. Section III describes the stator geometry optimization, which reduces the torque ripple. It shows the optimization results which are achieved using the lumped model and verifies them by FEM.

II. Simulation of TCW PMSMs by Lumped Model and Comparison of Results with FEM

The lumped model which takes the saturation into account was created and verified by FEM and by measurement results. The detailed description of the model can be found in [15], where it was shown, that the lumped model can precisely follow the performance results of the TCW PMSM found by FEM as well as synchronous inductance evaluation at different load conditions. Moreover, the lumped model can be also used for evaluation of the flux density as a function of time at different steel parts of the electrical machine. This flux density knowledge can be used in order to optimize the stator teeth geometry to get the needed performance of the electrical machine. For the sake of completeness, the described in [15] TCW PMSM lumped model is shown in Fig. 2.

The lumped model presented in Fig. 2 contains radial branches at each tooth pitch, which represent stator tooth and implement stator winding current linkage and permanent magnet current linkage. The value of the stator winding current linkage at each tooth is described by sine function of time, while sinusoidal current waveform is assumed.

TABLE I
FSPMSMs parameters

Parameter	FSPMSM1
Nominal torque T_{nom} [Nm]	25.6
Nominal speed n_{nom} [rpm]	1750
Number of winding turns per phase N_{ph}	184
Air gap length δ [mm]	0.8
Stack (physical) iron length l_{Fe} [mm]	120
Physical slot opening b_1 [mm]	3.2
Rotor outer diameter D_{re} [mm]	181.5
Stator outer diameter D_{se} [mm]	149.2
Stator yoke thickness h_{ys} [mm]	5.2
Stator tooth width w_{ys} [mm]	8.4
Permanent magnet height h_{PM} [mm]	10
Permanent magnet remanence B_{r} at the rated temperature (at 80 C)	0.34
Peak flux density in the tooth B_{peak} at rated temperature (at 80 C)	1.45
Stator core material	M400-50A

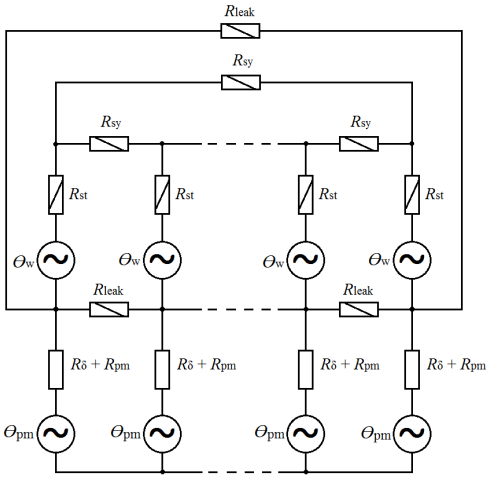

Fig. 2. Lumped model of a FSPMSM magnetic circuit (Rotor yoke is neglected). R_{leak} is the total slot leakage reluctance, R_{sy} is the stator yoke reluctance, R_{st} is the stator tooth reluctance, R_δ is the air gap reluctance, R_{pm} is the permanent magnet reluctance, θ_{PM} is the permanent magnet current linkage, θ_{w} is the stator winding current linkage.

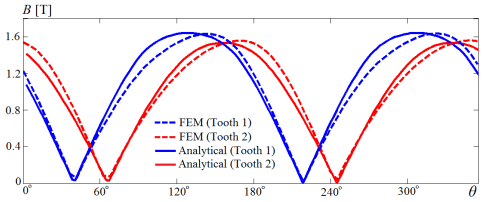

Fig. 3. Flux density (absolute value) in the stator teeth at nominal load as a function of rotor position in electric degrees (θ), estimated by FEM and by the lumped model ($I_{\mathrm{d}} = 0$ control is implemented).

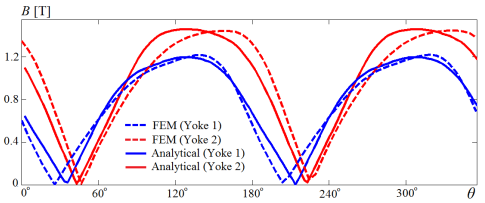

Fig. 4. Flux density (absolute value) in the stator yoke at nominal load as a function of rotor position in electric degrees (θ), estimated by FEM and by the lumped model ($I_{\mathrm{d}} = 0$ control is implemented).

The electrical machine analyzed and optimized in this paper is an outer rotor TCW PMSM with ferrite magnets. The machine is described in [16] and shown in Fig. 1. The main parameters of this electrical machine at operating conditions are shown in Table I. The same optimization can be applied to all kinds of TCW PMSMs: rotor inner permanent magnets (IPM) and rotor surface permanent magnets (SPM) , inner and outer rotor, radial and axial flux type machines. However, the investigation of PMSM with IPM is out of the scope of this article as well as TCW PMSM with different slot and pole combination.

As it can be seen in Fig. 1 and in Table I, the permanent magnets have a relatively wide thickness, which leads to a large equivalent air gap. Therefore, the armature current should not have an essential influence on the rotor steel magnetic state. However, as it is noted in [17], [15], the tooth-tip leakage inductance, the slot leakage inductance and the air-gap leakage inductance have significant contributions to the total synchronous inductance of the TCW PMSM. Therefore, it can be concluded that in PMSMs with rotor surface permanent magnets, the performance deterioration is mainly caused by the steel local over saturations in the stator side, but not in the rotor.

In order to estimate the armature reaction influence on the stator saturation level and optimize the stator geometry in such a way, that there is no significant performance deterioration at different load conditions, it is needed to have a fast model which takes the saturation effect into account. Despite the fact that FEM gives relatively precise parameters evaluation of an electrical machine, it is still computationally heavy. This means that it is not advisable to use FEM for optimization of an electrical machine at early design stages, which is very time consuming. Therefore, it was decided to create a simple analytical model, which takes the steel saturation into account (lumped model). The analytical model was verified by FEM, concerning the average output torque, with good agreement in [15]. However, a deeper analysis and verification of the model is given in this paper.

Flux densities in the stator teeth and in the stator yoke at the nominal load as functions of the rotor position can be seen in Figs. 3 and 4. These figures show that the flux densities estimated by FEM are in fairly good correlation with the flux densities evaluated by the lumped model. Also, Figs. 3 and 4 show that the two adjacent stator teeth and

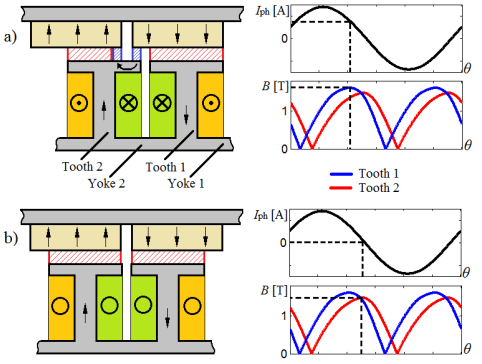

Fig. 5. Armature reaction influence on the difference between the peak flux densities in two adjacent stator teeth. a) Permanent magnet current linkage is maximum in Tooth 1 which is also boosted by the armature current, b) Permanent magnet current linkage is maximum in Tooth 2 and equals to current linkage of Tooth 1, but the armature current is zero ($I_{\mathrm{d}} = 0$ control is implemented).

the stator yokes can have different peak flux densities, due to the interactions of the armature reaction with the permanent magnet flux linkage. This means that these two adjacent teeth have different reluctance peaks, due to the saturation effect, which is even more apparent at higher loadings. This leads to the appearance of the synchronous inductance pulsating harmonics. These synchronous inductance harmonics are the main cause of the 6^{th} order torque ripple harmonic.

The effect which causes the different flux density peaks in the stator teeth is described by Fig. 5. In Fig. 5 (a) it can be seen that when Tooth 1 has the maximum value of the permanent magnet flux linkage (no inter-pole flux leakage and curvature effect are assumed), the phase current is still conducting in the slot, which increases the maximum flux density in Tooth 1. However, according to Fig. 5 (b), when Tooth 2 has the maximum value of the permanent magnet flux linkage, the phase current (current in the slot) is zero, which leads to the fact that the peak flux density in Tooth 1 is always higher than in Tooth 2.

III. Optimization of the Stator Geometry for the Torque Ripple Reduction

As it is mentioned above, the different flux density peaks in the stator teeth cause additional high order harmonic in the synchronous inductance as a function of rotor position at the nominal load. This can be eliminated by tuning the stator teeth widths. However, the current density in the stator slot should be kept the same, which means that the stator slot area should not be changed. Therefore, if one stator tooth is redesigned to be wider, the adjacent stator tooth should be narrower in the same extent, as it is illustrated in Fig. 6. With this approach the total slot area can be kept constant.

It should be noted that this approach, with unequal tooth widths, is not the same as was implemented in the single-layer TCW PMSM reported in [18]. There are several principal differences. Firstly, in single-layer 12-slot 10-pole TCW PMSM, only half the coil flux in wound teeth passes through adjacent teeth [18], because the single-layer and double-layer TCW PMSMs have different stator current linkage distribution waveforms. Secondly, together with the tooth width change, the tooth tip width is also modified, whereas in the proposed design the tooth tip width is kept constant in both adjacent teeth and only the teeth widths are optimized.

Fig. 7 shows the torque curves and their harmonic components at the nominal load of the original motor (Table I) and of the new motor, which was redesigned in such a way that the 6^{th} order harmonic is eliminated in the synchronous inductance, which is achieved at $w_1/w_2 = 1.15$, where w_1 is the width of the first tooth (Tooth 1) and w_2 is the width of the second tooth (Tooth 2). It can be seen that the 6^{th} order torque ripple harmonic is almost completely eliminated in the new design with unequal stator teeth widths at the nominal load. However, suppressing the torque ripple harmonic at the nominal load by stator teeth width adjustment, causes an appearance of torque ripple harmonic (cogging torque) with the same order at no-load.

Fig. 8 shows the torque curves and their harmonic components at no-load of the original motor and of the redesigned motor ($w_1/w_2 = 1.15$). In Fig. 8 it can be seen that at no-load the electrical machine with unequal teeth has the 6^{th} order torque ripple harmonic, whereas the cogging torque of the original torque includes only the 12^{th} order torque ripple harmonic. Therefore, it is not advisable to redesign the electrical machine if the application requires working mostly in low load conditions. However, it should be noted that if the electrical machine is designed in such a way that at no-load the BH-curve of the steel is in linear region (before the considerable saturation takes place), the unequal teeth widths will not bring the 6^{th} cogging torque harmonic at the no-load, but still can eliminate the 6^{th} torque ripple harmonic at the nominal load, if at this load condition the armature reaction increases the flux density in the stator teeth above the linear region.

The lumped model which is mentioned above can be used in order to estimate an approximate widths ratio of two adjacent stator teeth, which give the lowest 6^{th} order torque ripple harmonic at some particular load condition. Fig. 9 shows

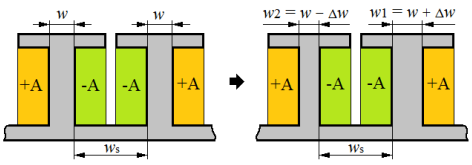

Fig. 6. Adjustment of the stator teeth widths. The stator slot width is kept constant.

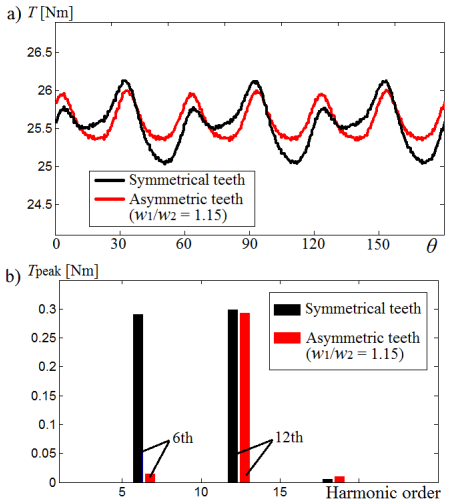

Fig. 7. Torque of the original and of the redesigned TCW PMSM at nominal load ($w_1/w_2 = 1.15$) evaluated by FEM a) Torque as function of rotor position, b) Torque harmonics.

the amplitude of the 6^{th} harmonic of the torque ripple at different load conditions as a function of the widths ratio of two adjacent stator teeth.

In Fig. 9 it can be seen that according to the lumped model results, at the nominal load, the lowest 6^{th} harmonic order component of the torque ripple is at $w_1/w_2 = 1.15$. However, for lower loads (between 25%–75% of the nominal load) the widths ratio of the adjacent stator teeth should be lower, in order to get the minimum 6^{th} harmonic of the torque ripple. Therefore, it can be concluded that the stator teeth widths ratio (w_1/w_2) should be selected according to the application specification.

It should be noted that according to [19], in the synchronous d–q reference frame the electromagnetic torque T is computed as

$$T = \frac{3}{2}p(\psi_{\text{d}} i_{\text{q}} - \psi_{\text{q}} i_{\text{d}}) + \frac{\partial W^*_{\text{m}}}{\partial \theta_{\text{m}}}, \tag{1}$$

, where p is the number of pole pairs, Ψ_{d} is d-axis flux linkage, Ψ_{q} is q-axis flux linkage, i_{d} is d-axis current, i_{q} is q-axis current, $\partial W^*_{\text{m}}/\partial\theta_{\text{m}}$ is the magnetic coenergy variation. Both terms together represent Maxwell's stress tensor, whereas the

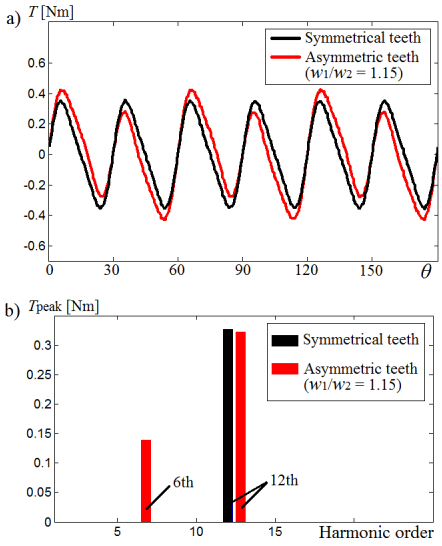

Fig. 8. Torque of the original and of the redesigned TCW PMSM at no-load ($w_1/w_2 = 1.15$) evaluated by FEM a) Torque as function of rotor position, b) Torque high order harmonics.

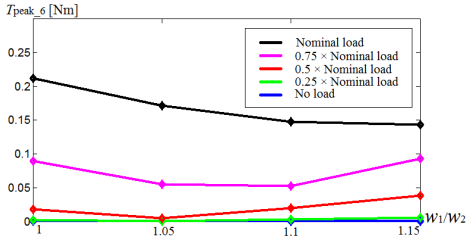

Fig. 9. Amplitude of the 6^{th} torque ripple harmonic at different load conditions as function of the widths ratio of two adjacent stator teeth, evaluated by the lumped model.

first term alone represents the torque by the vector theory, and the second term alone represents the torque by the coenergy variation. Due to the fact that the lumped model estimates the torque based on the vector theory, it can be concluded that it does not show the cogging torque of the electrical machine, which has a different behaviour with the variation of the stator teeth widths ratios, as it is illustrated in Fig. 8. Therefore, the torque ripples at no-load and at 25% of the nominal load cannot be captured by the lumped model (Fig. 9). Also, even at higher loads, the cogging torque can significantly contribute to the total torque ripple. Thus, the results of the lumped model were verified by FEM, which includes the cogging torque in the computation – the last part in (1). Fig. 10 shows the amplitudes of the 6^{th} and the 12^{th} torque ripple harmonics estimated by FEM at different load conditions as a function of the stator teeth width ratios.

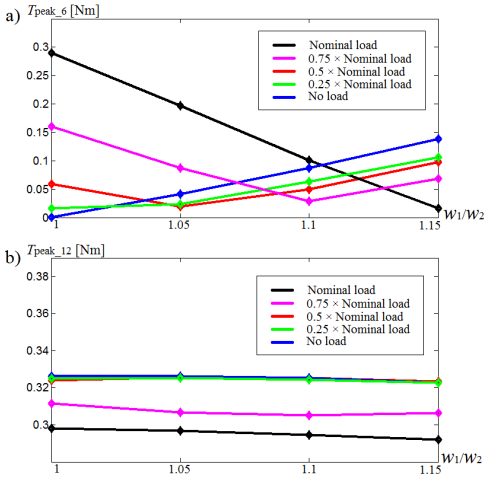

Fig. 10. Amplitude of a) the 6^{th} torque ripple harmonic and b) the 12^{th} torque ripple harmonic at different load conditions as function of the widths ratio of two adjacent stator teeth, evaluated by FEM.

It can be noticed in Fig. 10 (b), that the stator teeth widths do not vary significantly the 12^{th} order harmonic of the torque ripple. However, Fig. 10 (a) shows that the 6^{th} order harmonic of the torque ripple can be adjusted for each load condition to have the minimum value. For example, the electrical machine at the nominal load has the lowest 6^{th} order harmonic of the torque ripple at the widths ratio $w_1/w_2 = 1.15$, and the highest torque ripple at widths ratio $w_1/w_2 = 1$, whereas at no-load the situation is vice versa.

Despite the fact that the absolute values of the FEM results (Fig. 10) and the lumped model results (Fig. 9) do not coincide well with each other, these results give similar optimum widths ratios of the stator teeth for a particular load.

The described optimization method for the torque ripple reduction should be implemented only for special applications, which require rotation mainly in one direction. If the redesigned TCW PMSM rotates in reverse direction, the torque ripple increases, as it is shown in Fig. 11. Comparing Fig. 11 with Fig. 7 it can be seen that the 6^{th} torque ripple order harmonic of the redesigned PMSM is higher compared to the original design, if the redesigned PMSM rotates in reverse direction, whereas the 12^{th} order harmonics are almost the same. It should be noted that, if the redesigned TCW PMSM rotates in reverse direction in a generator mode, the torque ripple is again smaller compared to the original design.

IV. Conclusion

The reason for the appearance of the 6^{th} order torque ripple harmonic in 12-slot 10-pole TCW PMSMs with rotor surface permanent magnets is described in the paper. In order to reduce this ripple, the stator geometry optimization was done by using the lumped model. It was verified by FEM that the lumped model can be used for the evaluation of the optimum ratio of

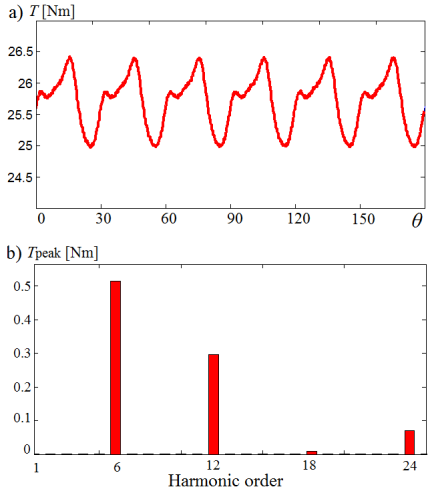

Fig. 11. Torque of the redesigned TCW PMSM at the nominal load ($w_1/w_2 = 1.15$) evaluated by FEM in reverse direction a) Torque as function of rotor position, b) Torque harmonics.

the stator teeth widths. Therefore, the lumped model is suitable for the estimation of the standard design parameters of the TCW PMSM as well as for the evaluation of the optimum widths ratio of the stator teeth for reduction of the 6^{th} order harmonic of the torque ripple.

The limitation of the lumped model is described and discussed. The lumped model is not suitable for observing the cogging torque in this case. However, it was shown that even with this drawback it is still a suitable tool for the electrical machine optimization routine.

REFERENCES

[1] A. EL-Refaie, "Fractional-slot concentrated-windings synchronous permanent magnet machines: Opportunities and challenges," *Industrial Electronics, IEEE Transactions on*, vol. 57, no. 1, pp. 107–121, 2010.

[2] H. Jussila, "Concentrated winding multiphase permanent magnet machine design and electromagnetic properties – case axial flux machine," Ph.D dissertation, Dept.Elect.Eng., Lappeenranta University of Technology, 2009.

[3] R. Dutta, M. F. Rahman, and L. Chong, "Winding inductances of an interior permanent magnet (ipm) machine with fractional slot concentrated winding," *Magnetics, IEEE Transactions on*, vol. 48, no. 12, pp. 4842–4849, 2012.

[4] T. D. Strous, H. Polinder, and J. Ferreira, "Inductance calculations for pm machines with concentrated windings," in *Electric Machines Drives Conference (IEMDC), 2011 IEEE International*, 2011, pp. 447–452.

[5] J. Montonen, P. Lindh, and J. Pyrhonen, "Design process of traction motor having tooth coil windings," in *Electrical Machines (ICEM), 2012 XXth International Conference on*, 2012, pp. 1264–1268.

[6] J. Islam, D. Svechkarenko, R. Chin, A. Szucs, J. Mantere, and R. Sakki, "Cogging torque and vibration analysis of a direct-driven pm wind generator with concentrated and distributed windings," in *Electrical Machines and Systems (ICEMS), 2012 15th International Conference on*, Oct 2012, pp. 1–6.

[7] V. Ruuskanen, "Design aspects of megawatt–range direct–driven permanent magnet wind generators," Ph.D dissertation, Dept.Elect.Eng., Lappeenranta University of Technology, 2011.

[8] L. Alberti, M. Barcaro, and N. Bianchi, "Design of a low torque ripple fractional-slot interior permanent magnet motor," in *Energy Conversion Congress and Exposition (ECCE), 2012 IEEE*, 2012, pp. 509–516.

[9] L. Alberti and N. Bianchi, "Theory and design of fractional-slot multilayer windings," *Industry Applications, IEEE Transactions on*, vol. 49, no. 2, pp. 841–849, 2013.

[10] M. Cistelecan, F. Ferreira, and M. Popescu, "Three phase tooth-concentrated multiple-layer fractional windings with low space harmonic content," in *Energy Conversion Congress and Exposition (ECCE), 2010 IEEE*, 2010, pp. 1399–1405.

[11] M. Barcaro and N. Bianchi, "Torque ripple reduction in fractional-slot interior pm machines optimizing the flux-barrier geometries," in *Electrical Machines (ICEM), 2012 XXth International Conference on*, 2012, pp. 1496–1502.

[12] P. Ponomarev, I. Petrov, and J. Pyrhonen, "Influence of travelling current linkage harmonics on inductance variation, torque ripple and sensorless capability of tooth-coil permanent magnet synchronous machines," pp. 1–1, 2013.

[13] K. Wang, Z. Zhu, and G. Ombach, "Torque enhancement of surface-mounted permanent magnet machine using 3rd order harmonic," pp. 1–1, 2013.

[14] J. Sopanen, V. Ruuskanen, J. Nerg, and J. Pyrhonen, "Dynamic torque analysis of a wind turbine drive train including a direct-driven permanent-magnet generator," *Industrial Electronics, IEEE Transactions on*, vol. 58, no. 9, pp. 3859–3867, 2011.

[15] I. Petrov, P. Ponomarev, S. Shirinskii, and J. Pyrhönen, "Inductance evaluation of fractional slot permanent magnet synchronous motors with non-overlapping winding by analytical approaches," in *Power Electronics and Applications (EPE), 2014 XVIth International Conference on*, 2014, pp. 1–8.

[16] I. Petrov and J. Pyrhonen, "Performance of low-cost permanent magnet material in pm synchronous machines," *Industrial Electronics, IEEE Transactions on*, vol. 60, no. 6, pp. 2131–2138, 2013.

[17] P. Ponomarev, J. Alexandrova, I. Petrov, P. Lindh, E. Lomonova, and J. Pyrhonen, "Inductance calculation of tooth-coil permanent-magnet synchronous machines," pp. 1–1, 2014.

[18] D. Ishak, Z. Zhu, and D. Howe, "Permanent-magnet brushless machines with unequal tooth widths and similar slot and pole numbers," *Industry Applications, IEEE Transactions on*, vol. 41, no. 2, pp. 584–590, 2005.

[19] M. Barcaro, N. Bianchi, and F. Magnussen, "Remarks on torque estimation accuracy in fractional-slot permanent-magnet motors," *Industrial Electronics, IEEE Transactions on*, vol. 59, no. 6, pp. 2565–2572, 2012.

Ilya Petrov received the M.Sc. degree from Lappeenranta University of Technology (LUT), Finland, in 2011. He is currently a Ph.D. student at the Laboratory of Electrical Drives Technology at LUT. His main research interest is in the design and optimization of PMSMs.

Pavel Ponomarev (M'05) born in 1985 in Arkhangelsk, Russia, received the D.Sc. degree in 2013 from Lappeenranta University of Technology (LUT), Finland. He worked as a software engineer at Automation Department of Central Research Institute of Ship's Electrical Technology, Saint-Petersburg, Russia. He is currently a post-doctoral researcher at the Laboratory of Electrical Drives Technology, LUT Energy. His current interests include electrical drives and permanent magnet machines.

Juha Pyrhnen (M'06) born in 1957 in Kuusankoski, Finland, received the Doctor of Science (D.Sc.) degree from Lappeenranta University of Technology (LUT), Finland in 1991. He became a Professor of Electrical Machines and Drives in 1997. He is currently the Head of the Department of Electrical Engineering at the Institute of Energy Technology (LUT Energy). He is engaged in the research and development of electric motors and electric drives.

Publication V

Petrov, I., Ponomarev, P., Alexandrova, Y., and Pyrhönen, J., "Unequal Teeth Widths for Torque Ripple Reduction in Permanent Magnet Synchronous Machines With Fractional-Slot Non-Overlapping Windings," *IEEE Transactions on Magnetics* , 2014

Unequal Teeth Widths for Torque Ripple Reduction in Permanent Magnet Synchronous Machines With Fractional-Slot Non-Overlapping Windings

Ilya Petrov, Pavel Ponomarev, Yulia Alexandrova, and Juha Pyrhönen

Department of Energy Technology, Lappeenranta University of Technology, Lappeenranta 53850, Finland

Permanent magnet synchronous machines (PMSMs) with fractional-slot non-overlapping windings, also known as tooth-coil winding PMSMs (TCW PMSM), have been under intensive research during the latest decade. There are many optimization routines explained and implemented in the literature to improve the characteristics of this machine type. This paper introduces a new technique for torque ripple minimization in TCW PMSM. The source of torque harmonics is also described. The low-order torque harmonics can be harmful for a variety of applications, such as direct drive wind generators, direct drive light vehicle electrical motors, and for some high-precision servo applications. The reduction of the torque ripple harmonics with the lowest orders (6th and 12th) is realized by machine geometry optimization technique using finite element analysis. The presented optimization technique includes the stator geometry adjustment in TCW PMSMs with rotor surface permanent magnets and with rotor embedded permanent magnets. Influence of the permanent magnet skewing on the torque ripple reduction and cogging torque elimination was also investigated. It was implemented separately and together with the stator optimization technique. As a result, the reduction of some torque ripple harmonics was attained.

Index Terms— **Fractional slot permanent magnet synchronous machine (PMSM), permanent magnet machines, TCW PMSM, tooth-coil winding (TCW), torque ripple.**

I. Introduction

MORE AND MORE applications start using tooth-coil winding permanent magnet synchronous machines (TCW PMSMs) instead of conventional distributed rotating-field slot winding PMSMs (DW PMSMs), due to their advantages that are described in detail in [1]–[9].

Due to an extensive research and investigation of TCW PMSMs, numerous advices and hints are presented in the literature regarding the design procedures for this type of electrical machines.

In [10], efficiency observation was done for TCW PMSMs with different slot/pole combinations by varying steel grades and permanent magnet thicknesses. It was shown that if a PMSM has a high electrical frequency, the steel grade has more significant influence on the electrical machine efficiency than the permanent magnet thickness. In addition, a procedure for analytical evaluation of the optimal permanent magnet thickness has been presented.

In [11], design optimizations of TCW PMSMs and DW PMSMs was done using computationally efficient finite element analysis (FEA) and differential evolution. It was shown that it is possible to reach relatively low-torque ripple with TCW PMSMs compared with DW PMSMs, which is especially important with low speed and high-torque applications (e.g., direct drive wind turbines).

In [12], detailed guidelines are given for the design of electric machines. However, some corrections are needed (e.g., for synchronous inductance evaluation) if the given recommendations are implemented for design of TCW PMSMs [9].

In [13] and [14], analytical approaches of the inductance evaluation were suggested for TCW PMSMs. It was shown that, in TCW PMSMs with rotor surface permanent magnets [14], as well as with rotor embedded permanent magnets [13], besides the air-gap leakage inductance, the slot leakage inductance, and the tooth-tip leakage inductance also have a significant contribution to the total synchronous inductance. This can cause a difficulty for TCW PMSM designers, which try to reduce the armature reaction. In these papers, recommendations for the selection of slot/pole number and stator geometry are given to reach the desirable synchronous inductance.

In [15], the performance of a TCW PMSM with different number of phase winding turns is compared. It was shown that the optimal solution design for a traction application can vary according to the desirable vehicle characteristics (maximum torque, constant power speed range, etc.).

With optimized designs, TCW PMSMs can achieve relatively low-torque ripple and cogging torque. However, to reduce acoustic noise and mechanical vibrations, which are an especial concern in some applications, development of new PMSM design optimizations (with reduced torque ripple) is still continuing. This can increase the range of possible applications for TCW PMSMs.

In [16], the torque ripple reduction was attained by increasing the number of winding layers in a stator slot of a TCW PMSM, and by the optimization of the rotor geometry with embedded magnets, or, more specifically, by selecting the barriers angles in the rotor, which gives the lowest torque ripple.

In [17], it was shown that it is possible to reduce the torque ripple in TCW PMSMs with rotor surface permanent magnets

Manuscript received April 24, 2014; revised June 20, 2014; accepted August 24, 2014. Date of publication September 5, 2014; date of current version March 20, 2015. Corresponding author: I. Petrov (e-mail: ilya.petrov@lut.fi).

Color versions of one or more of the figures in this paper are available online at http://ieeexplore.ieee.org.

Digital Object Identifier 10.1109/TMAG.2014.2355178

by elimination of some harmful permanent magnet flux density harmonics in the air gap, whereas other order flux density harmonics (e.g., 3^d) can be kept in the air gap, providing an increase of the total flux without torque quality degradation. A particular air-gap flux density waveform was achieved by adjusting the permanent magnet shape.

In [18], torque ripple minimization was achieved by a proper skewing. It was proven that it is not advisable to fully eliminate the torque ripple by skewing, because in this case the skewing pitch (angle) should be very large, which is not practical regarding to the average torque. In [18], the cogging torque and electromagnetic torque ripple harmonic components of the analyzed machine (DW PMSM) have the same harmonic order (i.e., 6th). Therefore, by eliminating the cogging torque, the torque ripple was also reduced. However, in TCW PMSMs the cogging torque can be of higher order compared with the electromagnetic torque ripple. For example, in 12-slot 10-pole PMSMs the main component of the cogging torque is 12th-order harmonic, whereas the largest torque ripple component is 6th-order harmonic. Therefore, as it is shown hereafter, it can be problematic to eliminate or even reduce 6th-torque ripple harmonic at the nominal load by implementing only skewing approach in TCW PMSMs.

In [19], behavior of d- and q-axes inductances of a TCW PMSM with embedded magnets has been studied. It was shown that the inductance variation at different rotor positions has a direct influence on the torque ripple. To eliminate the torque ripple, it was suggested to include this inductance variation in the machine control algorithm, whereas the technique, described in this paper, reduces the inductance variation in a PMSM at the nominal load by a machine design approach.

Summarizing the results found in the literature, which deal with the torque ripple reduction, it can be assumed that at the nominal load, torque ripple appears due to two main reasons: 1) non-ideal sinusoidal waveform of the back electromotive force (EMF) or phase current and 2) synchronous inductance variation.

This paper studies the appearances of asymmetric local saturations in TCW PMSMs, due to the interaction of the permanent magnet flux and armature winding flux in the stator side (in PMSM with rotor surface permanent magnets and with rotor embedded permanent magnets). The influence of these local saturations on the torque ripple at different load conditions is investigated and compared with the torque ripple impact by the interaction of the back EMF with the phase current. In addition, a skewing technique for elimination of the main cogging torque harmonic component is proposed for a 12-slot 10-pole PMSM. Thus, both of the most harmful torque ripple harmonics 6th and 12th can be significantly reduced or even eliminated 6th harmonic by the method proposed in this paper, and 12th by skewing).

The novelty of this paper is the consideration of the permanent magnet flux interaction with the armature reaction as a source of the local saturation, which causes inductance variation, as well as a significant magnetic coenergy variation. This phenomenon can increase the torque ripple in PMSMs. The aim of this paper is to describe the possibilities of the elimination of these effects. It should be noted that all dimensions were kept the same except those that were explicitly altered and described in the text, which means that the slot area and the current density were not changed. The optimization was realized using commercial software package.

Section II investigates the factors, which cause local saturations in TCW PMSM at the stator side. Section III shows the influence of these local saturations on the torque ripple generation. It also proposes some solutions, to reduce the local saturation in the stator teeth. The described method was compared with the skewing of the machine, which is conventional method of torque ripple and cogging torque reduction. The skewing was implemented alone without any additional changes in machine geometry, and together with the method described in this paper. Possible disadvantages of the investigated methods and tradeoffs, which should be considered, are described in this paper.

II. Factors of Local Saturations in TCW PMSMs at the Stator Side

Usually, during geometry optimization of a TCW PMSM it is assumed that at any load condition, the peak flux densities in each stator tooth are the same [10], [11], [14]. Therefore, all stator teeth in TCW PMSM have the same width. The only exceptions are TCW PMSMs with an armature winding, the current linkage of which creates the magnetic flux, where one stator tooth has twice as high as armature flux compared with the adjacent tooth (e.g., single layer 12-slot 10-pole TCW PMSMs) [20]. In this case, it is advisable to make unequal stator teeth to increase the total magnetic flux through the winding. However, it is not the case of double or multi-layer windings, where the armature current linkage alone (without permanent magnets) creates the magnetic flux with the same peak values in each stator tooth with a 3-phase symmetrical winding system and alternating current. However, due to the presence of permanent magnets in TCW PMSMs, which interact with the armature winding flux, the peak flux density in adjacent stator teeth can differ from each other at loaded conditions, as is shown hereafter.

If it is assumed that the steel used in the magnetic circuit has a linear B–H curve, and the stator teeth fluxes caused by the permanent magnets and caused by stator current linkage are sinusoidal, the total fluxes in two adjacent stator teeth $\Phi_{\text{tot.Tooth1}}$ and $\Phi_{\text{tot.Tooth2}}$ can be estimated by

$$\Phi_{\text{tot.Tooth1}} = \hat{\Phi}_{\text{PM.Tooth1}} \sin(\omega t + \varphi_1) + \hat{\Phi}_{\text{W.Tooth1}} \sin(\omega t + \varphi_2) \quad (1)$$

$$\Phi_{\text{tot.Tooth2}} = \hat{\Phi}_{\text{PM.Tooth2}} \sin(\omega t + \varphi_3) + \hat{\Phi}_{\text{W.Tooth2}} \sin(\omega t + \varphi_4) \quad (2)$$

where $\Phi_{\text{PM.Tooth1}}$ and $\Phi_{\text{PM.Tooth2}}$ are the fluxes created only by the permanent magnets, $\Phi_{\text{W.Tooth1}}$ and $\Phi_{\text{W.Tooth2}}$ are the fluxes created only by the armature current linkage, φ_1 and φ_3 are the phase shifts of the fluxes created only by the permanent magnets, φ_2 and φ_4 are the phase shifts of the fluxes created only by the armature current linkage, and ω is the electrical angular frequency. Variables in (1) and (2) are related to the first tooth (Tooth 1) and to the second tooth (Tooth 2), respectively.

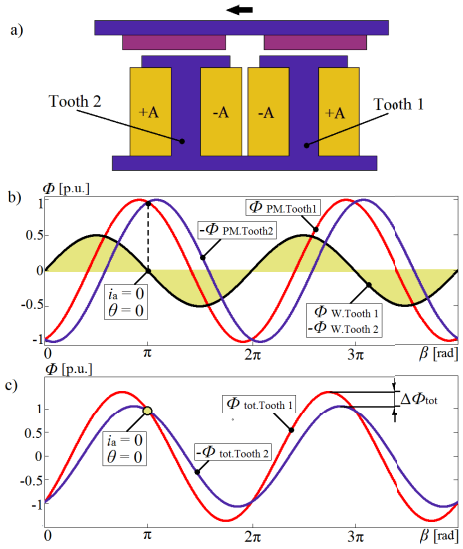

Fig. 1. Factors that lead to unbalanced peak flux densities in the stator teeth in TCW PMSM with $q = 0.4$. (a) Two adjacent stator teeth of one phase. (b) Fluxes in these teeth caused by permanent magnets (peak flux is 1 p.u.) and caused by the armature winding (peak flux is 0.5 p.u.). (c) Resultant flux in the teeth. Saturation is not considered. It is assumed that stator teeth fluxes caused by the permanent magnets and caused by the stator current linkage are sinusoidal, β is the electrical rotation angle, and θ is the stator current linkage.

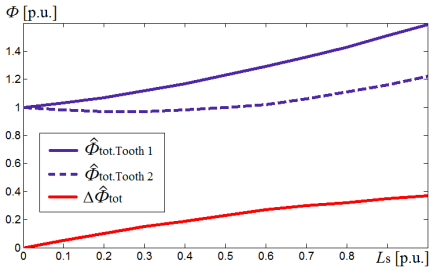

Fig. 2. Flux variations in adjacent stator teeth as function of the synchronous inductance. $\Delta\hat{\Phi}_{tot}$ is the difference between $\hat{\Phi}_{tot.Tooth1}$ and $\hat{\Phi}_{tot.Tooth2}$.

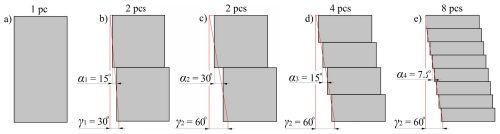

Fig. 3. (a) Non-skewed magnet. (b) Magnet skewing for the elimination of the 12th-order harmonic of the cogging torque. (c) Magnet skewing for the elimination of the 6th-order harmonic of the cogging torque. (d) Magnet skewing for the elimination of the 6th- and 12th-order harmonic of the cogging torque. (e) Magnet skewing for the elimination of the 6th-, 12th-, and 24th-order harmonic of the cogging torque. γ is the total skewing angle (if skewing is assumed to be continuous) and α is the skewing angle pitch.

In 12-slot 10-pole PMSMs with rotor surface permanent magnets (at $I_d = 0$ control), if the phase shift of the flux created by the armature current linkage in Tooth 1 is assumed to be $\varphi_2 = 0°$, then the phase shift of the flux created by the armature current linkage in Tooth 2 is $\varphi_4 = 180°$, because it is created by the same current linkage, but with opposite polarity for different teeth. In this case, the phase shifts of the fluxes created by the permanent magnets are $\varphi_1 = 75°$ and $\varphi_3 = 105°$ in Tooth 1 and Tooth 2, respectively. This means that the total fluxes $\Phi_{tot.Tooth1}$ and $\Phi_{tot.Tooth2}$ should have different peak values, as shown in Fig. 1.

In Fig. 1(b), it can be seen that, the values of the fluxes in the stator teeth created by the permanent magnets alone ($\Phi_{PM.Tooth1}$ and $-\Phi_{PM.Tooth2}$) have the same peaks. However, it is seen that the fluxes created by the armature winding ($\Phi_{W.Tooth1}$ and $-\Phi_{W.Tooth2}$) increases the total flux in Tooth 1 more intensively than in Tooth 2. The resultant total flux in Tooth 1 ($\Phi_{tot.Tooth1}$) and Tooth 2 ($\Phi_{tot.Tooth2}$) are shown in Fig. 1(c). It should be noted that it is true for TCW PMSMs with rotor surface permanent magnets and at maximum torque per ampere control, or in other words, at $I_d = 0$.

Fig. 1 shows the case, when the flux value produced by the current linkage is half of the flux value produced by the permanent magnets. However, electrical machines with different synchronous inductance values have different armature reactions, which affects the phenomenon described previously. Fig. 2 shows the fluxes variations in two adjacent stator teeth as a function of the synchronous inductance in a 12-slot 10-pole PMSM. It is assumed that the stator steel has linear permeability, and the teeth fluxes, caused by the permanent magnets, has a sinusoidal waveform.

According to Fig. 2, the higher the synchronous inductance is, the larger the difference between the fluxes in the adjacent stator teeth will be. If the stator teeth widths are the same, it can lead to a significant peak flux density difference in the adjacent teeth, and, as a result, one stator tooth can be subjected to a stronger saturation effect than the neighboring teeth of the same phase.

After the analysis of the phenomenon shown in Fig. 2, it can be concluded that the flux variation due to the armature current linkage, mostly takes place in one stator tooth (Tooth 1), whereas in the adjacent tooth (Tooth 2) the flux starts increasing only if the PMSM has a high synchronous inductance ($I_d = 0$).

In addition to the electromagnetic torque, caused by the saturation variation, the cogging torque also has a significant influence on the overall torque ripple [18]. The common approach used to eliminate the cogging torque is skewing. However, skewing reduces the average torque by the skewing factor [12]. Therefore, the skewing angle should be as small as possible. In case of a 12-slot 10-pole machine, the main harmonic component of the cogging torque is 12th. To eliminate this harmonic component in radial flux PMSMs, the permanent magnets can be divided into two parts in the axial direction and shifted by 15 electrical degrees, Fig. 3(b), whereas if the

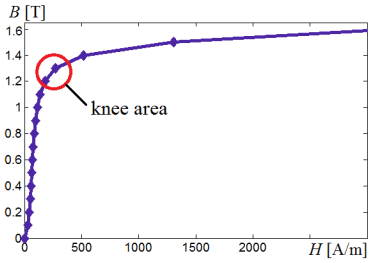

Fig. 4. B–H curve of M400-50A steel grade [21].

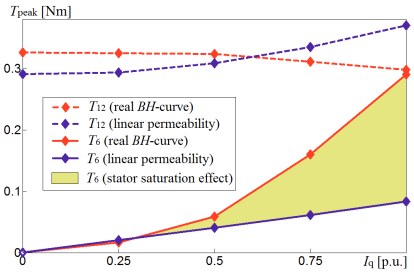

Fig. 5. 12th and 6th-torque ripple harmonics of the machine with linear permeability and with the real B–H curve at the nominal load. Additional torque ripple that appears due to the saturation in the stator teeth is highlighted.

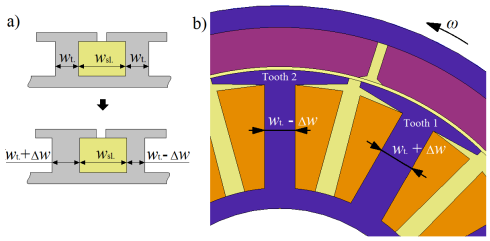

Fig. 6. Stator geometry optimization of a 12-slot 10-pole TCW PMSM for the torque ripple reduction at the nominal load. (a) Principle of the stator teeth width adjustment. (b) Resultant geometry of the TCW PMSM. $w_{t\_}$ is the teeth width of the original machine, $w_{sl\_}$ is the width of the slot (which is kept unchanged during the optimization), and Δw is the added (subtracted) width value, to adjust the flux density in stator teeth.

6th-torque ripple should be reduced, the permanent magnets can be divided into two parts in the axial direction and shifted by 30 electrical degrees, Fig. 3(c). However, as shown in [18], even if the permanent magnets are divided into two parts in the axial direction and shifted by 30 electrical degrees, in some working points, the 6th harmonic of the torque ripple does not reduce significantly, but it can even increase at high loads.

III. Torque Ripple Reduction Methods

Usually, the stator in a PMSM is made of laminated steel with high-magnetic permeability. However, this material has non-linear B–H curve, which represents the permeability reduction at higher flux density values in the steel. An example of a steel material B–H curve used in electrical machines is shown in Fig. 4.

In Fig. 4, it can be seen that the B–H curve of the steel has a so-called knee point, where the permeability of the steel rapidly reduces at a particular flux density level.

Often, the electrical machines are designed in a way that the maximum value of the flux density in the steel is in the knee area, shown in Fig. 4, or just below it, to efficiently use the materials, and at the same time to keep the power density as high as possible [12]. This means that the peak flux density in the stator lamination is, usually, selected so that at higher flux density values the permeability of the steel is significantly reduced, which decreases the synchronous inductance of the PMSM.

In [19], it was shown that the synchronous inductance variation in TCW PMSMs causes torque ripple, and that its harmonic order determines the harmonic order of the torque ripple. From this information, it can be concluded that it is preferable to keep the synchronous inductance constant, or to eliminate low-order harmonics of the synchronous inductance variation, because high-order harmonics of the torque ripple are less harmful compared with the low-order harmonics [22].

As described in Section II, in TCW PMSMs with rotor surface permanent magnets, the flux density peaks in the adjacent stator teeth can have different values, which leads to different teeth permeability and, as a consequence, to the synchronous inductance variation. This phenomenon can cause torque ripple in the PMSMs. However, to segregate the contributions of iron saturation and the non-ideal sinusoidal waveform of the back EMF to the torque ripple, 2-D FEM analysis of two similar PMSMs described in [8] and shown in Fig. 6 (but with equal teeth widths) was prepared, so that the first PMSM has linear permeability, whereas the second one has the B–H curve of the real steel (M400-50A). The 6th and 12th harmonic components of the torque ripples of both PMSMs are shown in Fig. 5.

In Fig. 5, it can be seen that in the machine with the real B–H curve, the 6th-torque ripple harmonic increases rapidly at higher loads. Therefore, it can be concluded that the saturation effect in the stator side can indeed have a significant impact on the total torque ripple. However, other high-order harmonics remained approximately at the same level and were not affected by different steel properties (except slightly different cogging torque). Therefore, mainly the 6th-torque ripple harmonic is affected, because the oversaturation in the phase occurs two times per electrical period, Fig. 1. The machine has three phases, which means that the affected torque ripple harmonic is $2 \times 3 = 6$.

It should be noted that no changes were made to tune the air-gap flux density by permanent magnets, during the optimization process, but only the stator geometry adjustment is considered. This means that if the 6th-torque ripple should be eliminated, the torque ripple by saturation effect can be adjusted to compensate the torque ripple by the non-ideal sinusoidal waveform of the back EMF.

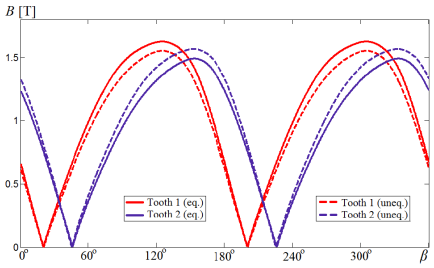

Fig. 7. Flux densities in the stator teeth of the original 12-slot 10-pole PMSM (with equal teeth widths) and of the redesigned PMSM (with unequal teeth widths) at the nominal load.

If the widths of the adjacent stator teeth are redesigned in a way that they have approximately the same peak flux density, it is possible to reduce or even fully eliminate some harmful harmonics of the torque ripple. Three different TCW PMSMs were analyzed using FEM—12-slots 10-poles PMSM with outer rotor and surface permanent magnets [8], 144-slots 120-poles PMSM with inner rotor and rotor surface permanent magnets [23], and 18-slots 16-poles with inner rotor and rotor embedded permanent magnets [9], [24].

The outer rotor 12-slot 10-pole PMSM was originally designed for a blower application [8]. This type of an application requires silent work, which together with tuning of the radial force (reduction of the radial force strength and elimination of its low-order harmonic components) [25], also demands a low-torque ripple. The geometry optimization of the stator is shown in Fig. 6. The widths of the stator teeth were changed that at the nominal load they have approximately the same flux density peaks, as shown in Fig. 7. It should be noted that the width of one stator tooth was increased to the same extent as the width of the second tooth was decreased, or in other words the slot width (area) remained unchanged. In addition, skewing is implemented in the same way, as shown in Fig. 3, which in theory should eliminate or reduce the 6th, 12th, and 24th harmonic components in the cogging torque and torque ripple.

The torque curves at the nominal load of the original motor and of the redesigned motor with and without skewing are shown in Fig. 8 with the spectrum analysis. For simplification purposes each design solution is marked as (γ = skewing angle, Uneq. or Eq., number of pcs), where γ shows the skewing angle (if skewing is assumed continuous), Uneq. or Eq. determines if the stator teeth have unequal or equal widths, and number of pcs shows how many divisions the permanent magnets have along the axial direction.

In Fig. 8, it can be seen that implementation of only unequal teeth widths can eliminate the 6th-torque ripple harmonic at the nominal load ($\gamma = 0°$, Uneq., 1 pc) compared with the original design ($\gamma = 0°$, Eq., 1 pc). In addition, it is possible to eliminate 12th and 24th-torque ripple harmonics using skewing ($\gamma = 30°$, Eq., 2 pcs), ($\gamma = 30°$, Uneq., 2 pcs), ($\gamma = 60°$, Eq., 4 pcs), ($\gamma = 60°$, Uneq., 4 pcs), ($\gamma = 60°$, Eq., 8 pcs), and ($\gamma = 60°$, Uneq., 8 pcs).

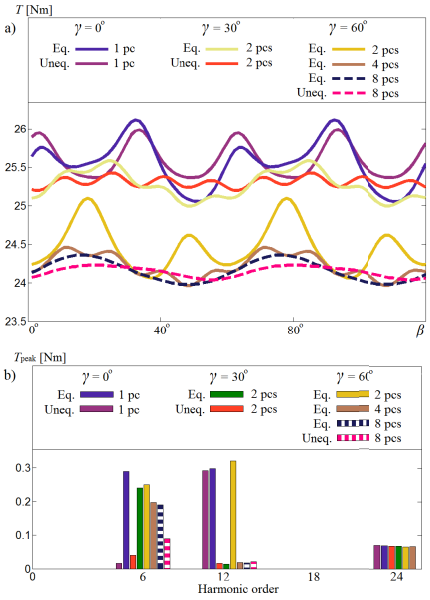

Fig. 8. (a) Torque curves of the skewed and non-skewed original 12-slot 10-pole PMSM (with equal teeth widths) and of the redesigned PMSM (with unequal teeth widths) at the nominal load. (b) Spectrum analysis of the torque curves.

However, as observed in Fig. 8, the skewing does not eliminate the 6th-torque ripple harmonic. The situation was similar to the one described in [18]. It is possible to achieve a reduction of the 6th-torque ripple harmonic, if the permanent magnets are divided into more than two parts during the skewing ($\gamma = 60°$, Eq., 4 pcs), ($\gamma = 60°$, Eq., 8 pcs), and ($\gamma = 60°$, Uneq., 8 pcs), but the total elimination of this harmonic is not possible if only skewing is implemented. The reason of this is the fact that skewing divides the machine in axial direction on several parts, where each part has different interaction of the armature flux with permanent magnet flux, due to different phase shifts of the fluxes created by the armature current linkage and permanent magnets along the axial direction. As it is shown previously, this is the main reason of the unequal maximum saturation levels in the stator teeth (1) and (2). In other words, there is different saturation level in the stator teeth in the axial direction, if the skewing is implemented. Therefore, it is suggested that if the 6th-torque ripple harmonic should be eliminated or significantly reduced, the technique with unequal teeth widths described in this paper should be implemented without skewing ($\gamma = 0°$, Uneq., 1 pc). However, in this case other torque ripple harmonics retain their presence.

The no-load cogging torque curves for different PMSM design solutions are shown in Fig. 9. The cogging torque can be eliminated using skewing technique, without any additional approaches, due to the fact that there is no

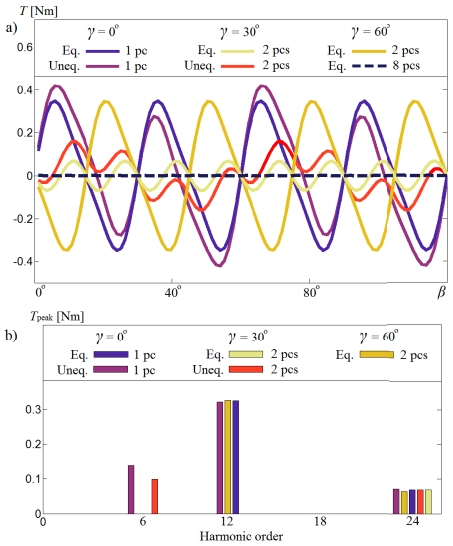

Fig. 9. (a) Cogging torque curves of the skewed and non-skewed original 12-slot 10-pole PMSM (with equal teeth widths) and of the redesigned PMSM (with unequal teeth widths) at no-load. (b) Spectrum analysis of the torque curves.

armature reaction at no-load [18]. In Fig. 9 and Table I, it can be seen that a particular cogging torque harmonic is eliminated, if the angle (in electrical degrees), which takes half of the period of this harmonic is divided by angle (α) between two adjusted permanent magnets of the skewing (Fig. 3) gives integer value. For example, if the 12th cogging torque harmonic is needed to be eliminated, the permanent magnets should be divided in the axial direction, so that the angle between two adjacent permanent magnets is 15 electrical degrees, Fig. 3(b) and (d), because half of the 12th cogging torque harmonic takes $180/12 = 15$ electrical degrees.

The limitation of using the unequal teeth widths approach comes from the fact that, if the teeth widths are optimized, to have approximately equal flux density peaks in the stator teeth at one working point, they are not the same at other loads, because in this case the armature reaction (flux created by the armature current linkage) is different. It means that the 6th-harmonic order of the torque ripple is not completely eliminated at other working points, as shown in Fig. 10(a). Therefore, the stator teeth widths optimization should be implemented with the knowledge of the prevailing loads. It is also shown that with negative torque (when I_q is negative) the torque ripple increases to the same extent as with positive torque in case of equal teeth widths, but with higher extent with the unequal stator teeth widths, due to the same reason (different armature reactions).

In Fig. 10(b), it is seen that skewing does not significantly change the 6th-torque order harmonic in the PMSM with equal teeth widths. However, skewing can significantly reduce this harmonic at smaller loads with unequal teeth widths in the case of ($\gamma = 60°$, Uneq., 8 pc), which makes this approach more practical, because in this case other torque ripple harmonics can be eliminated as well. The only disadvantage of using together skewing and unequal teeth widths approaches, as described previously, is the fact that in this case at high loads the 6th-order harmonic is somehow higher, compared with using unequal teeth widths alone, Fig. 10(a) and (b).

In Fig. 10(c), it can be noticed that skewing almost eliminates the 12th-torque ripple harmonic, which is not significantly dependent on the load level. Therefore, it can be assumed that the 12th harmonic and other higher order harmonics are only components of the cogging torque, which indeed are easily eliminated by a proper skewing.

Some torque waveforms for different PMSM geometry solutions are not shown in Fig. 9, because they are near to fully coincide with other (shown) torque waveforms. For example, ($\gamma = 30°$, Eq., 2 pcs) at no-load has the same cogging torque behavior as ($\gamma = 60°$, Eq., 4 pcs), and ($\gamma = 60°$, Uneq., 8 pcs) does not have any practical cogging torque as well as ($\gamma = 60°$, Eq., 8 pcs). However, all the simulated torque harmonic components for different design solutions can be found in Table I.

It should be noted that the described 12-slot 10-pole PMSM was analyzed with current supply. Therefore, the purely sinusoidal current was conducting in the stator windings. In this case, the local saturations, which causes synchronous

TABLE I
VALUES OF THE HARMONIC COMPONENTS OF THE TORQUE CURVES ILLUSTRATED IN FIGS. 8 AND 9

Geometry type	Harmonic order	No-load	Nominal load
($\gamma = 0°$) Eq. 1 pc	T_0 [Nm]	0	25.5
($\gamma = 0°$) Uneq. 1 pc	T_0 [Nm]	0	25.6
($\gamma = 30°$) Eq. 2 pcs	T_0 [Nm]	0	25.3
($\gamma = 30°$) Uneq. 2 pcs	T_0 [Nm]	0	25.3
($\gamma = 60°$) Eq. 2 pcs	T_0 [Nm]	0	24.5
($\gamma = 60°$) Eq. 4 pcs	T_0 [Nm]	0	24.2
($\gamma = 60°$) Eq. 8 pcs	T_0 [Nm]	0	24.2
($\gamma = 60°$) Uneq. 8 pcs	T_0 [Nm]	0	24.2
($\gamma = 0°$) Eq. 1 pc	T_6 [Nm]	0	0.29
($\gamma = 0°$) Uneq. 1 pc	T_6 [Nm]	0.14	0.02
($\gamma = 30°$) Eq. 2 pcs	T_6 [Nm]	0	0.24
($\gamma = 30°$) Uneq. 2 pcs	T_6 [Nm]	0.1	0.04
($\gamma = 60°$) Eq. 2 pcs	T_6 [Nm]	0	0.25
($\gamma = 60°$) Eq. 4 pcs	T_6 [Nm]	0	0.2
($\gamma = 60°$) Eq. 8 pcs	T_6 [Nm]	0	0.19
($\gamma = 60°$) Uneq. 8 pcs	T_6 [Nm]	0	0.09
($\gamma = 0°$) Eq. 1 pc	T_{12} [Nm]	0.33	0.3
($\gamma = 0°$) Uneq. 1 pc	T_{12} [Nm]	0.23	0.29
($\gamma = 30°$) Eq. 2 pcs	T_{12} [Nm]	0	0.01
($\gamma = 30°$) Uneq. 2 pcs	T_{12} [Nm]	0	0.02
($\gamma = 60°$) Eq. 2 pcs	T_{12} [Nm]	0.33	0.32
($\gamma = 60°$) Eq. 4 pcs	T_{12} [Nm]	0	0.02
($\gamma = 60°$) Eq. 8 pcs	T_{12} [Nm]	0	0.02
($\gamma = 06°$) Uneq. 8 pcs	T_{12} [Nm]	0	0.02
($\gamma = 0°$) Eq. 1 pc	T_{24} [Nm]	0.07	0.07
($\gamma = 0°$) Uneq. 1 pc	T_{24} [Nm]	0.07	0.07
($\gamma = 30°$) Eq. 2 pcs	T_{24} [Nm]	0.07	0.07
($\gamma = 30°$) Uneq. 2 pcs	T_{24} [Nm]	0.07	0.07
($\gamma = 60°$) Eq. 2 pcs	T_{24} [Nm]	0.07	0.07
($\gamma = 60°$) Eq. 4 pcs	T_{24} [Nm]	0.07	0.07
($\gamma = 60°$) Eq. 8 pcs	T_{24} [Nm]	0	0
($\gamma = 60°$) Uneq. 8 pcs	T_{24} [Nm]	0	0

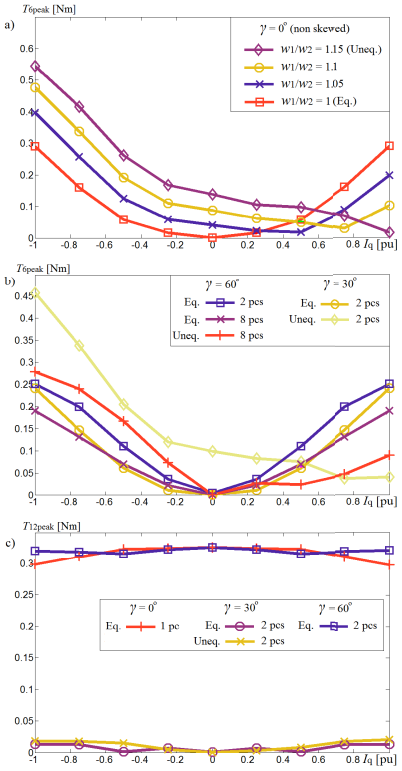

Fig. 10. (a) Amplitude of 6th-torque ripple harmonic at different ratios of the teeth widths (w_1/w_2) without skewing ($\gamma = 0°$) as function of the load. (b) Amplitude of 6th-torque ripple harmonic at different ratios of the teeth widths (w_1/w_2) with skewing ($\gamma = 30°$ and $60°$) as function of the load. (c) Amplitude of 12th-torque ripple harmonic at different ratios of the teeth widths (w_1/w_2) with and without skewing as function of the load, evaluated by FEA. When the I_q has negative value, the motor switches to the generator mode but rotates in the same direction.

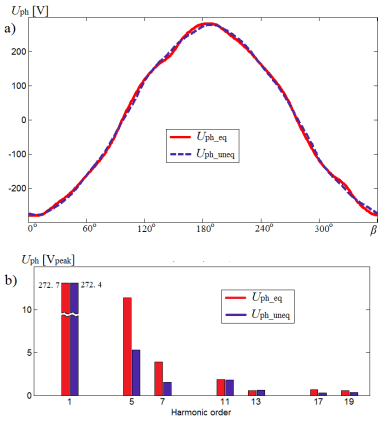

Fig. 11. (a) Voltage at the terminals of the phase current supply of the original machine (with equal teeth widths) and of the redesigned machine (with unequal teeth widths). (b) Spectrum analysis of the voltages.

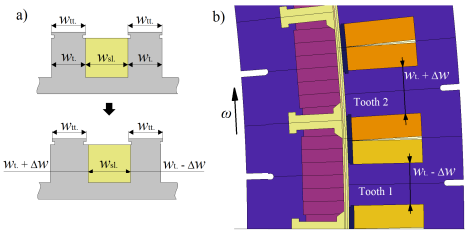

Fig. 12. Stator geometry optimization of 144-slot 120-pole TCW PMSM for the torque ripple reduction at the nominal load. (a) Principle of the stator teeth width adjustment. (b) Resultant geometry of the TCW PMSM. w_{tt} is the tooth tip width, which should be kept unchanged.

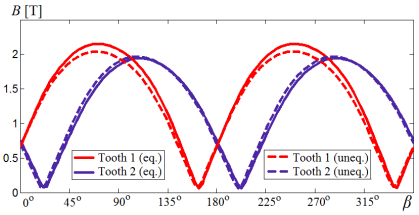

Fig. 13. Flux densities in the stator teeth of the original 144-slot 120-pole PMSM (with equal teeth widths) and those of the redesigned PMSM (with unequal teeth widths) at the nominal load.

inductance variation, should influence the voltage waveform of the current supply. In Fig. 11, it can be seen that the voltage waveform of the current supply with unequal teeth widths is less interfered by high-order harmonics compared with the original design.

Fig. 12 shows the geometry of a 144-slot 120-pole PMSM, which was designed for a direct drive wind generator [23]. One of the main design challenges of the PMSMs for this type of application is the reduction of the lowest harmonic components of the torque ripples, because otherwise it can degrade the performance of the whole system [22]. The stator teeth widths optimization of this electric machine was implemented in the same way as for 12-slot 10-pole PMSM (until the peak flux densities in the teeth have approximately the same values), as shown in Fig. 13. The resultant torque curves of the original PMSM (with equal teeth) and of the optimized PMSM (with unequal teeth) are shown in Fig. 14.

In Fig. 14, it can be observed that the 6th-harmonic order of the torque ripple was significantly reduced compared with the torque curve of the original PMSM. However, as it is noted previously, at lower load conditions the 6th-harmonic order of the torque ripple increases, whereas in the original design it reduces at lower torque. Therefore, the stator teeth widths should be selected according to the predicted load.

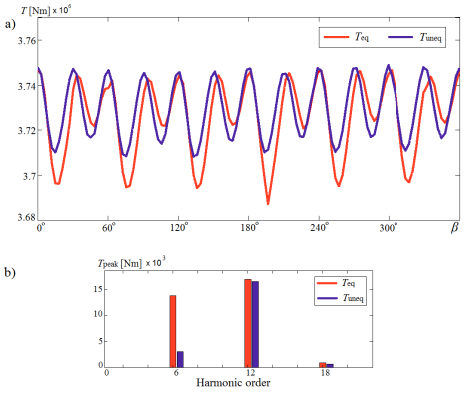

Fig. 14. (a) Torque curves of the original 144-slot 120-pole PMSM (with equal teeth widths) and of the redesigned PMSM (with unequal teeth widths) at the nominal load. (b) Torque ripples harmonic spectrum. In both cases, the voltage supply is used with the similar amplitude.

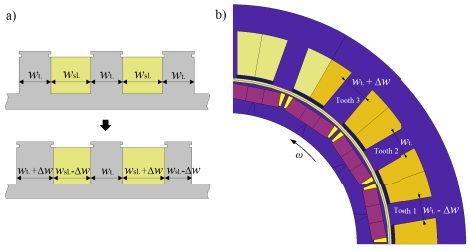

Fig. 15. Stator geometry optimization of a 18-slot 16-pole TCW PMSM for torque ripple reduction at the nominal load. (a) Principle of the stator teeth width adjustment. (b) Resultant geometry of the TCW PMSM.

During the analysis of the original and redesigned wind generators the voltage sources were used. However, the saturation in the stator teeth varies at different teeth widths, which leads to the synchronous inductance variation and consequently to the load angle change for the same working point. For example, to keep the same torque as of the original PMSM, the load angle δ of the redesigned wind generator was reduced from 52 to 50 electrical degrees. It means that the generator with unequal stator teeth has $\sim$3% higher overload capability than the original design.

It should be noted that the described optimization method should suit not only for TCW PMSMs with $q = 0.4$ and rotor surface permanent magnets, but also for PMSMs with other numbers of slots per pole and phase as well as with rotor embedded magnets. As an example, a TCW PMSM with 18-slot 16-pole was analyzed [24]. Fig. 15 shows the geometry of this TCW PMSM. The major difference between this electric machine ($q = 0.375$) and the above described PMSMs ($q = 0.4$) is the fact that there are three adjacent stator teeth with different peak flux densities at the nominal

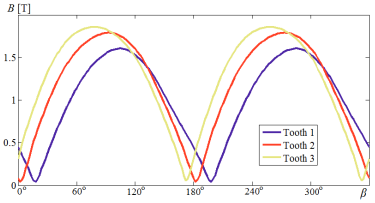

Fig. 16. Flux densities in three adjacent stator teeth of the original 18-slot 16-pole PMSM (with equal teeth widths) at the nominal load.

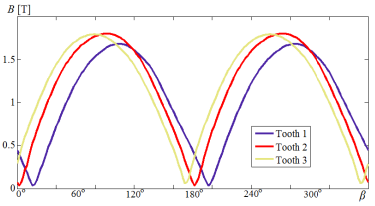

Fig. 17. Flux densities in the three adjacent stator teeth of the redesigned 18-slot 16-pole PMSM (with unequal teeth widths) at the nominal load.

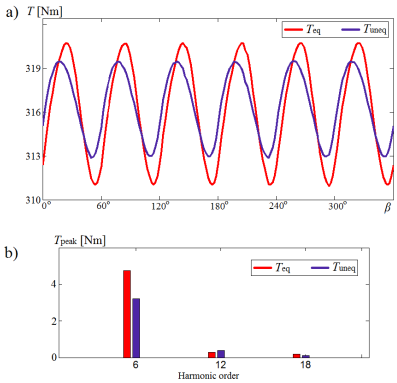

Fig. 18. (a) Torque curves of the original 18-slot 16-pole PMSM (with equal teeth widths) and of the redesigned PMSM (with unequal teeth widths) at the nominal load. (b) Torque ripples harmonic spectrum.

load, as shown in Fig. 16. To reduce the torque ripple, the stator teeth widths were adjusted accordingly to the above described procedure, and the resultant flux densities at the nominal load are shown in Fig. 17. The torque curves of the original PMSM and of the optimized one are shown in Fig. 18. One significant drawback, when three teeth widths are adjusted, is the fact that the stator slots have different widths (areas), and other approaches are needed to make the slot areas equal (e.g., alternate the stator yoke widths in each slot).

In Fig. 18, it is seen that the 6th-harmonic order of the torque ripple was reduced, but not so significantly as in the previous electric machines (with rotor surface

permanent magnets). It can be explained by the presence of the rotor steel near to the air gap, which can also have a strong local saturation.

IV. Conclusion

The reasons of local saturation in the stator side of TCW PMSMs are described. It is shown that these saturations, which cause asymmetrical permeability variations in the magnetic circuit, can produce some high-order harmonics in the PMSM torque.

Possible design solutions are suggested and verified by FEA, for the elimination of these effects and for reducing the torque ripple.

It was found that in TCW PMSMs, the 6th-torque ripple harmonic is partially produced by non-symmetrical peak flux density distributions in the stator teeth, due to interaction of the permanent magnet flux with armature flux. The 6th harmonic can be eliminated by teeth widths adjustment, whereas conventional skewing technique is not appropriate for the reduction of this harmonic. However, skewing is still favorable for the elimination of cogging torque in TCW PMSMs. The main disadvantage of the method with unequal stator teeth is that it gives the desirable results for only one working point, whereas for other loads the 6th-torque ripple harmonic increases.

The described methods can be used by designers, which should be aware of these local saturations in TCW PMSMs, especially when low-torque ripple is one of the design targets.

References

[1] H. Jussila, "Concentrated winding multiphase permanent magnet machine design and electromagnetic properties—Case axial flux machine," Ph.D. dissertation, Dept. Elect. Eng., Lappeenranta Univ. Technol., Lappeenranta, Finland, 2009.

[2] A. M. EL-Refaie, "Fractional-slot concentrated-windings synchronous permanent magnet machines: Opportunities and challenges," *IEEE Trans. Ind. Electron.*, vol. 57, no. 1, pp. 107–121, Jan. 2010.

[3] R. Dutta, M. F. Rahman, and L. Chong, "Winding inductances of an interior permanent magnet (IPM) machine with fractional slot concentrated winding," *IEEE Trans. Magn.*, vol. 48, no. 12, pp. 4842–4849, Dec. 2012.

[4] T. D. Strous, H. Polinder, and J. A. Ferreira, "Inductance calculations for PM machines with concentrated windings," in *Proc. IEEE Int. Electr. Mach. Drives Conf. (IEMDC)*, May 2011, pp. 447–452.

[5] L. Alberti and N. Bianchi, "Theory and design of fractional-slot multilayer windings," *IEEE Trans. Ind. Appl.*, vol. 49, no. 2, pp. 841–849, Mar./Apr. 2013.

[6] M. V. Cistelecan, F. J. T. E. Ferreira, and M. Popescu, "Three phase tooth-concentrated multiple-layer fractional windings with low space harmonic content," in *Proc. IEEE Energy Convers. Congr. Expo. (ECCE)*, Sep. 2010, pp. 1399–1405.

[7] M. Barcaro and N. Bianchi, "Torque ripple reduction in fractional-slot interior PM machines optimizing the flux-barrier geometries," in *Proc. 20th Int. Conf. Elect. Mach. (ICEM)*, Sep. 2012, pp. 1496–1502.

[8] I. Petrov and J. Pyrhonen, "Performance of low-cost permanent magnet material in PM synchronous machines," *IEEE Trans. Ind. Electron.*, vol. 60, no. 6, pp. 2131–2138, Jun. 2013.

[9] P. Ponomarev, "Tooth-coil permanent magnet synchronous machine design for special applications," Ph.D dissertation, Dept. Elect. Eng., Lappeenranta Univ. Technol., Lappeenranta, Finland, 2013.

[10] P. Sergeant and A. P. M. Van den Bossche, "Influence of the amount of permanent-magnet material in fractional-slot permanent-magnet synchronous machines," *IEEE Trans. Ind. Electron.*, vol. 61, no. 9, pp. 4979–4989, Sep. 2014.

[11] G. Sizov, P. Zhang, D. Ionel, N. Demerdash, and M. Rosu, "Automated multi-objective design optimization of PM AC machines using computationally efficient FEA and differential evolution," *IEEE Trans. Ind. Appl.*, vol. 49, no. 5, pp. 2086–2096, Sep. 2013.

[12] J. Pyrhönen, T. Jokinen, and V. Hrabovcová, *Design of Rotating Electrical Machines*. New York, NY, USA: Wiley, 2008.

[13] P. Ponomarev, Y. Alexandrova, I. Petrov, P. Lindh, E. Lomonova, and J. Pyrhonen, "Inductance calculation of tooth-coil permanent-magnet synchronous machines," *IEEE Trans. Ind. Electron.*, vol. 61, no. 11, pp. 5966–5973, Nov. 2014.

[14] A. M. EL-Refaie, Z. Q. Zhu, T. M. Jahns, and D. Howe, "Winding inductances of fractional slot surface-mounted permanent magnet brushless machines," in *Proc. IEEE Ind. Appl. Soc. Annu. Meeting (IAS)*, Oct. 2008, pp. 1–8.

[15] J. Montonen, P. Lindh, and J. Pyrhonen, "Design process of traction motor having tooth coil windings," in *Proc. 20th Int. Conf. Elect. Mach. (ICEM)*, Sep. 2012, pp. 1264–1268.

[16] L. Alberti, M. Barcaro, and N. Bianchi, "Design of a low torque ripple fractional-slot interior permanent magnet motor," in *Proc. IEEE Energy Convers. Congr. Expo. (ECCE)*, Sep. 2012, pp. 509–516.

[17] K. Wang, Z. Q. Zhu, and G. Ombach, "Torque enhancement of surface-mounted permanent magnet machine using third-order harmonic," *IEEE Trans. Magn.*, vol. 50, no. 3, Mar. 2014, Art. ID 8100210.

[18] W. Q. Chu and Z. Q. Zhu, "Investigation of torque ripples in permanent magnet synchronous machines with skewing," *IEEE Trans. Magn.*, vol. 49, no. 3, pp. 1211–1220, Mar. 2013.

[19] P. Ponomarev, I. Petrov, and J. Pyrhonen, "Influence of travelling current linkage harmonics on inductance variation, torque ripple and sensorless capability of tooth-coil permanent-magnet synchronous machines," *IEEE Trans. Magn.*, vol. 50, no. 1, Jan. 2014, Art. ID 8200108.

[20] D. Ishak, Z. Q. Zhu, and D. Howe, "Permanent-magnet brushless machines with unequal tooth widths and similar slot and pole numbers," *IEEE Trans. Ind. Appl.*, vol. 41, no. 2, pp. 584–590, Mar./Apr. 2005.

[21] *Typical Data for SURA M40050A*. [Online]. Available: http://www.sura.se, accessed 2014.

[22] J. Sopanen, V. Ruuskanen, J. Nerg, and J. Pyrhonen, "Dynamic torque analysis of a wind turbine drive train including a direct-driven permanent-magnet generator," *IEEE Trans. Ind. Electron.*, vol. 58, no. 9, pp. 3859–3867, Sep. 2011.

[23] Y. Alexandrova, R. Semken, and J. Pyrhönen, "Permanent magnet synchronous generator design solution for large direct-drive wind turbines," *Int. Rev. Elect. Eng.*, vol. 8, no. 6, p. 1728, 2013.

[24] P. Ponomarev, P. Lindh, and J. Pyrhonen, "Effect of slot-and-pole combination on the leakage inductance and the performance of tooth-coil permanent-magnet synchronous machines," *IEEE Trans. Ind. Electron.*, vol. 60, no. 10, pp. 4310–4317, Oct. 2013.

[25] J. Krotsch, T. Ley, and B. Piepenbreier, "Reduction of torque and radial force fluctuation in permanent magnet synchronous motors by means of multi-objective optimization," in *Proc. 1st Int. Electr. Drives Prod. Conf. (EDPC)*, Sep. 2011, pp. 40–48.

Publication VI

Ponomarev, P., Alexandrova, Y., Petrov, I., Lindh, P., Lomonova, E., and Pyrhönen, J., "Inductance Calculation of Tooth-Coil Permanent-Magnet Synchronous Machines," *IEEE Transactions on Industrial Electronics* , vol.61, no.11, pp.5966−5973, Nov. 2014

Inductance Calculation of Tooth-Coil Permanent-Magnet Synchronous Machines

Pavel Ponomarev, *Member, IEEE*, Yulia Alexandrova, Ilya Petrov, Pia Lindh, *Member, IEEE*, Elena Lomonova, *Senior Member, IEEE*, and Juha Pyrhönen, *Member, IEEE*

***Abstract*—Analytical calculation methods for all the major components of the synchronous inductance of tooth-coil permanent-magnet synchronous machines are reevaluated in this paper. The inductance estimation is different in the tooth-coil machine compared with the one in the traditional rotating field winding machine. The accuracy of the analytical torque calculation highly depends on the estimated synchronous inductance. Despite powerful finite element method (FEM) tools, an accurate and fast analytical method is required at an early design stage to find an initial machine design structure with the desired performance. The results of the analytical inductance calculation are verified and assessed in terms of accuracy with the FEM simulation results and with the prototype measurement results.**

***Index Terms*—Fractional slot winding, inductance calculation, leakage inductance, permanent-magnet synchronous machine (PMSM), tooth coil.**

I. Introduction

FRACTIONAL-SLOT concentrated nonoverlapping winding permanent-magnet synchronous machines (PMSMs) have become very popular over the last two decades [1]. They are nowadays used, for instance, in electrical hybrid vehicles and in ships as propulsion motors, in industry as low-speed direct-drive machines, and in wind energy applications as generators.

The term "fractional-slot nonoverlapping concentrated winding" is very long. Therefore, several shorter descriptions have been used in the literature, such as "concentrated winding" [2], [3], "nonoverlapping winding," [4], [5] or, most popularly, "fractional-slot winding" [1], [6]. All these condensed terms leave room for uncertainty in the description of fractional-slot nonoverlapping concentrated-winding permanent magnet machines with the number of slots per pole and phase $q \leq 0.5$.

The most popular definition "fractional-slot winding" leads to a confusion as the winding may be a fractional-slot one also with $q > 1$ (e.g., $q = 2.25$), which actually refers to a short-pitched distributed-winding machine [7, p. 105]. The term "concentrated winding" refers to a salient pole winding with one slot per pole (IEC 60050-411-37-18) and can be also easily mixed up with a distributed "concentric" winding (as an alternative to a diamond winding [7, p. 54]). The most felicitous definition "nonoverlapping winding" can also refer to a distributed integral-slot concentric winding with nonoverlapping coil ends of a single phase [7, p. 53].

In order to avoid such a confusion, the authors have adopted the term "tooth-coil (TC) winding" from [8] and [9] to refer to multiphase machines with fractional-slot concentrated nonoverlapping windings with the number of slots per pole and phase $q \leq 0.5$. This definition is very descriptive as the key feature of these machines is the very compact armature winding that comprises coils around each tooth or every second tooth.

The performance of a PMSM is strongly dependent on the synchronous inductance L_s, as can be seen from the equation of the maximum (pull-out) torque $T_{\max}$ of a nonsalient pole machine, i.e.,

$$T_{\max} = \frac{pmE_{\rm PM}U_{\rm ph}}{\omega^2 L_s} \tag{1}$$

where p is the number of pole pairs, m is the number of phases, $E_{\rm PM}$ is the back electromotive force, $U_{\rm ph}$ is the phase voltage, and ω is the electrical angular speed.

An analytical inductance model is required to construct an initial design, which can later on be enhanced and refined by finite element method (FEM) modeling in order to tailor the desired performance for a particular application.

The synchronous inductance L_s of a nonskewed PMSM is analytically calculated as a sum of partial inductances, i.e.,

$$L_s = L_m + L_\sigma = L_m + L_{\rm ew} + L_u + L_{\rm tt} + L_h \tag{2}$$

where L_m is the magnetizing inductance, L_σ is the total leakage inductance, $L_{\rm ew}$ is the end-winding leakage inductance, L_u is the slot leakage inductance, $L_{\rm tt}$ is the tooth-tip leakage inductance, and L_h is the air-gap harmonic leakage inductance.

The air-gap harmonic leakage inductance L_h and the magnetizing inductance L_m together comprise the air-gap inductance component L_δ [10]. The term "harmonic" is added to the definition of L_h in order to emphasize that this inductance component is caused by the leakage flux in the air gap produced only by the asynchronous current linkage harmonics and does not include the air-gap component of the leakage flux of the tooth-tip leakage.

The term "current linkage" denoted by Θ is used throughout this paper instead of magnetomotive force F. This is in accordance with the IEC standards when referring to the surface integral of the current density J produced by the winding currents in the air gap. The current linkage Θ (and the

Manuscript received August 15, 2013; revised December 5, 2013; accepted January 10, 2014. Date of publication February 6, 2014; date of current version June 6, 2014.

P. Ponomarev, Y. Alexandrova, I. Petrov, P. Lindh, and J. Pyrhönen are with the Laboratory of Electrical Drives Technology, Lappeenranta University of Technology, 53850 Lappeenranta, Finland.

E. Lomonova is with the Department of Electrical Engineering, Eindhoven University of Technology, 5600 Eindhoven, The Netherlands (e-mail: pavel.ponomarev@lut.fi).

Color versions of one or more of the figures in this paper are available online at http://ieeexplore.ieee.org.

Digital Object Identifier 10.1109/TIE.2014.2304933

magnetomotive force F) is measured, according to the International System of Units, in amperes and not in "ampere-turns" [11]. In analytic calculations, the current linkage Θ is normally calculated per pole, resulting in the amplitude exciting half of the closed magnetic circuit and, therefore, being also half of the magnetomotive force of the circuit.

In previous works, several models have been considered for the calculation of the synchronous inductance; nevertheless, these models are somewhat incomplete. In [4], the tooth-tip leakage inductance component was omitted from the analysis. In [12], the end-winding leakage inductance and the tooth-tip leakage inductance components were specified using traditional equations applied to the design of integral-slot machines. It is shown that the equations applied in this paper improve the analysis and give accurate results for the inductances of TC-PMSMs.

Many of the previous works do not distinguish L_h and L_m in the air gap, but in these works, the terms "phase self-inductance" L_U (which is equivalent to the air-gap inductance L_δ) and "phase mutual inductance" $M_{\rm UV}$ are used instead [12]. In this paper, the synchronous inductance is derived by separating the magnetizing inductance (torque-producing component) and the harmonic leakage inductance in the air gap. Without such a distinction, it is difficult to analytically compare TC-PMSMs with various slot/pole combinations with each other as L_h plays a significant role in the behavior of the TC-PMSMs [13].

The main objective of this paper is to present a complete analytical inductance model for the TC-PMSMs. This paper elaborates the inductance calculation of TC-PMSMs by re-evaluating the existing analytical approaches for all the major components of the synchronous inductance, taking into account the particular features of the TC-PMSMs. Furthermore, the rationale of the selection of the particular equations is presented. The analytical results are compared with the FEM analysis results and the experimental measurements.

Section II introduces the analytical evaluation of all the main inductance components of the synchronous inductance for a TC-PMSM. An equation for the magnetizing inductance L_m is derived. Furthermore, a mutual coupling factor between the phases m_c is determined, as a low value of the mutual coupling factor is important, for instance, in the design of fault-tolerant drives. Moreover, analytical equations for all the leakage components are listed. Then, a table to enable a comparison of TC-PMSMs with different slot/pole combinations is given.

Section III investigates the role of synchronous inductance in the torque production of a TC-PMSM. Methods to increase the torque capabilities are discussed.

Section IV summarizes the experimental verification of the proposed inductance model. Several double-layer TC-PMSMs with 18/16, 12/10, and 24/16 (slots/poles) are given as examples.

II. Inductance Calculation

Here, accurate analytical equations for each component of L_s are discussed.

A. Magnetizing Inductance

The main inductance of a phase of the stator winding $L_{\rm sp}$ is calculated by taking the approach in [7] as follows. The main stator flux linkage $\Psi_{\rm sp}$ (the flux linkage produced by the working harmonic of the stator single-phase current linkage) is generated by the U-phase stator current I_s and the main inductance $L_{\rm sp}$ when the other phases are nonexcited. Therefore, the single-phase main inductance can be expressed by using the peak values of the sinusoidal flux linkage and the sinusoidal phase current as

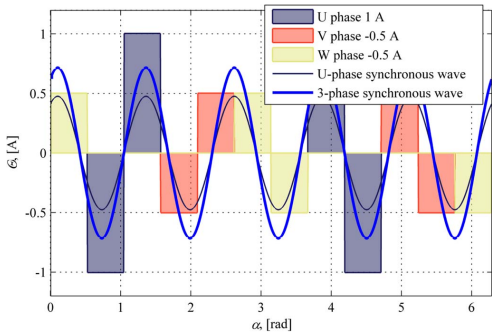

Fig. 1. Current linkage waveforms of a 12/10 TC-PMSM produced by the stator winding when the phase U carries its peak current. Although the mutual inductance seems negligible, also the phases V and W contribute to the synchronous current linkage harmonic in the TC machine resulting in a similar magnetizing inductance as in integral-slot machines.

$$L_{\rm sp} = \frac{\hat{\Psi}_{\rm sp}}{\hat{I}_s}. \tag{3}$$

The synchronous component of the air-gap flux density $B_{\rm sp}$ is sinusoidally distributed along the air gap. The peak value of the flux linkage $\Psi_{\rm sp}$ can, therefore, be expressed as

$$\hat{\Psi}_{\rm sp} = k_{\rm wp} N_s \frac{2}{\pi} \tau_p l' \hat{B}_{\rm sp} \tag{4}$$

where τ_p is the pole pitch, l' is the effective stator core length [14], [15], N_s is the number of phase turns in series, $k_{\rm wp}$ is the winding factor of the synchronous (operating) current linkage harmonic, the factor $2/\pi$ is the arithmetic per unit (p.u.) average value of a sinusoidal half-wave, and $\hat{B}_{\rm sp}$ is the peak value of the sinusoidal flux density in the air gap.

The synchronous component of the air-gap flux density $B_{\rm sp}$ produced by the stator current linkage $\Theta_{\rm sp}$ (see Fig. 1) is

$$\hat{B}_{\rm sp} = \mu_0 \frac{\hat{\Theta}_{\rm sp}}{\delta_{\rm ef}} = \frac{\mu_0}{\delta_{\rm ef}} \frac{4q}{\pi} \frac{z_Q}{c} k_{\rm wp} \hat{I}_s \tag{5}$$

where μ_0 is the permeability of vacuum $(4 \cdot \pi \cdot 10^{-7}\ \mathrm{V \cdot s/(A \cdot m)})$, $\delta_{\rm ef}$ is the effective air gap met by the stator synchronous current linkage component, q is the number of stator slots per pole and phase, z_Q is the number of stator conductors in a slot, the factor $c = 1$ is for single-layer windings, and the factor $c = 2$ is for double-layer windings. In the following, only double-layer windings are considered for simplicity. For double-layer windings, (5) can be rewritten as

$$\hat{B}_{\rm sp} = \frac{\mu_0}{\delta_{\rm ef}} \frac{4q}{\pi} \frac{m}{Q_s} k_{\rm wp} N_s \hat{I}_s \tag{6}$$

where m is the number of phases, and Q_s is the number of stator slots.

Combining (3), (4), and (6), the phase inductance can be found, i.e.,

$$L_{\rm sp} = \frac{2}{\pi}\tau_p l' \frac{\mu_0}{\delta_{\rm ef}} \frac{4q}{\pi} \frac{m}{Q_s} (k_{\rm wp} N_s)^2. \tag{7}$$

The effective air gap $\delta_{\rm ef}$ takes into account the magnetic voltage drops in the air gap (increased by the Carter factor [16]), in the stator teeth, in the permanent magnets, and in the rotor and stator yokes. The iron saturation effect should be also included here.

The magnetizing inductance L_m of an integral-slot rotating field winding is determined by multiplying (7) by a factor $m/2$ [7] that is due to the mutual inductance between the phases as the resultant current linkage wave is produced by all the m phases of the machine together, i.e.,

$$L_m = \frac{m}{2} L_{\rm sp} = \tau_p l' \frac{\mu_0}{\delta_{\rm ef}} \frac{4q}{Q_s} \left(\frac{m}{\pi} k_{\rm wp} N_s\right)^2. \tag{8}$$

Fig. 1 shows how the synchronous harmonic magnitude increases by a factor of $m/2$ also in a TC machine when the effects of all the three phases are taken into account. This happens although the real mutual coupling is low or almost nonexistent. Therefore, the magnetizing inductance of TC machines is calculated analogously to integral-slot machines, although the mutual inductance between the phases can be zero as in the case with the 12/10 machine.

B. Mutual Inductance Between Phases

The mutual inductance in TC machines behaves in a significantly more complicated way than in machines with integral-slot windings. For example, in a three-phase 12/10 machine, there is no V- or W-phase current linkage that could produce additional magnetic fluxes through the first phase winding (U). Fig. 1 illustrates how there are no sectors along the stator bore where the current linkages of different phases should interact. This justifies the use of a 12/10 machine as a fault-tolerant machine with magnetically decoupled phases and even provides an opportunity to build modular segmented stators with physically separate phase coil sections. Other machines having sectors of even numbers of adjacent coils of the same phase can be also built as modular machines, for instance, 12/14 or 24/20.

There are also other TC-PMSM topologies where the interaction between the current linkages of different phases is more complex. For example, an 18/16 machine has the current linkage waveforms of two phases, as illustrated in Fig. 2. In some sectors, the fluxes of different phases are summed up, but in other sectors, the fluxes weaken each other. Therefore, the mutual coupling factor m_c should be calculated as [10]

$$m_c = \frac{M_{\rm UV}}{L_U} = \frac{\int_0^{2\pi} \Theta_U \Theta_V \, d\alpha}{\int_0^{2\pi} \Theta_U \Theta_U \, d\alpha}. \tag{9}$$

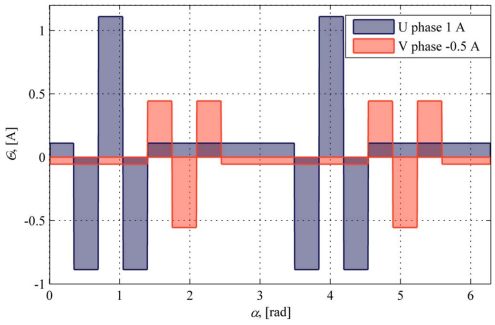

Fig. 2. Current linkage waveforms of two phases of an 18/16 TC-PMSM.

TABLE I
HARMONIC AIR GAP LEAKAGE FACTORS OF TC-PMSMS

Qs	2p	4	6	8	10	12	14	16	18	20
6	q	1/2		1/4	1/5		1/7	1/8		1/10
	$k_{\rm wp}$	0.866		0.866	0.5		0.5	0.866		0.866
	m_c	-0.5		-0.5	0		0	-0.5		-0.5
	σ_δ	**0.46**		**4.8**	**26**		**53**	**22**		**36**
9	q	3/4	1/2	3/8	3/10	1/4	3/14	3/16		3/20
	$k_{\rm wp}$		0.866	0.945	0.945	0.866	0.617	0.328		0.328
	m_c		-0.5	-0.039	-0.039	-0.5	-0.039	-0.039		-0.039
	σ_δ		**0.46**	**1.2**	**2.4**	**4.8**	**15**	**71**		**112**
12	q	1	2/3	1/2	2/5		2/7	1/4		1/5
	$k_{\rm wp}$			0.866	0.933		0.933	0.866		0.5
	m_c			-0.5	0		0	-0.5		0
	σ_δ			**0.46**	**0.96**		**2.9**	**4.8**		**26**
15	q	1 1/4	5/6	5/8	1/2		5/14	5/16		1/4
	$k_{\rm wp}$				0.866		0.951	0.951		0.866
	m_c				-0.5		-0.013	-0.013		-0.5
	σ_δ				**0.46**		**1.4**	**2.1**		**4.8**
18	q	1 1/2	1	3/4	3/5	1/2	3/7	3/8		3/10
	$k_{\rm wp}$					0.866	0.902	0.945		0.945
	m_c					-0.5	0	-0.039		-0.039
	σ_δ					**0.46**	**0.83**	**1.2**		**2.4**
21	q	1 3/4	1 1/6	7/8	7/10	7/12	1/2	7/16		7/20
	$k_{\rm wp}$						0.866	0.89		0.953
	m_c						-0.5	-0.007		-0.007
	σ_δ						**0.46**	**0.8**		**1.5**
24	q	2	1 1/3	1	4/5	2/3	4/7	1/2		2/5
	$k_{\rm wp}$							0.866		0.933
	m_c							-0.5		0
	σ_δ							**0.46**		**0.96**
27	q	2 3/4	1 1/2	1 3/8	9/10	3/4	9/14	9/16	1/2	9/20
	$k_{\rm wp}$								0.866	0.877
	m_c								-0.5	-0.004
	σ_δ								**0.46**	**0.75**

Unbalanced radial magnetic pull Invalid configurations

For integral-slot three-phase machines with essentially sinusoidal air-gap flux density, this factor is $m_c = -0.5$ [10]. For an 18/16 machine, the mutual coupling coefficient is $m_c = -0.0385$. A 12/10 machine has $m_c = 0$. Calculated mutual coupling coefficients m_c for different slot/pole combinations of TC-PMSMs are shown in Table I. A low value of m_c indicates a low magnetic coupling between the phases, which is beneficial from a machine's fault tolerance point of view.

If a fault occurs in one phase of a machine with $m_c = 0$, the magnetic flux densities in magnetic circuits of other phases will not be considerably influenced.

Although the mutual coupling m_c can be zero, it does not influence the equation of the magnetizing inductance (8). All the three phases contribute together to the magnetizing inductance (as shown in Fig. 1) even without air-gap interaction with each other, which is a distinctive feature of TC-PMSMs.

Table I only takes into account the mutual coupling m_c caused by the air-gap flux. Nevertheless, there are other magnetic couplings between the phases, namely, a coupling caused by the slot leakage flux and a coupling that is due to the end-winding leakage flux. The mutual coupling by the end-winding leakage flux is relatively weak in the TC-PMSMs as the end windings are compact, and different phases are usually coupled only through the air. The slot leakage mutual coupling, however, is strong when the coil sides of different phases are located in the same slot. This coupling is much more important and can make up to 50% of the total phase slot leakage inductance [12], [17] depending on the geometry and the winding layout.

C. Air-Gap Harmonic Leakage Inductance

Owing to the discrete nature of the TC windings, the current linkage generated by such a winding produces a very nonsinusoidal current linkage waveform in the air gap. This waveform contains a large proportion of current linkage harmonics, which produce harmonic magnetic fluxes [13]. These fluxes do not participate in the production of useful torque yet increase the armature reaction in the windings and thereby contribute to the leakage inductance. Additional eddy-current losses in the rotor are also generated [18]. The air-gap harmonic leakage inductance L_h can be defined as

$$L_h = \sigma_\delta L_m \tag{10}$$

where σ_δ is the harmonic air-gap leakage factor [8], [13], i.e.,

$$\sigma_\delta = \sum_{\substack{v=1 \\ v \neq p}}^{v=+\infty} \left(p \cdot \frac{k_{\mathrm{wv}}}{v \cdot k_{\mathrm{wp}}} \right)^2 \tag{11}$$

where k_{wv} is the winding factor of the vth spatial harmonic [13], [19]. The term $v = p$ represents the synchronous harmonic and, thus, the magnetizing inductance L_m component.

In TC machines, the highly distorted air-gap flux density strongly contributes to the air-gap harmonic leakage inductance. Possible subharmonic flux barriers in the stator and rotor, the slot openings, and the air-gap height can alter the spectrum of the air-gap flux density waveform and, thus, also the harmonic air-gap leakage factor, thereby influencing the rotor losses and torque [20]–[22].

Table I shows the calculated air-gap harmonic leakage factors σ_δ for different slot/pole combinations of TC-PMSMs. In addition, for these combinations, the numbers of slots per pole and phase q, the winding factors of synchronous harmonics k_{wv}, and the mutual coupling coefficients m_c are given.

As the magnetizing inductance L_m is a result of the current linkages of all the three phases, in a three-phase system, all third-order harmonics are excluded from the computation. In [13], the air-gap harmonic leakage coefficients σ_δ were erroneously calculated for single-phase current linkage waveforms taking into account the third-order harmonics. In Table I, this mistake is corrected.

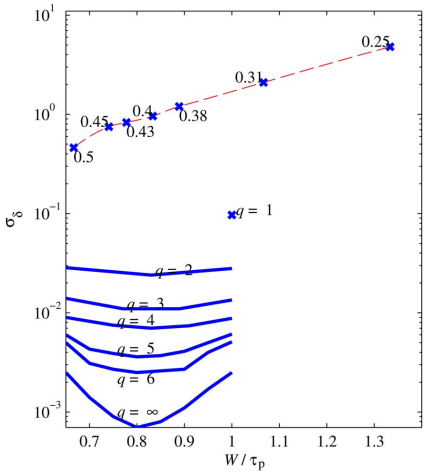

Fig. 3. Air-gap harmonic leakage factors σ_δ for integer-slot and TC winding machines versus the coil span W over the pole pitch τ_p (for TC windings, W is equal to slot pitch τ_u).

Table I enables the comparison of different TC-PMSMs. Combinations with higher air-gap harmonic leakage factors σ_δ have higher leakage inductances and, usually, also larger field weakening regions, but lower maximum torque at nominal speed (assuming that they have the same voltage limit).

A higher air-gap harmonic leakage factor may also indicate a higher amount of rotor losses resulting from asynchronous current linkage harmonics. Combinations with a very high σ_δ are not feasible at all, as their torque production is considerably limited by very high leakage inductances.

Fig. 3 shows that the trend specific for integral-slot machines [23]—machines with lower q have higher air-gap harmonic leakage factors σ_δ—is also valid for TC-PMSMs. However, in TC-PMSMs, the air-gap harmonic leakage factors σ_δ are significantly higher.

D. End-Winding Leakage Inductance

The end-winding leakage flux generally flows around the end-winding conductors through air. It can also flow through steel clamp rings, parts of the frame, or through the end laminations of the stator. Fig. 4 shows possible flux paths of the end-winding leakage.

The end-winding leakage inductance is a 3-D phenomenon. It requires a considerable effort to make a 3-D FEM model to accurately evaluate this leakage component. Solid parts having eddy currents also affect the paths of the magnetic fluxes and, thereby, the leakage inductance. Other leakage inductance components can be quite accurately evaluated by applying 2-D FEM machine models.

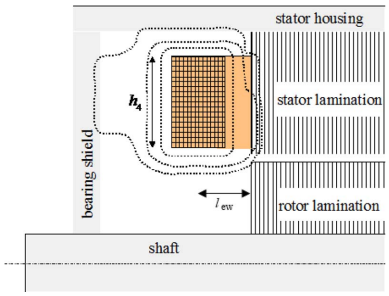

Fig. 4. End-winding leakage flux paths.

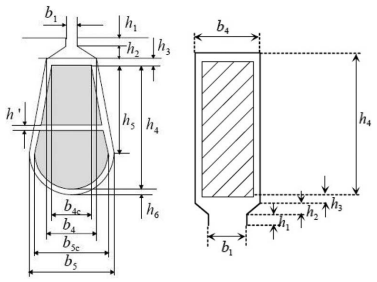

Fig. 5. Slot dimensions.

There are many empirical and analytical models to calculate the end-winding leakage inductances. However, these models give quite different results. Most of these models are developed for integral-slot distributed windings. For example, an empirical analytical model for calculating the end-winding leakage inductance L_{ew} is described in [7], i.e.,

$$L_{\mathrm{ew}} = \frac{4m}{Q_s}\mu_0 N_s^2 q l_w \lambda_{\mathrm{ew}} \tag{12}$$

where q is the number of slots per pole and phase, l_w is the average length of the end winding, and λ_{ew} is the end-winding leakage permeance factor, i.e.,

$$\lambda_{\mathrm{ew}} = \frac{2l_{\mathrm{ew}}\lambda_h + w_{\mathrm{ew}}\lambda_w}{l_w} \tag{13}$$

where l_{ew} is the axial length of the end winding measured from the end of the stack, λ_h is the empirical axial permeance factor, w_{ew} is the coil span, and λ_w is the empirical span permeance factor of the end winding.

The end-winding permeance factor λ_{ew} is usually determined relying on empirical values defined for various shapes of distributed end windings [7], [23], [24]. However, there are no end-winding permeance coefficients available for TC windings in the literature.

There is, however, a simple approach that can be used instead. In this approach, the end-winding sections of a TC-PMSM around the tooth can be considered halves of a solenoid. The end-winding leakage inductance of TC windings can be calculated by using an expression for an air-cored solenoid inductance, i.e.,

$$L_{\mathrm{sol}} = \mu_0\mu_{\mathrm{env}}\frac{\left(\frac{z_Q}{c}\right)^2 S}{h_4} \tag{14}$$

where h_4 is the height of the solenoid, S is the cross-sectional area, and μ_{env} is the relative permeability of the environment. Therefore, if the end turns are made as half-circles ($l_{\mathrm{ew}} = w_{\mathrm{ew}}/2$), the total inductance of the end windings of a double-layer winding can be expressed as

$$L_{\mathrm{ew}} = \frac{Q_s}{m}L_{\mathrm{sol}} = \mu_0\mu_{\mathrm{env}}\frac{Q_s}{m}\frac{\left(\frac{z_Q}{2}\right)^2 \pi l_{\mathrm{ew}}^2}{h_4}. \tag{15}$$

The relative permeability μ_{env} of air is 1. Nevertheless, because of the presence of iron parts in the vicinity (iron frame, end laminations of the stator stack), this factor can be chosen from the range of 1.2–2 depending on the materials and the compactness of the assembly of the machine end regions.

In [25], a more complex analytical empirical equation for evaluating the end-winding inductance is developed for TC windings. This equation takes into account the geometry of the end windings and the material of the core. A good correlation between the 3-D-FEM and the proposed method is found.

There is also a mutual coupling between the phases caused by the end-winding mutual inductance. Nevertheless, this coupling is very weak and can therefore be neglected without making a significant error [17].

E. Slot Leakage Inductance

The current flowing inside the slot conductors produces a flux, part of which crosses the air gap, the rest passing across the slot from one tooth to another [see Fig. 6(a) and (b)]. The latter part produces an inductance component L_u, which is called the slot leakage inductance.

The slot leakage inductance is analytically calculated by

$$L_u = \frac{4m}{Q_s}\mu_0 N_s^2 l' \lambda_u \tag{16}$$

where λ_u is the slot leakage permeance factor [7], [23], [24], [26].

The slot leakage permeance factor is calculated assuming that the leakage flux passes straight from one side of the slot to the other side crossing the center line of the slot in the orthogonal direction. The parameter λ_u is calculated using the slot dimensions in Fig. 5. The slot leakage permeance factor for a double-layer winding and horizontally divided layers can be calculated as [7], [10]

$$\lambda_u = k_1\frac{h_4 - h'}{3b_4} + k_2\left(\frac{h_3}{b_4} + \frac{h_1}{b_1} + \frac{h_2}{b_4 - b_1}\ln\frac{b_4}{b_1}\right) + \frac{h'}{4b_4} \tag{17}$$

where the factors k_1 and k_2 take into account the mutual inductance when the coils of different phases are present in one slot [17]. Without making a significant error, (17) can be also used for vertically divided layers. The factors k_1 and k_2 are calculated as

$$k_1 = \frac{5+3g}{8} \quad k_2 = \frac{1+g}{2} \quad g = \frac{1}{n_{\mathrm{ps}}}\sum_{n=1}^{n_{\mathrm{ps}}}\cos\gamma_n \tag{18}$$

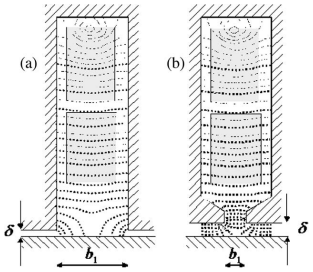

Fig. 6. Slot and tooth-tip leakage flux lines. (a) and (b) Open slot and semiclosed slot with the slot opening b_1 and the air gap δ, respectively.

where g is the average value of the temporal phase angle variation γ_n between the coils in the $n_{\rm ps}$ slots, where the coils of one phase are located. For a 12/10 machine, $g = 0.75$, and for a 9/8 machine, $g = 0.83$.

The slot leakage inductance is modeled assuming that the leakage flux lines crossing the slot are straight. Nevertheless, this is not completely true, particularly in the region close to the air gap, where the flux lines are bent because of the proximity of the iron parts of the rotor [27]. This fringing flux leakage in the slot close to the air gap can be taken into account by a tooth-tip leakage inductance model.

F. Tooth-Tip Leakage Inductance

The sum of the slot and tooth-tip leakage inductances is increased when the slot openings are narrow and the air gap is long. Instead, when the air gap is short and the slot openings are wide, as in the case of PMSMs with open slots, the sum of the slot and tooth-tip leakage inductances is decreased, as shown in Fig. 6(a). The flux in the slot bends toward the rotor decreasing the slot leakage.

This change in the slot leakage is taken into account by the tooth-tip leakage inductance $L_{\rm tt}$. In the case of large b_1/δ (open slots), $L_{\rm tt}$ can be even negative, making necessary corrections to the slot leakage inductance calculations. Thus

$$L_{\rm tt} = \frac{4m}{Q_s}\mu_0 N_s^2 l' k_2 \lambda_{\rm tt} \tag{19}$$

where $\lambda_{\rm tt}$ is the tooth-tip leakage permeance factor, and k_2 is a factor that takes into account the presence of different phases in a slot (18).

The permeance factor can be empirically calculated according to Richter and Brüderlink [23] or Müller *et al.* [24] and Voldek [26] (see Fig. 7). The model of Müller *et al.* gives better results as it allows negative values of $\lambda_{\rm tt}$ in the case of open slots and a short air gap. When the slot openings are narrow, $\lambda_{\rm tt}$ is considerable and positive. However, when the slot openings are wide, $\lambda_{\rm tt}$ becomes negative. The permeance factor can be calculated according to [24] and [26] as

$$\lambda_{\rm tt} = \frac{1}{2\pi}\left[\ln\left(\frac{\delta^2}{b_1^2}+\frac{1}{4}\right) + 4\frac{\delta}{b_1}\arctan\frac{b_1}{2\delta}\right]. \tag{20}$$

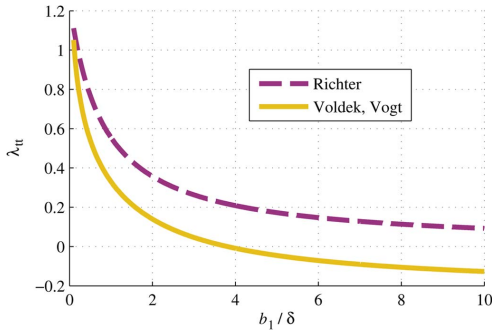

Fig. 7. Permeance factor of the tooth-tip leakage [23], [24], [26].

For surface permanent magnet (SPM) configurations, the air-gap length δ should include the physical air gap and the height of the magnets divided by the relative permeability $h_{\rm PM}/\mu_{\rm rPM}$ of the permanent magnet material. For an interior permanent magnet (IPM) configuration, only the physical air gap should be included in the tooth-tip leakage calculation.

III. Machine Performance

The maximum torque at a certain speed and voltage depends on the synchronous inductance of the machine. The per-unit equation for the maximum torque $T_{\rm max}$ of a nonsalient pole PMSM (1) is given in Section I. Combining (1), (2), and (10), we obtain

$$T_{\rm max} = \frac{pmE_{\rm PM}U_{\rm ph}}{\omega^2\left(L_m(1+\sigma_\delta)+L_{\rm ew}+L_u+L_{\rm tt}\right)}. \tag{21}$$

To reach a large overload capability (potential maximum torque at the rated speed and voltage) of the machine, the synchronous inductance should be small. As $E_{\rm PM}$ is proportional to L_m, it is not necessarily feasible to decrease the magnetizing inductance L_m when aiming to improve the performance of a machine according to (21). Hence, if the target is to increase the torque production of a machine, the leakage components of the synchronous inductance should rather be decreased. In the following, actions to increase $T_{\rm max}$ are outlined.

Different TC machines have different air-gap harmonic leakage factors. Therefore, machine topologies with low air-gap harmonic leakage factors should be selected. However, in some cases, such as in traction applications, a high leakage may be needed to obtain a long field-weakening range using a low demagnetizing current. Therefore, a topology with a high air-gap leakage may be advisable. Subharmonic flux barriers should be used to decrease the subharmonic component of the air-gap harmonic leakage inductance L_h. These flux barriers can be used in the rotor construction [21] and, in some cases, also in the stator construction [20]. Furthermore, the flux barriers considerably decrease the core losses. The effect of flux barriers on saliency should be also taken into account when flux barriers are used.

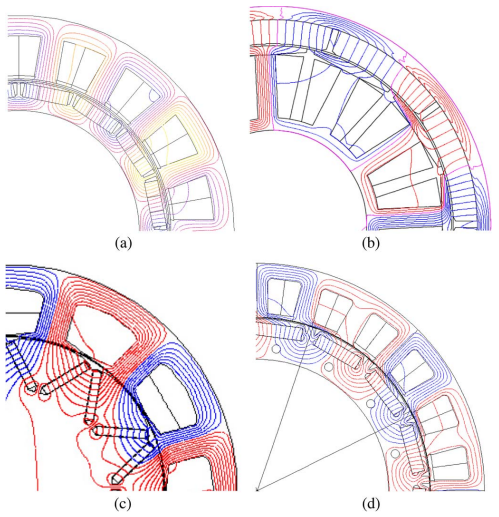

Fig. 8. Test machine geometries (not in scale). (a) 26 kW 18/16 IPM. (b) 4.7 kW 12/10 SPM outer solid rotor. (c) 45 kW 12/10 V-shaped IPM with a complex rotor geometry. (d) 110 kW 24/16 IPM.

End-winding leakage inductance $L_{\rm ew}$ can be decreased if the coils are wound as tight as possible. Clamping rings from stainless steel or other nonmagnetic material should be used for the stack assembly. The frame should be preferably nonmagnetic.

The slot leakage inductance L_u can be minimized by avoiding deep slots. To achieve a high torque density, the aspect ratio (height/width) of the slot should be as small as possible (even close to 1).

Considering the tooth-tip leakage inductance component $L_{\rm tt}$, open slots and nonmagnetic wedges should be used. This, however, also affects the magnetizing inductance by increasing the equivalent air gap in the rotor SPM configuration. The height of the air gap can be optimized by the FEM considering its effects on the magnetizing and leakage inductances and core losses.

IV. Experimental Results

Several radial flux double-layer TC-PMSMs were analytically designed. Their performances were predicted based on the estimated inductances. Then, FEM models were constructed and simulated. After that, prototypes were built, and parameters were measured. The measurement results were also practically supported by the identification run results with ACS M1 converters by ABB. The flux lines of the machines under the loading conditions are depicted in Fig. 8(a)–(d).

Table II shows the analytically estimated inductances for four different TC-PMSMs with the p.u. values in brackets. The p.u. values of the machines are based on the rated voltages, currents, and frequencies of the machines. For the 4.7-kW 12/10 machine, the values of slot and tooth-tip leakage inductances are overestimated, as saturation of the long tooth tips is not correctly accounted during analytical calculations. Simultaneously, the air-gap harmonic leakage inductance is overestimated because of the machine's solid nonlaminated rotor construction. Such a solid rotor damps the harmonic fluxes by the induced eddy currents. However, the constant dc flux produced by the synchronous harmonic is not dampened.

TABLE II
Calculated Inductance Components for Four TC-PMSMs

Component	26 kW 18/16	4.7 kW 12/10	45 kW 12/10	110 kW 24/16
$L_{\rm ew}$, [mH]	0.43 (0.10)	0.17 (0.01)	0.34 (0.03)	0.01 (0.01)
$L_{\rm u}$, [mH]	0.73 (0.18)	4.6 (0.21)	2.33 (0.19)	0.19 (0.12)
$L_{\rm tt}$, [mH]	0.03 (0.01)	3.8 (0.18)	-0.02 (-0.01)	-0.05 (-0.03)
$L_{\rm h}$, [mH]	0.63 (0.15)	2.6 (0.12)	3.27 (0.27)	0.22 (0.14)
$L_{\rm md}$, [mH]	0.53 (0.13)	2.8 (0.13)	3.41 (0.28)	0.44 (0.28)
$L_{\rm sd}$, [mH]	2.34 (0.56)	14.0 (0.65)	9.33 (0.76)	0.82 (0.52)

The complex geometry of the 45-kW 12/10 machine complicates the analytical estimation of the effective air gap. The presence of several magnets and multiple iron bridges and iron webs together with the nonlinear characteristics of the iron adds to the complexity of the analytical estimations. Such a complex geometry essentially requires FEM modeling in order to accurately estimate the machine parameters.

Experimental validation of the proposed analytical model is somewhat difficult. There is a standard method of measuring the stator leakage inductance with the rotor removed (IEC 60034-4, A39–A40); however, this method in current reading is applicable only for traditional distributed winding machines with $q \geq 1$ and does not accurately take into account the air-gap harmonic and tooth-tip leakage inductances of TC-PMSMs. It is practically very difficult to separately measure various inductance components, and therefore, an indirect validation method that only evaluates the total synchronous inductance $L_{\rm sd}$ is used.

The short-circuit test gives a higher value for the synchronous inductance when compared with the inductance in the nominal point because the stator core is not saturated during the short circuit. Therefore, the short-circuit tests are not feasible for the accurate estimation of synchronous inductances, particularly for high-torque-density machines operating deep in the saturation region. The total synchronous inductance was estimated by the FEM by performing zero-load-angle $\delta_{\rm load} = 0$ simulations using

$$L_{\rm sd} = \frac{U_{\rm ph} - E_{\rm PM}}{\omega I_s}. \tag{22}$$

During the zero-load-angle simulations, the $U_{\rm ph}$ was decreased well below the $E_{\rm PM}$ value or increased in order to reach the nominal current I_s. The average value of the synchronous inductance between the low and high supply voltage zero-load-angle tests is given in Table III for each machine. The analytically estimated synchronous inductances and the inductances measured by the M1s during the identification runs are also quantified.

TABLE III
SYNCHRONOUS INDUCTANCES FOR FOUR TC-PMSMs

	26 kW 18/16	4.7 kW 12/10	45 kW 12/10	110 kW 24/16
FEM ($\delta_{\text{load}} = 0$)	2.26 mH	12.7 mH	10.7 mH	0.83 mH
Measurements (ID)	2.33 mH	12.9 mH	11.2 mH	0.84 mH
Analytical	2.34 mH	14.0 mH	9.33 mH	0.82 mH

The error between the analytically calculated, experimental, and FEM-modeled inductance values is about 17%. The analytical model does not take into account the excessive saturation of the teeth heads and the cross-saturation effects, which can be accurately taken into account only by the FEM [28], [29]. If semimagnetic slot wedges are used, the saturation at the stator teeth heads is decreased, which can be also accurately estimated only by the FEM. However, the analytical model is accurate enough to be used for the performance evaluation of TC-PMSMs at early design stages.

V. CONCLUSION

In this paper, a quantitative and comparative study has been conducted to further develop the analytical calculation technique of different inductance components of TC machines. This paper re-evaluates the applicability of analytical calculation methods for the different inductance components of a TC machine. The approaches to calculate the components of the synchronous inductance have been discussed, and analytical equations have been proposed and validated.

In particular, it has been shown that the performance of TC-PMSMs is highly dependent on the leakage inductances, particularly the air-gap harmonic leakage inductance, which often appears to be the dominating component of all the inductance components in TC-PMSMs. Table I could be used by machine designers at an initial design of a TC-PMSM when selecting the winding configuration. The choice should be mainly based on the selection of an appropriate combination of the number of poles, the air-gap leakage factor, and the mutual inductance coefficient. This choice influences the operating frequency of the machine, the rotor losses, the torque production capability, and the field-weakening performance, as well as the short-circuit current and fault-tolerance characteristics of the machine.

To sum up, it is concluded that accurate calculation of the inductances is essential when the performance of a machine is estimated at the early stages of the electrical machine design.

REFERENCES

[1] A. EL-Refaie, "Fractional-slot concentrated-windings synchronous permanent magnet machines: Opportunities and challenges," *IEEE Trans. Ind. Electron.*, vol. 57, no. 1, pp. 107–121, Jan. 2010.

[2] J. Cros and P. Viarouge, "Synthesis of high performance pm motors with concentrated windings," *IEEE Trans. Energy Convers.*, vol. 17, no. 2, pp. 248–253, Jun. 2002.

[3] F. Magnussen and C. Sadarangani, "Winding factors and joule losses of permanent magnet machines with concentrated windings," in *Proc. IEEE IEMDC*, 2003, vol. 1, pp. 333–339.

[4] A. El-Refaie, Z. Zhu, T. Jahns, and D. Howe, "Winding inductances of fractional slot surface-mounted permanent magnet brushless machines," in *Conf. Rec. IEEE IAS Annu. Meet.*, 2008, pp. 1–8.

[5] Z. Zhu, D. Howe, and J. Mitchell, "Magnetic field analysis and inductances of brushless dc machines with surface-mounted magnets and non-overlapping stator windings," *IEEE Trans. Magn.*, vol. 31, no. 3, pp. 2115–2118, May 1995.

[6] N. Bianchi, S. Bolognani, M. Pre, and G. Grezzani, "Design considerations for fractional-slot winding configurations of synchronous machines," *IEEE Trans. Ind. Appl.*, vol. 42, no. 4, pp. 997–1006, Jul./Aug. 2006.

[7] J. Pyrhönen, T. Jokinen, and V. Hrabovcová, *Design of Rotating Electrical Machines*. Hoboken, NJ, USA: Wiley, 2008.

[8] G. Huth, "Permanent-magnet-excited ac servo motors in tooth-coil technology," *IEEE Trans. Energy Convers.*, vol. 20, no. 2, pp. 300–307, Jun. 2005.

[9] E. Schmidt and M. Susic, "Parameter evaluation of permanent magnet synchronous machines with tooth coil windings using the frozen permeabilities method with the finite element analyses," in *Proc. IEEE 25th CCECE*, 2012, pp. 1–5.

[10] J. Hendershot and T. Miller, *Design of Brushless Permanent Magnet Motors*. Lebanon, OH, USA: Magna Physics, 1994.

[11] *Standart IEC60027-1: Letter Symbols to be Used in Electrical Technology*, IEC60027-1, 1995, International Electrotechnical Commission.

[12] R. Dutta, M. F. Rahman, and L. Chong, "Winding inductances of an interior permanent magnet (IPM) machine with fractional slot concentrated winding," *IEEE Trans. Magn.*, vol. 48, no. 12, pp. 4842–4849, Dec. 2012.

[13] P. Ponomarev, P. Lindh, and J. Pyrhönen, "Effect of slot-and-pole combination on the leakage inductance and the performance of tooth-coil permanent-magnet synchronous machines," *IEEE Trans. Ind. Electron.*, vol. 60, no. 10, pp. 4310–4317, Oct. 2013.

[14] J. Pyrhönen, V. Ruuskanen, J. Nerg, J. Puranen, and H. Jussila, "Permanent-magnet length effects in ac machines," *IEEE Trans. Magn.*, vol. 46, no. 10, pp. 3783–3789, Oct. 2010.

[15] V. Ruuskanen, J. Nerg, M. Niemela, J. Pyrhönen, and H. Polinder, "Effect of radial cooling ducts on the electromagnetic performance of the permanent magnet synchronous generators with double radial forced air cooling for direct-driven wind turbines," *IEEE Trans. Magn.*, vol. 49, no. 6, pp. 2974–2981, Jun. 2013.

[16] H. VuXuan, D. Lahaye, H. Polinder, and J. Ferreira, "Improved model for design of permanent magnet machines with concentrated windings," in *Proc. IEEE IEMDC*, 2011, pp. 948–954.

[17] S. Chevailler, L. Feng, and A. Binder, "Short-circuit faults in distributed and concentrated windings of PM synchronous motors," in *Proc. Eur. Conf. Power Electron. Appl.*, 2007, pp. 1–10.

[18] E. Fornasiero, N. Bianchi, and S. Bolognani, "Slot harmonic impact on rotor losses in fractional-slot permanent-magnet machines," *IEEE Trans. Ind. Electron.*, vol. 59, no. 6, pp. 2557–2564, Jun. 2012.

[19] F. Scuiller, E. Semail, and J.-F. Charpentier, "General modeling of the windings for multi-phase ac machines," *Eur. Phys. J. -Appl. Phys.*, vol. 50, no. 3, pp. 1–15, 2010.

[20] G. Dajaku and D. Gerling, "A novel 12-teeth/10-poles pm machine with flux barriers in stator yoke," in *Proc. 20th ICEM*, 2012, pp. 36–40.

[21] L. Alberti, E. Fornasiero, and N. Bianchi, "Impact of the rotor yoke geometry on rotor losses in permanent-magnet machines," *IEEE Trans. Ind. Appl.*, vol. 48, no. 1, pp. 98–105, Jan./Feb. 2012.

[22] M. Barcaro and N. Bianchi, "Torque ripple reduction in fractional-slot interior PM machines optimizing the flux-barrier geometries," in *Proc. 20th ICEM*, 2012, pp. 1496–1502.

[23] R. Richter and R. Brüderlink, *Allgemeine Berechnungselemente. Die Gleichstrommaschinen,* Ser. Elektrische Maschinen. Basel, Switzerland: Birkhäuser, 1964.

[24] G. Müller, K. Vogt, and B. Ponick, *Berechnung elektrischer Maschinen,* Ser. Berechnungelektrischer Maschinen, no. Bd. 2. Hoboken, NJ, USA: Wiley, 2008.

[25] J. H. J. Potgieter and M. Kamper, "Evaluation of calculation methods and the effect of end-winding inductance on the performance of non overlap winding PM machines," in *Proc. 20th ICEM*, 2012, pp. 243–249.

[26] A. I. Voldek, *Electrical Machines*. Leningrad, Russia: Energy, 1974.

[27] H. Grop, J. Soulard, and H. Persson, "Stator slot leakage in ac-machines equipped with fractional conductor windings," in *Proc. ICEMS*, 2009, pp. 1–6.

[28] K. Meessen, P. Thelin, J. Soulard, and E. Lomonova, "Inductance calculations of permanent-magnet synchronous machines including flux change and self- and cross-saturations," *IEEE Trans. Magn.*, vol. 44, no. 10, pp. 2324–2331, Oct. 2008.

[29] B. Stumberger, G. Stumberger, D. Dolinar, A. Hamler, and M. Trlep, "Evaluation of saturation and cross-magnetization effects in interior permanent-magnet synchronous motor," *IEEE Trans. Ind. Appl.*, vol. 39, no. 5, pp. 1264–1271, Sep./Oct. 2003.

Authors' photographs and biographies not available at the time of publication.

Publication VII

Ponomarev, P., Petrov, I., and Pyrhönen, J., "Influence of Travelling Current Linkage Harmonics on Inductance Variation, Torque Ripple and Sensorless Capability of Tooth-Coil Permanent-Magnet Synchronous Machines," *IEEE Transactions on Magnetics* , vol.50, no.1, pp.1−8, Jan. 2014

Influence of Travelling Current Linkage Harmonics on Inductance Variation, Torque Ripple and Sensorless Capability of Tooth-Coil Permanent-Magnet Synchronous Machines

Pavel Ponomarev, Ilya Petrov, and Juha Pyrhönen

Laboratory of Electrical Drives Technology, Lappeenranta University of Technology, 53850 Lappeenranta, Finland

This paper introduces an important source of torque ripple in permanent-magnet synchronous machines with tooth-coil windings (TC-PMSMs). It is theoretically proven that saturation and cross-saturation phenomena caused by the nonsynchronous harmonics of the stator current linkage cause a synchronous inductance variation with a particular periodicity. This, in turn, determines the magnitude of the torque ripple and can also deteriorate the performance of signal-injection-based rotor position estimation algorithms. An improved dq-inductance model is proposed. It can be used in torque ripple reduction control schemes and can enhance the self-sensing capabilities of TC-PMSMs.

***Index Terms*—Current linkage harmonics, high torque density, inductance model, permanent-magnet machines, saturation, sensorless control, TC-PMSM, tooth-coil winding, torque ripple.**

I. Introduction

THE dq-model, or rotor flux oriented model for rotating ac electrical machines, was originally introduced to simplify the analysis and control of multi-phase electric motor drives. It significantly reduces the number of control variables. The dq-model is the enabling technique for controlled ac machine drives and the most important concept to understanding how field-oriented control works.

After the transformation of 3-phase quantities to the dq-quantities the voltages are defined by a two-component vector U_{dq} instead of a 3-component vector U_{UVW}. The vector model of a PMSM in the rotor-flux-oriented frame (dq-coordinates) consists of

$$U_{\mathrm{d}} = R_{\mathrm{s}} i_{\mathrm{d}} + \frac{\mathrm{d}\Psi_{\mathrm{d}}}{\mathrm{d}t} - \omega \Psi_{\mathrm{q}} \tag{1}$$

$$U_{\mathrm{q}} = R_{\mathrm{s}} i_{\mathrm{q}} + \frac{\mathrm{d}\Psi_{\mathrm{q}}}{\mathrm{d}t} + \omega \Psi_{\mathrm{d}} \tag{2}$$

$$T_{\mathrm{e}} = \frac{3}{2} p (\Psi_{\mathrm{d}} i_{\mathrm{q}} - \Psi_{\mathrm{q}} i_{\mathrm{d}}) \tag{3}$$

$$\Psi_{\mathrm{d}} = L_{\mathrm{d}} i_{\mathrm{d}} + \Psi_{\mathrm{PM}} \tag{4}$$

$$\Psi_{\mathrm{q}} = L_{\mathrm{q}} i_{\mathrm{q}} \tag{5}$$

where U_{d} and U_{q} are the d- and q-axis components of the stator voltage, Ψ_{d} and Ψ_{q} are the d- and q-axis components of the airgap flux linkage, T_{e} is the electromagnetic torque, i_{d} and i_{q} are the d- and q-axis components of the stator current and Ψ_{PM} is the permanent-magnet flux linkage.

The dq-model is widely used in electrical drives. The vector control and field-oriented control techniques take their origins from the dq-model of the machine.

Manuscript received August 12, 2013; revised September 02, 2013; accepted September 19, 2013. Date of publication September 23, 2013; date of current version December 23, 2013. Corresponding author: P. Ponomarev (e-mail: pavel.ponomarev@lut.fi).

Color versions of one or more of the figures in this paper are available online at http://ieeexplore.ieee.org.

Digital Object Identifier 10.1109/TMAG.2013.2283067

There are several assumptions under which the dq-transformation is valid:

- materials have linear characteristics (no saturation);
- windings are assumed to create sinusoidal waveforms for flux densities, flux linkages, and back-EMFs, being supplied with sinusoidal currents.

Such assumptions are quite well valid for three-phase integral slot winding machines, however, tooth-coil windings produce significant amounts of current linkage harmonics, which rotate asynchronously with the rotor and may locally saturate iron core.

The analysis of a tooth-coil permanent-magnet synchronous machine (TC-PMSM) can be based on a fact that the operation of the machine takes place not at the fundamental current linkage harmonic, but at a higher order harmonic. In case of a 9/8 machine (base machine for 18/16) the operating (synchronous) harmonic is the 4th one. Correspondingly, in a 12/10-machine the operating harmonic is the 5th harmonic. The frequencies and the pole pitches of these synchronous harmonics correspond to the frequencies and pole pitches of the rotor-created travelling flux linkage waveforms.

Fig. 1 shows the current linkage harmonics of a 9/8 double layer TC-PMSM–the base machine for the 18/16 TC-PMSM [1]. The spectrum includes the magnitude of the main working harmonic, which is the 4th, and the magnitudes of other current linkage travelling harmonics in the air gap. The relative strengths of the first and the second harmonics–the sub-harmonics rotating faster than the operating harmonic–are high enough to cause adverse effects in the machine [2].

The waves of the current linkage harmonics spectrum for a 9/8 TC-PMSM at a time instant when $i_{\mathrm{U}} = 1$ A, $i_{\mathrm{V}} = -0.5$ A and $i_{\mathrm{W}} = -0.5$ A are illustrated in Fig. 2. During sinusoidal current supply these current linkage harmonics have the same angular speed as the main working harmonic. However, because of the fact that their pole pitches are different, the rotation speed along the stator bore of the harmonic with the lowest order is the fastest (e.g., if the 4th harmonic has travelled once around the circumference, the 1st has rotated four times around the circumference). The sub-harmonics have the widest pole pitches

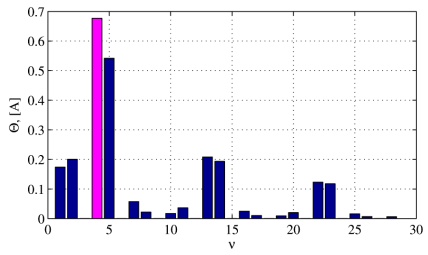

Fig. 1. Current linkage harmonics of a 9/8 machine.

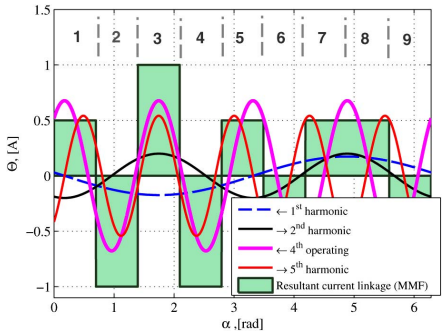

Fig. 2. Travelling current linkage harmonic waves in the air gap of a 9/8 machine. $i_{\mathrm{U}} = 1$ A, $i_{\mathrm{V}} = -0.5$ A and $i_{\mathrm{W}} = -0.5$ A. Tooth numbers are shown above the waveforms.

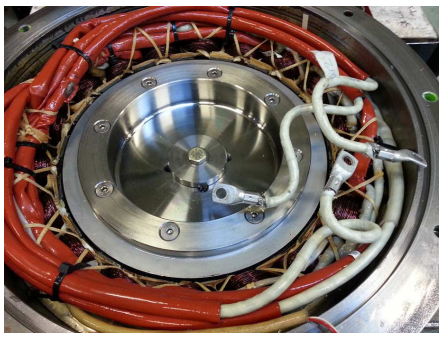

Fig. 3. A photograph of the inside of the 18/16 machine.

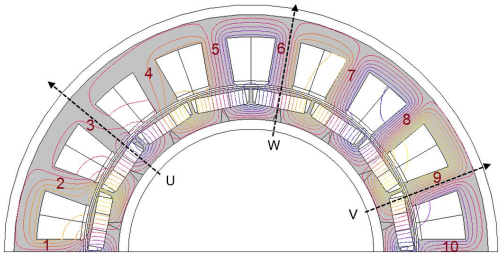

Fig. 4. The modelled 9/8 base machine of the 18/16 machine with flux lines at full loading conditions ($i_{\mathrm{d}} = -30$ A, $i_{\mathrm{q}} = 120$ A). FEM modeling, Rotangle $\Theta = 0$. None of the phase magnetic axes are ideally aligned with the magnetic axes of the rotor. Even though there is the fundamental present in the flux it is so weak that it cannot been observed in the plot. Teeth are numbered.

and, therefore, tend to penetrate deep in the rotor. Having high speed on the rotor surface the sub-harmonics easily cause a lot of losses in conducting parts of the rotor. Therefore, as it was also proven in [3], the current linkage sub-harmonics are the main cause of the losses in the rotor and the permanent magnets. However, the main objective of this article is not the estimation of the losses due to asynchronous harmonics, but the analysis of the influence of these harmonics on the synchronous inductance and, consequently, on the electromagnetic torque quality (smoothness).

The synchronous harmonic order of a 9/8 TC-PMSM is $\nu = 4$ and harmonic travels to the positive direction with the rotor. The 1st harmonic and the 7th also travel to the positive direction, whereas, the 2nd and 5th harmonics travel to the opposite direction.

In this paper it is shown that saturation and cross-saturation should be included in the dq-model of TC-PMSMs, especially for high-torque-density TC-PMSMs, in order to model their behaviour completely. It is also indicated that the saturation due to the asynchronously-rotating low-order current linkage harmonics produces a considerable torque ripple (5% at the nominal point of the analysed TC-PMSM).

Section II describes saturation and cross-saturation effects in TC-PMSMs. Section III discusses the influence of saturation and cross-saturation on the use of the high-frequency signal-injection methods in sensorless (or self-sensing) control. Section IV explains that the classical inductance model is not reliable enough when applied to TC-PMSMs; the variation of the synchronous inductance with the rotor position should be also considered for this type of machine. Section V explains that the inductance variation is the main cause for the torque ripple in TC-PMSMs. Finally, Section VI shows approaches to take into account this inductance variation during the design of a TC-PMSM and using an improved dq-model.

Examples and FEM modeling are given for an 18/16 TC-IPMSM which was reported in earlier publications [1], [4]. The outlines of this machine are shown in Figs. 3 and 4.

II. Role of Saturation and Cross Saturation

In real machines the electrical steel lamination is subjected to saturation. Therefore, the first assumption in the dq-model is not fulfilled. Usage of such electrical steel imposes the non-linear dependency of magnetic flux linkage on the armature current. It means that the synchronous inductances along the d- and q-axes are not constants and depend on the magnetic state of the machine [5]. Usually, this effect is ignored and vector control of electric motor drives is implemented with the assumption that the dq-synchronous inductances are constants. However, in cases where variable speeds and torques are required (e.g., in traction applications), saturation can have a dramatic effect on the torque ripple at low speeds, or in the field-weakening region [6].

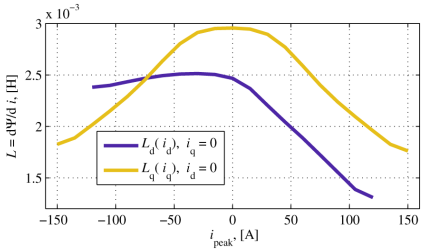

Fig. 5. Inductance variations due to the saturation effect. FEM modeling. Sinusoidal current supply.

A. Saturation

The d-axis current i_d influences the saturation along the d-axis flux path which, in turn, changes the d-axis synchronous inductance L_d of the machine. The same is valid also for q-axis current i_q and the q-axis inductance L_q. Also cross-saturation is present.

When dealing with the non-linear saturation effect the machine model should use differential (incremental) inductances which better represent the local changes of the flux linkages $\partial\Psi_\mathrm{d,q}$ depending on the current changes $\partial i_\mathrm{d,q}$ [7]. The differential inductances can be derived according to

$$L_\mathrm{d,q} = \frac{\partial\Psi_\mathrm{d,q}(i_\mathrm{d,q})}{\partial i_\mathrm{d,q}} \approx \frac{\Delta\Psi_\mathrm{d,q}(i_\mathrm{d,q})}{\Delta i_\mathrm{d,q}}. \tag{6}$$

Fig. 5 shows the L_d and L_q inductances behavior due to the saturation effect. The plots are obtained by linearization of differential inductances with discretization on a grid of the peak phase current with a step of $\Delta i_\mathrm{d,q} = 15$ A.

These direct and quadrature inductance values $L_\mathrm{d}(i_\mathrm{d})$ and $L_\mathrm{q}(i_\mathrm{q})$ can be embedded into the machine model and, therefore, the saturation effect can be taken into account. In this case the model equations (4) and (5) look as follows:

$$\Psi_\mathrm{d} = L_\mathrm{d}(i_\mathrm{d})i_\mathrm{d} + \Psi_\mathrm{PM}(i_\mathrm{d}, i_\mathrm{q}) \tag{7}$$

$$\Psi_\mathrm{q} = L_\mathrm{q}(i_\mathrm{q})i_\mathrm{q}. \tag{8}$$

It should be noted that the Ψ_PM is also dependent on the level of saturation and is a function of the current. However, the influence of saturation on PM flux linkage and back-EMF is not the main scope of this study. This influence is very complex and strongly depends on the operating point. Separate study should cover the influence of saturation and cross-saturation on the back-EMF and torque production in order to build an accurate model according to (7). In this paper the back-EMF (and Ψ_PM) variation is not studied. Only the inductance variation is under the scope.

Modern controllers of PMSMs can have dq-inductances stored in look-up tables in the memory [7].

B. Cross-Saturation

As shown in [5] in PMSMs the individual axis analysis is not sufficient for accurate modeling. There is also a cross-saturation effect [8] when dq-axes inductances depend on both current components i_d and i_q simultaneously. It happens because, e.g., the q-axis current can saturate direct magnetic axis and d-axis current can influence the magnetic state of the q-axis. Therefore, the cross-saturation effect should be taken into account by calculating the dq-inductances as functions of two variables according to

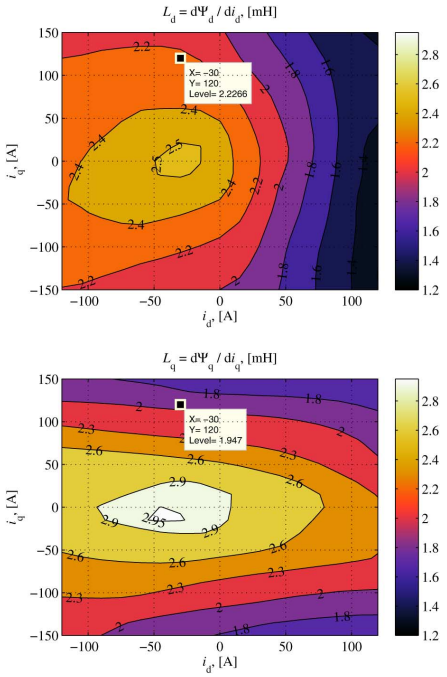

Fig. 6. Direct-axis synchronous differential inductance L_d (top) and quadrature-axis synchronous differential inductance L_q (bottom) maps taking saturation and cross-saturation effects into account. FEM modeling. Rotor position is the same as shown in Fig. 4. Inductance maps are not symmetrical relatively d-axis. Length of a current vector in i_d, i_q-plane corresponds to the peak phase sinusoidal current.

$$L_\mathrm{d,q} = \frac{\partial\Psi_\mathrm{d,q}(i_\mathrm{d,q}, i_\mathrm{q,d})}{\partial i_\mathrm{d,q}} \approx \frac{\Delta\Psi_\mathrm{d,q}(i_\mathrm{d,q}, i_\mathrm{q,d})}{\Delta i_\mathrm{d,q}}. \tag{9}$$

Fig. 6 shows inductance maps (plots from functions of two variables) obtained by (9) where fluxes and currents are simulated using FEM. Values are obtained by linearization of the differential inductances at operating points with the step size $\Delta i_\mathrm{d,q} = 15$ A of peak phase current.

It can be noticed that the q-axis synchronous inductance L_q saturates fast with increasing q-axis current. This is a result of the thin iron webs between the magnets in the rotor construction as it can be seen in Fig. 4.

With 3-D look-up tables of $L_\mathrm{d}(i_\mathrm{d}, i_\mathrm{q})$ and $L_\mathrm{q}(i_\mathrm{q}, i_\mathrm{d})$ stored in the memory of the motor drive controller, the saturation and cross-saturation effects can be taken into account, and optimal control trajectories (e.g., maximum torque per ampere (MTPA) or maximum efficiency control) can be calculated [9], [10]. The

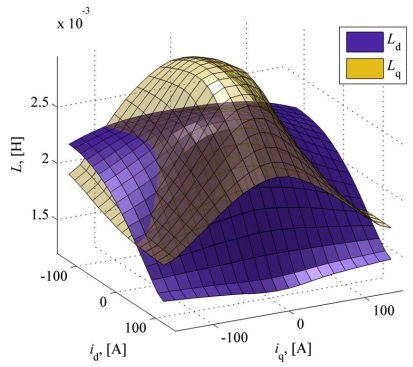

Fig. 7. Intersection of the d- and q-axis inductances. FEM modeling. Operation near the lines of intersection is not recommended for sensorless control.

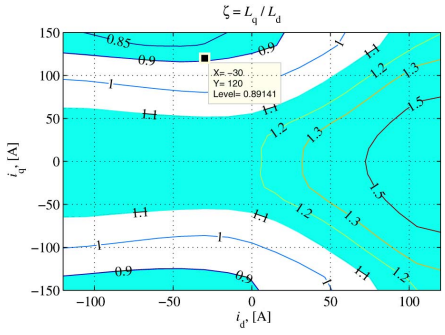

Fig. 8. Forbidden region $0.9 < L_q/L_d < 1.1$ (white) for sensorless control using high-frequency signal injection. Low-speed sensorless operation is forbidden here. FEM modeling.

behavior of a PMSM can be precisely predicted [5]. Flux equations (4) and (5) take a form of

$$\Psi_d = L_d(i_d, i_q)i_d + \Psi_{PM}(i_d, i_q) \tag{10}$$

$$\Psi_q = L_q(i_q, i_d)i_q. \tag{11}$$

The permanent-magnet flux linkage Ψ_{PM} can be also influenced by the cross-saturation, hence, it is a function of the currents i_d and i_q.

III. Sensorless Capability

The saturation effect should be carefully considered in case of sensorless (or self-sensing) control. Many sensorless signal-injection control schemes rely on the inductance ratio $\zeta = L_q/L_d$ which should considerably differ from 1 at the whole region of operation [11]. But, as can be seen in Figs. 7 and 8, at certain values of d- and q-currents the inductance ratio becomes very close to 1 (values of d- and q-inductances become very close to each other).

Fig. 7 shows the intersection of the direct and quadrature axis inductance surfaces. At the line of intersection the inversion occurs. At the inversion point the L_d axis inductance becomes higher than the L_q inductance because of the saturation effects. At this point the sensorless signal-injection control may fail due to the loss of observability. Therefore, in the region of inversion a low-speed sensorless operation of the drive should be forbidden, as in this region only back-EMF-tracking-based sensorless schemes will work. But EMF-based methods of sensorless control fail at zero and low speeds [12]. Therefore, if a low- or zero-speed sensorless control is required, the inversion region should be forbidden in the machine design or operation.

In order to ensure for the described TC-PMSM that the inductance ratio is higher than one within the whole range of intended sensorless operation, the L_q axis inductance should be high enough [13]. Therefore, the thickness of the iron web between the poles should be increased [14] in order to make the saliency inversion occur at higher values of the q-axis current well above the intended operation region.

As it is seen in Figs. 7 and 8 the saliency inversion happens when the q-axis component of the stator current is close to its nominal value. This is the point at which the PMSM obtains its nominal torque. Therefore, if an electric machine has a similar inductance maps as illustrated in Fig. 7, and if sensorless field-oriented control is implemented, then, the maximum torque should be reduced to the point where reverse saliency is apparent [15], even if there is still a current reserve from the thermal capability point of view. Alternatively, the low-speed sensorless operation should be forbidden, and back-EMF-based sensorless technique should be used in that region.

Measurement noise, distortion of injected signals, manufacturing unidealities, and dependence of PM flux—and consequently the saturation—from the thermal conditions require widening of the forbidden region in order to ensure the minimum ratio of detectable saliency [11]. Fig. 8 shows the forbidden region for sensorless control using high-frequency signal-injection with 10% safety limit ($0.9 < \zeta < 1.1$).

IV. Local Saturation

In many papers during the last decade it was reported that the dq-model developed for PMSMs with integral-slot distributed windings is not reliable enough for TC-PMSMs. Experiments show that the output of the classical dq-model of PMSMs applied to TC-PMSMs differs from measurements [16], especially, in FW region of operation and at high loadings.

It is observed that, because of the TC-windings, the saturation of TC-PMSMs is position- and time-dependent under the influence of current linkage sub-harmonics. In [17] it is reported that inductances of TC-PMSMs vary with the rotor position. This inductance variation is caused mainly by local saturation effects due to the asynchronous harmonic magnetic fluxes. For TC-SPMSMs the effect of harmonic fluxes is limited by a high effective air gap length. Whereas, in TC-IPMSMs the saturation produced by the harmonic fluxes can be noticeable. Iron saturation is the fundamental cause for the torque ripple in TC-PMSMs [18].

In Fig. 6 it can be seen that the inductance maps are not symmetrical with the positive and negative values of quadrature-axis current in both L_d and L_q as the case usually is for low-torque-density machines with $q > 1$ [5]. Usually, inductance maps are obtained with FEM when the direct or quadrature rotor axis is aligned with the geometrical magnetic axis of

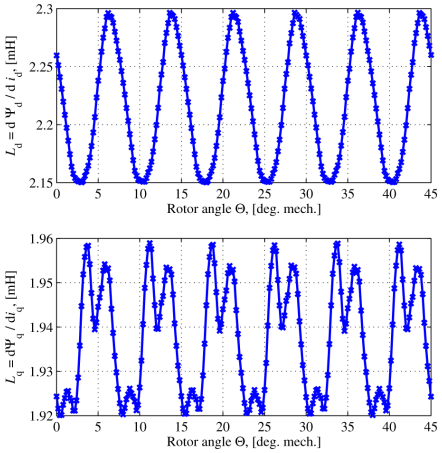

Fig. 9. Direct-axis differential inductance L_d variation (top) and quadrature-axis differential inductance L_q variation (bottom) with the rotor position during one electrical period (for 18/16 machine it corresponds to 45 mechanical degrees rotation). FEM modeling. Sinusoidal current supply, $i_\mathrm{d} = -30$ A and $i_\mathrm{q} = 120$ A.

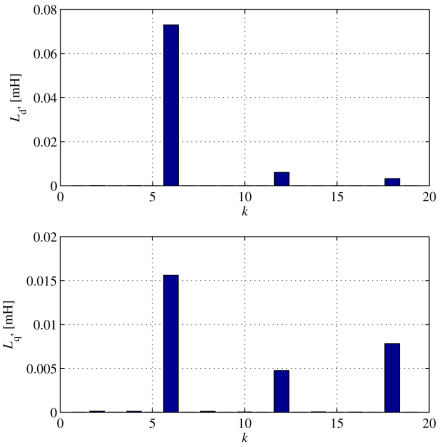

Fig. 10. Direct differential inductance L_d variation spectrum (top) and quadrature differential inductance L_q variation spectrum (bottom) at operating point captured during one electrical period. FEM modeling. The peak-to-peak inductance ripple is 7%.

a phase. Maps in Fig. 6 were obtained when the rotor position was not aligned with the geometrical magnetic axis of a stator phase as it is shown in Fig. 4.

Fig. 9 shows the variations of the d- and q-axes inductances at different rotor positions at $i_\mathrm{d} = -30$ A and $i_\mathrm{q} = 120$ A. The d-axis inductance varies almost sinusoidally with the magnitude $L_\tau = 0.07$ mH.

This inductance variation induces an alternating voltage U_dL in the windings. The value of this induced voltage can be estimated by

$$U_\mathrm{dL} = i_\mathrm{d}\frac{\mathrm{d}L_\mathrm{d}}{\mathrm{d}t} = i_\mathrm{d}\frac{\mathrm{d}L_\tau \sin(k\omega t)}{\mathrm{d}t}. \tag{12}$$

The RMS value of this varying voltage at working point when $i_\mathrm{d} = -30$ A and $i_\mathrm{q} = 120$ A is

$$U_\mathrm{dL} = i_\mathrm{d}\frac{L_\tau}{\sqrt{2}}k2\pi f = 30\ \mathrm{A}\frac{0.07\ \mathrm{mH}}{\sqrt{2}}6\ 2\pi 200\ \mathrm{Hz} = 11.2\ \mathrm{V} \tag{13}$$

which is higher than the resistive voltage drop of this machine $R_\mathrm{s}i_\mathrm{s} \approx 7$ V. Therefore, for the precise control, this inductance variation should be taken into account.

The inductance varies because of the local temporal saturation caused by interaction of the travelling current linkage harmonics with the magnetic flux waveform of the rotor. At an instant depicted in Fig. 2, when maximum current is flowing in the phase U, the 4th and the 5th harmonics contribute the most to the current linkage under teeth 2–4 (phase U). This current linkage induces the magnetic flux which, together with the magnetic flux of the PMs, locally saturates the iron core in and below the teeth 2–4. This saturation decreases the inductance in the phase U and contributes to inductance variation along the dq-axes. Such a situation repeats 6 times during one electrical period for three phases and positive and negative peaks of the phase currents. That is the 6th harmonic is produced in the spectra of the inductance variation waveforms during one electrical period (see Fig. 10).

As it can be noticed in Fig. 10, the 6th harmonic pulses are the dominating pulses in the inductance variations. Therefore, the inductance variation pulses are caused by the saturation due to the travelling harmonics in the gap.

From the spectra of the inductance variations the 12th and 18th harmonics are also noticeable in the d- and q-axes inductances. These variations are due to the interaction of the synchronous flux wave of the rotor and the 2nd and the 5th current linkage harmonics travelling to the opposite direction

$$k = 2(\nu_\mathrm{syn} - (-\nu_2)) = 2(4 - (-2)) = 12 \tag{14}$$

$$k = 2(\nu_\mathrm{syn} - (-\nu_5)) = 2(4 - (-5)) = 18 \tag{15}$$

where factor 2 is due to the fact that saturation can be produced by the intersection of the positive half-waves of the synchronous and the first current linkage harmonics as well as by the intersection of the negative half-waves.

The slotting effect also causes variation of the d- and q-axes inductances. The slotting introduces intrinsic magnetic anisotropy of the stator bore which results in cogging torque produced by reluctance forces due to anisotropy (see Fig. 14). The harmonic ordinal of this variation k_cog during one electrical period can be determined according to [19]

$$k_\mathrm{cog} = \frac{\mathrm{lcm}(Q_\mathrm{s}, 2p)}{p} \tag{16}$$

where lcm is the least common multiplier, Q_s is the number of stator slots, and p is the number of pole pairs. For 18/16 machine $k_\mathrm{cog} = 18$. Therefore, the 18th harmonic in the d- and q-axes inductances of the 18/16 machine is caused both–by local temporal harmonic saturation, and by stator anisotropy.

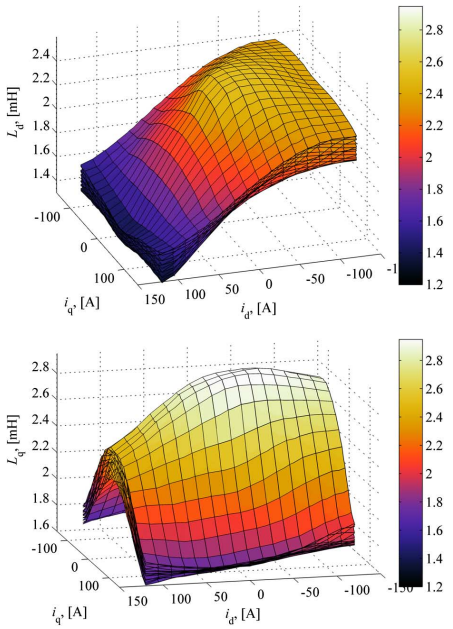

Fig. 11. Sets of direct differential inductance $L_{\mathrm{d}}(i_{\mathrm{d}}, i_{\mathrm{q}})$ maps (top) and quadrature differential inductance $L_{\mathrm{q}}(i_{\mathrm{q}}, i_{\mathrm{d}})$ maps (bottom) obtained at different rotor positions during one electrical period. Maximum discrepancy at high current values is 12%. FEM modeling. Sinusoidal current supply.

Fig. 11 shows a set of direct and quadrature differential inductance maps obtained at different rotor positions. These inductance variations are not included in the classical dq-model of PMSM. Therefore, a TC-PMSM can not be precisely represented by an inductance map obtained at a single rotor position.

Fig. 12 shows the magnitude of inductance variation in percents of $L_{\mathrm{d}}(i_{\mathrm{q}}, i_{\mathrm{d}})$ and the amplitude of $L_{\tau\mathrm{d}}(i_{\mathrm{q}}, i_{\mathrm{d}})$. It can be noticed that at low currents the inductance almost has no variation, but at higher currents the magnitude of inductance variation increases significantly. This inductance variation should be considered when choosing the forbidden region for sensorless HF signal injection (see Fig. 8). Higher safety limit should be chosen.

Fig. 13 shows the magnitude of the inductance variation in percents of $L_{\mathrm{q}}(i_{\mathrm{q}}, i_{\mathrm{d}})$. The L_{q} inductance variation along $i_{\mathrm{d}} = 0$ A is very low, and, therefore, can be neglected for this particular machine shown in Fig. 4, which has thin iron webs. With MTPA control, which trajectory is usually close to the $i_{\mathrm{d}} = 0$ with moderate negative d-axis current component, the q-axis inductance can also be assumed as constant along the stator bore. However, the d-axis inductance variation can not be neglected for this particular TC-PMSM.

V. Torque Quality

Torque quality can be assessed by cogging torque and torque ripple. The cogging torque is the pulsating torque due to the permanent-magnet flux and angular magnetic anisotropy of the

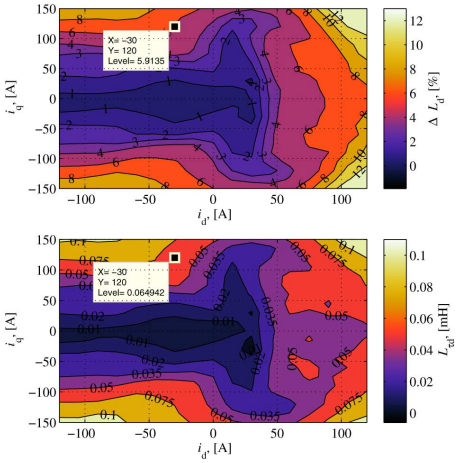

Fig. 12. Direct inductance variation map in percents of L_{d} (top) and direct inductance variation magnitude $L_{\tau\mathrm{d}}$ (bottom). FEM computation.

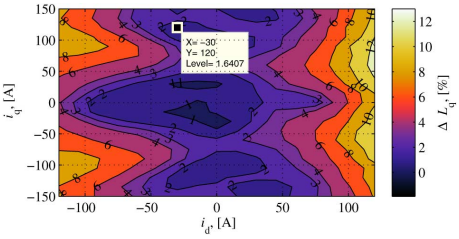

Fig. 13. Quadrature inductance variation map in percents of L_{q}. FEM computation.

stator. The ripple torque is due to interaction of the stator current linkage and the rotor electromagnetic properties (saliency, saturation and PM flux linkage).

Fig. 14 shows the cogging torque of the 18/16 machine during one electrical period. The harmonic decomposition of the cogging torque is also shown. The 18th slotting harmonic is clearly seen. The magnitude of the cogging for this TC-IPMSM is negligibly small.

The cogging torque can be decreased by diminishing the stator magnetic anisotropy—by skewing, decreasing the slot openings, using IPM rotor, increasing the air gap or by using semi-magnetic wedges. The cogging torque can be ultimately eliminated if slotless windings (air gap windings) are used. However, the last measure is only theoretical for industrial high-torque machines as it significantly lowers the air gap flux density and, therefore, decreases the torque density.

Fig. 15 shows the torque profile of the loaded 18/16 TC-IPMSM during one electrical period at operating point when $i_{\mathrm{d}} = -30$ A and $i_{\mathrm{q}} = 120$ A. The torque harmonic content is also shown.

The magnitude of $k = 12$ torque harmonic is very small as the $\nu = -2$ current linkage harmonic has relatively small magnitude. The magnitude of $k = 18$ torque harmonics is also low

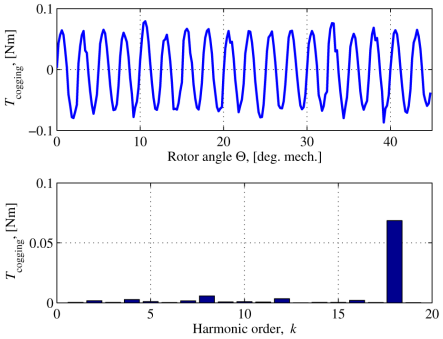

Fig. 14. Cogging torque due to angular anysotropy (slotting) of the stator (top) and cogging torque harmonics (bottom). FEM simulation during one electrical cycle, $i = 0$.

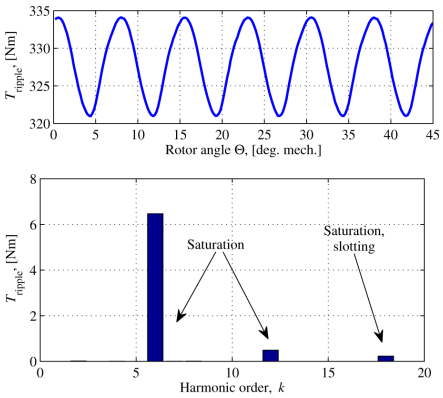

Fig. 15. Pulsating torque at nominal operating point (top) and harmonics of the pulsating torque (bottom). FEM simulation during one electrical cycle, $i_{\text{d}} = -30$ A and $i_{\text{q}} = 120$ A.

because of the low contribution of the cogging and local saturation. The pole-pitch of the corresponding current linkage harmonic $\nu = -5$ is short and the saturation is not so apparently localized. The dependence of the torque from the dq-axes inductances can be seen from equations (3)–(5).

At higher currents the sub-harmonic saturation is deeper and the torque ripple magnitude will also be higher. At low currents, when the machine is operated at linear magnetic region, only the cogging torque frequencies can be observed in the torque waveform due to the absence of saturation.

VI. Improved dq-Model for TC-PMSMs

One possible way to avoid problems with inductance variation along the stator bore due to the harmonics is to design a machine which will not be vulnerable to saturation. It means that the operating point of the machine should be placed well below the point where saturation starts–meaning in practice thicker teeth and yokes and lower values of the flux density in the machine. This, however, decreases the torque and power densities of the machine, which is not desirable, especially, in mobile applications, such as hybrid electric vehicles or aviation. In these applications high-torque-density electrical machines are required.

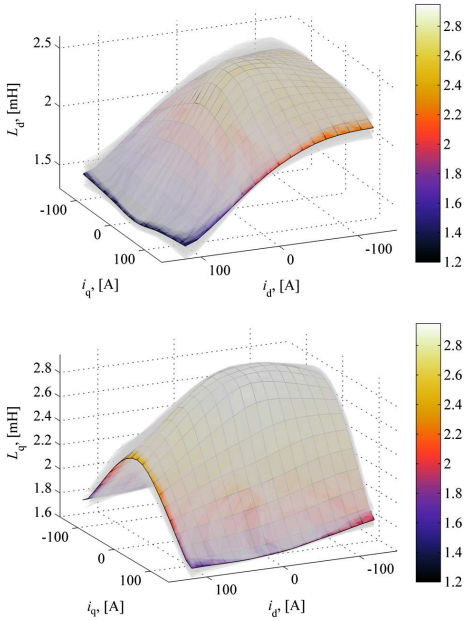

Fig. 16. Averaged inductance maps along with transparent inductance maps at different rotor positions.

The classical dq-model can still be used if the inductance variation is not very significant. It happens, for example, when machine operation region mainly lies below the point where saturation becomes noticeable.

If a smooth torque output is not the main requirement from the machine, the inductance variation along the stator bore can be neglected. The inductance can be approximated with a certain level of accuracy by using averaged inductance maps along the stator bore (see Fig. 16).

However, when the inductance variation, as a function of position and time, is significant (which should be valid for high-torque- and high-power-density machines), and the smooth torque production is desired, the inductance variation should be directly modelled in the equivalent circuits of d- and q-axes in order to obtain smooth output torque. At least the most significant inductance variations $L_{\tau\text{d}6}\cos(6\omega t + \phi_{\text{d}})$ and $L_{\tau\text{q}6}\cos(6\omega t + \phi_{\text{q}})$ should be included [20]. When current linkage harmonic saturation is taken into account the d-axis can be represented by an equivalent circuit in Fig. 17.

The magnitudes of $L_{\tau\text{d}6}$ and $L_{\tau\text{q}6}$ are dependent on the magnetic state of the machine and additional inductance maps should be calculated beforehand for $L_{\tau\text{d}6}(i_{\text{d}}, i_{\text{q}})$ and $L_{\tau\text{q}6}(i_{\text{d}}, i_{\text{q}})$. Information for $L_{\tau\text{d}6}$ and $L_{\tau\text{q}6}$ can be taken using similar maps as shown in Fig. 12.

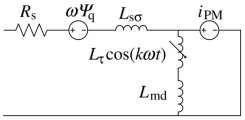

Fig. 17. Equivalent circuit along the d-axis of TC-PMSM taking the saturation-caused inductance variation into account.

Voltage equation for the d-axis becomes

$$U_d = R_s i_d + L_d \frac{di_d}{dt} + i_d \frac{dL_d}{dt} - \omega\Psi_q \tag{17}$$

$$U_d = R_s i_d + L_d \frac{di_d}{dt} + i_d L_{\tau d6} \frac{d\cos(6\omega t + \phi_d)}{dt} - \omega\Psi_q \tag{18}$$

and for the q-axis

$$U_q = R_s i_q + L_q \frac{di_q}{dt} + i_q \frac{dL_q}{dt} + \omega\Psi_d \tag{19}$$

$$U_q = R_s i_q + L_q \frac{di_q}{dt} + i_q L_{\tau q6} \frac{d\cos(6\omega t + \phi_q)}{dt} + \omega\Psi_d. \tag{20}$$

When localized sub-harmonic saturation plays a significant role in the operation of a machine, this approach should be used for the precise modeling of the machine behavior. This model can be used together with torque ripple minimization techniques using active stator current excitation to compensate the torque pulsations [21]–[23].

VII. Conclusion

In this paper it was shown that torque quality is strongly dependent on the saturation caused by the asynchronous current linkage harmonics. These harmonics locally saturate the stator core which results in the inductance variation along the d- and q-magnetic axes. This inductance variation should be taken into account during the design process of the machine, and in control design for TC-PMSM drives, particularly for sensorless control schemes.

The high-torque- and high-power-density TC-PMSMs are especially vulnerable to the rotating current linkage harmonic saturation as these machines work at high values of flux density and the localised saturation is especially apparent in this case.

References

[1] P. Ponomarev, P. Lindh, and J. Pyrhonen, "Effect of slot-and-pole combination on the leakage inductance and the performance of tooth-coil permanent-magnet synchronous machines," *IEEE Trans. Ind. Electron.*, vol. 60, no. 10, pp. 4310–4317, 2013.

[2] F. Magnussen and H. Lendenmann, "Parasitic effects in PM machines with concentrated windings," *IEEE Trans. Ind. Appl.*, vol. 43, no. 5, pp. 1223–1232, 2007.

[3] N. Bianchi, S. Bolognani, and E. Fornasiero, "An overview of rotor losses determination in three-phase fractional-slot PM machines," *IEEE Trans. Ind. Appl.*, vol. 46, no. 6, pp. 2338–2345, Nov.-Dec. 2010.

[4] P. Ponomarev, M. Polikarpova, O. Heinikainen, and J. Pyrhonen, "Design of integrated electro-hydraulic power unit for hybrid mobile working machines," in *Proc. 2011-14th Eur. Conf. Power Electron. Appl. (EPE 2011)*, Sep. 1, 2011, vol. 30, pp. 1–10.

[5] M. Rilla, "Design of Salient Pole PM Synchronous Machines for a Vehicle Traction - Analysis and Implementation," Doctpral dissertation, Lappeenranta University of Technology, Lappeenranta, Finland, 2012.

[6] L. Alberti, M. Barcaro, and N. Bianchi, "Design of a low torque ripple fractional-slot interior permanent magnet motor," in *2012 IEEE Energy Conversion Congress and Exposition (ECCE)*, Sep. 2012, pp. 509–516.

[7] C. Dufour, S. Cense, T. Yamada, R. Imamura, and J. Belanger, "FPGA permanent magnet synchronous motor floating-point models with variable-dq and spatial harmonic finite-element analysis solvers," in *2012 15th Int. Power Electron. and Motion Control Conf. (EPE/PEMC)*, Sep. 2012, pp. LS6b.2–1–LS6b.2–10.

[8] B. Stumberger, G. Stumberger, D. Dolinar, A. Hamler, and M. Trlep, "Evaluation of saturation and cross-magnetization effects in interior permanent-magnet synchronous motor," *IEEE Trans. Ind. Appl.*, vol. 39, no. 5, pp. 1264–1271, Sep.-Oct. 2003.

[9] A. Consoli, G. Scarcella, G. Scelba, and A. Testa, "Steady-state and transient operation of IPMSMs under maximum-torque-per-ampere control," *IEEE Trans. Ind. Appl.*, vol. 46, no. 1, pp. 121–129, 2010.

[10] S.-Y. Jung, J. Hong, and K. Nam, "Current minimizing torque control of the IPMSM using Ferrari's method," *IEEE Trans. Power Electron.*, vol. 28, no. 12, pp. 5603–5617, 2013.

[11] T. Matzen and P. Rasmussen, "Sensorless characteristics of hybrid PM machines at zero and low speed," in *IEEE Energy Conversion Congress and Exposition, 2009 ECCE*, Sep. 2009, pp. 2374–2380.

[12] S.-K. Sul and S. Kim, "Sensorless control of IPMSM: Past, present, and future," *IEEJ J. Ind. Appl.*, vol. 1, no. 1, pp. 15–23, 2012.

[13] Y. Kano, T. Kosaka, N. Matsui, and T. Nakanishi, "Sensorless-oriented design of IPM motors for general industrial applications," in *18th Int. Conf. Electrical Machines, 2008 ICEM*, pp. 1–6.

[14] P. Sergeant, F. De Belie, and J. Melkebeek, "Rotor geometry design of interior PMSMs with and without flux barriers for more accurate sensorless control," *IEEE Trans. Ind. Electron.*, vol. 59, no. 6, pp. 2457–2465, 2012.

[15] N. Bianchi and S. Bolognani, "Sensorless-oriented design of PM motors," *IEEE Trans. Ind. Appl.*, vol. 45, no. 4, pp. 1249–1257, 2009.

[16] N. Dai, R. Dutta, and M. Rahman, "Comparative performance analysis of field-oriented control and direct torque control for a fractional-slot concentrated winding interior permanent magnet synchronous machine," in *2012 XXth Int. Conf. Electrical Machines (ICEM)*, Sep. 2012, pp. 879–885.

[17] E. Schmidt and M. Susic, "Finite element analysis of permanent magnet synchronous machines with fractional slot tooth coil windings," *Elektrotechnik und Informationstechnik*, vol. 128, no. 3, pp. 86–94, 2011.

[18] M. Barcaro, N. Bianchi, and F. Magnussen, "Remarks on torque estimation accuracy in fractional-slot permanent-magnet motors," *IEEE Trans. Ind. Electron.*, vol. 59, no. 6, pp. 2565–2572, Jun. 2012.

[19] Z. Zhu and D. Howe, "Influence of design parameters on cogging torque in permanent magnet machines," *IEEE Trans. Energy Convers.*, vol. 15, no. 4, pp. 407–412, 2000.

[20] W. Qian, J. X. Xu, and S. Panda, "Periodic torque ripples minimization in PMSM using learning variable structure control based on a torque observer," in *The 29th Annu. Conf. IEEE Ind. Electron. Society, 2003 IECON '03*, vol. 3, pp. 2983–2988.

[21] G.-H. Lee, "Active cancellation of PMSM torque ripple caused by magnetic saturation for EPS applications," *J. Power Electron.*, vol. 10, no. 2, pp. 176–180, 2010.

[22] J. Holtz and L. Springob, "Identification and compensation of torque ripple in high-precision permanent magnet motor drives," *IEEE Trans. Ind. Electron.*, vol. 43, no. 2, pp. 309–320, 1996.

[23] V. Petrovic, R. Ortega, A. Stankovic, and G. Tadmor, "Design and implementation of an adaptive controller for torque ripple minimization in PM synchronous motors," *IEEE Trans. Power Electron.*, vol. 15, no. 5, pp. 871–880, 2000.

Publication VIII

Ponomarev, P., Petrov, I., and Pyrhönen, J., "Torque Ripple Reduction in Double-Layer 18/16 TC-PMSMs by Adjusting Teeth Widths to Minimize Local Saturation," *in XIX International Conference on Electrical Machines (ICEM), 2014*, vol., no., pp.1,6, 2-5 Sept. 2014

Torque Ripple Reduction in Double-Layer 18/16 TC-PMSMs by Adjusting Teeth Widths to Minimize Local Saturation

Pavel Ponomarev, Ilya Petrov and Juha Pyrhönen
Laboratory of Electrical Drives Technology, Lappeenranta University of Technology, Finland
e-mail: pavel.ponomarev@lut.fi

***Abstract*—The saturation in the stator teeth of an 18-slots 16-poles TC-PMSM with sinusoidal current supply caused by the interaction of armature reaction fluxes and rotor-PM-produced fluxes is studied. It is found that under load some teeth are saturated deeper than others. An increase in the width of these teeth reduces the oversaturation, which locally prevents the decrease in the inductance and back-EMF, and, consequently, reduces the torque ripple in the machine. The proposed technique can also be applied to other types of TC-PMSMs.**

***Keywords*—Armature reaction, current linkage, permanent magnet machines, TC-PMSM, tooth-coil winding, torque ripple, saturation.**

I. Introduction

TOOTH-coil permanent magnet synchronous machines (TC-PMSMs, also known as fractional slot non-overlapping winding permanent magnet synchronous machines with number of slots per pole and phase $q \leq 0.5$) due to their advantages are utilized extensively in many applications – traction and propulsion drives, wind turbines, air conditioning and ventilation, robotics, home appliances, fault-tolerant actuators in aerospace industry, and various direct-drive industry applications. [1]–[4]

In all of these applications the minimization of the torque ripple is an important aspect. In home appliances and ventilation equipment a minimized torque ripple allows to lower the acoustic noise level of the equipment. In wind turbines and traction motors a lower torque ripple reduces vibrations and mechanical wearing in different parts of equipment. In direct-drive applications low torque ripple can be an important requirement from the driven machinery side.

There are two approaches for minimization of torque ripple – active control approach, and machine design approach. Active control methods are applied by precisely controlling the current waveform by the drive controller in order to generate smooth output torque [5]. The second approach focuses on adjustments of the design parameters of electrical machine itself, and it is the main focus of this paper.

The torque ripple in PMSMs is comprised from two components – cogging torque and pulsating torque.

A. Cogging Torque

The first component is due to magnetic anisotropy of the stator due to the slotting. The rotor with permanent magnets tends to align itself along the magnetic path with lowest magnetic reluctance. In internal permanent magnet rotor machines (IPMSMs) with smooth rotor surface this torque component tends to be lower than in rotor surface permanent magnet machines (SPMSMs), because of the steel parts above the magnets which magnetically smoothen the air gap and stator anisotropy seen by the magnets. On the stator side, wide tooth tips and semi-magnetic wedges decrease the magnetic anisotropy [6].

An open slot PMSM equipped with semi-magnetic wedges will exhibit lower iron losses and lower torque ripple in case of higher permeability wedges. However, if wedges of too high permeability are installed, then, the machine performance can degrade. [6]

All design measures to reduce the cogging torque in sinusoidal-field rotor machines are based on the idea of magnetically smoothening the anisotropy of the stator seen by the magnetic fluxes of the permanent magnets. Among the most utilized approaches are – skewing by one cogging period, closed slots, magnetic slot wedges, increased air gap, IPM rotor topology, dummy (auxiliary) teeth and slots, air gap (slotless) windings [5,7]–[9]. However, most of these approaches somewhat degrade the performance of an electrical machine, particularly the back-EMF is decreased [10].

The periodicity of the cogging torque depends on the number of slots and poles in integral-slot and in tooth-coil winding permanent magnet synchronous machines. A TC-PMSM with an appropriate combination of slots and poles can be selected in order to lower the cogging torque magnitude and maximize the number of cogging periods per revolution, keeping high performance at the same time. [11,12]

If PMs-produced flux density waveform in the air gap is not sinusoidal, but rather rectangular, then an optimal magnet pole-arc to pole-pitch ratio, which gives lowest cogging torque, can be found. [12]

B. Pulsating Torque

The second torque ripple component is the pulsating torque. This pulsating torque can originate from harmonics in permanent-magnet-produced magnetic flux density waveform, or harmonics in the current supply, or from the saturation of the magnetic material under loaded conditions when high-magnitude currents are flowing in the windings.

978-1-4799-4389-0/14/$31.00 ©2014 IEEE

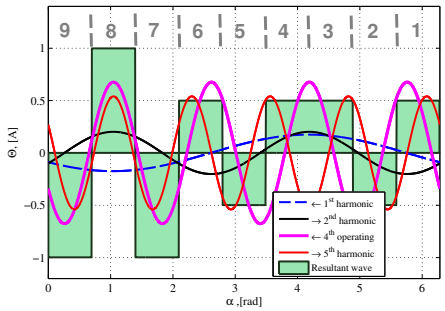

Fig. 1. Winding function harmonic decomposition of a 9/8 machine at a time instant when $i_{\mathrm{U}} = 1$ A, $i_{\mathrm{V}} = i_{\mathrm{W}} = -0.5$ A. In steady state rotor moves with the same speed as the 4^{th} harmonic.

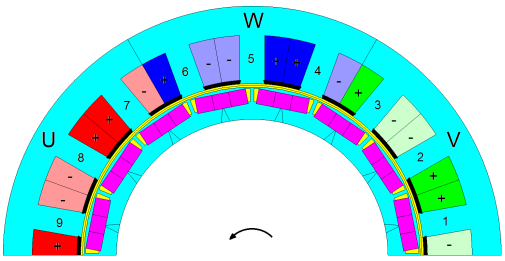

Fig. 2. Modelled 9/8 segment of an 18/16 TC-IPMSM. Three sectors of windings U, V, and W with the coils of the same phase are shown. Rotor position is zero. Direction of rotation is counter-clockwise.

Usually, the saturation in the magnetic circuit in industrial rotating electrical machines is avoided as much as possible, to keep current-to-torque ratio small, and maintain low volume of PM material. However, in some applications, such as aerospace, robotics, traction drives for electric vehicles, wind turbine generators, the dimensions and weight are important. These parameters should be as small as possible, meaning high torque and power density machines. These machines have high magnetic loading in order to decrease weight and size, and often they operate in the saturation region of electrical steel.

Saturated magnetic material has lower permeability, and hence lower flux linkage is seen by the windings (meaning lower inductance in the region of saturation), which leads to lower back-EMF in the area of saturation. In three-phase machines the peak currents in the windings occur 6 times per one electrical period (two peak values – negative and positive – in each of three phases), which can result in 6 torque pulses. Other torque harmonics ($k = 6n, n = 1, 2, 3..$) are also present in the torque spectrum. [13]

The pulsating torque can be decreased by current linkage sub-harmonic cancellation [13]. Fig. 1 shows the winding function of a 9/8 TC-PMSM, and its decomposition on current linkage harmonics. In [14] the sub-harmonic in a TC-PMSM is minimized by introduction of flux barriers in the stator. In [15,16] the influence of sub-harmonics is minimized by rotor flux barriers.

Another way of cancellation of a specific current linkage harmonic in a TC-PMSM is usage of multi-layer (> 2) windings as it is done in [17]. However, the winding construction becomes much more complicated as number of interconnections between winding coils increases. We, however, think that using multi-layer windings is not often practically feasible, when a TC-PMSM has a high number of slots. In case of a multi-layer winding the slot fill factor is somewhat lower as the winding requires additional interlayer insulation in the slot. This also degrades the heat transfer in the slot.

The technique of stator shifting also can be used for attenuation of current linkage harmonics [18]. This approach can lead to a machine with unequal teeth widths and pseudo-distributed windings. However, a TC-PMSM machine in this case looses one of its main advantages – windings become overlapping, and axial length of a stator-shifted machine can be higher than of a similar TC-PMSM because of complex interconnections between slots. This somewhat limits the possibility of automatized winding assembly from prefabricated coil modules as in plug-in-tooth, or joint-lapped core stator machines [1]; and copper losses are increased.

In this paper a new design technique for torque ripple reduction in TC-PMSMs is demonstrated using FEM model of a radial flux double-layer 18/16 TC-IPMSM. However, this approach can be applied to other topologies of TC-PMSMs as well [19]. The proposed method reduces the pulsating torque caused by temporal local oversaturations in TC-PMSMs [13]. The method is applicable to machines which are designed mainly for single direction of rotation, such as generators in wind turbines and hybrid cars, propulsion or traction drives, fans and blowers.

The output of the proposed technique is a stator with unequal teeth widths. In literature, the unequal teeth were applied for single-layer TC-PMSMs. The usage of unequal teeth demonstrated reduction of pulsating torque in machines with rectangular current supply. The slot pitches were also unequal [8]. The technique described in this paper can be applied to two-layer and multi-layer TC-PMSMs as well. The slot pitches are left the same, hence, the cogging torque is not changed significantly, and only pulsating torque is reduced.

II. Localized Saturation

Often, when a PMSM is designed, the flux density in the air gap is assumed sinusoidal. However, when applied to TC-PMSMs this assumption is not valid under loading conditions as it can be seen from the winding function on Fig. 1. [3]

Fig. 2 shows a FEM model of an 18/16 open slot TC-IPMSM. Remanent flux density of permanent magnets is 1.2 T, electrical steel is M270-35A, semi-magnetic wedges with relative permeability $\mu_{\mathrm{r}} = 5$ are utilized. The coils of each phase are located in groups of 3. Therefore, this 18-slots machine can be assembled using 6 phase sectors with 3 coils each.

Fig. 3 shows the flux densities in the centers of teeth 1, 2, and 3 of phase V during one electrical period when the

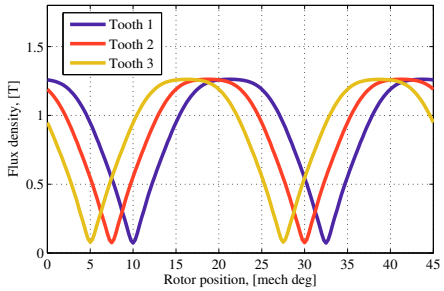

Fig. 3. Flux densities in the teeth of phase V during one electrical period when current is set to zero. Only permanent magnet flux is presented in the model. With rotor motion the peak flux densities appear in consequent teeth.

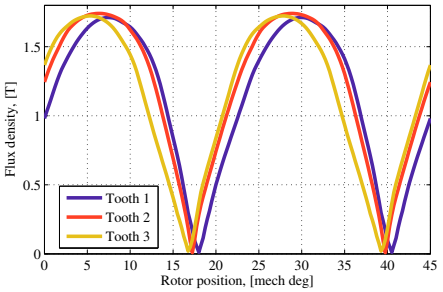

Fig. 4. Flux densities in the teeth of phase V during one electrical period when PM flux is set to zero. Only winding created flux is presented in the model. All 3 teeth of a phase sector experience the same flux densities simultaneously. Discrepancy is caused by the moving rotor with saliency. $i_{\mathrm{d}} = -30$ A, $i_{\mathrm{q}} = 120$ A. Highest magnitude phase current is at time instants when rotor position is 6.5 and 29 degrees.

winding current is set to zero. At initial time instant, when the rotor angle is zero (as it is depicted in the Fig. 2), the fluxes in teeth 1 and 2 are at maximum, because the magnets of the rotor are almost aligned with those teeth. As the rotor rotates counter-clockwise with time the flux densities decrease as the magnets loose their alignment with the teeth. Further, the next magnets are going to align with the teeth, and the flux density again rises. At a time instant when the rotor position is 10 degrees the flux density in tooth 3 is almost 0.9 tesla, in tooth 2 it is 0.5 tesla, and in tooth 1 the flux density is 0.1 tesla. At every time instant the flux density induced by the permanent magnets is different in all the teeth of the same phase.

The armature reaction field is very complex. It contains, beside the synchronous sinusoidal flux wave, also other asynchronous flux space harmonics in the air gap. These asynchronous fluxes are due to the current linkage harmonics [20,21]. Fig. 1 shows the harmonic decomposition of the current linkage waveform of a 9/8 TC-PMSM, which is the base machine for the 18/16 TC-PMSM with periodicity of 2. From this figure one can conclude that flux densities in the teeth of one phase should be the same at every time instant when permanent magnet flux is zero for SPM machines.

Fig. 4 shows the flux densities in teeth 1, 2 and 3 during one electrical period, when PM remanence is set to zero. Only winding created flux is presented in the model. The highest flux density is reached at rotor positions $\alpha = 6.5$ and 29 degrees, that corresponds to positive and negative peaks of sinusoidal phase current.

From this figure it is seen that fluxes in all the teeth of one phase are almost the same at every time instant. The slight discrepancy in the flux densities is caused by the saliency in the IPM rotor of the studied machine.

Using Figs. 3 and 4 it can be predicted that at the working point the flux densities and saturation levels in all 3 teeth, which belong to the same phase winding sector, will be different, when the peak current will be flowing in the winding. In the motoring mode (and counter-clockwise direction of rotation) tooth 3 will have the highest flux density and it will be oversaturated. Tooth 1 will have the lowest flux density, and the level of saturation will be low. In the generating mode

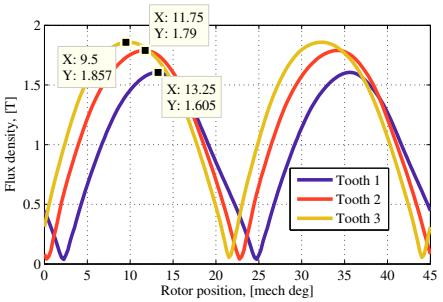

Fig. 5. Flux densities in the teeth of phase V during one electrical period at nominal loading conditions. Maximum torque per ampere (MTPA) control strategy. $i_{\mathrm{d}} = -30$ A, $i_{\mathrm{q}} = 120$ A.

and the same direction of rotation the highest flux will be in tooth 1, and lowest in tooth 3.

Fig. 5 shows the FEM-simulated flux densities at the nominal working point in motoring mode, that completely prove the prediction. All teeth under loading conditions, when peak current flows in the V-phase winding, exhibit different levels of saturation. The highest flux density is in the tooth 3 at rotor angle $\alpha = 9.5$ degrees. Fig. 6 shows the flux diagram in the machine under nominal load. The highest flux density is in the tooth 3.

Fig. 7 shows the torque ripple of the machine during one electrical period. The magnitude of the 6^{th} harmonic is 4.8 Nm.

III. Effect of Non-Linear Steel Properties on Torque Quality

Fig. 8 shows the BH-curve of M270-35A electrical steel. Two regions can be seen in the figure divided by a knee – linear region (below the knee), and saturation region (above

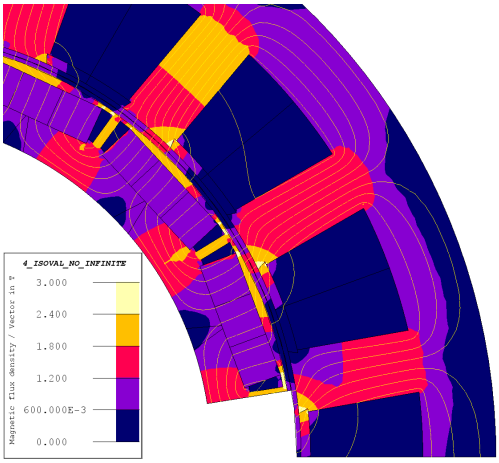

Fig. 6. Flux density in the machine section under nominal load (peak current in the winding) when rotor angle is 9 degrees. FEM simulation, M270-35A. Maximum torque per ampere (MTPA) control strategy. $i_\mathrm{d} = -30$ A, $i_\mathrm{q} = 120$ A. The flux density in tooth 3 is above 1.8 T.

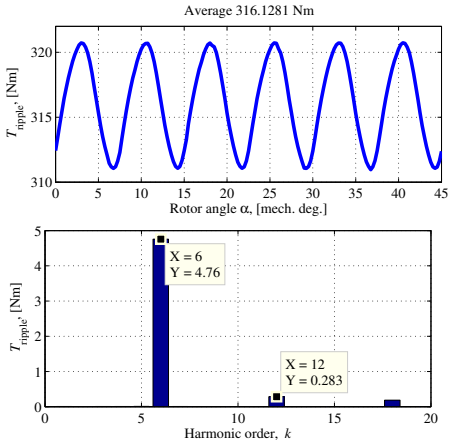

Fig. 7. Torque waveform and torque ripple harmonics of the conventional stator. Peak-to-peak torque ripple is 3 %.

the knee). From the plot it is seen that the knee center is near the flux density level $B_\mathrm{k} = 1.8$ T.

Linear region is a region where electrical machines are conventionally designed analytically. Usually, the properties of electrical steel are assumed linear, and magnetic circuits of stator and rotor are designed in the linear region. It is very difficult to take into account back-EMF and inductance sags due to the saturation with analytical design approach. Hence,

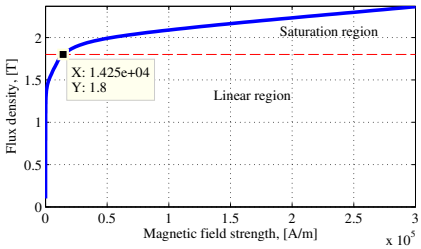

Fig. 8. BH-curve of electrical steel M270-35A. Knee level is $B_\mathrm{k} = 1.8$ T.

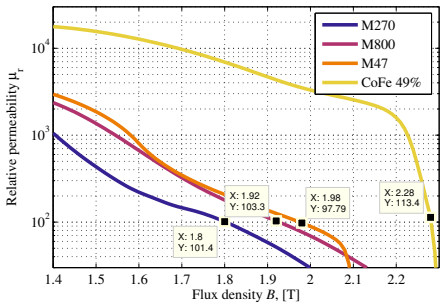

Fig. 9. Relative permeability curves for M270-35A, M800-65A, M47, and CoFe electrical steels as functions of flux density. Knee level ($\mu_\mathrm{r} = 100$) is marked for each curve.

the traditional analytical design procedure leads to a machine with no torque ripples and sinusoidal back-EMF, assuming sinusoidal winding distribution, sinusoidal currents and sinusoidal permanent-magnet-produced flux density waveform.

When the flux densities reach the saturation region, the flux linkage (and, consequently, the back-EMF) of analytically designed machine is no longer sinusoidal, which results in torque ripples. [22]

Fig. 9 shows the plots of relative permeabilities as functions of flux density for four electrical steels. For most silicon electrical steels the level of knee on the correspondent BH-curve lies near the relative permeability value of $\mu_\mathrm{r} = 100$. Therefore, this value divides region of heavy saturation from linear region, and it is a good empirical design criterion for low-torque ripple machines.

Therefore, if a low torque ripple is expected from an electrical machine, then it should be designed in the linear magnetic region of electrical steel and relative permeability should be high enough (e.g. $\mu_\mathrm{r} \geq 100$ for silicon steels) in order to avoid torque ripple.

Hence, if one wants the designed machine to satisfy the desired performance with smooth torque, levels of saturation at which the relative permeability goes below $\mu_\mathrm{r} = 100$ should be avoided along the main flux paths. Otherwise, significant torque ripple, inductance variation and high harmonics content

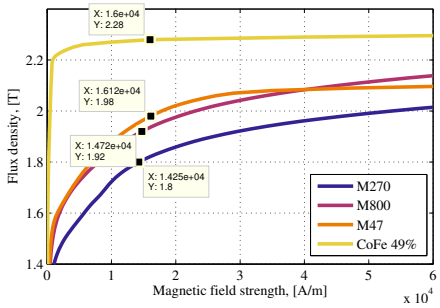

Fig. 10. BH-curves of M270-35A, M800-65A, M47, and CoFe electrical steels. Knee levels when $\mu_{\mathrm{r}} = 100$ are marked for each curve.

in the back-EMF should be expected from the designed machine driven with sinusoidal current supply, as a result of deep saturation in the magnetic core.

If smooth torque is required from the designed machine with low permeability in the main magnetic circuit ($\mu_{\mathrm{r}} \leq 100$), then an active current waveform control method should be utilized.

For various silicon electrical steel grades the knee flux density can vary from $B_{\mathrm{k}} = 1.5$ T to $B_{\mathrm{k}} = 2$ T. The relative permeability criterion can be utilized to evaluate the saturation level in different silicon electrical steels instead of flux density value.

For cobalt-based electrical steels the knee level lies higher, at about $B_{\mathrm{k}} = 2.2$ T. And relative magnetic permeability is significantly higher along the whole linear region. This means that higher torque values can be achieved before the saturation point is reached, which results in higher torque density, or lower amount of torque harmonics and lower current-to-torque ratio within the same dimensions, compared to a silicon-steel-based electrical machine.

Fig. 10 shows the BH-curves for several electrical steels. It can be seen that saturation occurs at various flux density levels for various steels. Fig. 11 shows a torque profile obtained from FEM simulation of the same machine geometry, but made with M800 electrical silicon steel laminations. The average torque in case of M800 electrical steel is higher than in case of M270 electrical steel at the same current. It can be concluded that higher torque- and power-density can be expected from a machine which utilizes higher-permeability M800 electrical steel, compared to a machine with M270 electrical steel. However, the iron losses can be significantly higher in case of M800 electrical steel [23], and a lower-losses-grade of electrical steel is usually preferred.

IV. Teeth Widths Adjustment and Torque Ripple

As it is shown in Figs. 5 and 6, the flux density in the tooth 3 is above 1.8 T when the peak current is flowing in the windings, which indicates that the relative permeability in the region of tooth 3 is below 100, and tooth 3 is heavily saturated.

In order to increase the permeance in this tooth under loading conditions, the tooth 3 width is slightly increased from

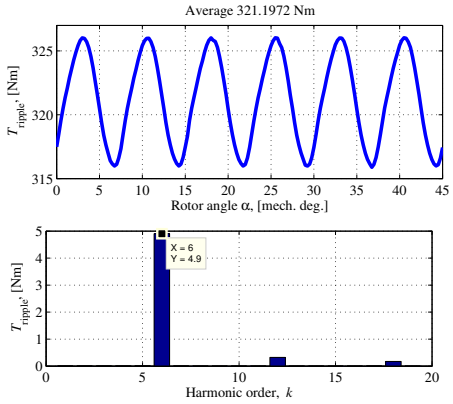

Fig. 11. Torque waveform and torque ripple harmonics of the conventional stator made of M800 electrical steel. The average torque is higher, than in case of M270 electrical steel at the same current loading, due to higher iron permeability.

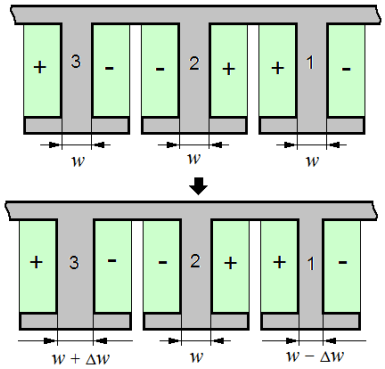

Fig. 12. Adjustment of the teeth widths. Slot depths adjustment is not shown.

$w = 20$ mm up to $w + \triangle w = 22$ mm. At the same time the width of tooth 1 is decreased by the same $\triangle w = 2$ mm in order to keep the same machine weight. The inequality in the slot areas between different slots is compensated by altering the slot depth, which is possible as the width of the stator yoke is high enough (the flux density in the yoke is well below the saturation level) and the magnetic state of the machine does not change considerably. Fig. 12 shows how the geometry of the stator has been altered.

Fig. 13 indicates that the flux density in all the teeth is $B \leq 1.8$ T, which ensures that the level of permeability is higher than 100. Significant oversaturation in the teeth area is cancelled. Fig. 14 shows the flux density diagram of modified machine. The width of tooth 3 is increased. All slot areas are the same, which is achieved by varying the slot depths.

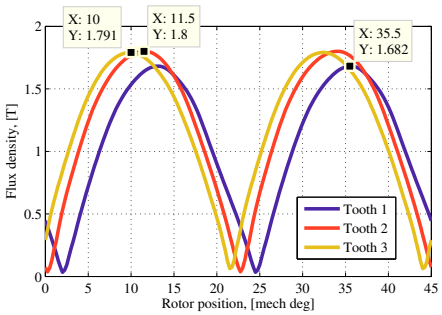

Fig. 13. Flux densities in the teeth of phase V during one electrical period at nominal loading conditions with unequal teeth. The maximum flux densities are below 1.8 T, which ensures that the relative permeability in the teeth along the main flux path is above $\mu_r = 100$ for M270 electrical steel.

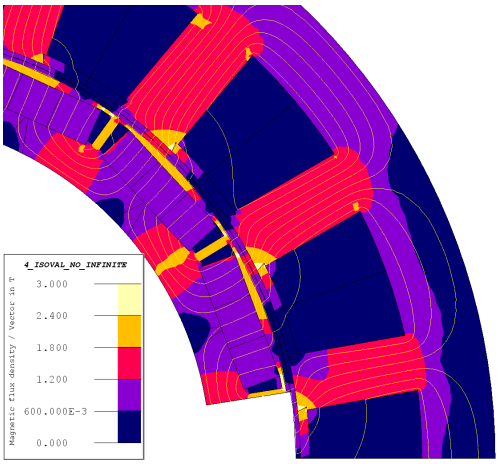

Fig. 14. Flux density in the modified machine section under nominal load when rotor angle is 9 degrees. FEM simulation. Maximum torque per ampere (MTPA) control strategy. $i_d = -30$ A, $i_q = 120$ A. It is clearly seen, comparing this figure with Fig. 6, that significant oversaturation in tooth 3 is cancelled.

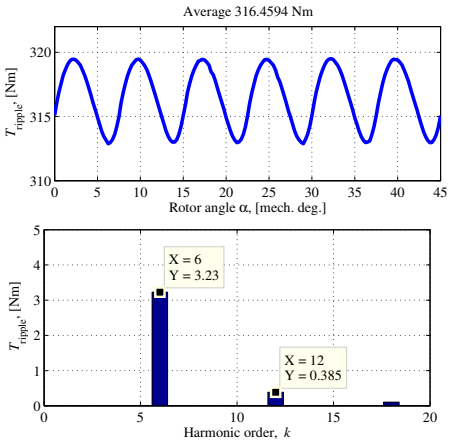

Fig. 15. Torque waveform and torque ripple harmonics of the stator with unequal teeth widths. Peak-to-peak torque ripple is 2 %.

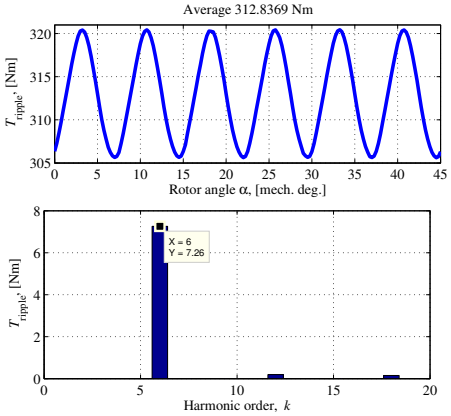

Fig. 16. Torque waveform and torque ripple harmonics of the stator with unequal teeth during reversed rotation. Peak-to-peak torque ripple is 5 %.

The only remaining area of a significant saturation is right side of a tooth head as it can be seen in Fig. 14. Decrease of saturation level in this area can be achieved by utilizing semi-closed slots, or increasing the height and permeability of semi-magnetic wedges. This is a question of more thorough optimization and is not considered in this paper.

Fig. 15 shows the torque ripple of the modified machine during one electrical period. The magnitude of the 6^{th} harmonic is decreased to 3.2 Nm.

Adjustment of the teeth widths has reduced the torque ripple by 33 %; and all other characteristics of the machine have not changed considerably. This justifies the proposed technique for torque ripple minimization in high-torque-density TC-PMSMs. If even lower torque ripple is required from the machine, then teeth widths of all teeth should be increased in order to decrease the flux density and avoid excessive saturation.

The adjustment positively influences on the torque ripple reduction in applications where single direction of rotation is prevailing. If the direction of rotation needs to be changed, this torque ripple reduction technique is not effective, as the obtained machine structure is not symmetrical. If the direction of rotation in motoring mode needs to be reversed, then the torque ripple will increase and machine performance will degrade. Fig. 16 shows the torque profile if direction of rotation

is reversed. Due to oversaturations in all the teeth, the average torque is decreased and torque ripple is increased.

However, if with reversed direction the mode of operation changes from motoring to generating, the performance of the machine is not degraded. Therefore, this method is applicable for machines with prevailing single direction of operation – such as wind generators, propulsion drives, fans and blowers, conveyor drives.

V. Conclusion

In this paper a new approach for torque ripple reduction in TC-PMSMs is introduced. The main idea is to adjust the teeth widths according to the saturation levels in order to decrease the oversaturation under loading conditions. The effectiveness of this method is demonstrated and validated by FEM simulations for single direction of rotation. The simulation results show 33 % reduction in torque ripple.

An empirical criterion for non-linear behaviour of tooth-coil electrical machines, which causes significant torque ripple, harmonics in back-EMF and inductance variation, is also suggested. The criterion simply indicates deep saturation in the main magnetic circuit of the machine when the relative permeability of the iron core in the region falls below $\mu_{\mathrm{r}} = 100$ for silicon electrical steels as a result of region saturation under loading with peak currents.

References

[1] A. EL-Refaie, "Fractional-slot concentrated-windings synchronous permanent magnet machines: Opportunities and challenges," *Industrial Electronics, IEEE Transactions on*, vol. 57, no. 1, pp. 107–121, 2010.

[2] A. El-Refaie, "Fractional-slot concentrated-windings: A paradigm shift in electrical machines," in *Electrical Machines Design Control and Diagnosis (WEMDCD), 2013 IEEE Workshop on*, 2013, pp. 24–32.

[3] P. Ponomarev, *Tooth-Coil Permanent Magnet Synchronous Machine Design for Special Applications*. Lappeenranta, Finland: Acta Universitatis Lappeenrantaenisi 531, 2013.

[4] I. Petrov and J. Pyrhonen, "Performance of low-cost permanent magnet material in pm synchronous machines," *Industrial Electronics, IEEE Transactions on*, vol. 60, no. 6, pp. 2131–2138, 2013.

[5] T. Jahns and W. Soong, "Pulsating torque minimization techniques for permanent magnet ac motor drives-a review," *Industrial Electronics, IEEE Transactions on*, vol. 43, no. 2, pp. 321–330, 1996.

[6] P. Lindh, J. Pyrhonen, P. Ponomarev, and D. Vinnikov, "Influence of wedge material on losses of a traction motor with tooth-coil windings," in *Industrial Electronics Society, IECON 2013 - 39th Annual Conference of the IEEE*, Nov 2013, pp. 2941–2946.

[7] Z. Azar, Z. Q. Zhu, and G. Ombach, "Influence of electric loading and magnetic saturation on cogging torque, back-emf and torque ripple of pm machines," *Magnetics, IEEE Transactions on*, vol. 48, no. 10, pp. 2650–2658, 2012.

[8] D. Ishak, Z. Zhu, and D. Howe, "Permanent-magnet brushless machines with unequal tooth widths and similar slot and pole numbers," *Industry Applications, IEEE Transactions on*, vol. 41, no. 2, pp. 584–590, March 2005.

[9] Y. Chen, Z. Zhu, and D. Howe, "Slotless brushless permanent magnet machines: influence of design parameters," *Energy Conversion, IEEE Transactions on*, vol. 14, no. 3, pp. 686–691, Sep 1999.

[10] N. Bianchi and S. Bolognani, "Design techniques for reducing the cogging torque in surface-mounted pm motors," *Industry Applications, IEEE Transactions on*, vol. 38, no. 5, pp. 1259–1265, Sep 2002.

[11] F. Magnussen and C. Sadarangani, "Winding factors and joule losses of permanent magnet machines with concentrated windings," in *Electric Machines and Drives Conference, 2003. IEMDC'03. IEEE International*, vol. 1, 2003, pp. 333–339 vol.1.

[12] Z. Zhu and D. Howe, "Influence of design parameters on cogging torque in permanent magnet machines," *Energy Conversion, IEEE Transactions on*, vol. 15, no. 4, pp. 407–412, 2000.

[13] P. Ponomarev, I. Petrov, and J. Pyrhonen, "Influence of travelling current linkage harmonics on inductance variation, torque ripple and sensorless capability of tooth-coil permanent-magnet synchronous machines," *Magnetics, IEEE Transactions on*, vol. 50, no. 1, pp. 1–8, 2014.

[14] G. Dajaku and D. Gerling, "A novel 12-teeth/10-poles pm machine with flux barriers in stator yoke," in *Electrical Machines (ICEM), 2012 XXth International Conference on*, Sept 2012, pp. 36–40.

[15] P. Ponomarev and J. Pyrhonen, "Current linkage harmonics and air-gap harmonic leakage inductance of tooth-coil permanent-magnet synchronous machines," in *Industrial Electronics Society, IECON 2013 - 39th Annual Conference of the IEEE*, Nov 2013, pp. 2703–2708.

[16] L. Alberti, E. Fornasiero, and N. Bianchi, "Impact of the rotor yoke geometry on rotor losses in permanent-magnet machines," *Industry Applications, IEEE Transactions on*, vol. 48, no. 1, pp. 98–105, Jan 2012.

[17] L. Alberti, M. Barcaro, and N. Bianchi, "Design of a low torque ripple fractional-slot interior permanent magnet motor," pp. 1–1, 2013.

[18] P. Reddy, K. Huh, and A. El-Refaie, "Generalized approach of stator shifting in interior pm machines equipped with fractional-slot concentrated windings," pp. 1–1, 2014.

[19] I. Petrov, P. Ponomarev, Y. Alexandrova, and J. Pyrhnen, "Torque ripple reduction in permanent magnet synchronous machines with fractional-slot non-overlapping windings by geometry adjustment," *Magnetics, IEEE Transactions on*, pp. 1–8, under review 2014.

[20] P. Ponomarev, P. Lindh, and J. Pyrhonen, "Effect of slot-and-pole combination on the leakage inductance and the performance of tooth-coil permanent-magnet synchronous machines," *Industrial Electronics, IEEE Transactions on*, vol. 60, no. 10, pp. 4310–4317, 2013.

[21] P. Ponomarev, J. Alexandrova, I. Petrov, P. Lindh, E. Lomonova, and J. Pyrhonen, "Inductance calculation of tooth-coil permanent-magnet synchronous machines," pp. 1–1, 2014.

[22] M. Islam, S. Mir, T. Sebastian, and S. Underwood, "Design considerations of sinusoidally excited permanent-magnet machines for low-torque-ripple applications," *Industry Applications, IEEE Transactions on*, vol. 41, no. 4, pp. 955–962, July 2005.

[23] P. Sergeant and A. Van Den Bossche, "Influence of the amount of permanent magnet material in fractional-slot permanent magnet synchronous machines," pp. 1–1, 2013.

Pavel Ponomarev (M'05) born in 1985 in Arkhangelsk, Russia, received the D.Sc. degree in 2013 from Lappeenranta University of Technology (LUT), Finland. He worked as a software engineer at Automation Department of Central Research Institute of Ship's Electrical Technology, Saint-Petersburg, Russia. He is currently a post-doctoral researcher at the Laboratory of Electrical Drives Technology, LUT Energy. His current interests include electrical drives and permanent magnet machines.

Ilya Petrov received the M.Sc. degree from Lappeenranta University of Technology (LUT), Finland, in 2011. He is currently a Ph.D. student at the Laboratory of Electrical Drives Technology at LUT. His main research interest is in the design and optimization of PMSMs.

Juha Pyrhnen (M'06) born in 1957 in Kuusankoski, Finland, received the Doctor of Science (D.Sc.) degree from Lappeenranta University of Technology (LUT), Finland in 1991. He became a Professor of Electrical Machines and Drives in 1997. He is currently the Head of the Department of Electrical Engineering at the Institute of Energy Technology (LUT Energy). He is engaged in the research and development of electric motors and electric drives.

ACTA UNIVERSITATIS LAPPEENRANTAENSIS

600. SAUKKONEN, ESA.Effects of the partial removal of wood hemicelluloses on the properties of kraft pulp. 2014. Diss.

601. GUDARZI, DAVOOD.Catalytic direct synthesis of hydrogen peroxide in a novel microstructured reactor. 2014. Diss.

602. VALKEAPÄÄ, ANTTI.Development of finite elements for analysis of biomechanical structures using flexible multibody formulations. 2014. Diss.

603. SSEBUGERE, PATRICK.Persistent organic pollutants in sediments and fish from Lake Victoria, East Africa. 2014. Diss.

604. STOKLASA, JAN.Linguistic models for decision support. 2014. Diss.

605. VEPSÄLÄINEN, ARI. Heterogenous mass transfer in fluidized beds by computational fluid dynamics. 2014. Diss.

606. JUVONEN, PASI.Learning information technology business in a changing industry landscape. The case of introducing team entreneurship in renewing bachelor education in information technology in a university of applied sciences. 2014. Diss.

607. MÄKIMATTILA, MARTTI.Organizing for systemic innovations – research on knowledge, interaction and organizational interdependencies. 2014. Diss.

608. HÄMÄLÄINEN, KIMMO.Improving the usability of extruded wood-plastic composites by using modification technology. 2014. Diss.

609. PIRTTILÄ, MIIA. The cycle times of working capital: financial value chain analysis method. 2014. Diss.

610. SUIKKANEN, HEIKKI. Application and development of numerical methods for the modelling of innovative gas cooled fission reactors. 2014. Diss.

611. LI, MING. Stiffness based trajectory planning and feedforward based vibration suppression control of parallel robot machines. 2014. Diss.

612. KOKKONEN, KIRSI. From entrepreneurial opportunities to successful business networks – evidence from bioenergy. 2014. Diss.

613. MAIJANEN-KYLÄHEIKO, PÄIVI. Pursuit of change versus organizational inertia: a study on strategic renewal in the Finnish broadcasting company. 2014. Diss.

614. MBALAWATA, ISAMBI SAILON. Adaptive Markov chain Monte Carlo and Bayesian filtering for state space models. 2014. Diss.

615. UUSITALO, ANTTI. Working fluid selection and design of small-scale waste heat recovery systems based on organic rankine cycles. 2014. Diss.

616. METSO, SARI. A multimethod examination of contributors to successful on-the-job learning of vocational students. 2014. Diss.

617. SIITONEN, JANI. Advanced analysis and design methods for preparative chromatographic separation processes. 2014. Diss.

618. VIHAVAINEN, JUHANI. VVER-440 thermal hydraulics as computer code validation challenge. 2014. Diss.

619. AHONEN, PASI. Between memory and strategy: media discourse analysis of an industrial shutdown. 2014. Diss.

620. MWANGA, GASPER GODSON. Mathematical modeling and optimal control of malaria. 2014. Diss.

621. PELTOLA, PETTERI. Analysis and modelling of chemical looping combustion process with and without oxygen uncoupling. 2014. Diss.

622. NISKANEN, VILLE. Radio-frequency-based measurement methods for bearing current analysis in induction motors. 2014. Diss.

623. HYVÄRINEN, MARKO. Ultraviolet light protection and weathering properties of wood-polypropylene composites. 2014. Diss.

624. RANTANEN, NOORA. The family as a collective owner – identifying performance factors in listed companies. 2014. Diss.

625. VÄNSKÄ, MIKKO. Defining the keyhole modes – the effects on the molten pool behavior and the weld geometry in high power laser welding of stainless steels. 2014. Diss.

626. KORPELA, KARI. Value of information logistics integration in digital business ecosystem. 2014. Diss.

627. GRUDINSCHI, DANIELA. Strategic management of value networks: how to create value in cross-sector collaboration and partnerships.2014. Diss.

628. SKLYAROVA, ANASTASIA. Hyperfine interactions in the new Fe-based superconducting structures and related magnetic phases.2015. Diss.

629. SEMKEN, R. SCOTT.Lightweight, liquid-cooled, direct-drive generator for high–power wind turbines: motivation, concept, and performance. 2015. Diss.

630. LUOSTARINEN, LAURI. Novel virtual environment and real-time simulation based methods for improving life-cycle efficiency of non-road mobile machinery. 2015. Diss.

631. ERKKILÄ, ANNA-LEENA. Hygro-elasto-plastic behavior of planar orthotropic material. 2015. Diss.

632. KOLOSENI, DAVID. Differential evolution based classification with pool of distances and aggregation operators. 2015. Diss.

633. KARVONEN, VESA. Identification of characteristics for successful university-company partnership development. 2015. Diss.

634. KIVYIRO, PENDO. Foreign direct investment, clean development mechanism, and environmental management: a case of Sub-Saharan Africa. 2015. Diss.

635. SANKALA, ARTO. Modular double-cascade converter. 2015. Diss.

636. NIKOLAEVA, MARINA. Improving the fire retardancy of extruded/coextruded wood-plastic composites. 2015. Diss.

637. ABDEL WAHED, MAHMOUD. Geochemistry and water quality of Lake Qarun, Egypt. 2015. Diss.